NIST
National Institute of
Standards and Technology
U.S. Department of Commerce

*NIST Technical Note 1549*

# Electromagnetic Airframe Penetration Measurements of the FAA's 737-200

C. Grosvenor
D. Novotny
D. Camell
G. Koepke
R.T. Johnk
N. Canales

NIST Technical Note 1549

# Electromagnetic Airframe Penetration Measurements of the FAA's 737-200

Chriss Grosvenor, David Novotny, Dennis Camell, Galen Koepke
*Electromagnetics Division*
*Electromagnetics and Electrical Engineering Laboratory*
*National Institute of Standards and Technology*
*Boulder, CO 80305-3328*

Robert T. Johnk
*National Telecommunication and Information Agency*
*Institute for Telecommunications Sciences*
*Boulder, CO 80305-3328*

Seturnino Canales
*Formerly with the National Institute of Standards and Technology*
*5857 Scenic Ave.*
*Firestone, CO 80504-5652*

March 2010

**U.S. Department of Commerce**
Gary Locke, Secretary

**National Institute of Standards and Technology**
Patrick Gallagher, Director

National Institute of Standards and Technology
Technical Note 1549
Natl. Inst. Stand. Technol.
Tech. Note 1549
**237 pages** (March 2010)
CODEN: NTNOEF

U.S. Government Printing Office
Washington: 2010

For Sale by the
Superintendent of Documents
U.S. Government Printing Office
Stop SSOP, Washington, DC 20402-0001
Phone: (202) 512-1800
Fax: (202) 512-2250
Internet: bookstore.gpo.gov

## Contents

# Electromagnetic Airframe Penetration Measurements for the FAA Passenger Jet 737-200

Chriss Grosvenor, David Novotny, Dennis Camell, and Galen Koepke

Electromagnetics Division
National Institute of Standards and Technology
325 Broadway
Boulder, CO 80305

and

Robert T. Johnk

National Telecommunication and Information Agency
Institute for Telecommunication Sciences
325 Broadway
Boulder, CO 80305

and

Seturnino Canales
Formerly with NIST
5857 Scenic Ave.
Firestone, CO 80504-5652

*The National Institute of Standards and Technology has completed shielding effectiveness/penetration studies on three different aircraft types for the Federal Aviation Administration. The studies are used to understand the cavity coupling characteristics between antennas placed in various compartments inside the aircraft and antennas placed at various angular positions around an aircraft. This document shows how penetration varies as a function of frequency, antenna type, antenna polarization, and cavity susceptibility for a 737-200 passenger jet. The document discusses initial numerical analysis, antenna gain dependence, and ground bounce effects and how they impact the data. Internal coupling between two antennas placed in the aircraft at different locations was studied and a statistical analysis of the insertion loss between various compartments is also presented.*

*Key words: aircraft; cavity coupling; digital signal processing; HIRF; numerical modeling; penetration; shielding effectiveness; synthetic time-domain measurements.*

# 1. History and Background

The Federal Aviation Administration (FAA) is responsible for the safety of civilian aviation [1]. Included in this function is the responsibility to ensure that the flight hardware is safe from an electromagnetic interference (EMI) event that could jam navigational equipment and render flight hardware inoperable. The avionics systems are flight critical, and uninterrupted operation is required in order to fly the aircraft safely. There is a history of EMI-induced system failures in both military and commercial electronic systems [2–5]. This is one of the reasons why manufacturers of aircraft are required to submit test data showing that their aircraft can provide enough protection or shielding of interior flight systems from outside electromagnetic sources. These tests are called high intensity radiated field (HIRF) measurements and are used to determine the shielding effectiveness of the aircraft from radiating sources [6–13]. HIRF sources are only those emitters that intentionally generate emissions. HIRF sources include radio and TV transmitters, airport and weather radar, and various military systems, both ground-based and airborne, such as surveillance radar, electronic warfare (EW) systems, and electromagnetic weapons. These radiating sources can also include ground tracking radars, electromagnetic pulse (EMP) events, both natural and man-made, such as lightning or EMP ordnance, cell phones, electrostatic discharge (ESD), and other events. The hazard levels for these interferers have been studied [14] and are incorporated into HIRF test methodologies [15].

Manufacturer's HIRF data are given to the FAA for inspection but are often not accompanied by a detailed test report as to how the tests were performed. Often the data have very noise-like characteristics and are difficult to interpret. The National Institute of Standards and Technology (NIST) has had previous experience with measuring the shielding effectiveness of aircraft [16 - 19]. For this reason, the FAA approached NIST to provide guidance on the interpretation of the HIRF measurement results. The project was three-fold: (1) analyze canonical structures by use of numerical methods, (2) develop efficient measurement and data-processing methods based on the numerically modeled results, and (3) perform an extensive set of measurements on an actual aircraft. Once these tasks were completed, the FAA would have a more complete understanding of common measurement methods supported by detailed numerical analyses.

The Field Parameters and EMC Applications Project of the National Institute of Standards and Technology (NIST) has now completed shielding effectiveness/penetration studies of three representative aircraft for the Federal Aviation Administration (FAA). These studies will provide the FAA with the procedures and data-reduction techniques for typical low-signal-level airframe penetration for high-intensity radiated field (HIRF) attenuation/shielding tests. This technical note addresses aircraft shielding tests conducted on a 737-200 passenger jet owned and operated by the FAA. Two additional reports have been completed involving studies of (1) a Bombardier Global 5000 business jet owned and operated by the FAA [18] and (2) a Beechcraft Premier IA owned by the Hawker-Beechcraft Corporation [19]. The Bombardier Global 5000 represents a commercial business jet, and the Premier IA represents a typical carbon-composite aircraft. By measuring all three aircraft and comparing them, we have the potential to provide a "design roadmap" for the optimization of HIRF testing standards for the electromagnetic compatibility (EMC) aircraft manufacturing community.

The FAA currently has specific certification policies addressing the effects of HIRF on an aircraft's electrical and electronic systems that have been applied since around 1990 [15]. This document is presently being rewritten, and a new draft is expected to be completed in 2010. In the current FAA document, the regulatory authorities and industry have defined HIRF environments, requirements for aircraft HIRF protection, and methods for testing and verifying the level of HIRF protection. Most of reference [15] discusses HIRF testing for electronic and electrical subsystems, which this technical note does not address. In this technical note, we specifically address both high- and low-level airframe shielding compliance testing. The HIRF procedures are found in Section 6.6.2.6 and Section 6.6.4 of Reference [15].

The basic problem is to evaluate the coupling of an external source into a large, electromagnetically leaky cavity [20 – 27]. The cavity could represent the whole aircraft or part of it (cargo bay, flight deck, etc.), depending on the expected vulnerability. In a typical HIRF measurement, the measurement system is calibrated, and a reference measurement is taken without the aircraft embedded in the test setup. The aircraft is then placed into the test setup and various measurements are taken in susceptible cavities. These attenuation tests are typically conducted by use of either mechanical stirring or frequency-stirring methods [13–15]. The airframe attenuation is calculated by use of the following equation:

$$A_{atten} = S.E. = \frac{reference\ measurement}{cavity\ measurement}, \qquad (1)$$

where $A_{atten}$ is the airframe attenuation and *S.E.* is defined as the shielding effectiveness. These numbers, expressed in decibels, are typically positive, so that the more positive the number, the greater the protection the aircraft provides to electromagnetic fields, and as the number approaches zero we expect almost no shielding protection. The aircraft HIRF attenuation data vary as a function of frequency, physical position of the measurement antenna, angle of incidence, polarization, characteristics of the aircraft, and configuration of the test site. After a company tests and processes the data, the information is given to the FAA, which uses it in conjunction with the subsystem susceptibility tests to determine an aircraft's HIRF vulnerability.

The detailed method used to process aircraft HIRF attenuation data is not well documented and is closely held by the handful of test service providers. Therefore, the interpretation of the data is not immediately obvious to the certification engineer. This technical note and the previous two technical notes consider attenuation measurements as a function of frequency, antenna position, antenna type, and cavity selection. Our data-processing methodology will be shown in detail. Using this information, we hope to provide guidelines for both the FAA and test engineers to develop a uniform and transparent test method for data processing and documentation. We know that the confidence levels are expected to depend on the number of sample points (measurement geometries), but we should be able to assess the trade-offs between measurement effort (sample number) and risk (confidence level).

## 2. Overview

This report summarizes results of two measurement efforts conducted by the Field Parameters and EMC Applications Project team of NIST. This effort consisted of an extensive series of penetration, internal, and ground-condition measurements performed on a 737-200 passenger jet owned and operated by the FAA. The aircraft was tested at the FAA site in Atlantic City, New Jersey during two periods from October 2004 to October 2005. The purpose of these efforts is to provide the FAA with a database of penetration and insertion loss data on the 737-200 passenger jet.

Both efforts utilized NIST-developed measurement systems consisting of ultra-wideband transverse electromagnetic (TEM) horn antennas, 3115 dual-ridged guided (DRG) horn antennas, commercially available vector network analyzers (VNAs), interconnecting transmission media, and an amplifier for the second effort. The first effort measured penetration from approximately 100 MHz to 2.5 GHz. Interconnections between transmitting and receiving antennas were made using an 11 GHz precision, analog electro-optic link. The second effort combined both the 11 GHz and the 18GHz precision, analog electro-optic links. These efforts were the first time NIST researchers used a broadband, analog, electro-optic link with a COTS (commercially available off-the-shelf) VNA for airframe shielding studies up to 18 GHz. Shielding data were obtained from a direct comparison of two measurements: (1) a transmission measurement between boresighted antennas located outside the aircraft to obtain a reference, and (2) transmission measurements with one antenna located inside a selected compartment of the aircraft and a pair of horizontally and vertically polarized antennas for both low-frequency-band and high-frequency-band antennas located outside the aircraft at specified locations. Shielding data were obtained by comparing processed reference and aircraft transmission data. This was achieved by use of an efficient sequence of Fourier and inverse Fourier transformations, frequency domain convolutions, and filtering combined with time gating and frequency averaging. Shielding values were obtained by taking the ratio of the gated amplitude spectra of the aircraft measurement and the gated amplitude spectra of the references. Data smoothing was performed by use of the frequency-averaging of signal power over a specified bandwidth as described in [16]:

$$\left\langle SE(f_n)\right\rangle = \frac{1}{2N+1}\sum_{i=n-N}^{n+N}\left|SE\left(f_i\right)\right|^2 . \tag{1}$$

Shielding data were obtained with a receiving antenna located in one of four internal compartments: (1) the main passenger cabin, (2) the flight deck, (3) the cargo bay, and (4) the avionics bay. A pair of transmitting antennas was positioned outside the aircraft at a fixed height of approximately 5 m, which is the approximate height of the windows, at a fixed distance of 23 m from the center of the aircraft. The transmitting antennas were boresighted at the center of the aircraft, and data were obtained for both the horizontal and vertical polarizations. We based our tests on HIRF standard test procedures and other questions we felt were important to ask. These standards are concerned with detecting possible leakage into the aircraft. Key areas include the flight deck, the avionics bay, any windows/doors/joints, and the wing/tail section of the fuselage. During our first effort, we developed a test plan designed to understand the effect of varying ground conditions on the data [28], and how many positions are necessary to fully characterize an electrically large object and to fully characterize the fields penetrating into the aircraft for a particular high-frequency limit [29–32]. For this reason, we included a number of angular positions to study penetration apertures around the aircraft and at six positions around the rear one-fourth sector of the aircraft at a constant distance from the center of the aircraft. Finally, we concluded with an extensive set of internal coupling measurements designed to understand the interaction between compartments and the reverberation characteristics of the aircraft. This first effort consisted of the following measurements: (1) Extrapolation measurements at 6.1 m (20 ft.), 9.1 m (30 ft.), 12.1 m (40 ft.), 15.2 m (50 ft.), 23.5 m (75 ft.), and 30.1 m (100 ft.); (2) Extrapolation measurements at 15.2 m, 23.5 m, and 30.5 m for ground conditions including the tarmac and a sheet of rFoil (radiant barrier foil), which consists of a layer of polyethylene bubbles bonded to and sandwiched between two highly reflective surfaces [33], for both vertical and horizontal polarization; (3) sector measurements at 90°,100°, 110°, 120°, 125°, 130°, 135°, 140°, 145°, 150°, 160°, 170° and 180° to look at the angular dependence of radiating apertures. Finally, in the first effort, we concluded with a set of internal coupling measurements to understand the reverberant environment internal to the aircraft. An aircraft's level of electromagnetic field protection, referred to as shielding, depends on the level of treatment, the compartment, the frequency, the transmitting antenna polarization, and the angle of illumination. In this document, we will display penetration values, which are the reciprocal of shielding values. In the graphs that follow, a penetration near 0 dB means electromagnetic fields can easily penetrate into that part of the aircraft. Penetration levels for the FAA's Boeing 737-200 commercial aircraft range from approximately −10 dB to −40 dB. The dynamic range of this system is a function of the compartment in which it is located. For the system in the main cabin, the estimated dynamic range is −70 dB at 1000 MHz and −50 dB at 3000 MHz. For the system in the cargo bay, the estimated dynamic range is −60 dB at 1000 MHz and −40 dB at 3000 MHz.

This report is divided into five main sections: (1) Initial theoretical and simulation analysis, (2) a description of the measurement system, (3) an overview of the measurement technique, (4) an overview of the signal processing, (5) a summary of results for the four different aircraft compartments and various internal measurements, and (6) an uncertainty analysis. Appendices A through E discuss the number of positions versus the average power, whisker-box plots showing how frequency bandwidths affect the statistics of the Bombardier Global 5000 and Beechcraft Premier IA results, simple numerical modeling results, an equipment list, and the gain characteristics of the ultra-wideband antennas that were used.

## 3. Initial Simulations, Theoretical Analysis, and Measurements

### 3.1 Frequency averaging

We began these efforts by doing some theoretical analysis to understand the importance of certain parameters and their impact on aircraft measurements. An initial finite-difference, time-domain (FDTD) model was developed for a pulsed source in free-space. Other models have been developed for HIRF radiation levels [20–21]. Figure 1 shows the time-domain waveform that results from the model. The electromagnetic fields can be seen emanating from the pulsed source on the left to a monitor point on the right. A plot showing the initial time-domain pulse is shown on the right. The onset of the impulse occurs at around 20 ns and the impulse response is around 2 ns. We then modeled a slot in an infinite ground plane as shown in Figure 2. The pulsed source was on one side of the infinite ground plane, and the monitor point was on the other. The frequency-domain waveform corresponding to Figure 2 is shown in Figure 3. The plot shows the resonances that result from the electromagnetic waves penetrating through the slot and being received at the monitor point.

The next model took a portion of the infinite ground plane with the slot and backed it with a box based on the dimensions of a reverberant box designed by NIST and the Naval Surface Warfare Center. The dimensions were selected to permit sufficient modal density above 1 GHz, to achieve reverberant behavior inside the box, and to exhibit characteristics of an electrically large cavity (see Figure 4). Aluminum was chosen for fabrication ease and its high electrical conductivity. A rotatable aluminum paddle, powered by an external d.c. motor, was installed within the box to provide mode-stirring. Five holes 1.6 cm in diameter were randomly punched on each side of the box. We chose this diameter so that all apertures were electrically small from 2 GHz to 4 GHz and to achieve a shielding effectiveness in the range of 20 dB to 30 dB. This range of shielding values is based on theoretical guidelines and was verified by use of measurements performed in the reverberation chamber [25]. The FDTD box model is shown in Figure 5. The time-domain and frequency-domain signatures of the slotted box problem are shown in Figures 6 and 7. The time-domain figures show that the signal reaches the monitor point starting at around 25 ns. From this time forward we obtain a slowly decaying electric field amplitude. When an Fast-Fourier Transform (FFT) is applied to the time-domain waveform we obtain the frequency-domain plot, also shown in Figure 6. The result shows a noisy looking waveform where not much important information is available. To bring out important details and minimize the noise, we averaged the frequency-domain data over a small bandwidth of frequencies [16]. Figure 7 shows the result of frequency averaging for bandwidths of 50 MHz and 100 MHz, respectively. The wider the bandwidth the greater the effect of smoothing the data; however, we do see that the original resonances that occurred for the slit in the infinite round plane are now revealed.

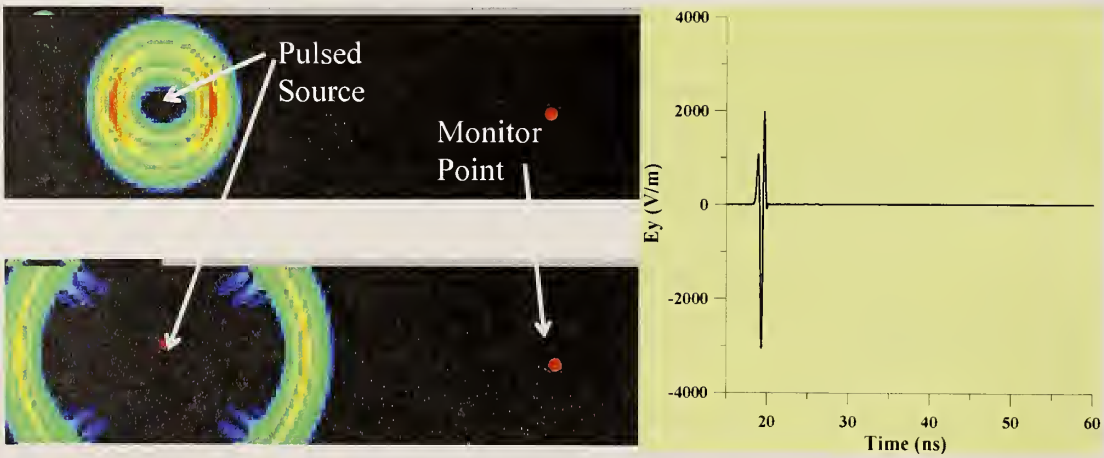


Figure 1. FDTD Modeling and result for pulsed source in free space.

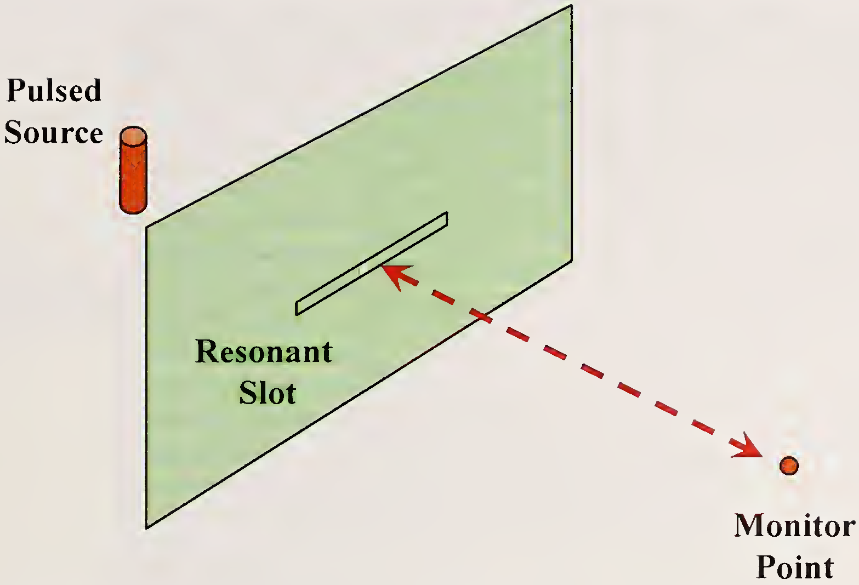


Figure 2. Resonant slot in an infinite ground plane.

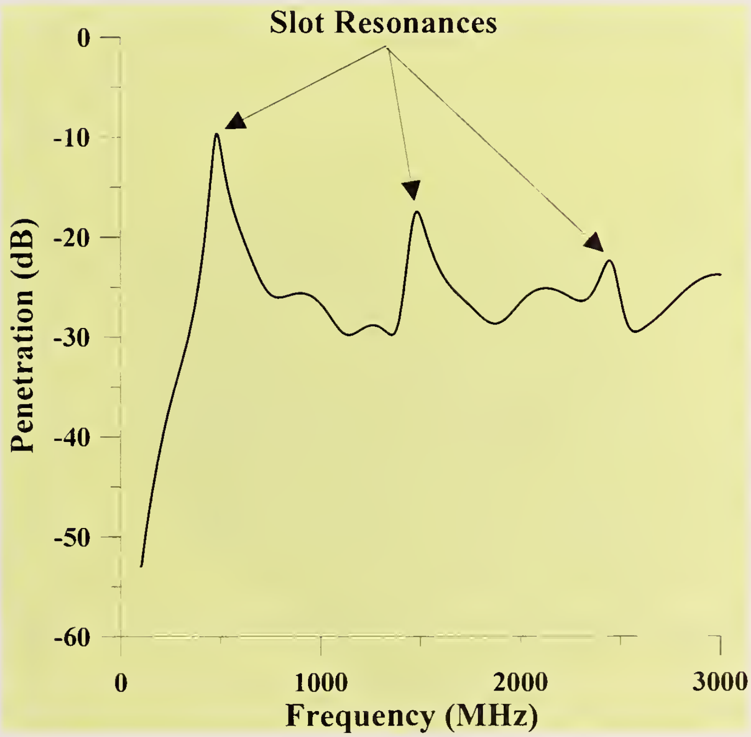


Figure 3. Slot resonances from a slit in an infinite ground plane.

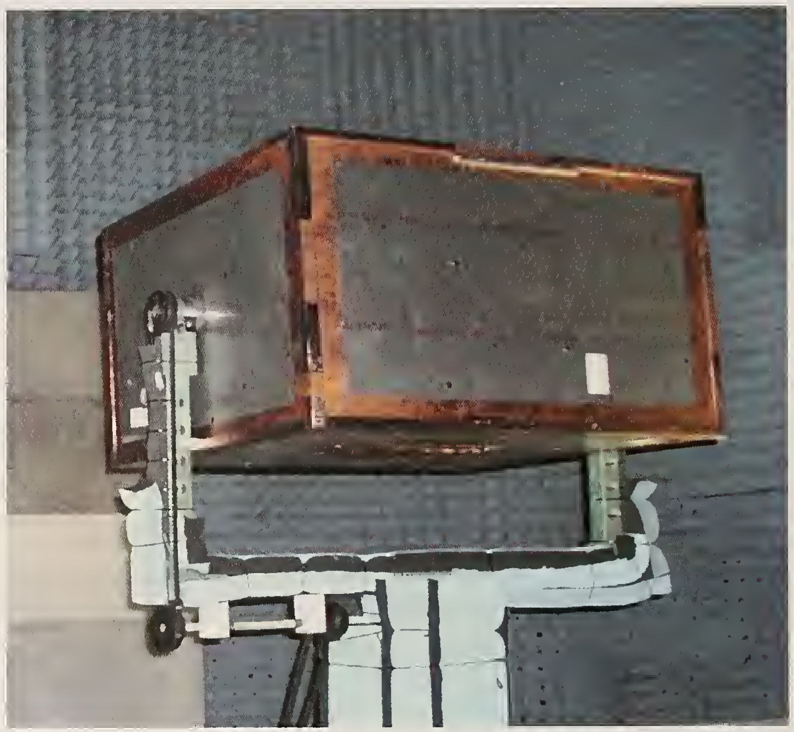

Figure 4. Aluminum reverberant box designed to simulate 20 to 30 dB of shielding.

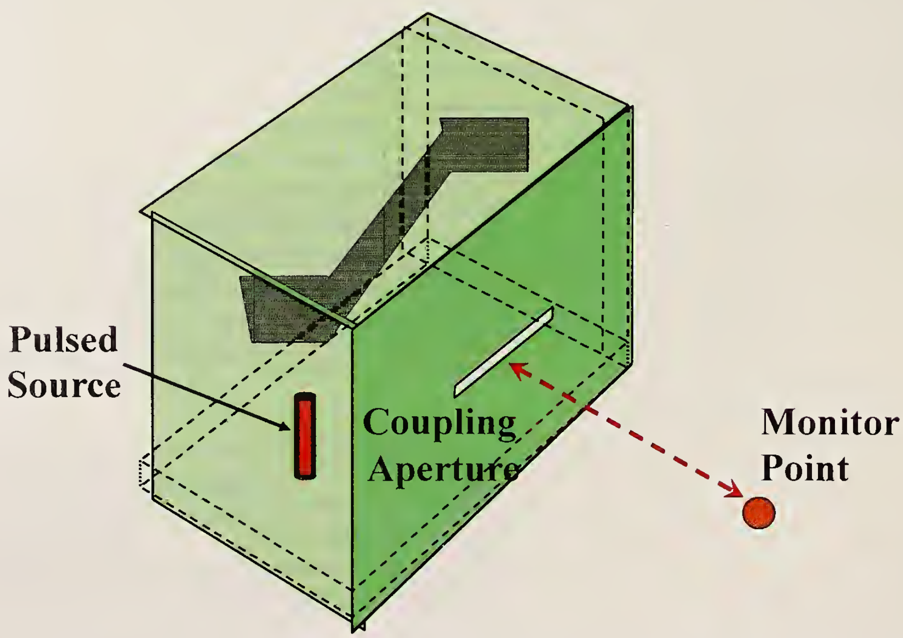


Figure 5. FDTD Model of the NIST/Naval Surface Warfare Center Shielded Enclosure.

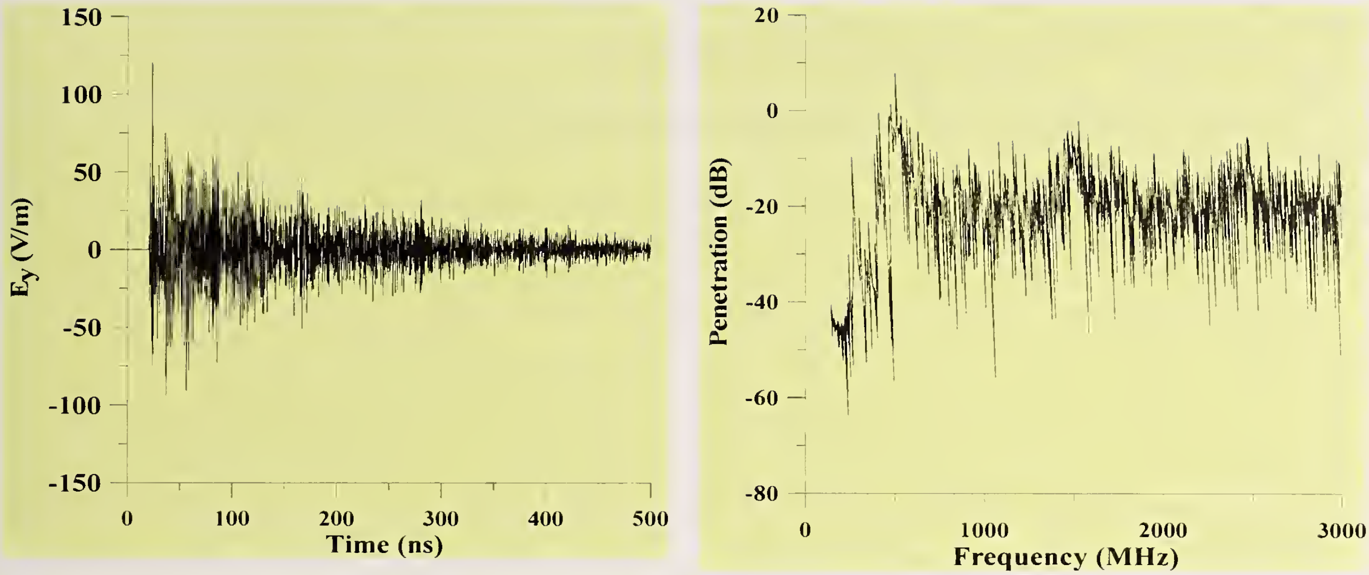


Figure 6.  Time-domain and frequency-domain waveforms for a pulsed source in a slotted box.

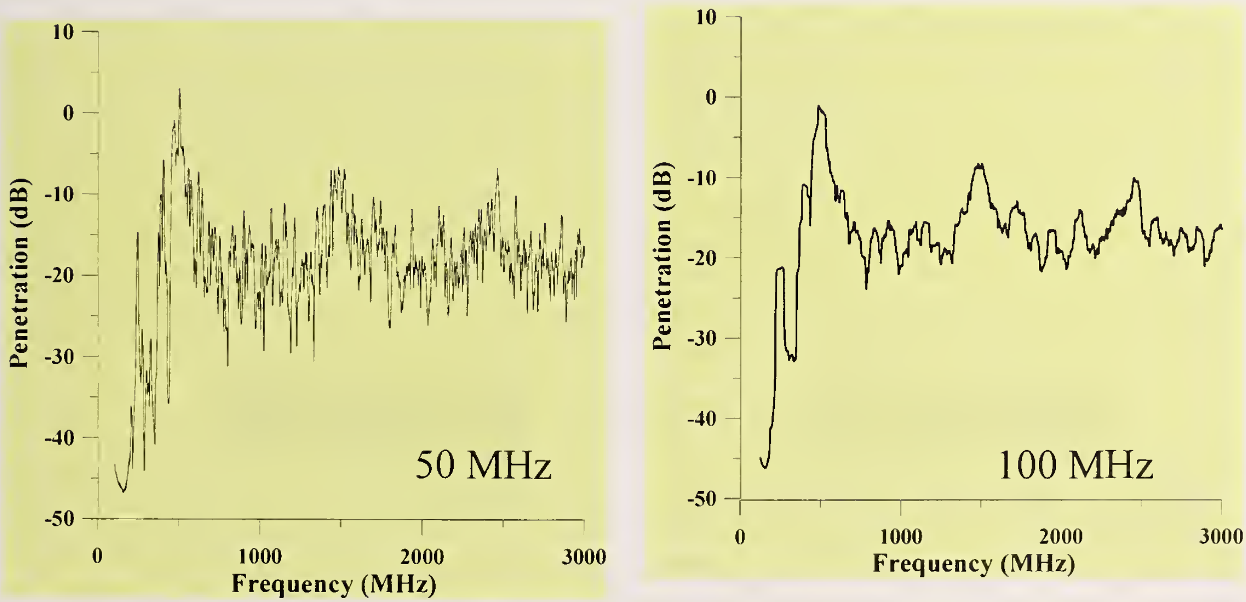


Figure 7.  A 50 MHz and 100 MHz frequency averaging bandwidth applied to the waveform in Figure 6.

## 3.2 Ground Bounce and other Effects

### 3.2.1 Ground Bounce in a Laboratory Environment

#### 3.2.1.1 Time-of-flight for direct antenna response and ground bounce response

The effect of ground bounce and ground conditions are important when one measures penetration into an aircraft either sitting on a hangar floor or on the tarmac [28]. This is because ground bounce is not an effect seen when an aircraft is in flight as the electromagnetic radiating field impinges on the aircraft. Ideally, the aircraft should be measured in flight to avoid these types of effects; however costs and ease of measurements are impractical. To understand the effect of ground bounce on our measurements, we began with the following analysis. We measure the transmission in our laboratory for two 1.2 m TEM horn antennas. These antennas have a short impulse response [34], so the initial direct antenna-to-antenna response can be isolated from the response due to the interaction with the ground, also known as ground bounce. A diagram showing the measurement setup is shown in Figure 8. From the geometry, we can determine the signal delay from one antenna to another for both the direct component and the ground-bounce component. If the antenna apertures are separated by 1.9 m and the additional delay due to 15 cm of cable and the antenna transition from the end of one calibration reference plane to another is taken into account, then the time of flight for the direct signal response will be approximately 23 ns. We can compute the time of flight for the ground-bounce component by knowing that the aperture center of the antenna was 1.7 m above the ground plane. The geometrical calculations tell us that the signal due to ground bounce should arrive at approximately 27 ns. Figure 9 shows two time-domain responses for the direct transmission component and the ground-bounce component. The black trace shows an initial direct

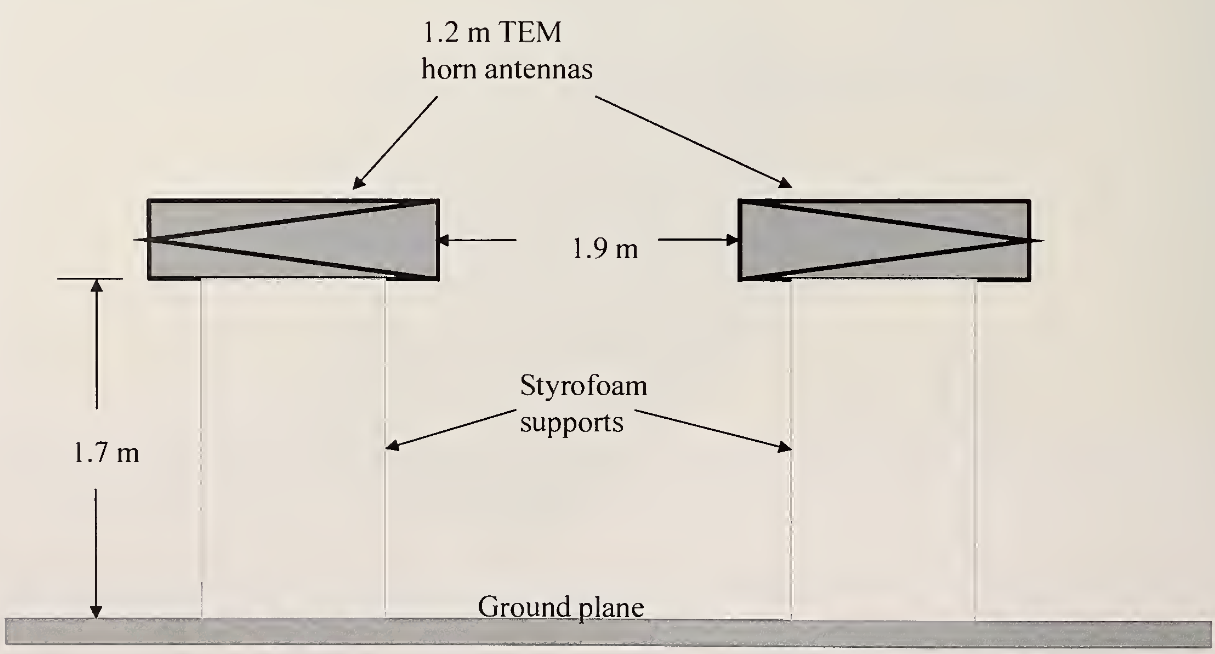


Figure 8. Laboratory setup for transmission measurement between 1.2 m TEM horn antennas.

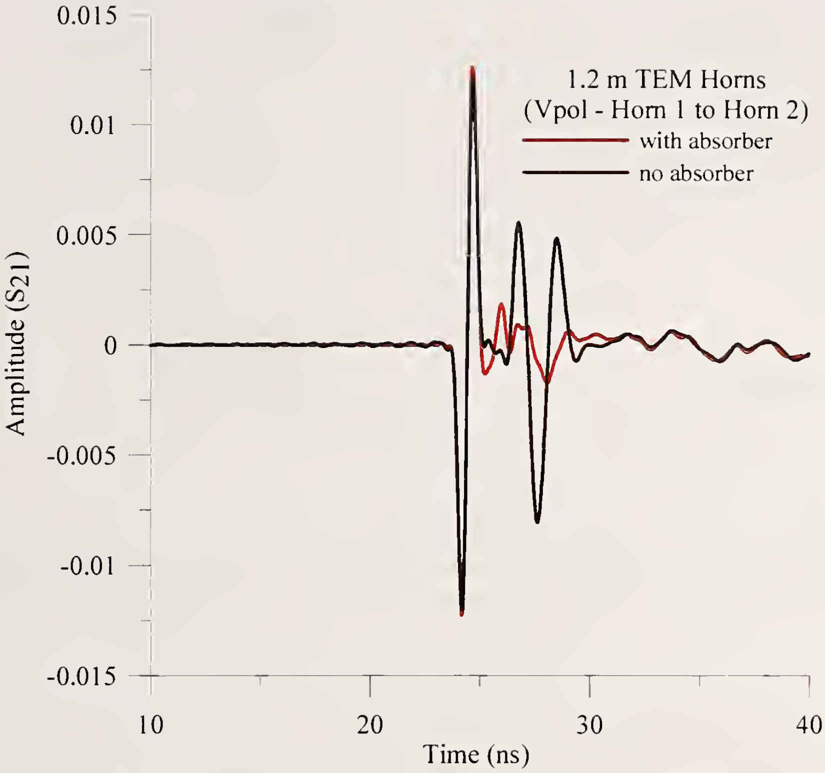


Figure 9. Typical reference measurement setup for 1.2 m TEM horn antennas on a laboratory ground plane. Distances are shown for the direct path and the secondary ground-bounce path.

component for signal transmission between the antennas and a second component due to the ground bounce. If absorber is placed on the ground plane between the antennas, then the red trace shows that the ground bounce has been minimized due to the presence of the absorber. By looking at the initial time for both responses, we see that the direct antenna-to-antenna impulse response begins at around 23 ns and the response due to the ground plane reflection occurs at around 27 ns, just as our geometrical ray-tracing model predicted.

### 3.2.1.2 Simulating ground bounce into a shielded enclosure

To look at ground-bounce effects and how they impact measurements into a shielded cavity, we set up a shielded cavity in our laboratory at NIST. The measurement setup is shown in Figure 10. A reference measurement was taken with the antennas at a height of 1.50 m and separated by a distance of 2 m. The antenna was placed inside the box (aperture facing the door), and another measurement with the door of the box fully open was taken. The door of the box was closed until a 15.24 cm (6 in.) gap existed at the top, and a measurement was taken. More measurements were taken with a 7.62 cm (3 in.) and a 2.54 cm (1 in.) gap. One measurement was taken with the antenna facing toward the back of the shielded box. The antenna was lowered on the tripod to a height of 1.35 m and measured with the 15.24 cm, 7.62 cm, and 2.54 cm gaps. Again the antenna was lowered to a height of 1.21 m and measurements of the same door gaps were taken. A time-domain reference waveform is shown in Figure 11 for two DRG horn antennas mounted on tripods and separated by a distance of 2 m at a height of 1.5 m.

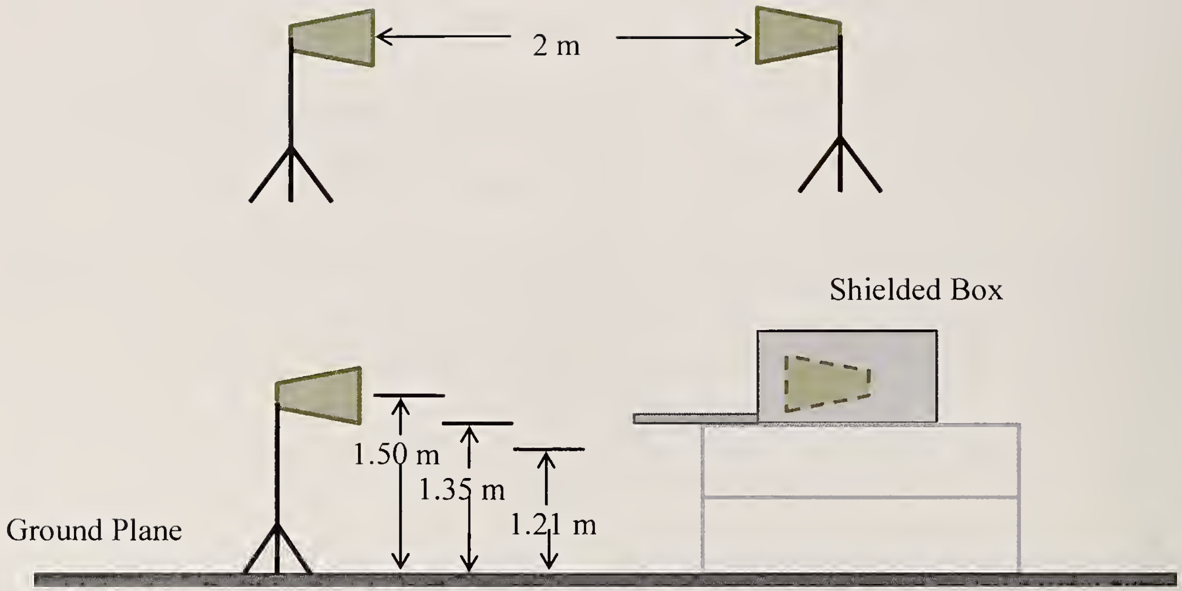


Figure 10. Measurement setup for ground-bounce experiment.

The red box shows the direct antenna-to-antenna response and the blue box shows the ground-bounce response. The antennas were placed into the shielded enclosure with the front door to the box fully open, and the time-domain waveform, shown in Figure 12, was acquired. Differences between the two waveforms can be seen due to the presence of the box, but the ground-bounce

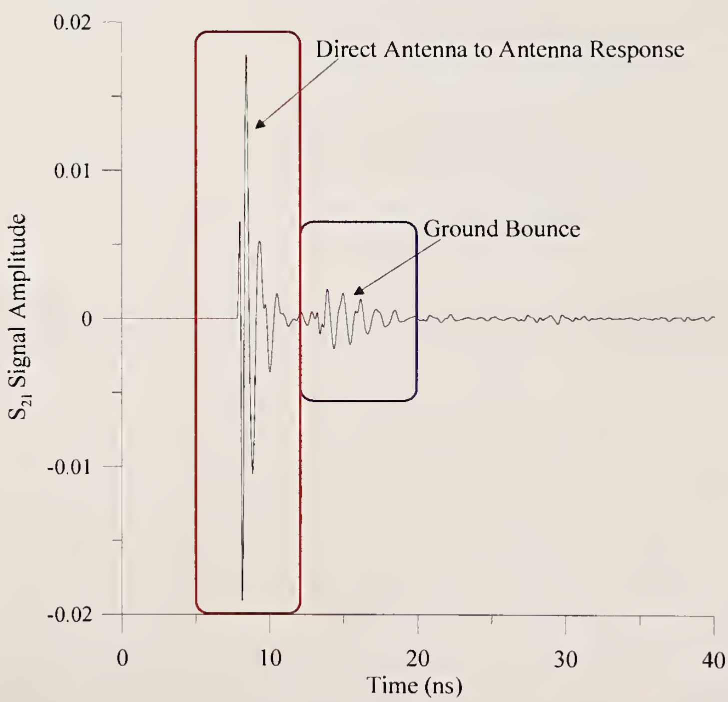


Figure 11. Time-domain reference waveform for two DRG antennas separated by 2 m.

response is still visible. The frequency spectrum for the two DRG antennas on tripods is shown in Figure 13. The black trace shows the frequency spectrum for the entire captured waveform including the direct antenna-to-antenna response and ground-bounce response. The red trace shows the frequency spectrum of the direct response only (the ground bounce has been time-gated out). The blue trace shows the frequency spectrum of the ground bounce with the direct response gated out. The separate, gated components (the direct antenna-to-antenna response and the ground bounce component) were then added together to see whether we obtained the original frequency spectrum. This is shown in Figure 14. The full spectrum is shown by the black trace, which includes all frequency responses including the laboratory environment. The separated, gated, ground-bounce component added to the gated, direct component is shown by the red trace. The extra noise-like behavior on the black trace is due to the laboratory's response.

Then we wanted to investigate the waveforms as the door to the shielded enclosure was shut incrementally. The ground bounce will begin to be unseparable from the initial impulse response of the antenna. However, if we assume that the ground bounce response occurs at the same time and we gate this part of the waveform from the total response, what happens to the frequency spectrum? Figure 15 shows the time-domain responses for a DRG antenna in the shielded box with the door open 15.24 cm and the transmitting antenna at a height of 1.5 m and 1.21 m, respectively. Figure 16 shows the time-domain responses for a DRG antenna in the shielded box with the door open 2.54 cm and the transmitting antenna at a height of 1.5 m and 1.21 m, respectively. The location where the ground bounce is expected is shown by the blue box as in Figures 11 and 12. The frequency spectra for the reference measurement (black trace) and the respective shielded box waveforms (blue trace) were plotted and are shown in Figure 17 for the shielded box door open 15.24 cm and the transmitting antenna at a height of 1.5 m and 1.21 m, respectively. Figure 18 shows the frequency spectra for the shielded box door open 1 inch and the transmitting antenna at a height of 1.5 m and 1.21 m, respectively. The direct spectrum of the reference and the shielded box was overlaid with the ground bounce gated out for both measurements. The direct antenna-to-antenna reference is shown by the red trace, and the direct antenna-to-antenna response for the shielded box is shown by the green trace. The conclusion for these measurements is that the ground bounce affects only the frequency content of the waveform and not the amplitude. Figure 19 shows data from the reference measurement and Figure 20 shows the results from the shielded cavity measurements. These graphs show the relationship between the direct component, the ground bounce component, and the laboratory or cavity response. Figure 19 shows the entire waveform (black trace), including the ground bounce, laboratory and direct antenna-to-antenna responses, a waveform (red trace) with the ground bounce and laboratory responses gated out, leaving just the direct antenna-to-antenna response, the laboratory response (blue trace) with the direct and ground bounce gated out, and a corresponding system noise floor. Figure 19 shows the same information but with the shielded cavity. The additional traces show the shielded cavity direct antenna-to-antenna component plus ground bounce and cavity response (light blue trace), and direct-to-direct antenna response with shielded cavity (green trace). The purple trace, in this case, is the shielded cavity response with the direct antenna-to-antenna response and ground bounce both gated out.

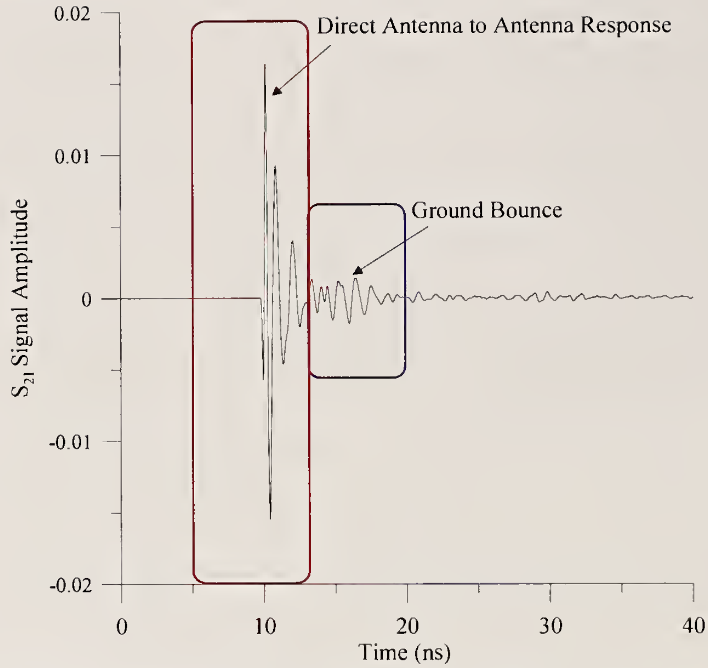


Figure 12. Time-domain reference waveform for one DRG antenna on a tripod and the other in the shielded box, separated by 2 m.

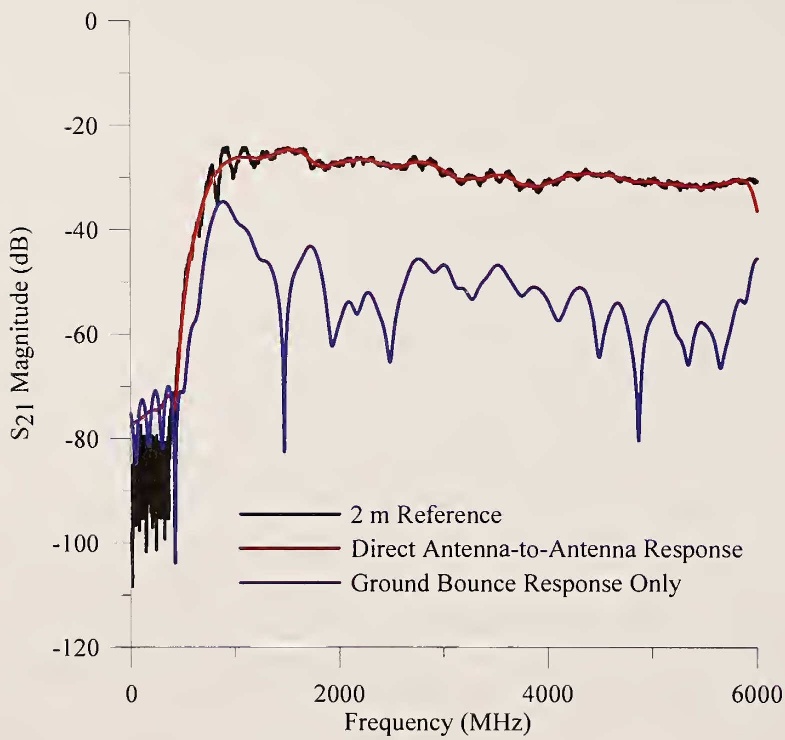


Figure 13. Frequency-domain reference waveform for two DRG antennas separated by 2 m. The black trace is the spectrum that includes the direct response and ground bounce; the red line is the spectrum of the direct response only; the blue line shows the spectrum of the ground bounce.

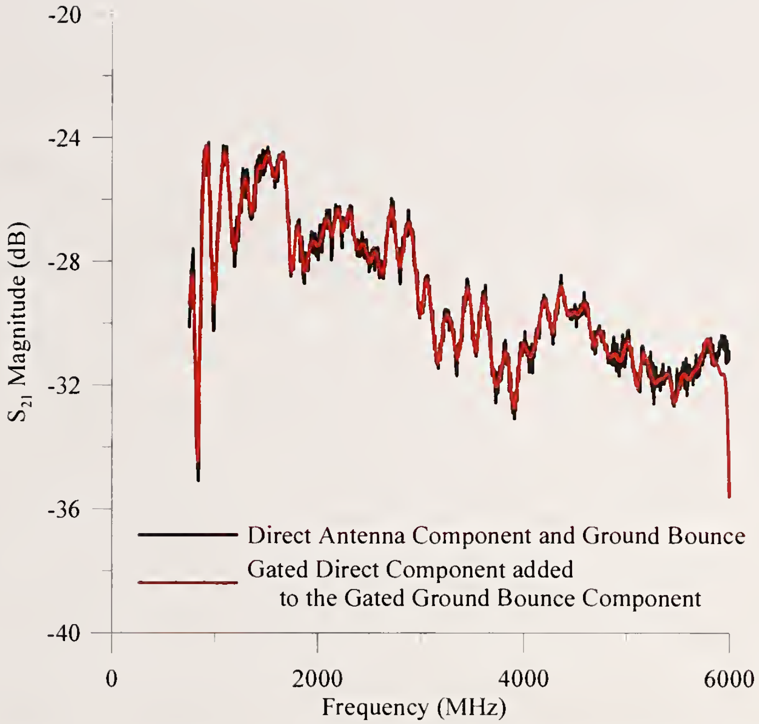


Figure 14. Frequency-domain waveforms for the full spectrum (red trace) compared to the gated, ground-bounce component added to the gated, direct component.

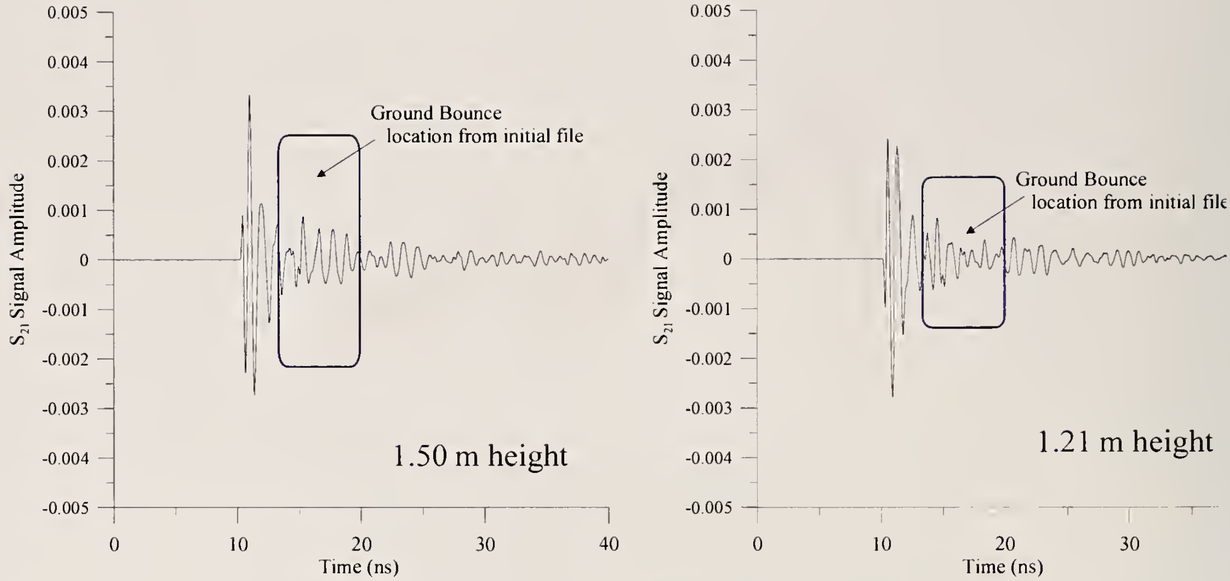


Figure 15. Time-domain waveforms for a DRG antenna in shielded box with transmit antennas at a height of 1.5 m and 1.21 m, respectively, and the door of the box open 15.24 cm.

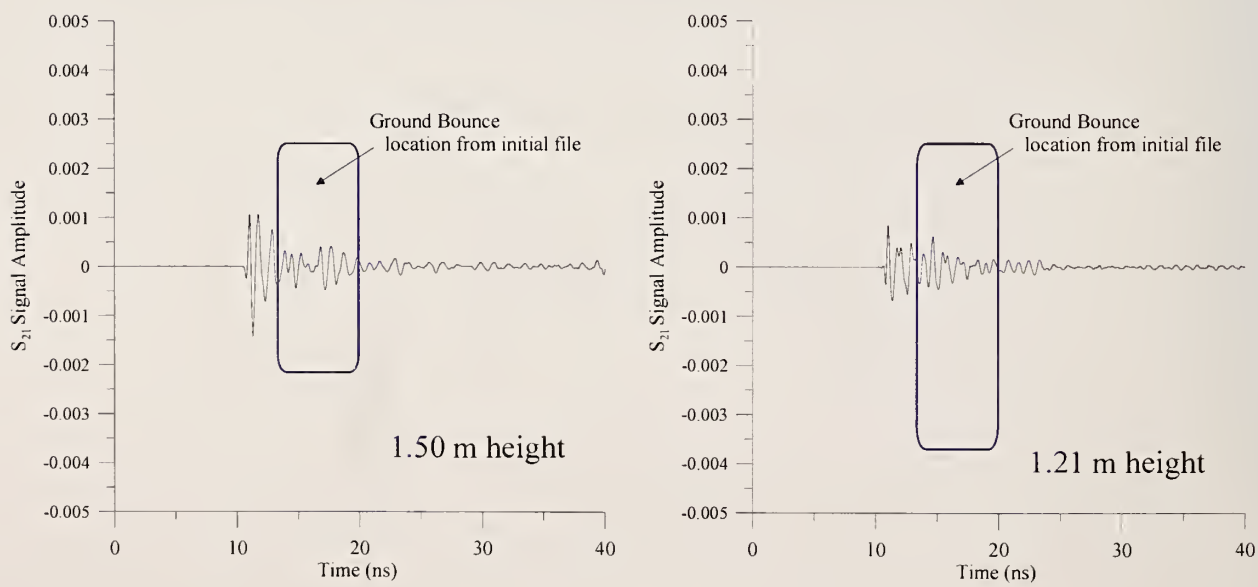


Figure 16. Time-domain waveforms for a DRG antenna in shielded box with transmit antennas at a height of 1.5 m and 1.21 m, respectively, and the door of the box open 2.54 cm.

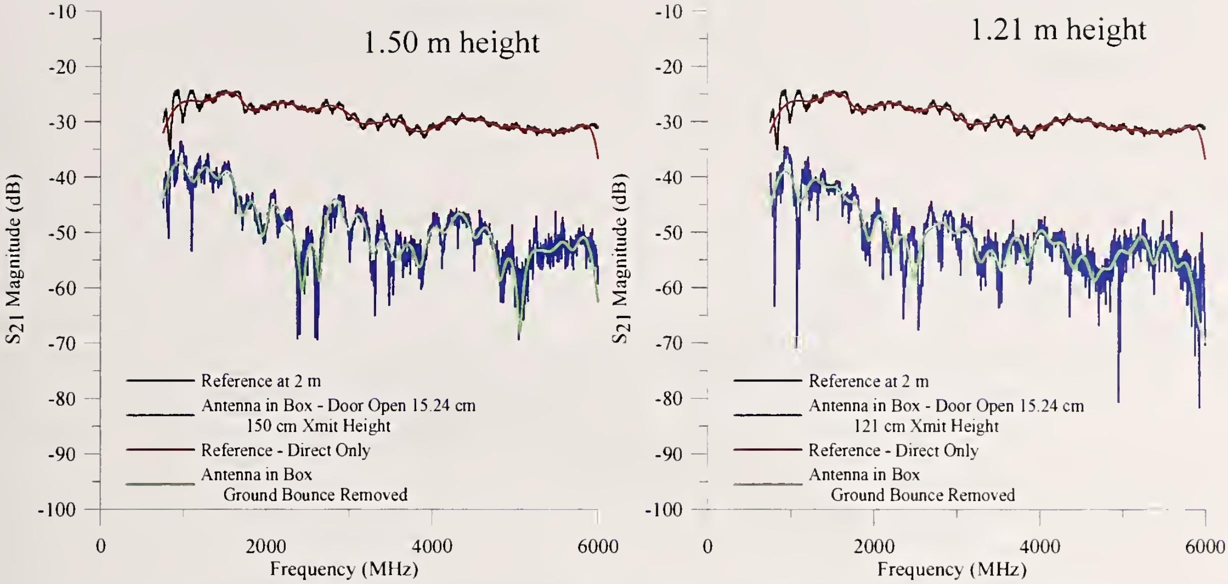


Figure 17. Frequency domain waveforms for a DRG antenna in shielded box with transmit antennas heights of 1.5 m and 1.21 m, respectively, with the door of the box open 15.24 cm (6 in.).

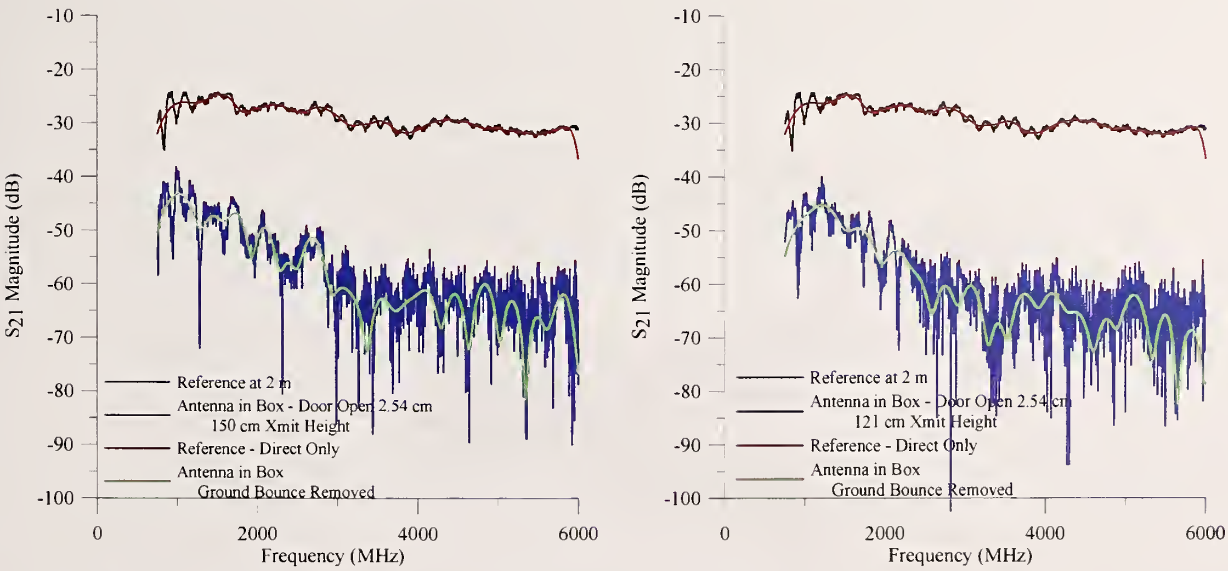


Figure 18. Frequency domain waveforms for a DRG antenna in shielded box with transmit antennas at a height of 1.5 m and 1.21 m, respectively, and the door of the box open 2.54 cm (1 in.).

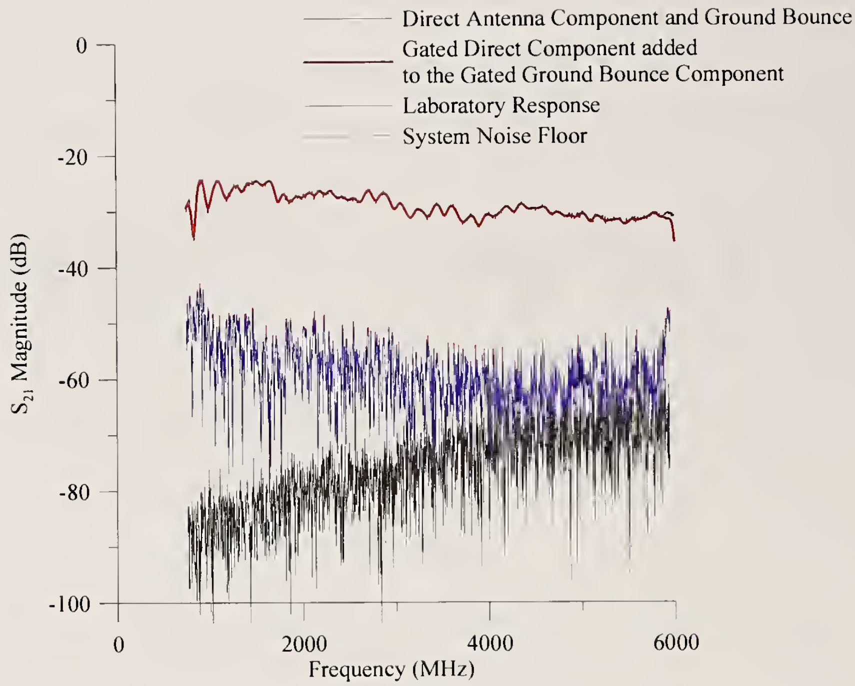


Figure 19. Frequency spectrum showing the 2 m reference measurement showing how the various components of the signal add and subtract.

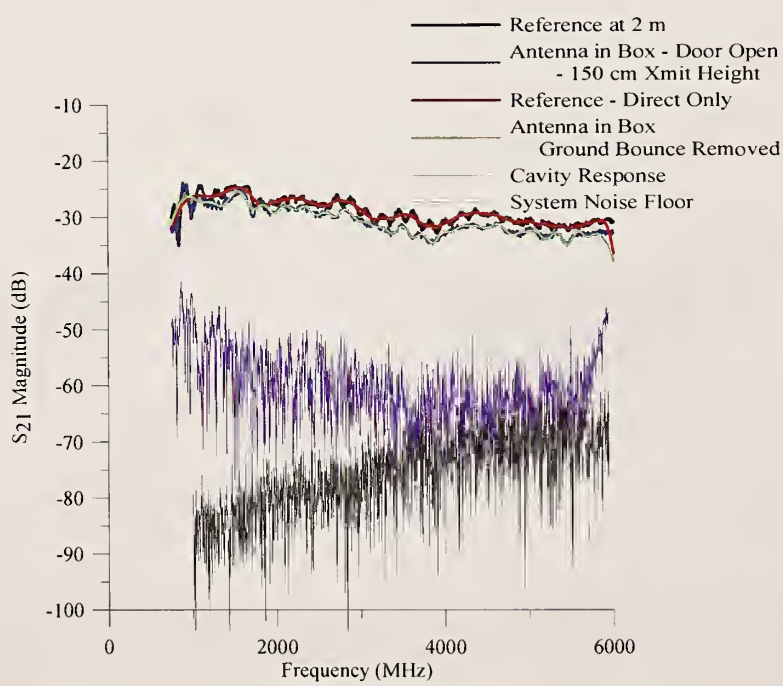


Figure 20. Frequency spectrum showing results of shielded box experiment at 150 cm height – door open. Cavity response is found by subtracting the gated ground bounce from the full spectrum.

### 3.2.2 Ground Bounce in an Aircraft Testing Environment

To take the understanding we gained from the laboratory, we can apply a similar analysis for an aircraft as was done in Section 3.2.1.1. A schematic is shown in Figure 21 of a measurement where the antennas are located at approximately 4 m above the tarmac at the FAA's Atlantic City location. In a typical reference measurement, the antennas are located on a tower 4 m above the tarmac and separated by 23.0 m (75 ft.). Performing the same geometrical analysis as above, we determine that the time of flight should be around 76 ns for the direct antenna-to-antenna response, and the ground reflection should appear around 81 ns. Figure 22 is a time-domain plot of an actual reference measurement taken at the FAA Atlantic City facility showing a direct antenna-to-antenna component around 74 ns and a ground-bounce component around 76.5 ns. Typically in this type of reference measurement we time-gate out the reflection due to the ground bounce, which transforms this measurement into a free-space reference. This free-space reference is then used to deconvolve antenna effects from the measurement to get aircraft penetration values. If we try to time-gate out the ground bounce from our aircraft measurement (prior to deconvolution) we run into problems. Since we try to maintain the same antenna separations for an antenna inside the aircraft, we can assume that the ground bounce will again appear at around 77 ns, and the initial antenna-to-antenna response should be seen at around 74 ns. A time-domain plot of a measurement at the 70 degree position for the receive DRG horn antenna located in the main passenger cabin is shown in Figure 23. In this figure, we see that the initial response occurs at approximately 73 ns, and what appears to be a secondary response occurs at around 90 ns, which is a delay of 13 ns from where we would expect the ground bounce to show up in our measurement. This would result in a geometrical difference of approximately 4 m or 12 ft. This analysis suggests that the secondary response is due not to ground bounce but to some other interaction of the electromagnetic waves with either the aircraft or something internal to the aircraft, and therefore the ground bounce is contained within the first initial decay response and cannot be gated out of the measurement.

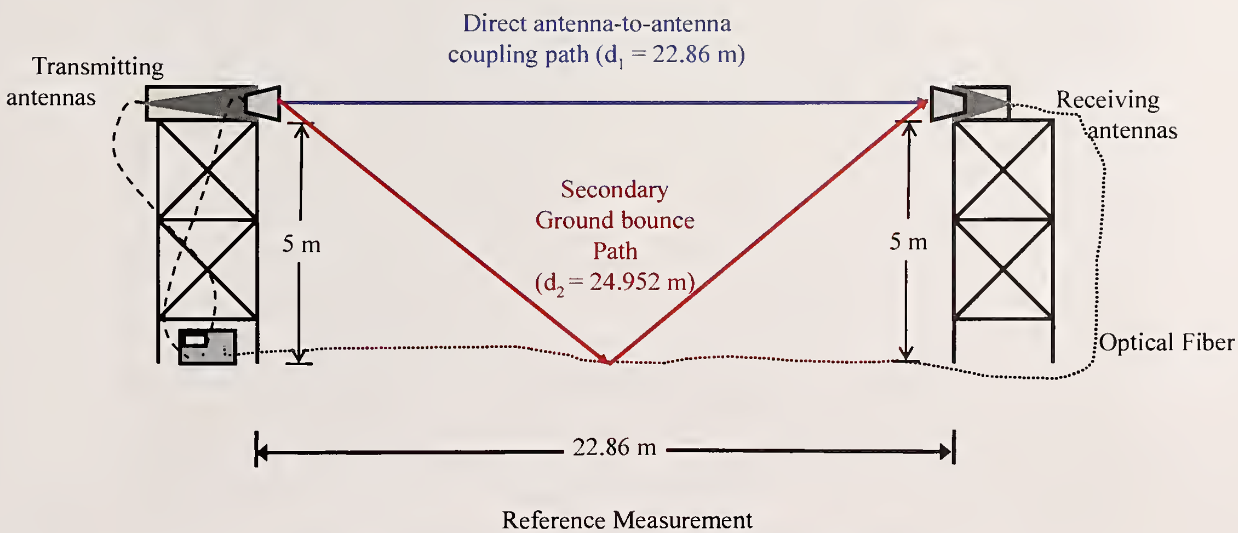


Figure 21. Schematic showing typical measurement setup for a reference measurement between antenna towers.

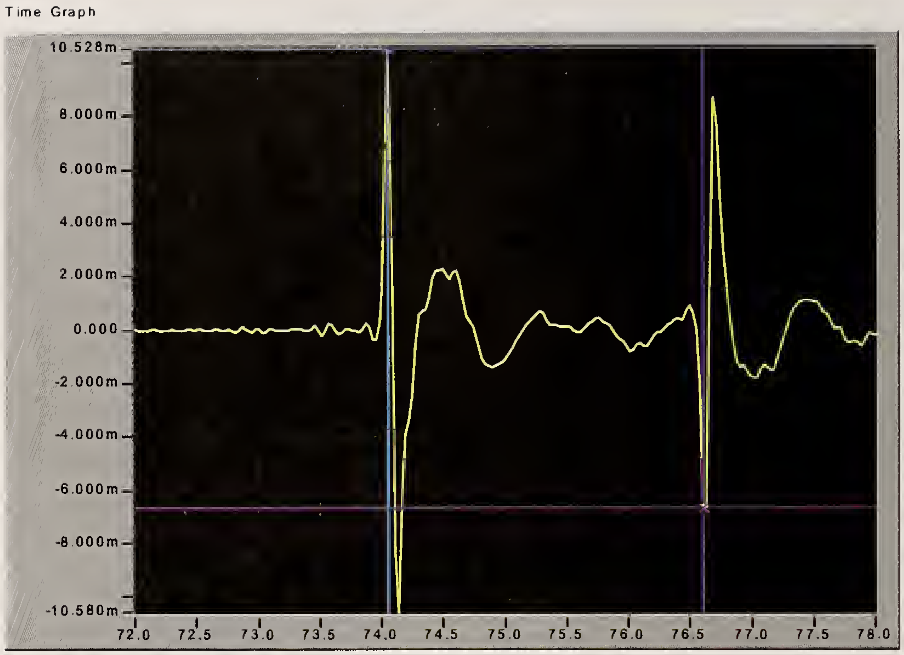


Figure 22. Time-domain graphs for DRG Hpol antennas showing the direct antenna-to-antenna response and the secondary reflection due to the ground for an antenna separation of approximately 23 m and an antenna height of 4 m.

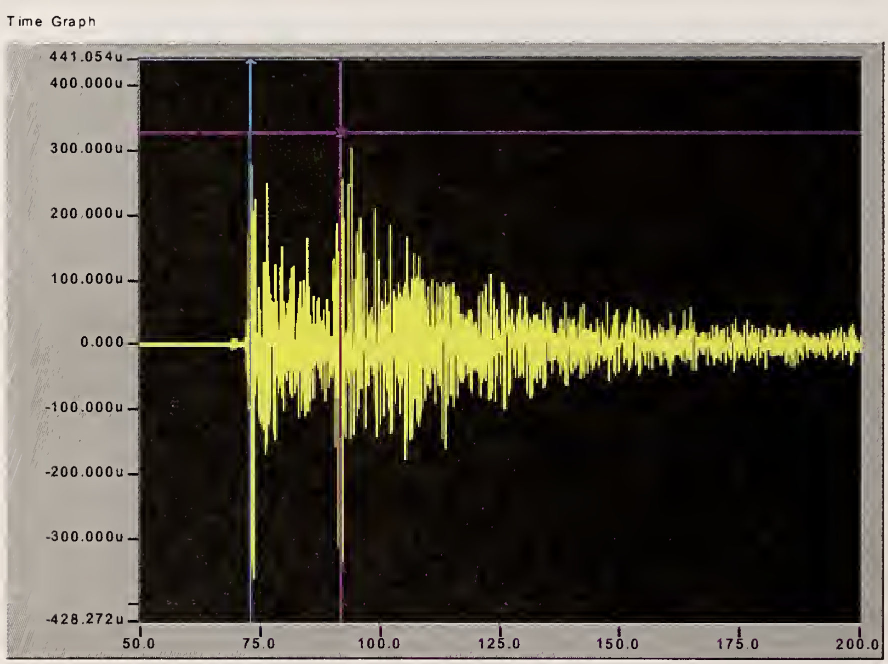


Figure 23. A time-domain plot showing a 23 m measurement for a transmitting DRG Hpol antenna at the 70 degree position and a DRG receiving antenna in the main passenger cabin.

### 3.2.3 Effects of varying ground conditions on antenna measurements

What happens when measurements are performed over the earth when the surface changes from earth or pavement to metal? This question was answered on a previous measurement effort at the GM Proving Grounds in March 2004.

We went to understand the problems they were experiencing with field uniformity on their large, outdoor automotive test antenna range [35–37] due to varying ground conditions along the measurement path. The antenna range is shown in Figure 24. To study this problem, a numerical simulation was developed for the FM (frequency modulation) band from 88 MHz to 108 MHz. Two different ground conditions were modeled. The first was "earth", consisting of a semi-infinite asphalt medium, having a relative permittivity $\varepsilon' = 5$, relative permeability $\mu' = 1.0$, and a conductivity of $\sigma = 0.01$ Siemens/m. A 5 m by 5 m perfectly conducting ground plane was then placed over the ground to simulate the turntable found inside the measurement radome at the GM facility. The simulated environment is depicted in Figure 25. A 1.5 m long transmitting dipole was positioned above the "earth" interface or ground plane at a height of 2 m. The results of the simulation are shown in Figure 26 with the dipole in the horizontal polarization. Figure 26a shows the "earth" ground and that interactions with the "earth" ground are minimal. When a ground plane is added over the earth, the field uniformity is minimally disrupted as shown in Figure 26b. The fields looking down from the dipole over the ground plane are shown in Figure 26c. The results for the dipole in the vertical polarization of this simulation are shown in Figure 27. For the "earth", Figure 27a shows uniform fields tilting slightly upwards. When the ground plane is installed, the field uniformity is greatly disturbed, as shown in Figure 27b. The fields looking down from the dipole over the ground plane are shown in Figure 27c. These simulations show that dissimilar ground interfaces along the measurement path disrupt the fields more than just having a single continuous ground interface.


Figure 24. Outdoor Automotive Antenna Test Range.

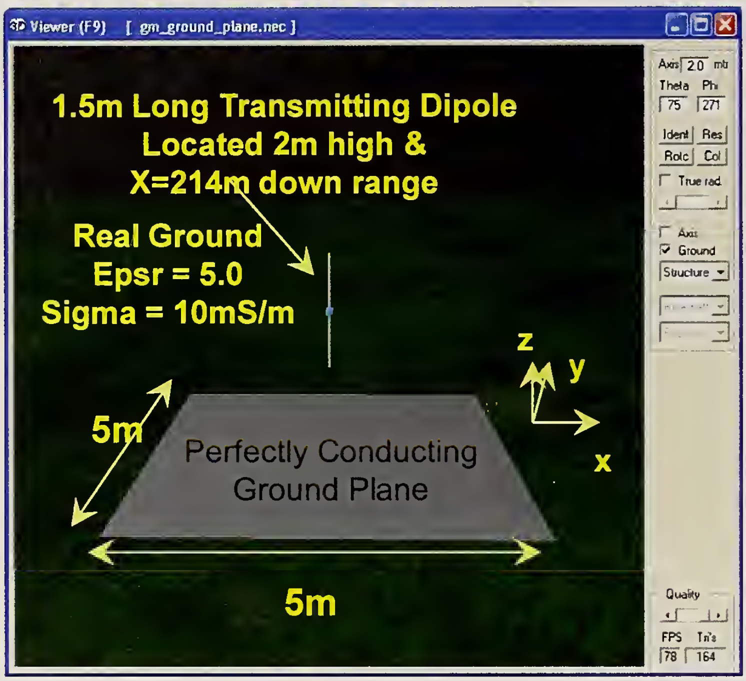


Figure 25. Simulation of GM Turntable over an asphalt dielectric medium.

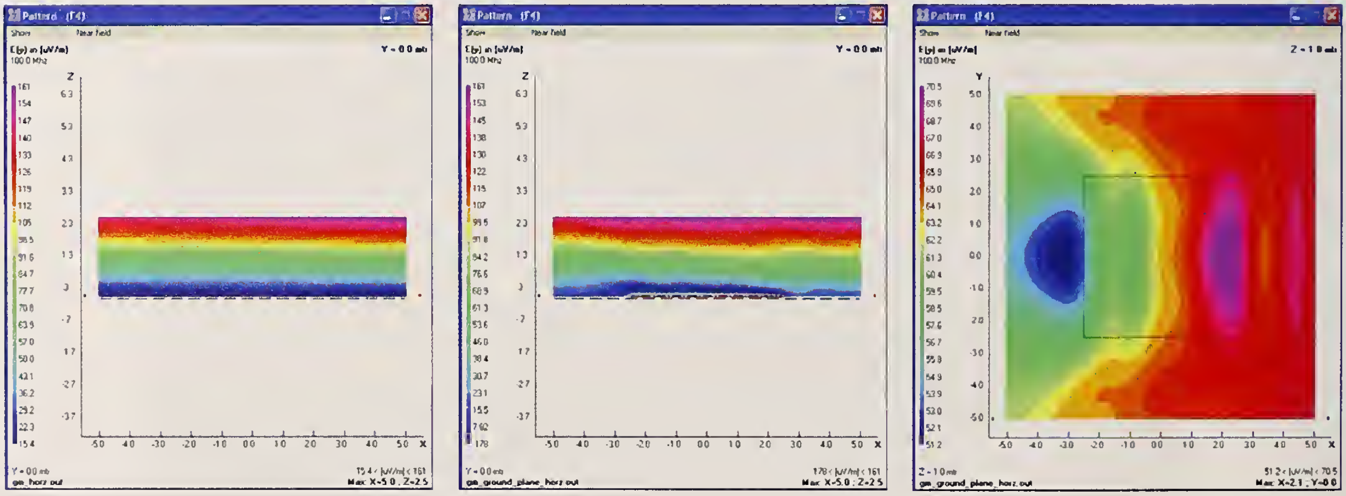

(a) (b) (c)

Figure 26. Simulation of GM turntable over an asphalt dielectric medium. The dipole is in the horizontal polarization. The results in (a) show the field uniformity above "earth". The results in (b) show the field uniformity above a 5 m by 5 m "turntable". The results in (c) are the fields looking down from the dipole over the ground plane.

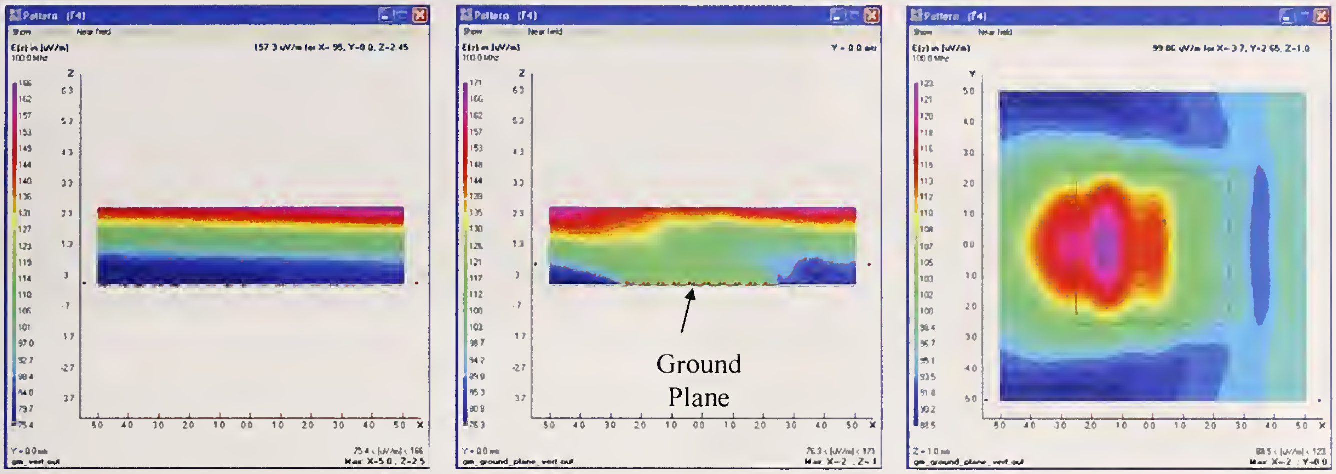


(a) (b) (c)

Figure 27. Simulation of GM turntable over an asphalt dielectric medium. The dipole is in the vertical polarization. The results in (a) show the field uniformity above "earth". The results in (b) show the field uniformity above a 5 m by 5 m "turntable". The results in (c) are the fields looking down from the dipole over the ground plane.

### 3.2.4 Effects of ground bounce for aircraft measurements

To understand how ground conditions affect the measurements, we decided to investigate the difference between reflections from the tarmac and reflections from a sheet of rFoil. The measurement setup is shown in Figure 28. These measurements were taken along the 45° extrapolation line (Figure 44) at distances of 15.2 m (50 ft.), 23.5 m (75 ft.), and 30.5 m (100 ft.). These results are shown in Figure 29. The green traces are results for tarmac ground conditions, and the orange traces are for the rFoil ground conditions. Vertical polarization results are shown by the solid traces, and the horizontal polarization results are shown by the dotted traces. It is interesting to note that the results for vertical polarization show a slight polarization inversion for the rFoil which is what we would expect from theory [38]. However, for the horizontal polarization there is no polarization inversion. The differences in magnitude are anywhere from 0 dB to 10 dB depending on the frequency.

Figure 28. Photographs showing Rfoil laid out beneath aircraft for the various ground condition experiments.

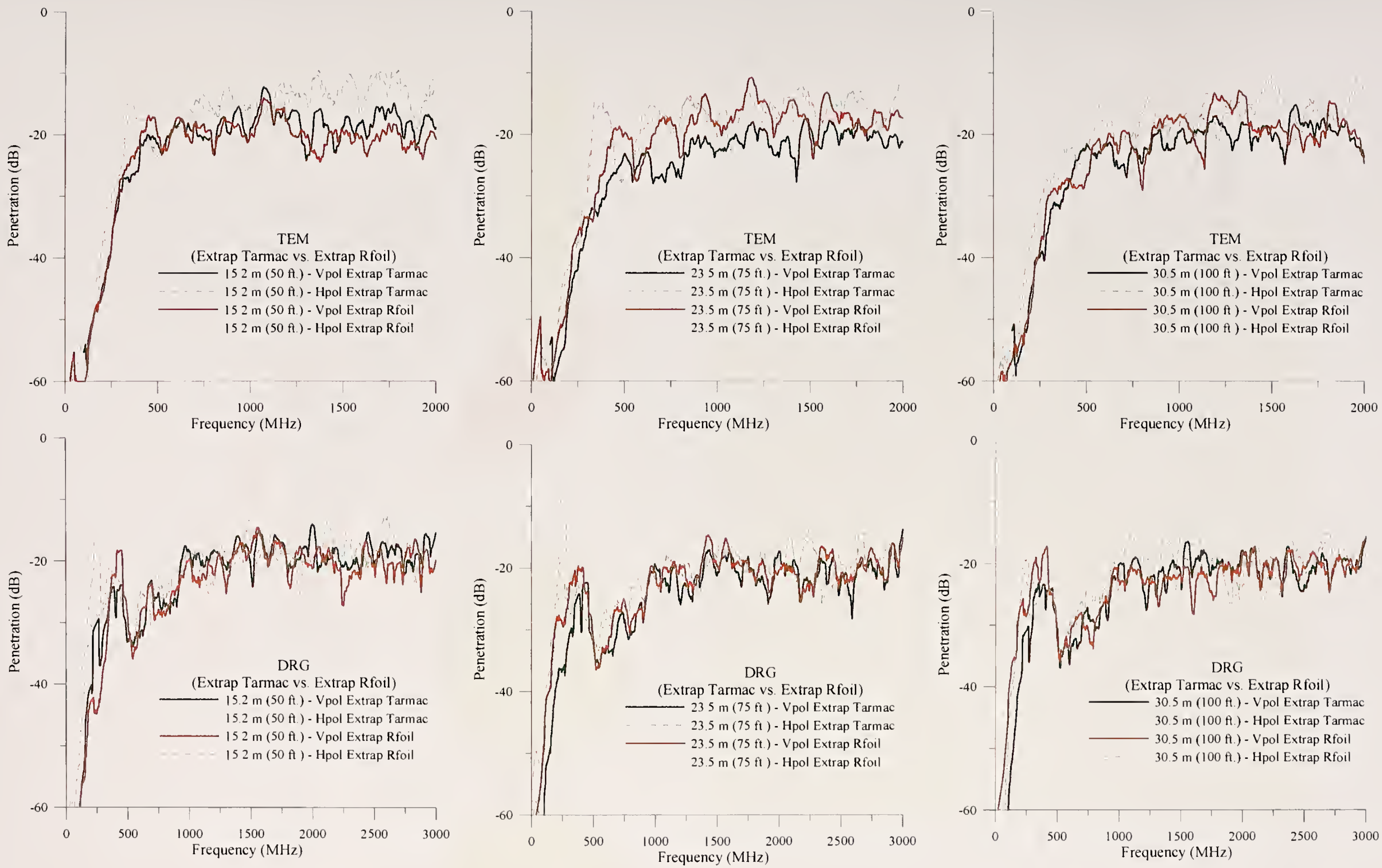


Figure 29. Extrapolation measurements with various ground conditions. The orange traces show Rfoil results and the green traces show tarmac results. The solid traces are vertical polarization results and the dotted traces are horizontal polarization results. From left to right results are shown for distances from 15.2 m to 30.5 m.

### 3.3 Antenna Gain

A simulation was performed to understand how antenna gain impacts the field penetration into an aircraft. Using two antenna types we evaluated the shielding effectiveness. The first was a short dipole and the second an aperture antenna to represent a DRG horn antenna. These models are shown in Figure 30. Simulated reference measurements were taken for both antennas at the same distances, and then the receiving antennas were placed at the same position inside a shielded structure. The shielding effectiveness of the structure was obtained and a 200 MHz frequency averaging was applied to obtain an average shielding value per unit frequency. The theoretical gains were then computed for each antenna and the gain difference was computed. This was then plotted against the shielding difference of the two antenna types for the two shielding simulations and is shown in Figure 31. The result of the simulation shows that with higher antenna gains, higher shielding values can be obtained. For a reference measurement, the gains of both antennas are taken into account by the measurement. When the receiving antenna is placed inside a cavity, the gain of the cavity plus antenna changes and the gain of the receiving antenna must be corrected. Thus we correct for this gain in the processing of the data. This is considered in our uncertainty analysis. Figure 32 shows an actual set of measurements and the difference in penetration that can occur between applying a gain correction (black trace) and not applying gain correction (red trace) for a measurement on a Bombardier Global 5000 [18] with the receiving antenna in the main passenger cabin and the transmitting tower at the 0° position.

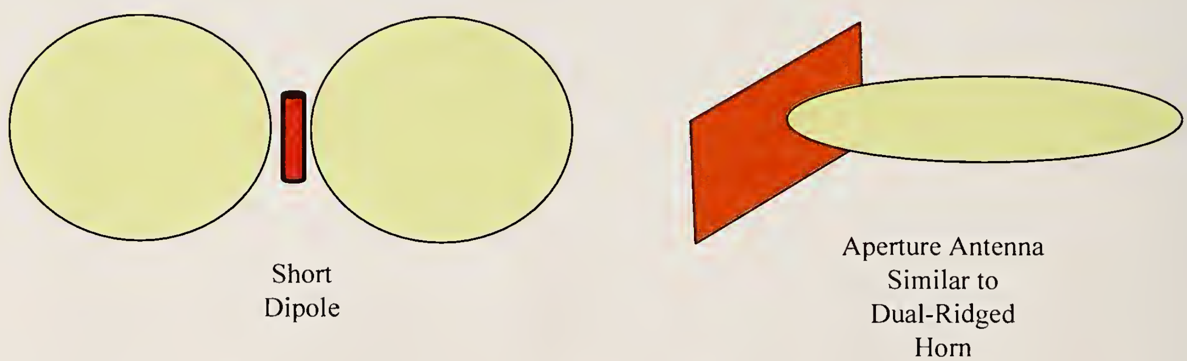


Figure 30. Two antenna types used for antenna gain simulation.

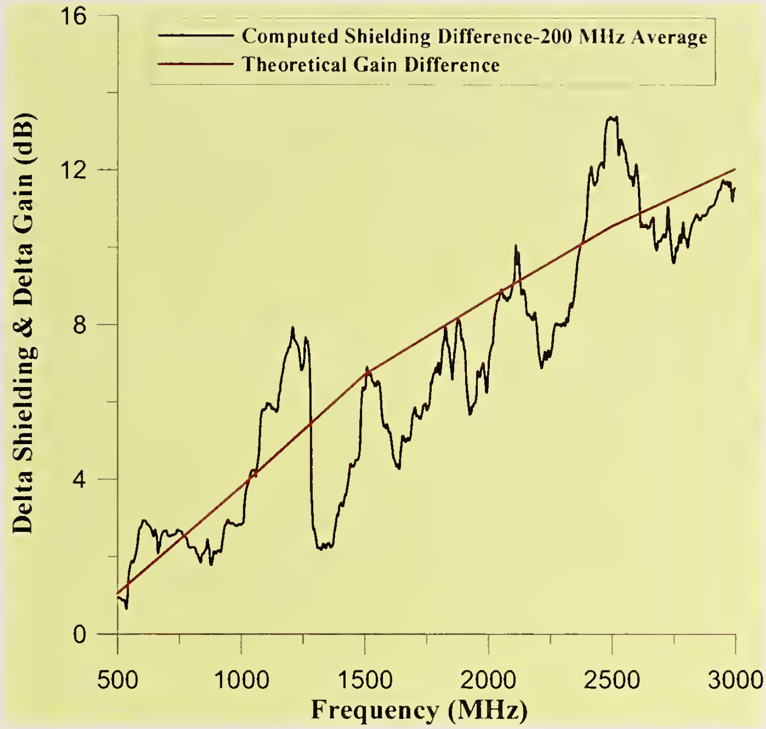


Figure 31. Shielding difference plotted against the theoretical gain difference.

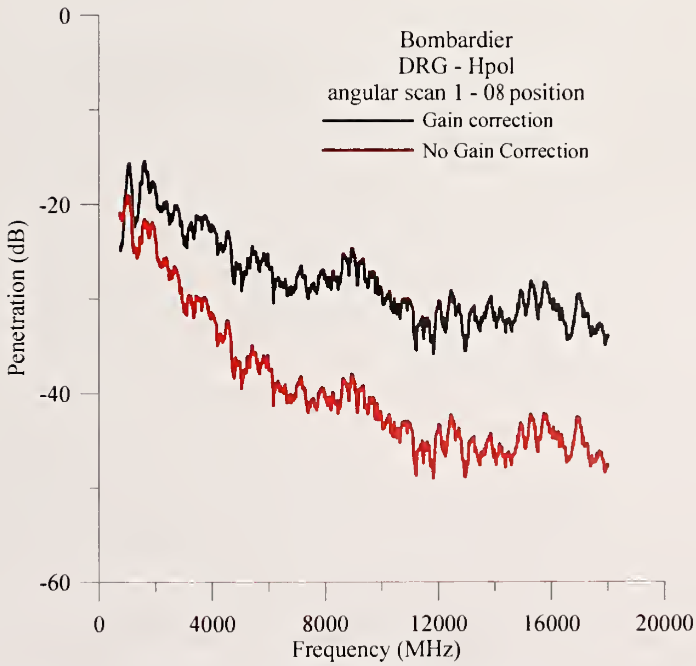


Figure 32. Difference between using a gain correction and no gain correction for a DRG horn antenna.

## 4. Measurement System

The configuration of the NIST measurement systems for these aircraft measurements is shown in Figures 33, 34, and 35. Figure 33 shows the equipment used on the receiving side of the system inside the aircraft. The transmitting side of the aircraft measurement system is shown in Figures 34 and 35 for (a) the original system that made measurements to 3000 MHz, and (b) the upgraded system that made measurements up to 18 GHz, respectively. The system consists of: (1) a VNA, (2) two transmitting TEM horn antennas, and two DRG horn antennas configured for the horizontal and vertical polarizations, respectively, (3) a receiving TEM horn antenna and DRG antenna, (4) two coaxial microwave switches to select the polarization of the transmit antennas, and (5) two precision analog electro-optic links to cover both frequency bands (only the 11 GHz optical link was used during the first effort) and to provide an interconnection between the transmitting antennas outside the aircraft and the receiving antenna inside. Both links provide a significant improvement in performance over that of conventional microwave cables. The optical links exhibit low transmission losses and low noise, and do not pick up common-mode noise from environmental ambient signals. The optical links also improve dynamic range and have better immunity from electromagnetic interference. The heart of this system is a commercially available VNA that has been configured to acquire complex transmission data ($S_{21,}$ in-phase and quadrature signals). During the first effort, the VNA was limited to a maximum of 1601 points due to internal hardware limitations. During the second effort, the VNA was limited to a maximum of 16001 frequencies; however for both efforts, we developed software that extends the number of frequencies to any desired value. If we need more than the maximum number of points per window, then the software will subdivide a given frequency range into a user-selected number of either 1601 or 16001 point sub-bands. The DRG horn antennas operate from 1 GHz to 18 GHz and were configured by use of two bands, resulting in 32002 equally spaced measurement points from approximately 0.5 MHz to 18 GHz. The TEM horn antennas operate from 0.1 GHz to 4 GHz and were configured by use of one band, resulting in 6401 equally spaced measurement points from approximately 0.5 MHz to 4 GHz. A reduced frequency spacing is necessary to avoid problems due to aliasing. Prior to connecting the cables to the antennas, all channels were calibrated to remove systematic transmission effects due to cabling, switches, and the frequency and phase variations of the optical transmission link. This procedure calibrates the system with respect to the input of the transmitting and the output of the receiving antennas. Three NIST-developed ultra-wideband TEM horn antennas were used: two 1.2 m antennas on a tower located outside of the aircraft, either to transmit horizontally and vertically polarized fields, and a more compact 36 cm TEM horn located in a pre-selected aircraft compartment to detect energy coupled into the airframe. For the higher-frequency bands, three commercially available DRG antennas were used: two on the same transmitting tower located outside of the aircraft to transmit horizontally and vertically polarized fields, and a DRG antenna located in the same preselected aircraft compartment to detect energy coupled into the airframe. The frequency data were digitized and transferred to a laptop computer for subsequent data analysis and signal processing.

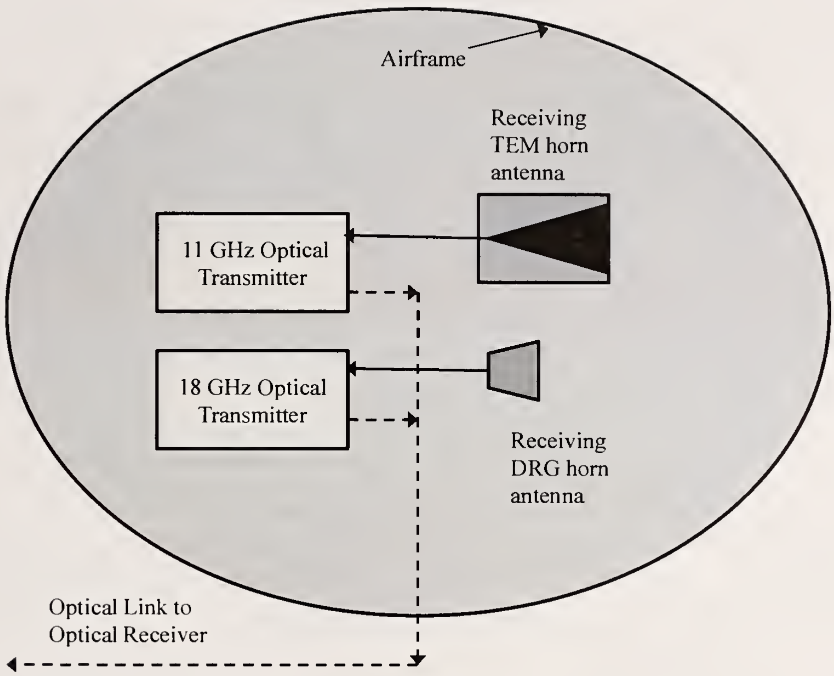


Figure 33. Airframe shielding measurement system (receiving side). The reverberant nature of the airframe permits the reception of both horizontally and vertically polarized signals.

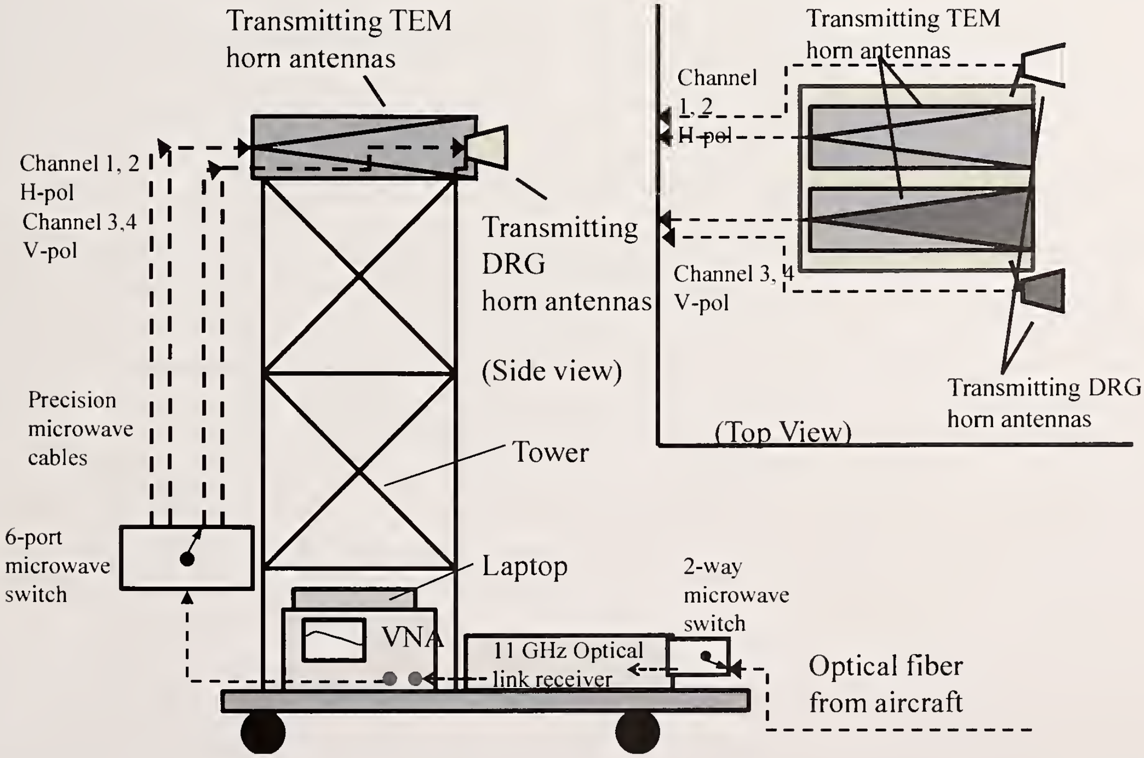


Figure 34. Transmitting side of the airframe shielding measurement system for measurements to 3000 MHz.

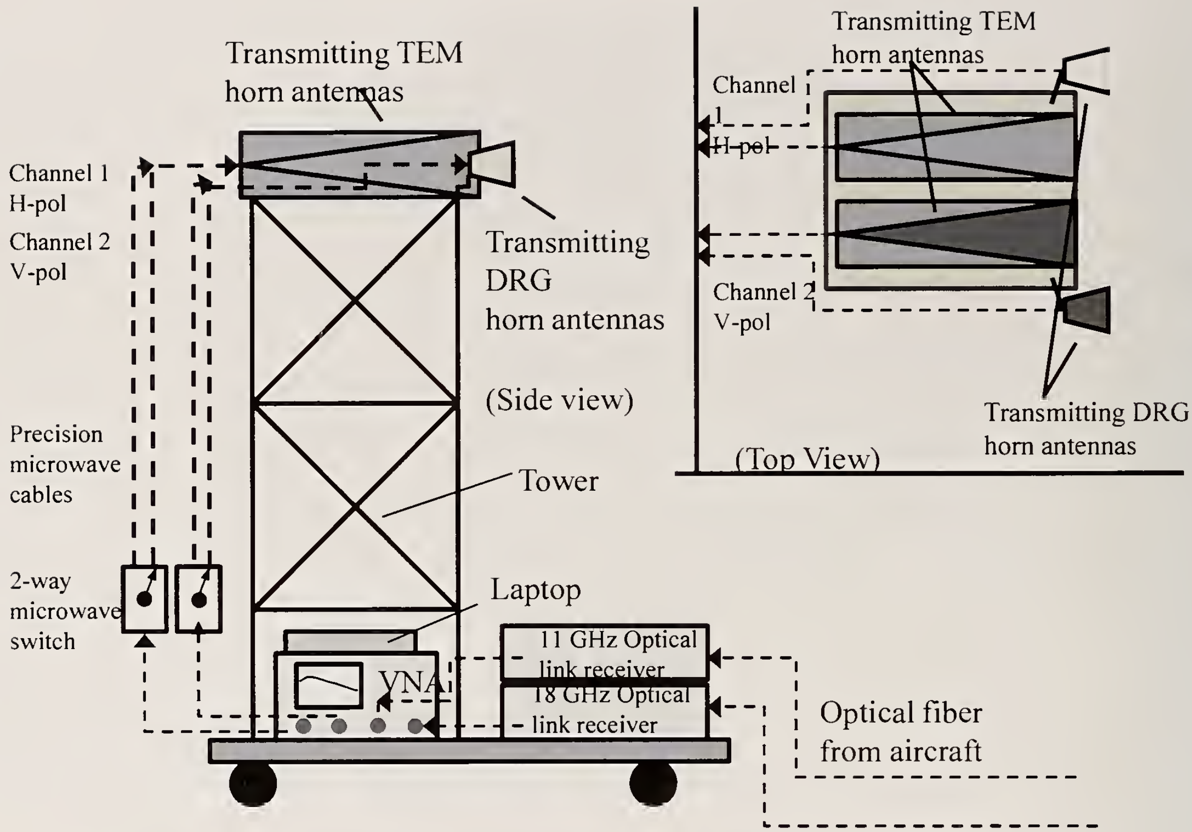


Figure 35. Transmitting side of the airframe shielding measurement system for measurements to 18000 MHz.

## 5. Measurement of Electromagnetic Airframe Penetration

The extraction of airframe penetration characteristics requires a reference measurement without the shield or cavity and then a measurement with the shield or cavity placed between the two antennas. This two-step measurement process for an aircraft is shown in Figure 36. In the first step, a reference transmission measurement is performed by boresighting the transmitting and receiving antennas at a fixed distance. The reference measurements were performed at a location away from the aircraft in order to minimize reflections from the aircraft. This measurement quantifies the energy incident on the aircraft, and enables us to calibrate and remove the frequency-dependent effects of the antennas and interconnecting hardware. In the second step, the receiving antenna was placed in a selected aircraft compartment; the transmitting antennas were placed at fixed locations, external to the aircraft, and stepped-frequency transmission data were acquired.

The reference and airframe data were processed by use of a sequence of filtering, Fourier transforms, and time gating to obtain the penetration values. The basic signal-processing sequence through which the data were obtained is shown in Figure 37. The raw frequency data were first filtered to maximize the signal-to-noise ratio and to minimize effects from the low-frequency cut-off of our electro-optic link. Next, a tapered frequency-domain window was applied to both sets of data to reduce Gibbs ringing in subsequent processing. An inverse Fourier transform (IFT) was then applied to the processed data to obtain time-domain waveforms. Time gates were then applied to isolate the desired portions of waveforms and remove undesired portions. In the case of the reference, the time gate was applied to isolate the direct antenna-to-antenna coupling and remove the effects of ground bounce and late-time reflections. We use this to reference every measurement to the attenuation seen in free space. Time gating was applied to the airframe data to isolate either the direct illumination, the direct propagation path between the two antennas, or the reverberant fields that are the reflected waves in the aircraft. Reflections due to ground bounce are embedded in the waveforms at this distance and therefore cannot be removed by time-gating. The time-gated data sets were then transformed back into the frequency domain, and the penetration *(PE),* was computed from the deconvolution:

$$PE = DC \cdot \left| \frac{S_{42}(gated\ airframe)}{S_{42}(gated\ reference)} \right|^2, \tag{2}$$

where $S_{42}$ (*gated reference*) is the antenna-to-antenna coupling with environmental effects gated out. The signal propagates from port 4 and is transmitted to port 2. $S_{42}$ (*gated airframe*) is the airframe transmission with gating applied to minimize noise. Since the reference and airframe measurements are typically carried out at different distances, a distance correction *(DC)* was applied:

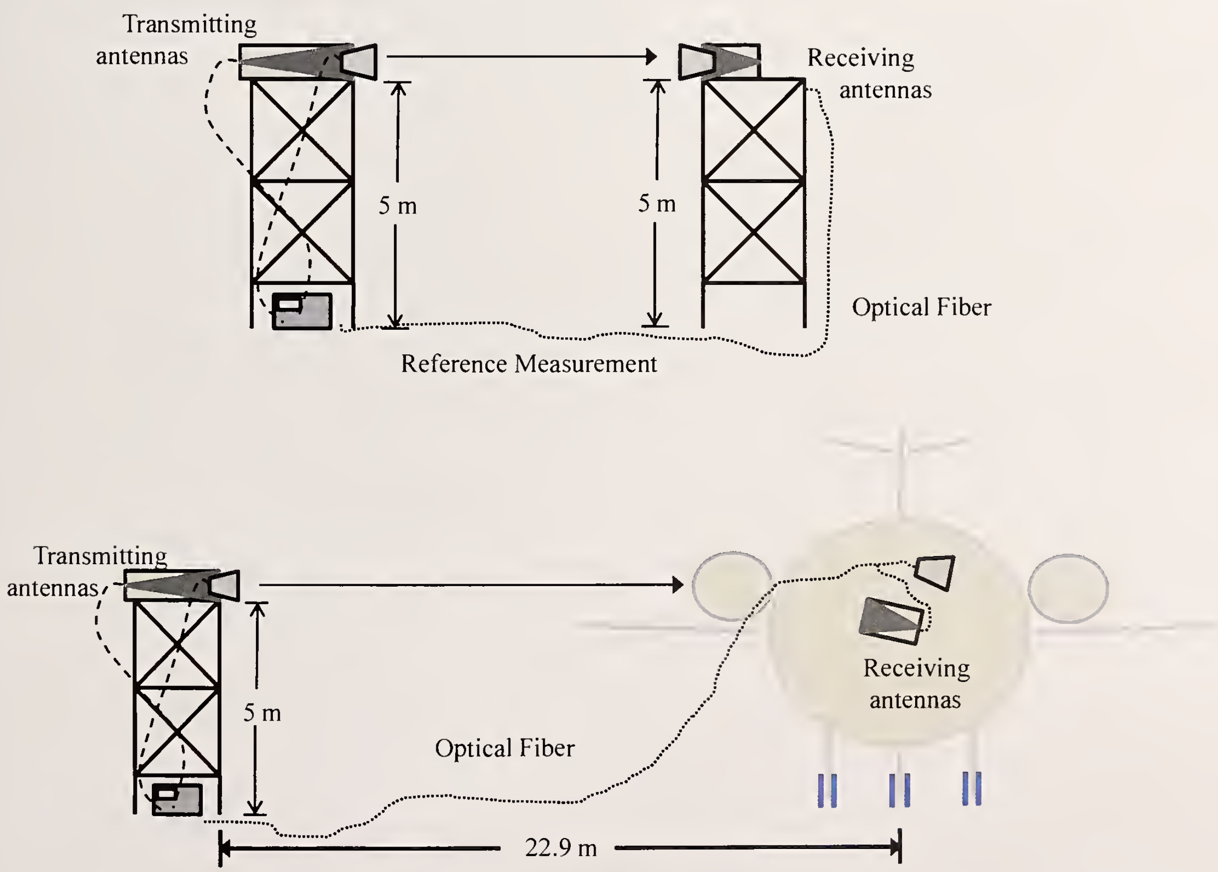


Figure 36. Two-step airframe shielding measurement procedure used in the FAA's Boeing 737-200 evaluation.

$$DC(dB) = 20\log_{10}\left(\frac{D}{D_{ref}}\right), \tag{3}$$

where $D$ is the distance from the aperture of the transmitting antenna to the geometric center of the aircraft and $D_{ref}$ is the distance between the reference antennas. A detailed description of this procedure is given in [16]. Thus, our definition of penetration is based on a comparison of a direct antenna-to-antenna coupling and signal transmission through the airframe. The penetration, as we define it here, is the reciprocal of shielding (in decibels, penetration is the negative of shielding). We prefer to display results in terms of penetration because of a better graphical display and to normalize the results by our reference measurement.

Single-aspect penetration characteristics for aircraft exhibit rapid variations with frequency, due to the large, complex cavity behavior of the aircraft. In order to obtain the volumetric-averaged penetration for a compartment, the processed penetration data were frequency-averaged over a specified bandwidth by use of the process shown in Figure 38. Averaging the penetration data reduces the complex cavity variations, increases modal randomness, and highlights systematic coupling effects, but may mask narrowband details, depending on the amount of averaging applied. These effects are discussed in detail in references [16, 25, 26].

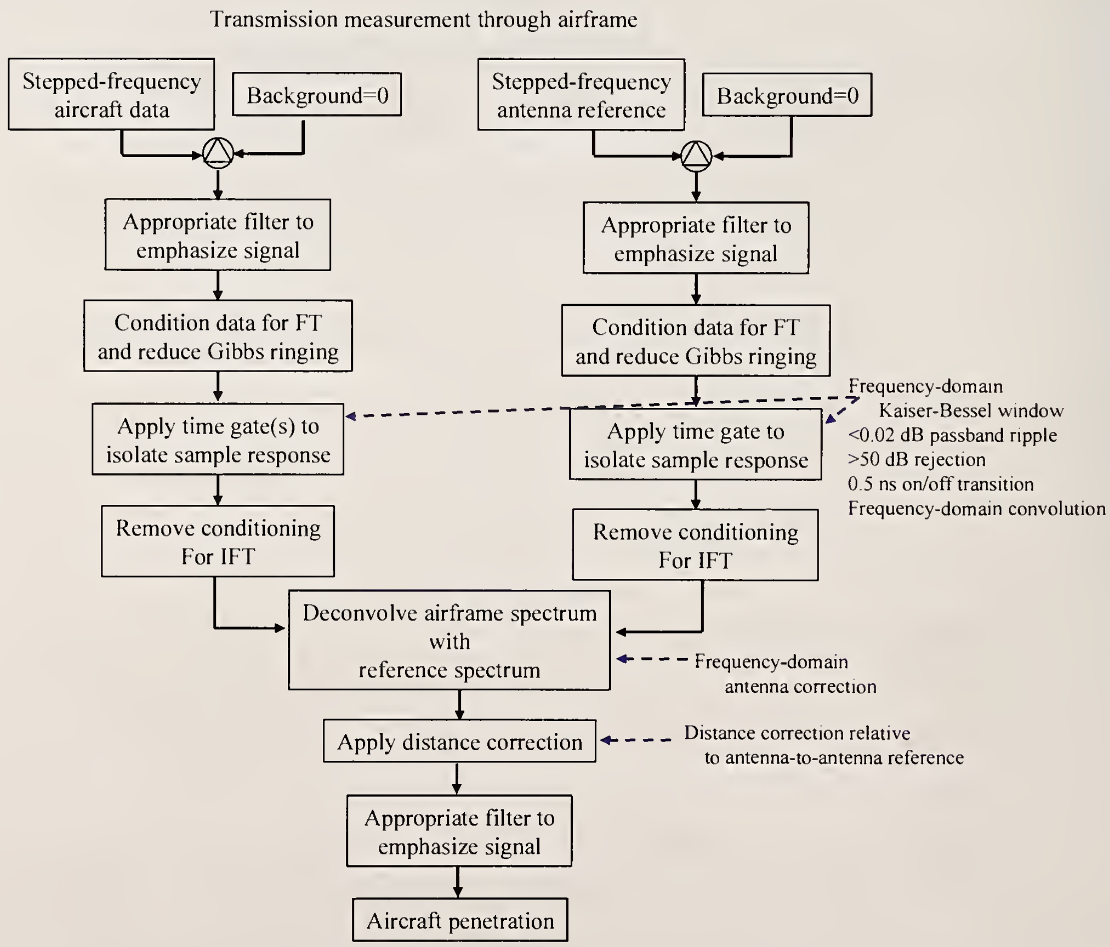


Figure 37. Signal-processing sequence to obtain airframe penetration.

Processed penetration data $PE(f_i)$

↓

Perform averaging over a selected bandwidth (BW)

$$\frac{1}{N}\sum_{i=1}^{N} PE(f_i)$$

↓

Frequency-averaged penetration

$$\langle PE(f_i) \rangle$$

Figure 38. The frequency-averaging definition.

## 5.1 Reference Measurements

The test setup for the reference measurements is shown in Figure 39. The transmitting antennas are shown mounted on one tower with aperture centers located 4 m above the ground. The receiving antennas were mounted on a second tower. The towers were constructed from PVC pipes and plywood platforms to produce a low-density support structure with minimal scattering. The antennas were then boresighted and a distance extrapolation was performed to determine an optimal reference distance to minimize near-field effects and maximize the period between the signal and ground bounce. We performed multiple reference measurements with antenna-to-antenna separations ranging from 2 m to 35 m. We found that a separation of 6 m was optimal in terms of accuracy and time separation. Two transmission measurements were performed namely, one each for the vertical and horizontal channels. This process required a manual reorientation of the receiving antenna to be co-polarized with each of the transmitting antennas. Once the reference data were taken, the receiving antenna was dismounted from the support tower and placed at selected locations inside the aircraft. The external antenna tower and aircraft are shown in Figure 40. The reference waveforms for the DRG antenna are shown in Figures 41, 42, and 43. The reference waveforms for the TEM horn antenna are shown in Figures 42, 43, and 44. The ungated time-domain reference waveforms are shown in Figures 41 and 44. The doublets that occur at approximately 50 ns in Figure 41 and 60 ns in Figure 44 correspond to direct antenna-to-antenna coupling. The subsequent waveform activity was due to a combination of internal antenna reflections and environmental scattering due to ground bounce and reflections from nearby objects. Figures 42 and 45 show the ungated frequency-domain responses for the DRG and TEM horn references, respectively. The noise-like hash on the waveform is due to ground bounce and spurious reflections which were time-gated out of the reference measurement. The frequency-domain transmission amplitude spectra of Figures 43 and 46 show

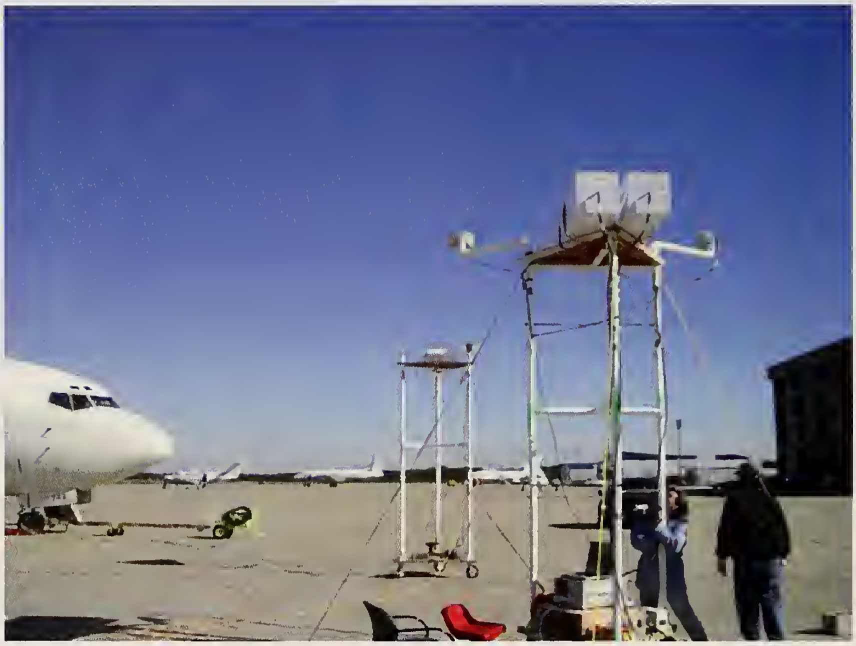

Figure 39. Reference measurement setup. The transmitting tower is configured for all measurements, and the receiving tower is configured for reference measurements only.

the impact of applying this time gate, thus isolating direct antenna-to-antenna coupling and yielding the reference for penetration measurements.


Figure 40. The transmitting antennas placed on top of a support tower and boresighted at the center of the aircraft.

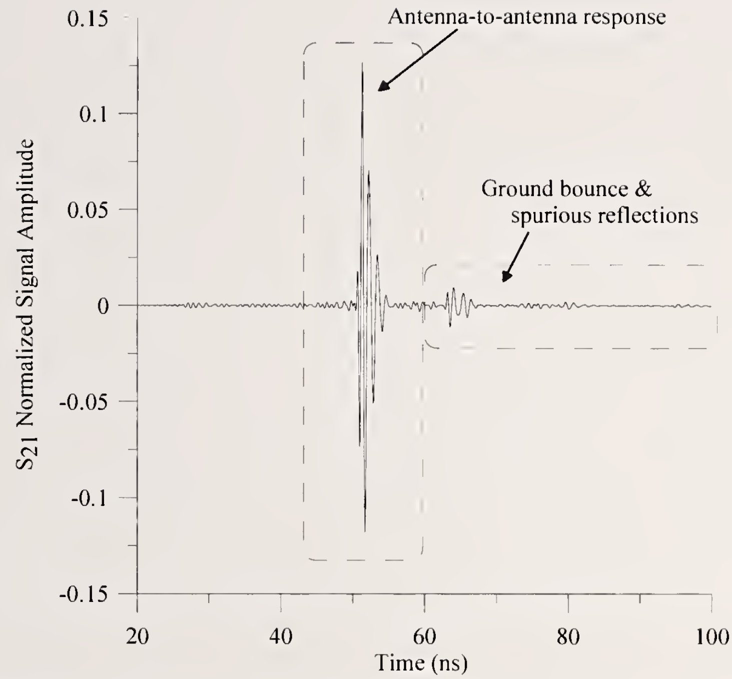


Figure 41. Ungated time-domain transmission waveform for a DRG antenna obtained at a separation of 6 m and horizontal polarization.

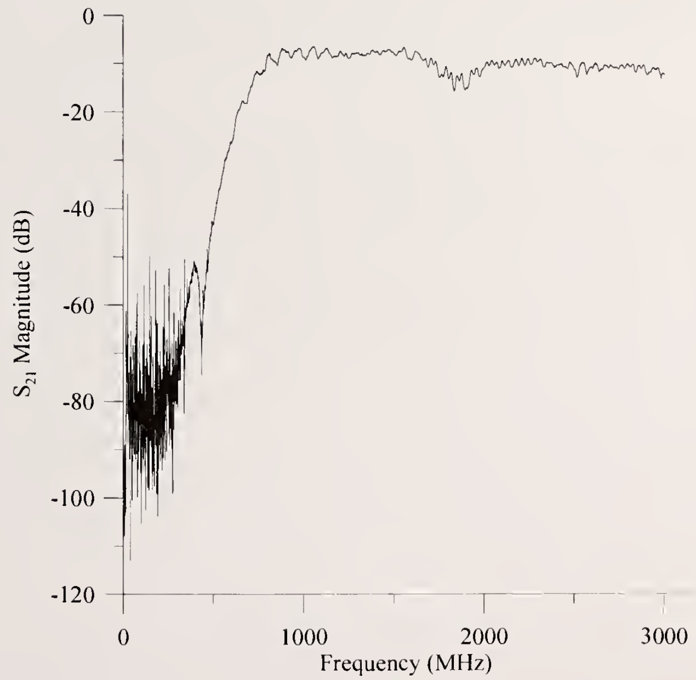


Figure 42. Ungated frequency-domain amplitude spectrum for a DRG horn antenna obtained at a separation of 6 m and vertical polarization. Note the hashy behavior due to the spurious reflections shown in Figure 41.

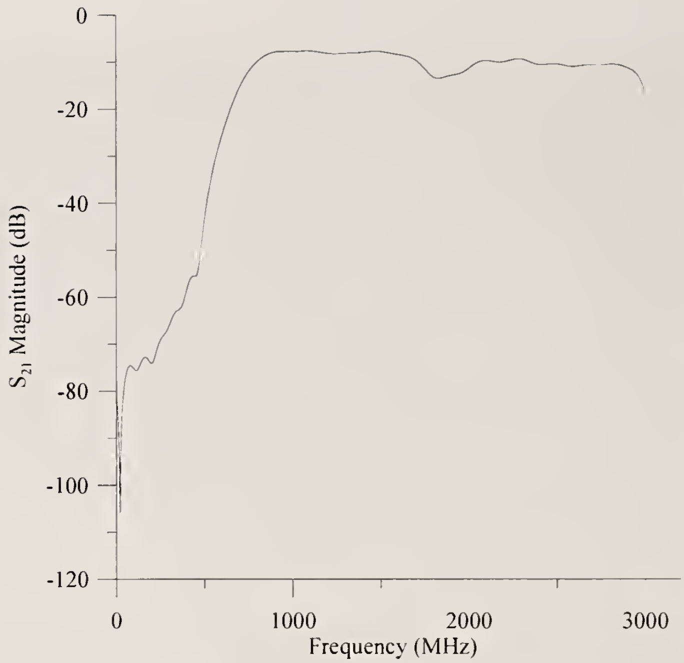


Figure 43. Gated frequency-domain amplitude spectrum for the DRG horn antenna corresponding to the waveform of Figure 41.

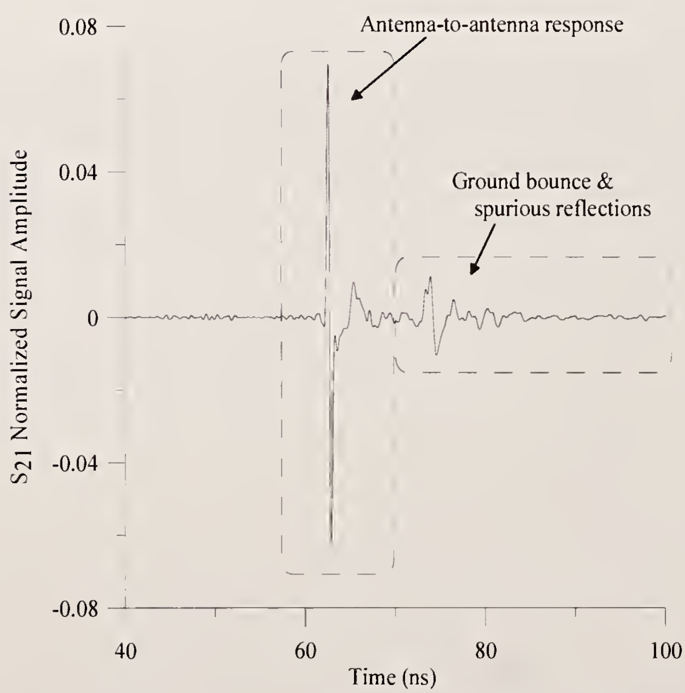


Figure 44. Ungated time-domain transmission waveform for a TEM antenna obtained at a separation of 6.0 m and vertical polarization.

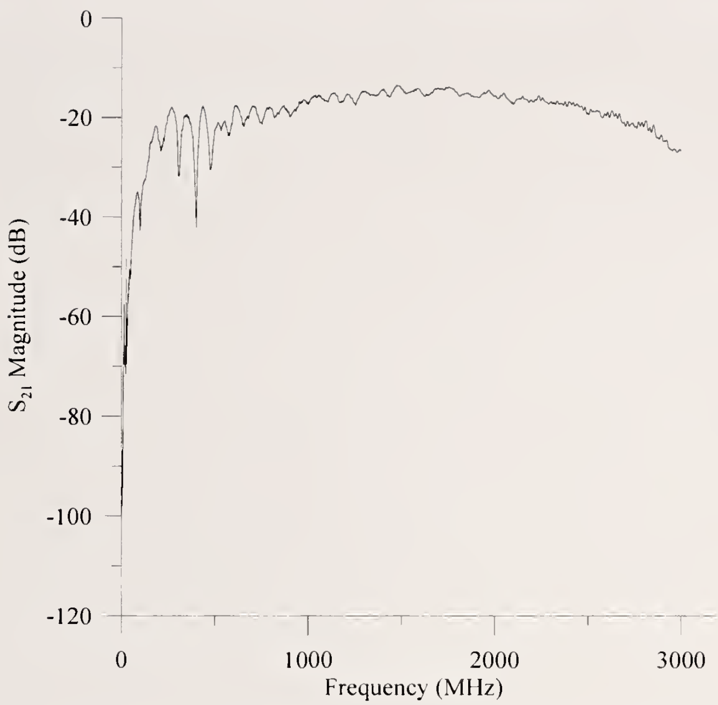


Figure 45. Ungated frequency-domain amplitude spectrum for a TEM horn antenna obtained at a separation of 6.0 m and vertical polarization. Note the scalloping due to the large ground-bounce reflection shown in Figure 44.

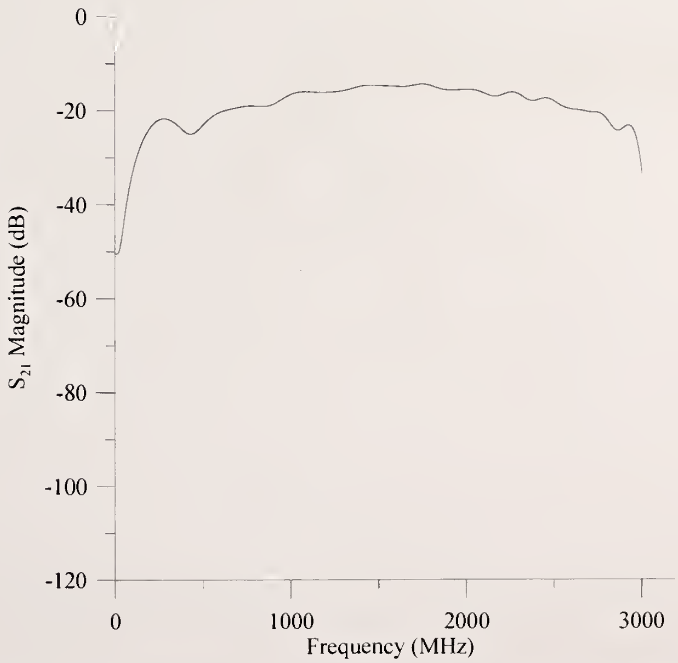


Figure 46. Gated frequency-domain amplitude spectrum for the TEM horn antenna corresponding to the waveform of Figure 44.

# 6. Airframe Penetration Measurements — Overview

We began by measuring the penetration at several extrapolation points on the 45° line, as shown by the black X's in Figure 46. These measurements are completed for every effort to ensure the system is performing correctly and to determine that the reference antenna separations are in the far-field. The data for both measurement efforts will be presented in this section; therefore some data will be shown for an upper frequency of 3 GHz, and other data are shown for an upper frequency of 18 GHz. The following measurements were performed over the course of both measurement efforts: (1) the transmitting antenna was placed along the 45° extrapolation line at the 23.5 m (75 ft.) distance, then the receiving antenna was placed in the front galley, the rear galley, the flight deck, and the mid-passenger cabin; (2) the receiving antenna was placed in the mid-passenger cabin, and the transmitting antenna was moved around the aircraft to the 0°, 90°, 135°, and 180° positions. At the 90° position the transmitting antenna was moved in a small circle around this position to look at antenna pattern effects; (3) sector measurements were performed with the receiving antenna in the mid-passenger cabin and the transmitting antenna moved to the 90°, 100°, 110°, 120°, 125°, 130°, 135°, 140°, 145°, 150°, 160°, 170°, and 180° positions; and (4) internal propagation between cavities were measured. The transmitting antenna was placed in the mid-passenger cabin and the receiving antenna was placed in the flight deck, the main cabin, the cargo bay, and the avionics bay. The transmitting antenna was then moved to the cargo bay and the receiving antenna was located in the avionics bay. Each of these positions is shown by the red X's in Figure 44. Where applicable, we applied antenna gain and distance correction factors to maintain consistency in the results.

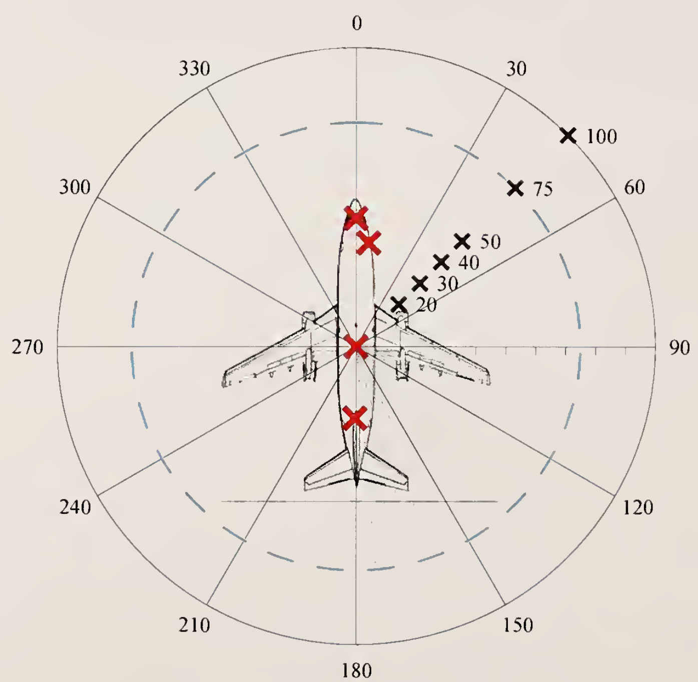


Figure 47. Test master graphic showing internal measurement positions (red X's), Extrapolation distances (black X's), measurements around aircraft (blue, dashed line) at a distance of 23 m (75 ft).

## 6.1 Extrapolation Results

We performed a set of extrapolation measurements from 6.1 m (20 ft) to 30.5 m (100 ft). The transmitting antennas were moved along the 45° line and the receiving antennas were located in the main cabin. These measurements were used to determine whether we were in the far-field and to understand how penetration changes as a function of distance from the aircraft. Distance correction was applied to the data by use of a reference distance of 6.1 m. These data are shown in Figures 48 to 51. These measurements show a spread in the data of about 7 dB to 10 dB across the frequency spectrum for the DRG antennas and around 10 dB for the TEM horn antennas. The large spread in the data is due mostly to the 6.1 m distance for the DRG antennas and the 6.1 m, 9.1 m and 30.5 m distances for the TEM horn antennas. If we remove these data sets, we tighten up the spread to between 3 dB and 6 dB for both sets of antennas. We believe this is because, at the closer distances, our antennas see only a spot size of the aircraft, but as we move further from the aircraft the antennas see more of the aircraft and the surrounding environment. The DRG antennas have higher directivity than the TEM horn antennas, which corresponds to the greater spread in penetration data for the TEM horn antennas. These results have been both corrected for distance and for antenna gain. A discussion of the gain for the DRG horn antenna and TEM horn antenna is given in Appendix A.

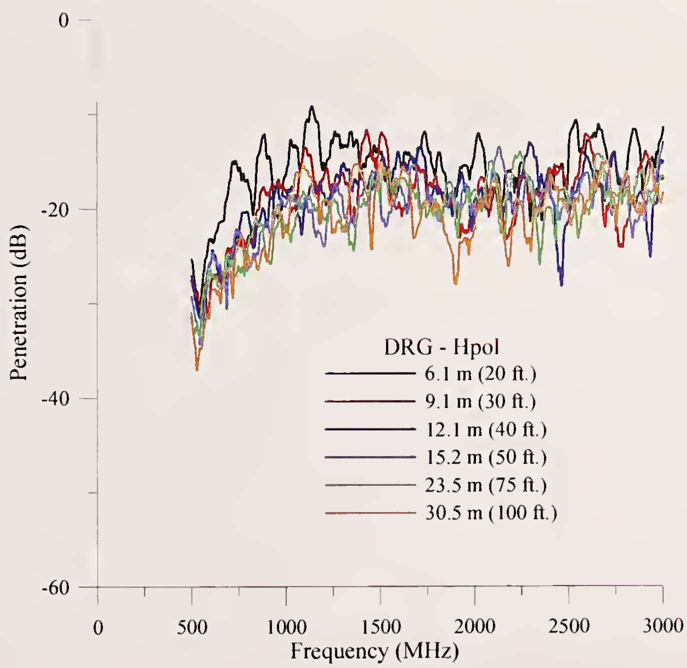


Figure 48. Extrapolation measurements for the DRG antenna, horizontal polarization.

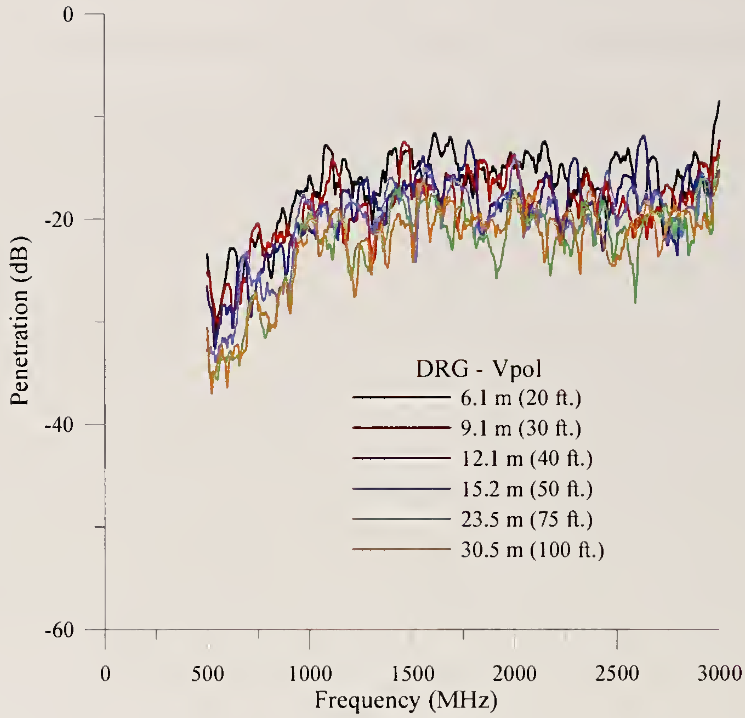


Figure 49. Extrapolation measurements for the DRG antenna, vertical polarization.

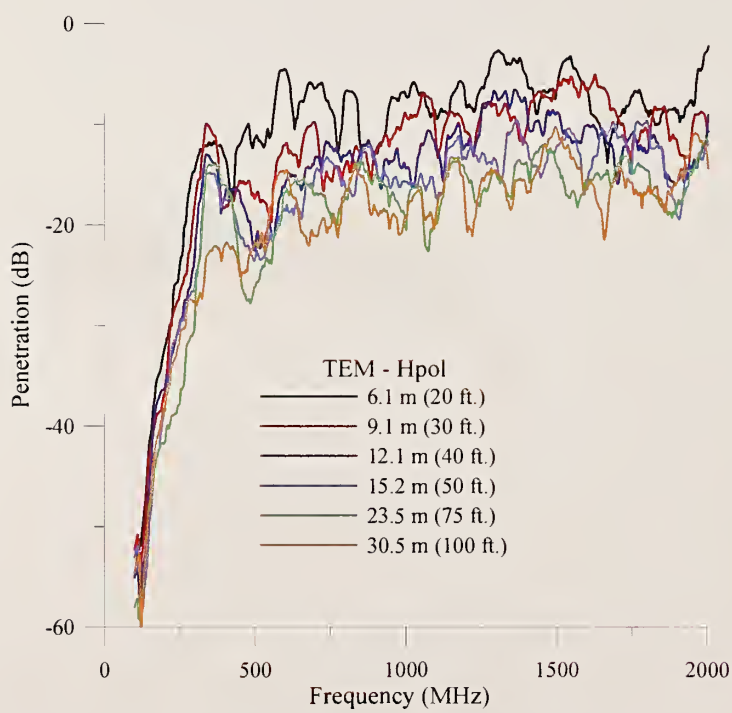


Figure 50. Extrapolation measurements for the TEM antenna, horizontal polarization.

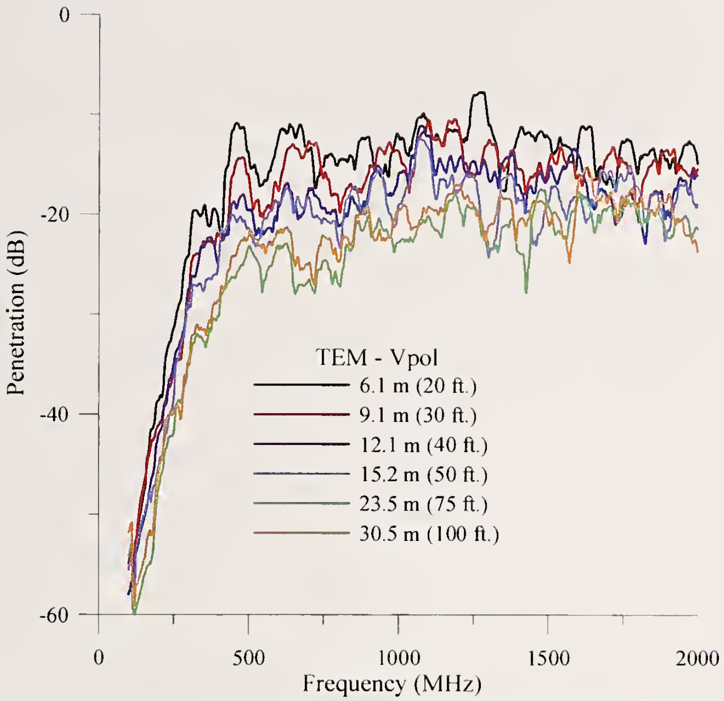


Figure 51. Extrapolation measurements for the TEM antenna, vertical polarization.

## 6.2 Penetration into aircraft from 45° extrapolation line

These measurements were used to study penetration as a function of the receiving antenna's internal position. To accomplish this, the receiving antenna was moved to several locations within the aircraft. Internal receiving antennas were located in the flight deck, the front and rear galleys, and the mid-passenger cabin. The transmitting antenna was located on the 45° extrapolation line at 23.5 m (75 ft.). This location was chosen because we had performed more than one measurement at this position. At some positions, more than one measurement was taken.

### 6.2.1 Measurements in the Flight Deck

Figure 52 shows the placement of the receiving antennas for measurements taken at position 4 in the flight deck (see Figure 53). The TEM horn antenna was placed on the pilot's seat facing the outside of the aircraft. The DRG horn antenna was placed on the co-pilot's seat facing the instrument panel. Results at this position are shown in Figure 53. The graph shows that horizontally polarized fields allow greater penetration into the flight deck than vertically polarized fields. The TEM results are shown at the lower frequencies (red and light blue traces) and the DRG results are shown at the higher frequencies (orange and dark blue traces). The horizontally polarized TEM horn antenna results show penetration values on the order of −15 dB and the vertically polarized TEM horn antenna shows an average penetration around −22 dB. The horizontally polarized DRG horn antenna results show penetration values of approximately −15 dB, at around 4000 MHz with a constant decay up to 18,000 MHz, where values are approximately −30 dB. The vertically polarized DRG horn antenna starts with a penetration of around −20 dB at 2000 MHz, has a sharp drop from 3000 MHz to 4000 MHz, and then has a fairly constant value of −35 dB across the rest of the frequency band, with values ranging from −30 dB to −40 dB, depending on the frequency.

The placement of the receiving antennas for measurements taken at position 5 (see Figure 55) in the flight deck, is shown in Figure 54. The TEM horn antenna was in the pilot's seat pointing upward toward the flight deck windows. The DRG horn antenna was in the co-pilot's seat pointing toward the ceiling of the flight deck. Results at this position are shown in Figure 55. The graph shows that horizontally polarized fields allow greater penetration into the flight deck than vertically polarized fields. The horizontally polarized TEM horn antenna results show penetration values on the order of −10 dB at around 1000 MHz, and for the vertically polarized TEM horn antenna penetration shows a peak value at around −12 dB at 1000 MHz. The horizontally polarized DRG horn antenna penetration values rise from −20 dB to −15 dB from 1000 MHz to 2000 MHz and then have a constant decay up to 18,000 MHz, where we show values around −30 dB. The vertically polarized DRG horn antenna values start with a penetration of around −15 dB at 2000 MHz, drops from −15 dB to −35 dB from 2000 MHz to 6000 MHz and then has an average value around −30 dB across the rest of the frequency band, with values ranging from −20 dB to −40 dB, depending on the frequency.

Figure 52. Placement of receiving DRG and TEM horn antennas in the flight deck for position 4.

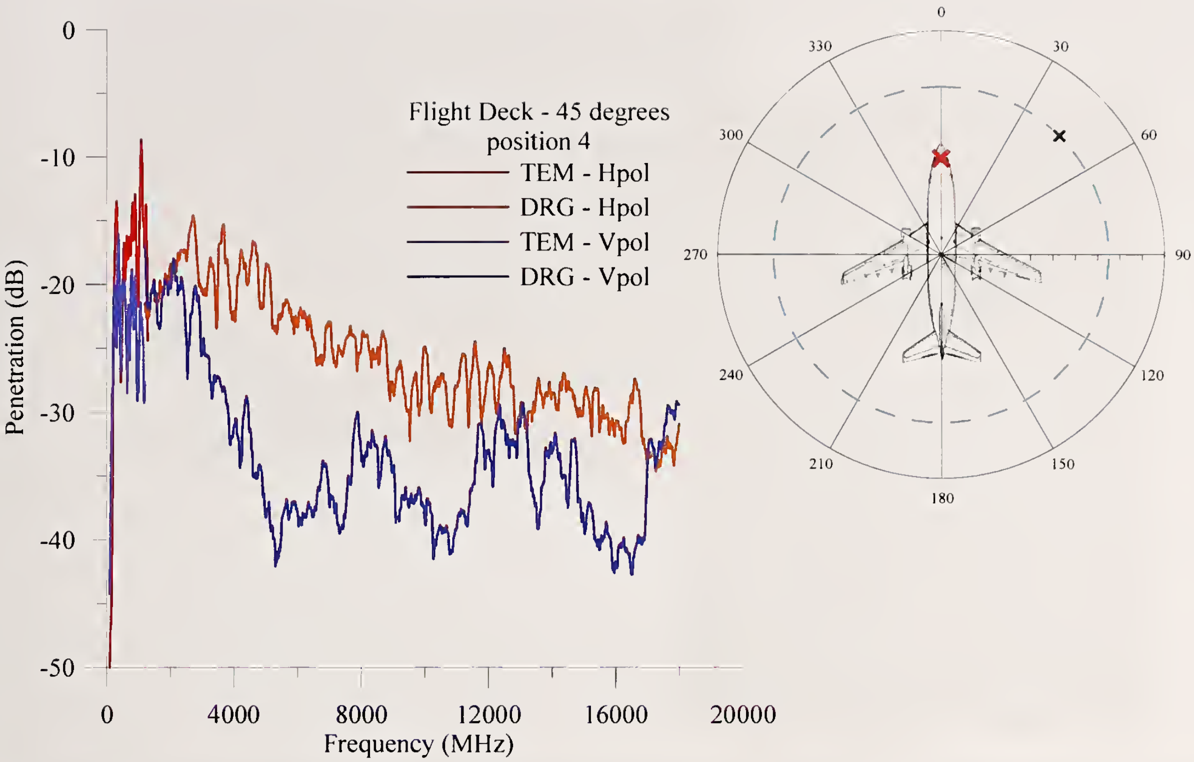


Figure 53. Penetration versus frequency for all antennas and polarizations for the transmitting tower placed the 45° extrapolation line and the receiving antennas placed in the flight deck.

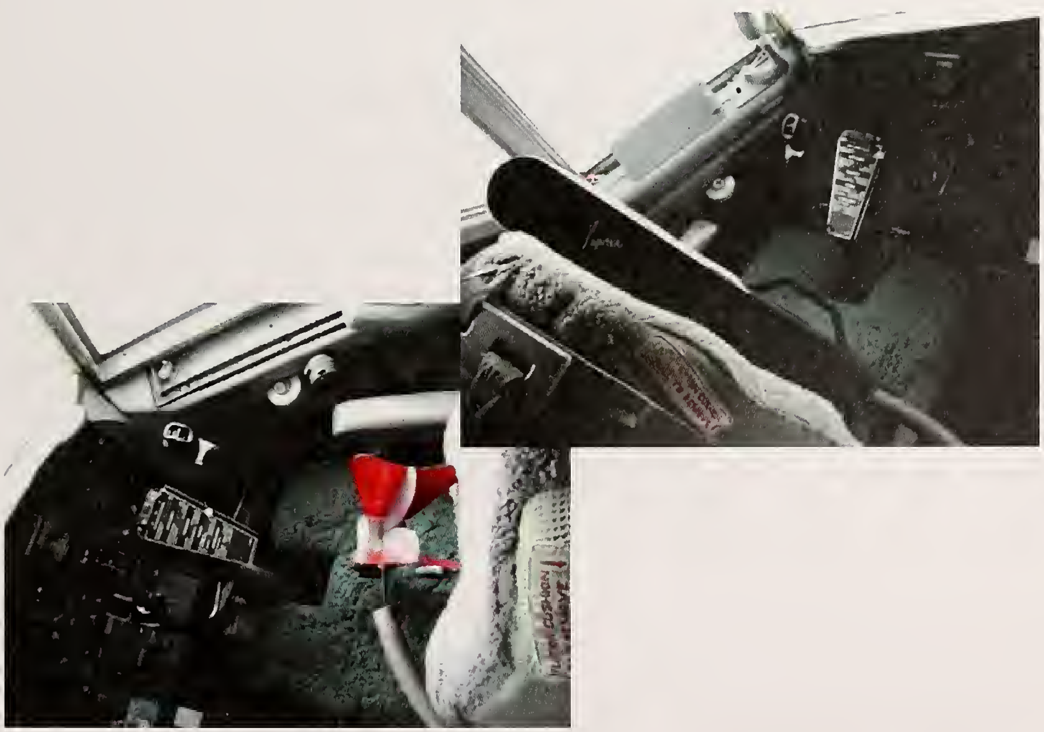

Figure 54. Placement of receiving DRG and TEM horn antennas in the flight deck for position 5.

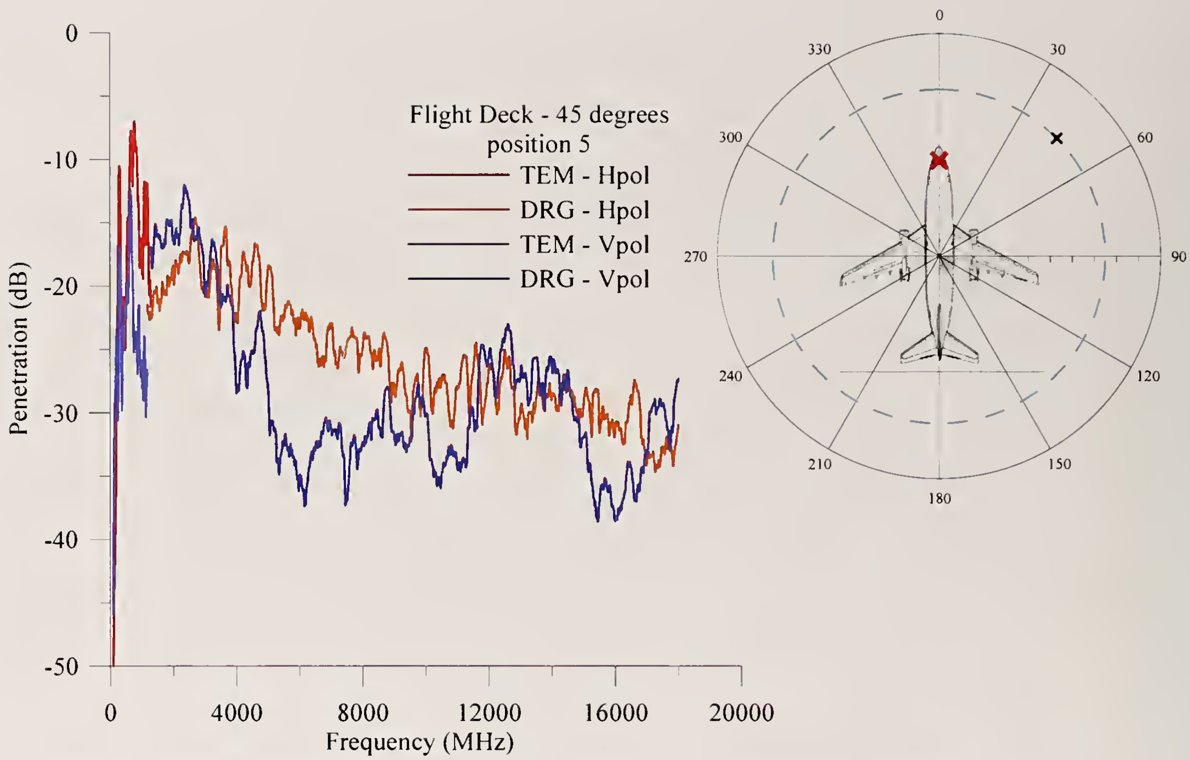


Figure 55. Penetration versus frequency for all antennas and polarizations for the transmitting tower placed along the 45° extrapolation line and the receiving antennas placed in the flight deck.

### 6.2.2 Measurements in the Front Galley

The placement of the receiving antennas for measurements taken at position 3 (see Figure 57) in the front galley is shown in Figure 56. The TEM horn antenna is shown pointing toward the cabin door. The DRG horn antenna is shown pointing toward the galley closet on the opposite side of the aisle. Results for this position are shown in Figure 57. The horizontally polarized fields penetrate into the aircraft better than the vertically polarized fields. The horizontally polarized TEM horn antenna peaks at a penetration value of −15 dB between 1000 MHz and 2000 MHz, and the vertically polarized TEM horn antennas peaks at a value of −18 dB between 1000 MHz and 2000 MHz. The horizontally polarized DRG horn antenna penetration values begin at −15 dB between 3000 MHz and 4000 MHz and drop to a value of approximately −28 dB at 18,000 MHz. Penetration values for the vertically polarized DRG horn antenna begin at a value of approximately −22 dB at 2000 MHz and drop to a value of −38 dB at 18,000 MHz. These values are slightly higher than for the flight deck. This could be due to the contribution from the windows in the mid-passenger cabin.

Figure 56. Placement of receiving DRG and TEM horn antennas in the front galley for position 3.

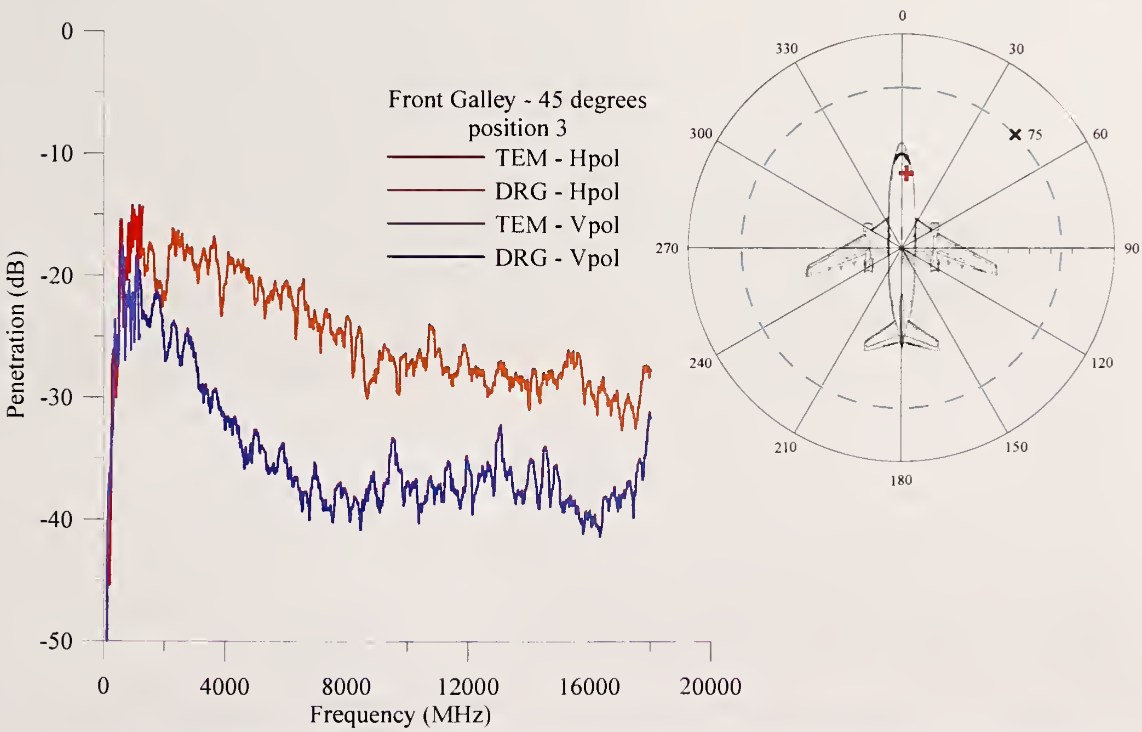


Figure 57. Penetration versus frequency for all antennas and polarizations for the transmitting tower placed along the 45° extrapolation line and the receiving antennas placed in the front galley for position 3.

### 6.2.3 Measurements in the Rear Galley

The antennas were then moved to the rear galley and two sets of measurements were taken. The placement of the receiving antennas, for measurements taken at position 6 (see Figure 59) in the rear galley, is shown in Figure 58. The TEM horn antenna is shown pointing upward into the corner between the ceiling and the rear cabin door. The DRG antenna is shown pointing toward the corner between the bathroom area and the rear cabin door on the opposite side of the aisle. Results for this position are shown in Figure 59. The difference in penetration between the horizontally polarized fields and the vertically polarized fields is not as pronounced as in the previous measurements and are on the order of a few decibels at certain frequencies. The horizontally polarized TEM horn antenna penetration values begin at a value around −30 dB at approximately 100 MHz and peak at a value of −20 dB at around 1000 MHz. The vertically polarized TEM horn antenna penetration values begin at values around −35 dB at 100 MHz and peak at a value of about −22 dB at 1000 MHz. The horizontally polarized DRG horn antenna penetration values begin at a value of −23 dB at 1000 MHz, rise to a value of −20 dB at 4000 MHz, and then drop to a value of around −28 dB at 18,000 MHz. The vertically polarized DRG horn antenna penetration values begin at a value of approximately −22 dB at 1000 MHz, rise to a value of approximately −21 dB at 2000 MHz, and drop to a value of −30 dB at 18,000 MHz. The variation in penetration values is less dramatic than for the previous positions.

For measurements taken at position 7 (see Figure 61) in the rear galley, the receiving antennas were placed as shown in Figure 60. The TEM horn antenna is shown pointing upward toward the ceiling and toward the front of the aircraft. The DRG antenna is shown pointing almost directly toward the front of the aircraft in the horizontal polarization, but on the opposite side of the aisle. Results for this position are shown in Figure 61. The difference in penetration between the horizontally polarized fields and the vertically polarized fields is now increased to around 5 dB to 10 dB as the frequency increases. The horizontally polarized fields have greater penetration. The horizontally polarized TEM horn antenna penetration values begin at a value around −30 dB at approximately 100 MHz and peak at a value of −20 dB at around 1500 MHz. The vertically polarized TEM horn antenna penetration values begin at values around −35 dB at 100 MHz and peak at a value −25 dB at 1000 MHz. The horizontally polarized DRG horn antenna penetration values begin at a value of −20 dB at 1000 MHz, show values from −20 dB to −25 dB between 2000 MHz and 14000 MHz, and then vary from −20 dB to −25 dB from 15,000 MHz to 18,000 MHz. The vertically polarized DRG horn antenna peaks at a value of approximately −20 dB at 2000 MHz, varies from −23 dB to −30 dB from 2000 MHz to 12,000 MHz and averages to a penetration value of −30 dB from 12,000 MHz to 18,000 MHz.

A distance correction is applied when the reference measurement distance and the shielding measurement distance are different, as discussed at the beginning of Section 5. Common sense would lead us to process the data using the actual geometric distance between antennas; however, in this type of an environment, this approach does not work because the actual flight path is not known, due to multiple apertures. Typically, we use the geometric center of the aircraft for distance corrections so that results can be compared. Another possibility is to observe the onset of the signal in the time-domain and use this value (converted to distance) to distance-correct the data. For this set of measurements in the rear galley, we applied a distance correction of 29.3 m (96 ft.). Results for position 6 are shown in Figure 62, and results for position 7 are shown in Figure 63. This experiment shows that penetration values can vary by about 2 dB, depending on the distance correction that is used. The difference in distance between the time-domain signal onset and the 23.5 m (75 ft.) is approximately 6 m. For consistency between this technical note and previous technical notes, a 23.5 m (75 ft.) distance correction has been used. The time-of-flight distance correction has not been used but could be a topic of discussion for future measurements.

Figure 58. Placement of receiving DRG and TEM horn antennas in the rear galley for position 6.

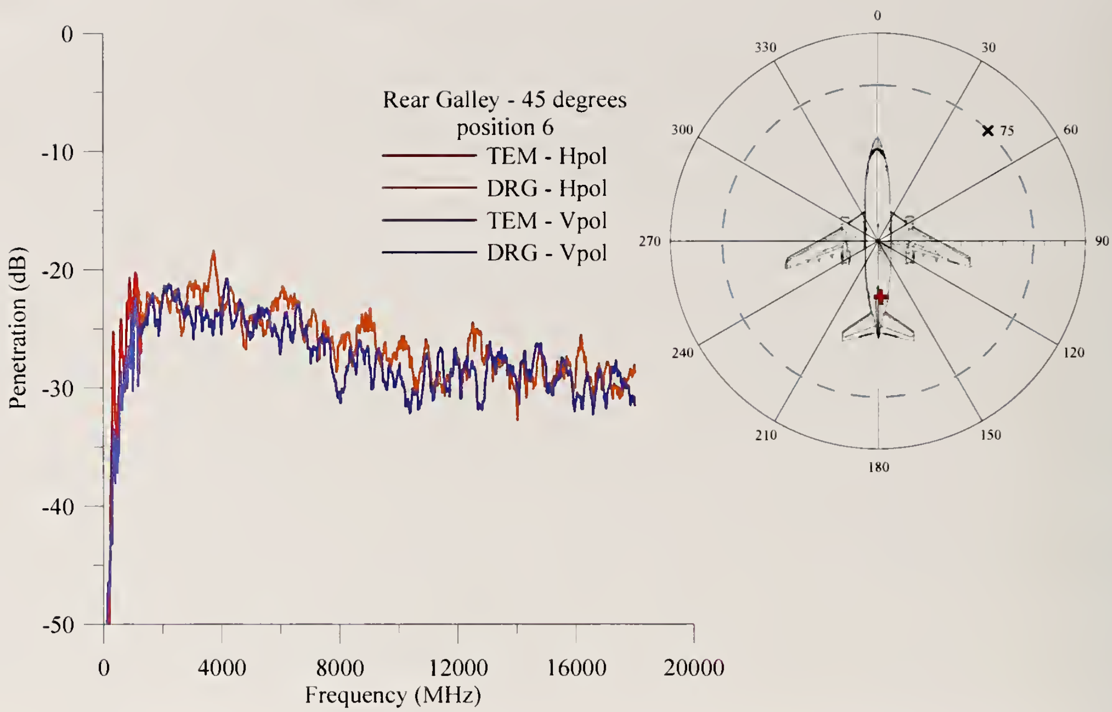


Figure 59. Penetration versus frequency for all antennas and polarizations for the transmitting tower placed along the 45° extrapolation line and the receiving antennas placed in the rear galley at position 6.

Figure 60. Placement of receiving DRG and TEM horn antennas in the rear galley for position 7.

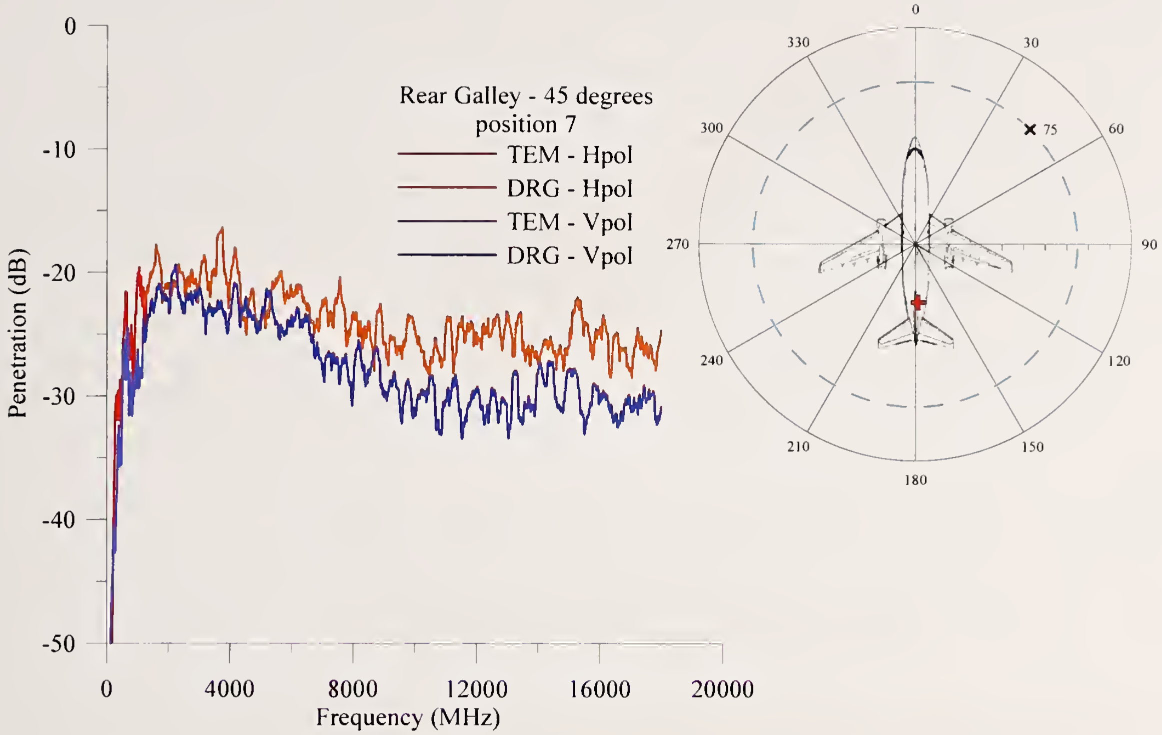


Figure 61. Penetration versus frequency for all antennas and polarizations for the transmitting tower placed along the 45° extrapolation line and the receiving antennas placed in the rear galley at position 7.

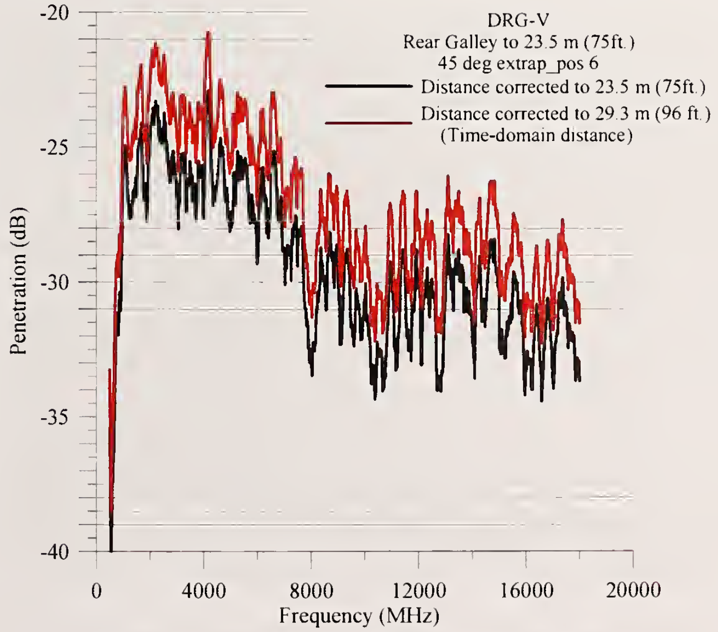


Figure 62. Results showing penetration difference due to distance correction factor for rear galley data.

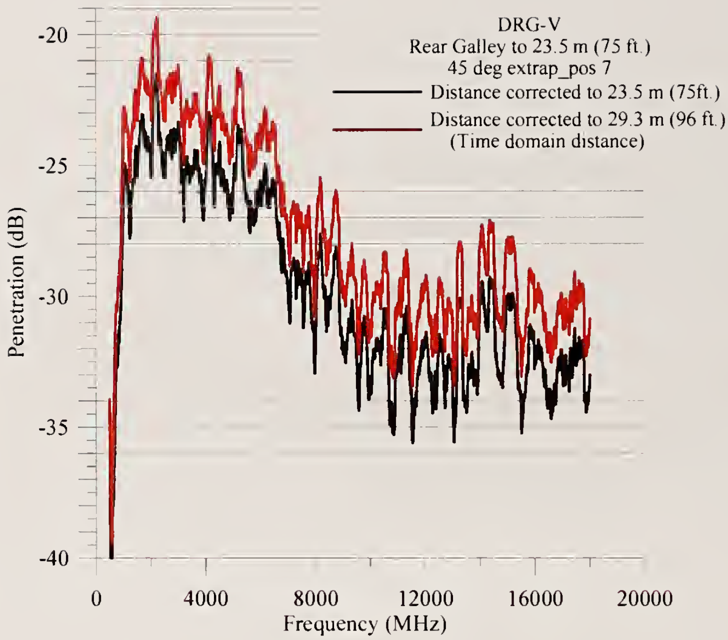


Figure 63. Results showing penetration difference due to distance correction factor for rear galley data.

### 6.2.4 Measurements in the Mid-Passenger Cabin

The final location for the extrapolation-line measurements was in the mid-passenger cabin. Two sets of measurements were completed here. The placement of the receiving antennas, for measurements taken at position 2 (see Figure 65) in the mid-passenger cabin, is shown in Figure 64. Both antennas were pointing toward the ceiling and were positioned at approximately the same angles. Results for this position are shown in Figure 65. The horizontally polarized fields have greater penetration than the vertically polarized fields. The horizontal polarized TEM horn antenna penetration values begin at a value around −20 dB at approximately 100 MHz and peak at a value of −10 dB at around 1000 MHz. The vertically polarized TEM horn antenna penetration values begin at values around −25 dB at 100 MHz and peak at a value of −25 dB at 1000 MHz. The horizontally polarized DRG horn antenna penetration values begin at a value of −10 dB at 1000 MHz and vary from −10 dB at 2000 MHz to −15 dB at 18,000 MHz. The vertically polarized DRG horn antenna peaks at a penetration value of approximately −15 dB at 2000 MHz and varies from −15 dB to −30 dB from 2000 MHz to 18,000 MHz.

For the second set of data the antennas remained in the same location, but both receiving antennas were positioned to point into the floor of the main passenger cabin. Beneath the main passenger cabin floor is the cargo bay. This is position 3 (see Figure 67) as shown in Figure 66, and results for this position are shown in Figure 67. Again, the horizontally polarized fields have greater penetration than the vertically polarized fields and this penetration is most likely due to the main cabin windows. The horizontally polarized TEM horn antenna penetration values begin around −20 dB at approximately 100 MHz and peaks at a value of −10 dB at around 1000 MHz. The vertically polarized TEM horn antenna penetration values begin around −25 dB at 100 MHz and peak at a value of −15 dB at 1000 MHz. The horizontally polarized DRG horn antenna penetration begins at a value of −10 dB at 1000 MHz and varies slowly down to a value of −20 dB at 18,000 MHz. The vertically polarized DRG horn antenna penetration peaks at a value of approximately −15 dB at 1500 MHz and drops to −35 dB at 8000 MHz and then varies at values from −30 dB to −35 dB from 8000 MHz to 18,000 MHz.

Figure 64. Placement of receiving DRG and TEM horn antennas in the mid-passenger cabin for position 2.

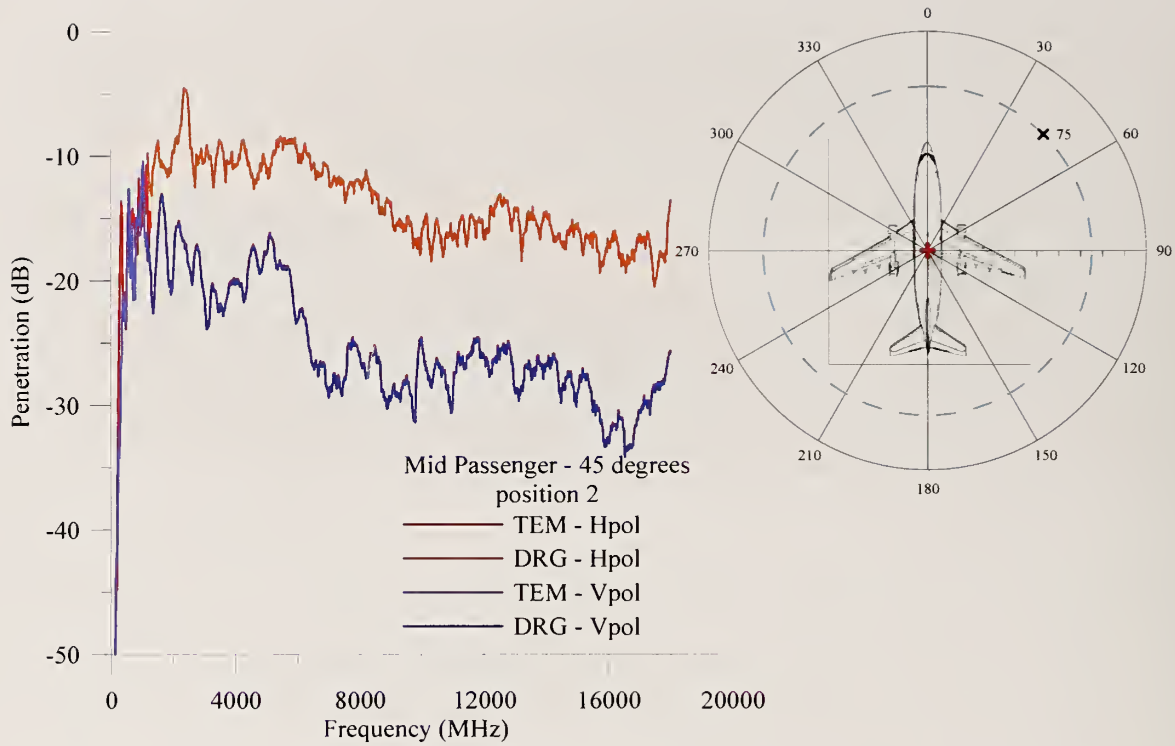


Figure 65. Penetration versus frequency for all antennas and polarizations for the transmitting tower placec along the 45° extrapolation line and the receiving antennas placed in the mid-passenger cabin at position 2

Figure 66. Placement of receiving DRG and TEM horn antennas in the mid-passenger cabin for position 3.

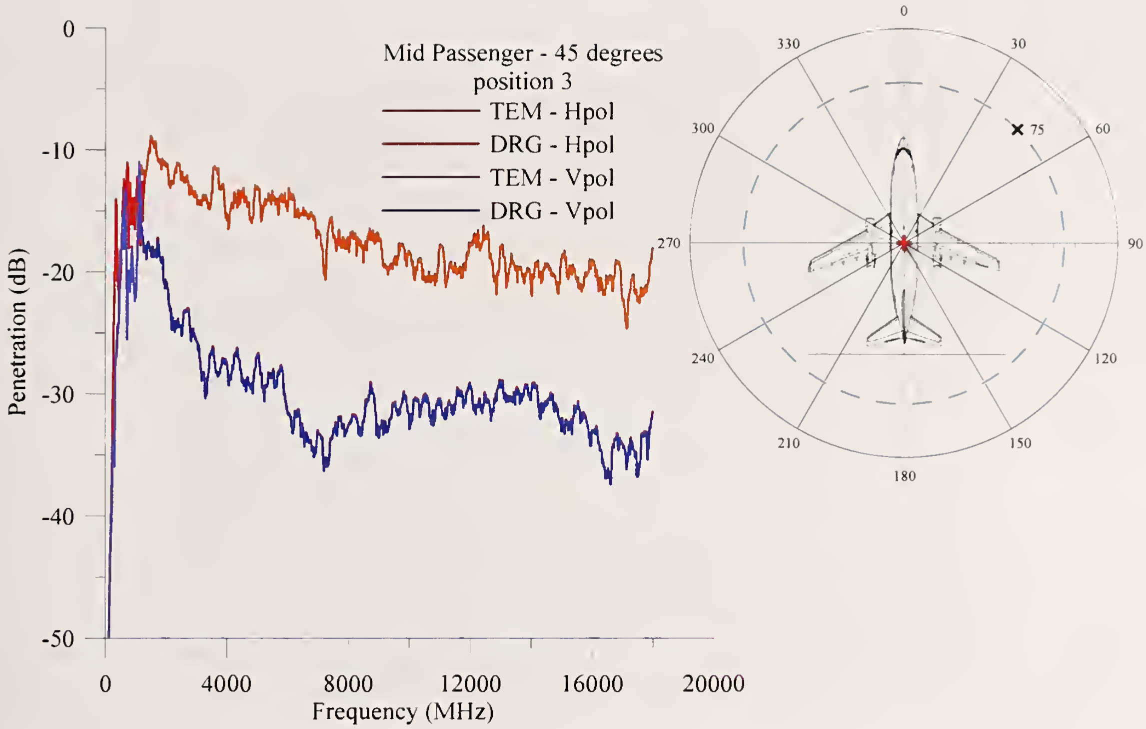


Figure 67. Penetration versus frequency for all antennas and polarizations for the transmitting tower placed along the 45° extrapolation line and the receiving antennas placed in the mid-passenger cabin at position 3.

## 6.3 Mid-Passenger Cabin Penetration Results

For the next series of measurements, the receiving TEM and DRG antennas were placed in the mid-passenger cabin and were positioned as shown in Figures 68 and 69. The setup is the same in both photos, but a photograph was taken from the front of the antennas and from behind the antennas to show their proximity to the front and rear of the aircraft.

### 6.3.1 Single-Position Quadrant Measurements

Four transmitting locations were measured with the receiving antennas at the same location and in the same orientation for all four measurements in the mid-passenger cabin. The transmitting antennas were located at the 23.5 m (75 ft.) radius at the 0° position, the 90° position, the 135° position and the 180° position, as shown by the red X's in Figure 70. We again notice that the horizontally polarized fields tend to penetrate more easily into the aircraft than do the vertically polarized fields, although the differences are not as large as in some of the previous measurements. At the 0° position, for the transmitting antennas in the horizontal polarization, the penetration values vary from −25 dB at 100 MHz to a peak value of −17 dB at around 2000 MHz. The penetration also varies from −20 dB to −30 dB from 2000 MHz to 18,000 MHz. For the transmitting antennas in the the vertical polarization, the penetration values vary from −25 dB to −30 dB across the frequency spectrum. At the 90° position, the vertical and horizontal polarization results lie almost directly on top of each other. Penetration values rise to a peak value of −10 dB around 2000 MHz down to −20 dB at 18,000 MHz. We measured approximately the same behavior for the 135° position. At the 180° position the horizontally polarized fields penetrate more easily at the lower frequencies up to about 12,000 MHz, and then the values are only slightly above those of the vertically polarized fields. The highest penetration occurs for the horizontally polarized fields from 500 MHz to 1000 MHz at a value of −20 dB; it then drops to a value of −35 dB at 12,000 MHz, and is constant at a value of −35 dB from 12,000 MHz to 18,000 MHz. The maximum penetration for the vertically polarized fields occurs at around 2000 MHz at a value of −30 dB;p it then drops to a value of −40 dB between 8000 MHz and 12,000 MHz and then increases to a value of −35 dB at 18,000 MHz. We moved the tower approximately 0.3 m to the left and then took another set of measurements and notice that the results are virtually the same as those from the 180° position. We see maximum penetration into this aircraft at the measured angles of 90° and 135°. The minimum penetration occurs at the 180° position, and the penetration through the flight deck shows results between these two extremes.

At the 90° position, from the previous set of measurements, we took a tight circular sweep around this position to look at results and how they depend on the antenna pattern of both the DRG horn antennas and the TEM horn antennas. While at the 90° position, we initially boresighted the antenna at the midsection of the aircraft. We then moved the transmitting antenna tower 45° degrees to the left and took another measurement; we then moved the tower another 45° at this same 90° clock position to a 90° offset from boresight and then again with the antennas facing 180° from boresight of the aircraft. The results of these measurements are shown in Figure 68. With the antenna boresighted at the aircraft, the vertically polarized and horizontally polarized penetration values lie almost directly on top of each other. They rise to a peak value of −10 dB at around 2000 MHz, and down to −20 dB at 18,000 MHz. This measurement taken at 90º is the same as in the previous section 6.3.1. With the antenna pointing 45° to the left of the boresight position (pointing at the tail) we obtain the results shown in Figure 71. We immediately see two results: the first is the band-edge discontinuity between the results of the vertically polarized TEM horn antenna and the DRG horn antenna. The second is the large spike in the vertically polarized data that occurs at approximately 17,000 MHz. We can speculate that this might be an ambient signal picked up only with the antennas in the vertical polarization. At the 90º offset, we see dominant influences for vertically polarized antennas. There is a band-edge discontinuity between the results for the TEM horn antennas and the DRG horn antennas, and then a large signal drop in the 8000 MHz to 10,000 MHz frequency band. Finally, as the antennas are pointed 180° away from the aircraft, we see a large discontinuity between the horizontally and vertically polarized TEM horn antenna low-frequency band and the horizontally and vertically polarized DRG horn antenna high-frequency band. This is most likely due to small signal levels from the back-lobes of the antennas.

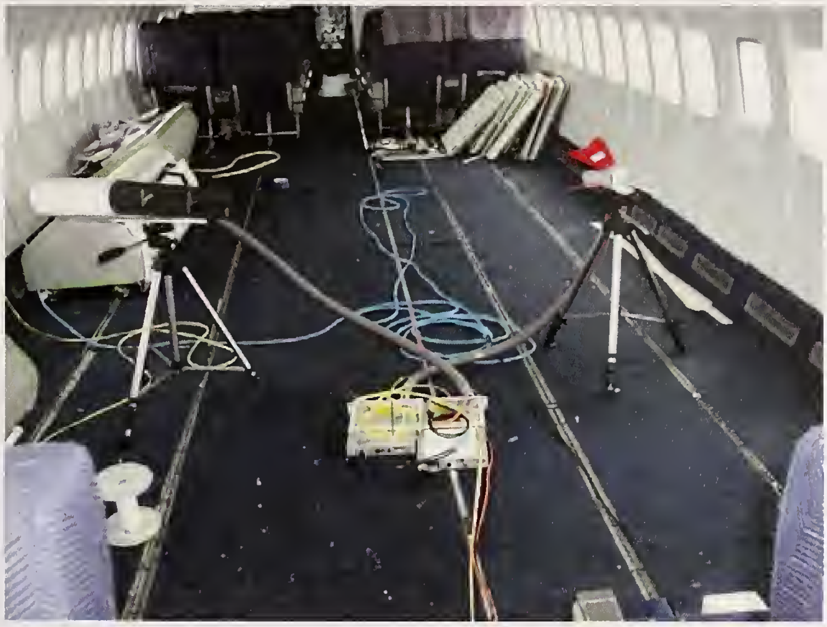

Figure 68. Placement of receiving DRG and TEM horn antennas in the mid-passenger cabin for single-position quadrant measurements looking toward front of aircraft.

Figure 69. Placement of receiving DRG and TEM horn antennas in the mid-passenger cabin for single-position quadrant measurements looking toward rear of aircraft.

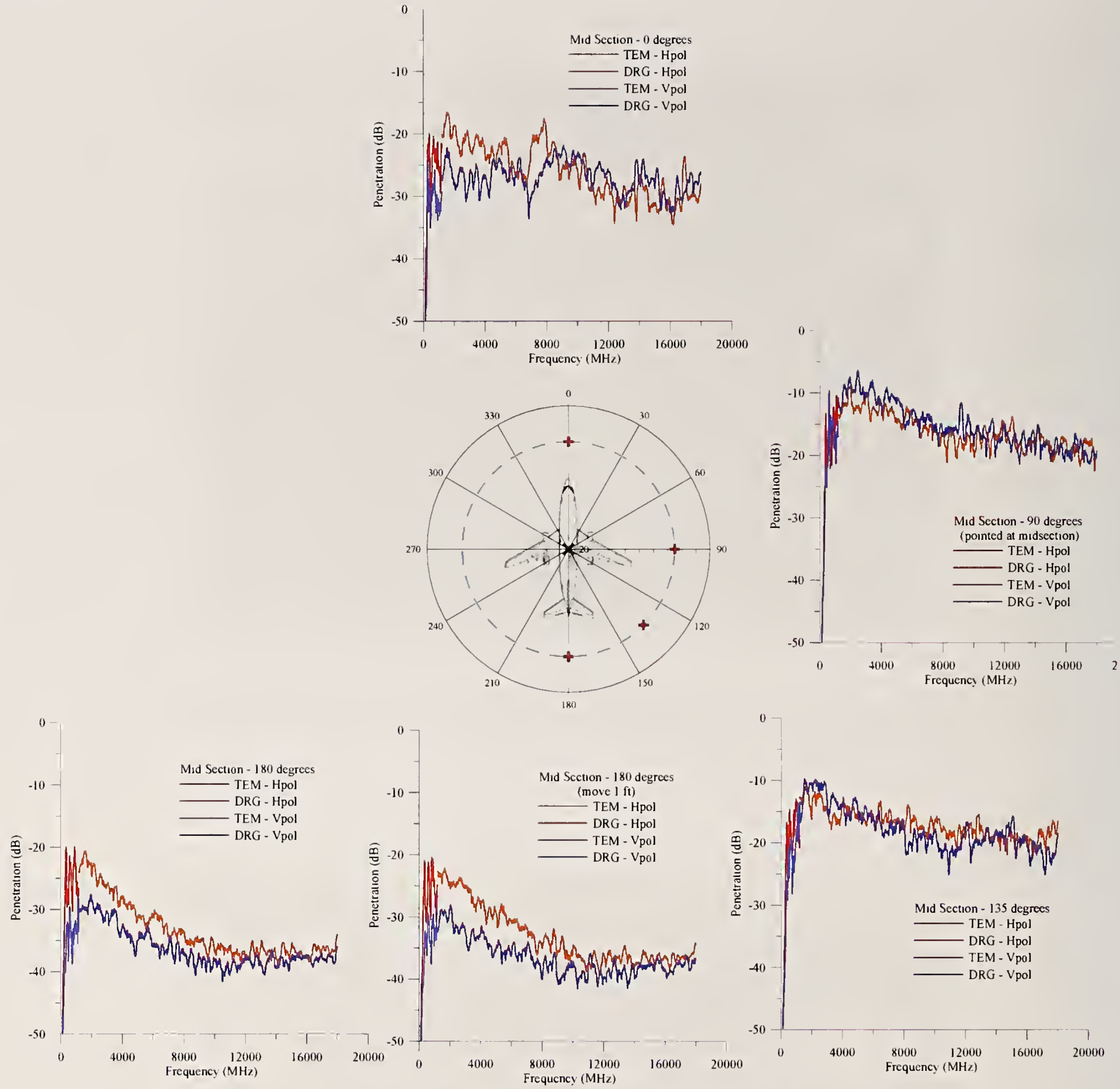


Figure 70. Penetration versus frequency for all antennas and polarizations for the transmitting tower moved around the aircraft at single positions in each quadrant. The receiving antenna is in the mid-passenger cabin.

### 6.3.2 Rear Quadrant Sector Measurements

The receiving antennas remained in the same position as for the previous set of measurements. The transmitting antenna tower was moved to positions around the rear quadrant of the aircraft from 90° to 180°. Measurements were taken every 10° from 90° to 120° and from 150° to 180° and then every 5° from 120° to 150°. These tests were designed to give us information on how many positions around the aircraft are required to fully characterize the penetration [29]. Further information is given in Appendix B. Based on a theoretical analysis for a single cut-plane, the number of positions required to fully characterize the Bombardier Global 5000 at 1 GHz is 1197,

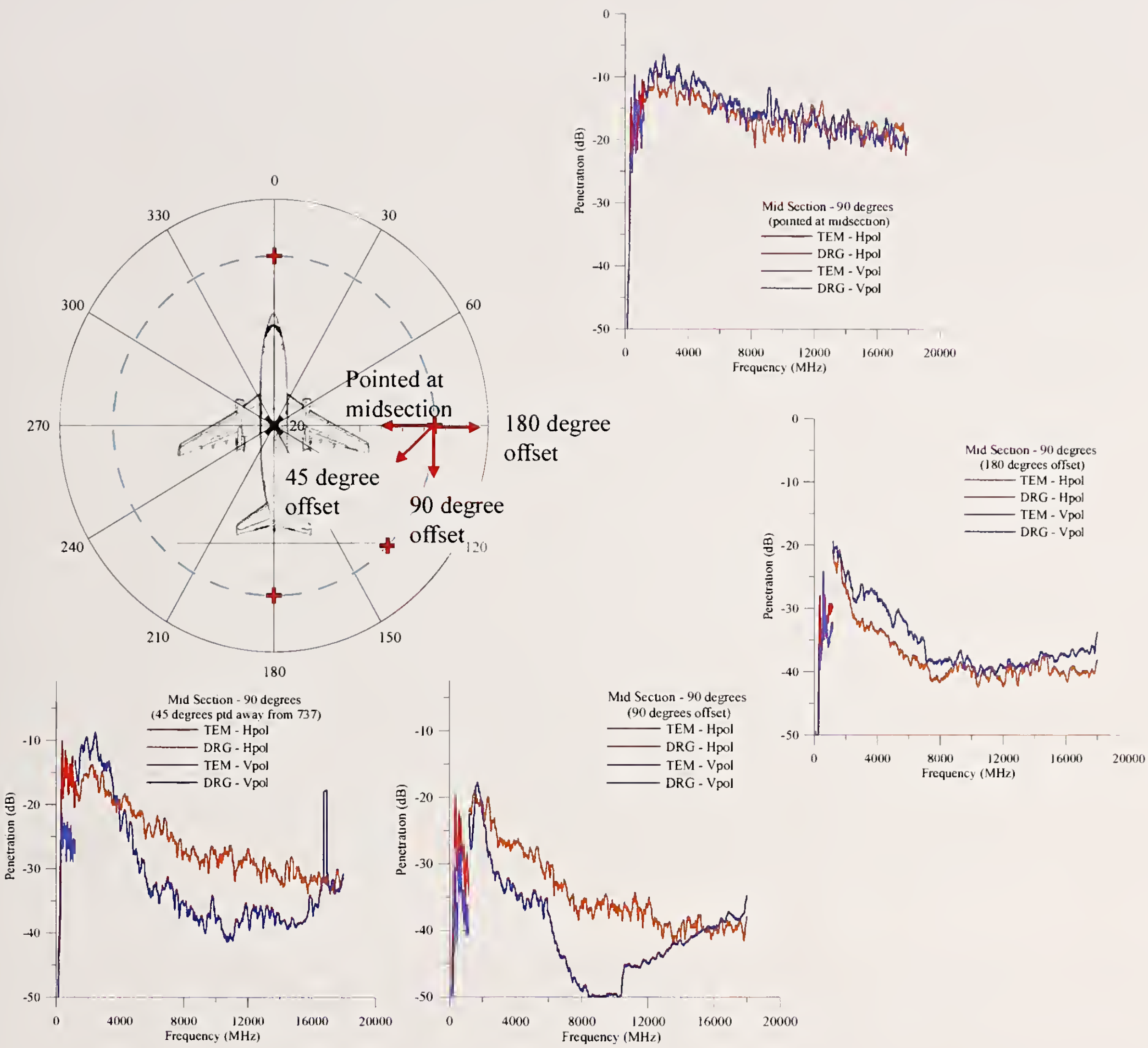


Figure 71. Penetration versus frequency for all antennas and polarizations for the transmitting tower moved in a small circle at the 90° position. The receiving antenna is in the mid-passenger cabin.

at 5 GHz it is 5973, and at 18 GHz, the number of positions required to fully characterize the aircraft increases to 21505 [31]. This is based on the equation

$$N_c = 4ka + 2 \qquad for\ ka > 1, \tag{4}$$

where $k$ is the propagation constant $k = 2\pi / \lambda$, and $a$ is the radius of the object. For the Bombardier Global 5000, we used the largest dimension for the radius, which would be the length of the aircraft. Since the number of positions required to fully characterize the aircraft are impractical to implement for testing, we wanted to know whether any major penetration points would be missed, and thus we decided to sample at the positions given above.

The results for angular positions from 90° to 130° are shown in Figure 72. For the measurements in general, we see that the horizontally polarized TEM horn antenna shows penetration values that are lower than those for the vertically polarized TEM horn antenna. Also, there seems to be a resonance that occurs at around 400 MHz for the horizontally polarized fields; we have seen this in several other aircraft types. For the measurement at 90°, we see that at the higher frequencies the traces for horizontally and vertically polarized antennas lie almost directly on top of one another. There is a discontinuity between band edges at around 1 GHz that could have something to do with antenna alignment, as discussed in the previous section. Penetration values appear to average out around −20 dB across this bandwidth. Because these measurements were taken at a later date than results shown in the previous measurements and with a different system, we would expect the measurements to be the same only to within a specified uncertainty. These uncertainties will be addressed at the end of this technical report. However, for comparison, we introduce the measurement results from the previous section (6.3.1) into Figure 73. The plot on the left shows measurement results from October 2004, which are the same results shown in Figure 72. The average value is about −20 dB across the frequency bandwidth. The plot on the right shows the measurement results from October 2005, which shows that the average value varies from −10 dB to −15 dB. Although these two results are different, we have to remember that repeatability is a function of both the transmitting location on the outside of the aircraft and the receiving location on the inside of the aircraft and the orientation of the receiving or transmitting antennas. At the 100° position, we see a 1 dB to 2 dB difference at the band edges and the penetration value seems to average around −22 dB across this bandwidth of interest. For the 90°, 100° and 110° positions, there appears to be a slight peaking of values from approximately 500 MHz to 1000 MHz for the vertically polarized antennas. At the 110° position, the penetration values for the horizontally and vertically polarized antennas tend to overlap in the higher frequency band with an approximate average of −22 dB. For the angular positions from 120° to 130°, the penetration values average out to around −20 dB and the differences between the values for horizontally polarized and vertically polarized antennas are minimal.

Figure 74 shows the penetration results for angular positions from 135° to 180°. Again, in these plots we see a resonance that occurs at around 400 MHz for the horizontally polarized TEM horn antenna. Band edges tend to align to within 1 dB to 2 dB, and there is not much difference between the horizontally and vertically polarized antennas until we reach 160° to 180°. The average penetration value for 135° and 140° is around −20 dB to −22 dB. At 145° the average penetration value has dropped to around −22 dB, and at 150° the average penetration value has dropped to around −25 dB. For the 160° angular position, frequencies below 1000 MHz show the same penetration values of around −30 dB, but above 1000 MHz, the horizontally polarized antenna shows an average penetration value of approximately −25 dB and the vertically polarized antenna shows an average penetration value of approximately −28 dB. At 170° the two different polarizations split further, with results for the horizontally polarized antenna maintaining an average penetration value of −25 dB, and those for the vertically polarized antenna having an average penetration value around −35 dB. At the 180° position, the two polarizations have greater differences in the high-frequency band and are now at approximately −30 dB and −40 dB in the horizontal polarization and vertical polarization, respectively. For the lower frequency band, these results compare to within 5 dB of those shown in Figure 75, and to within 5 dB to 7 dB in the upper frequency band.

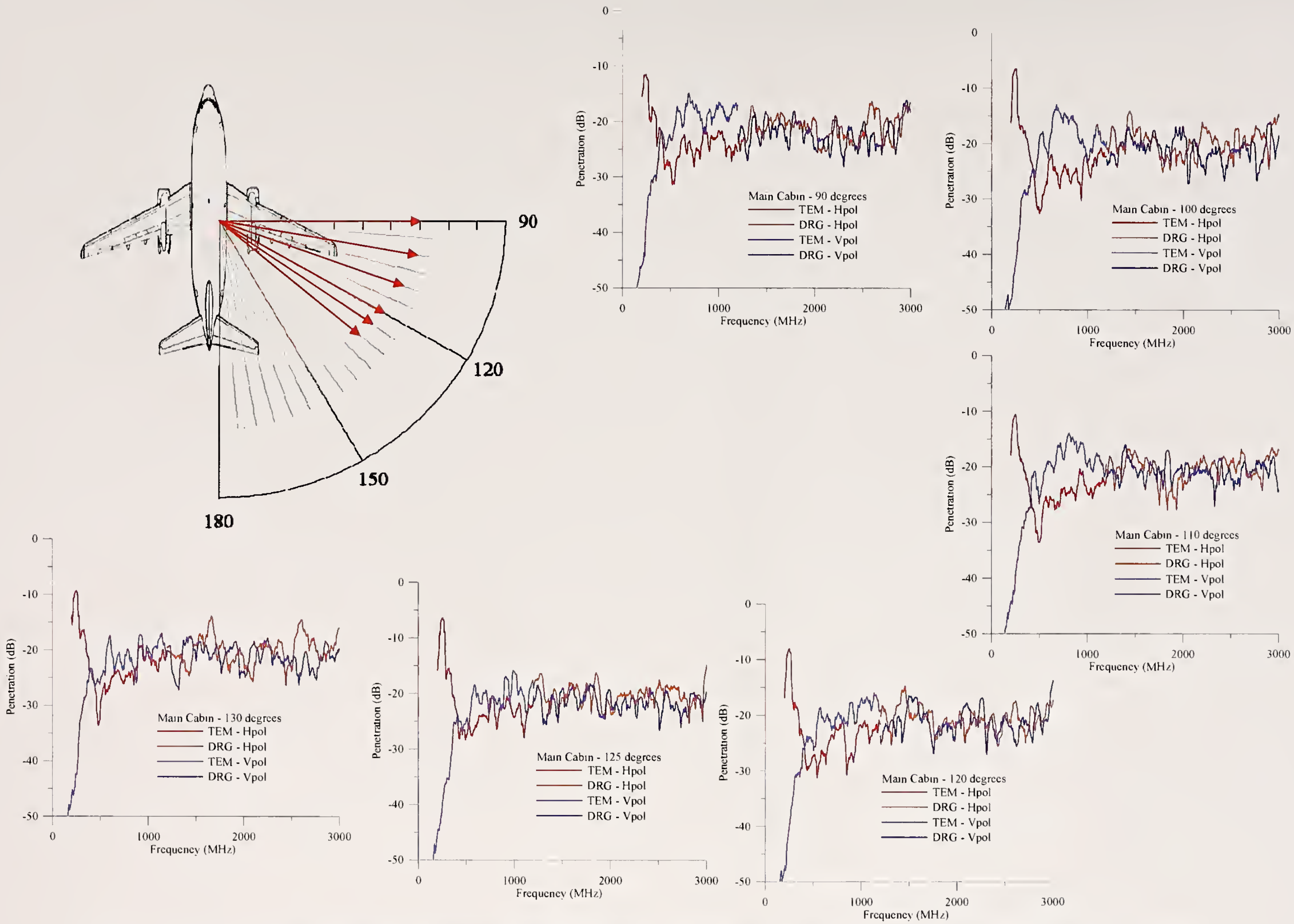


Figure 72. Penetration versus frequency for all antennas and polarizations for the transmitting tower moved to angular positions, 90°, 100°, 110°, 120°, 125°, and 130°. The receiving antenna is in the mid-passenger cabin.

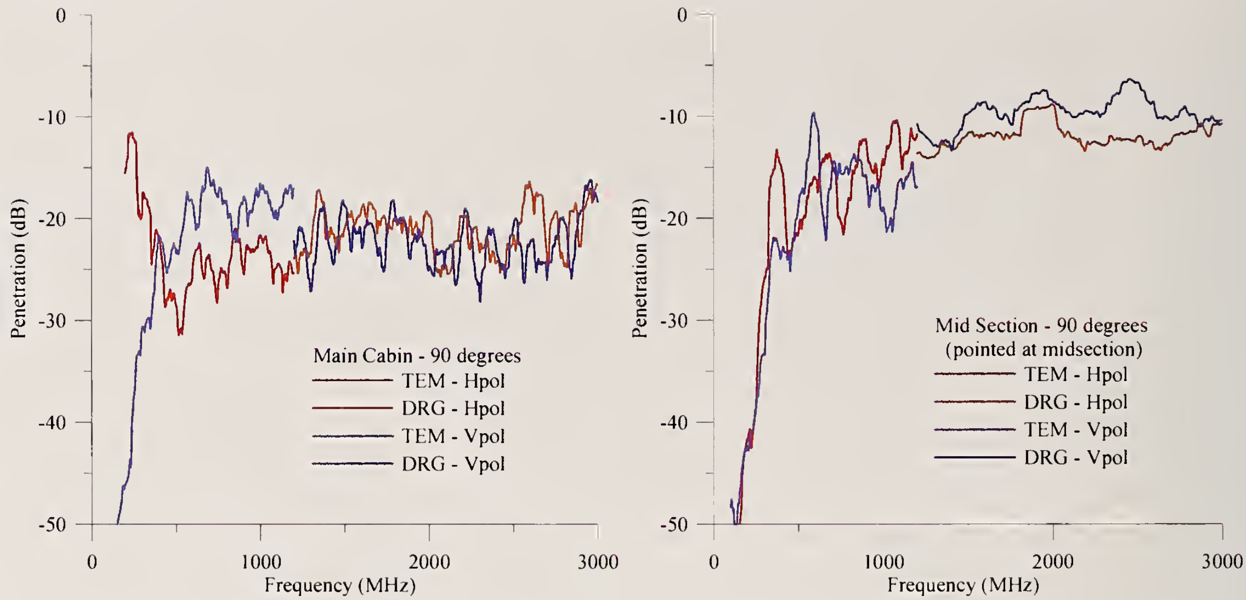


Figure 73. Comparison between Oct 2004 tests (left) and October 2005 tests (right) at the 90° position. The tests on the left were taken with a system having a bandwidth of 6000 MHz and the tests on the right were taken with a system having a bandwidth of 18,000 MHz.

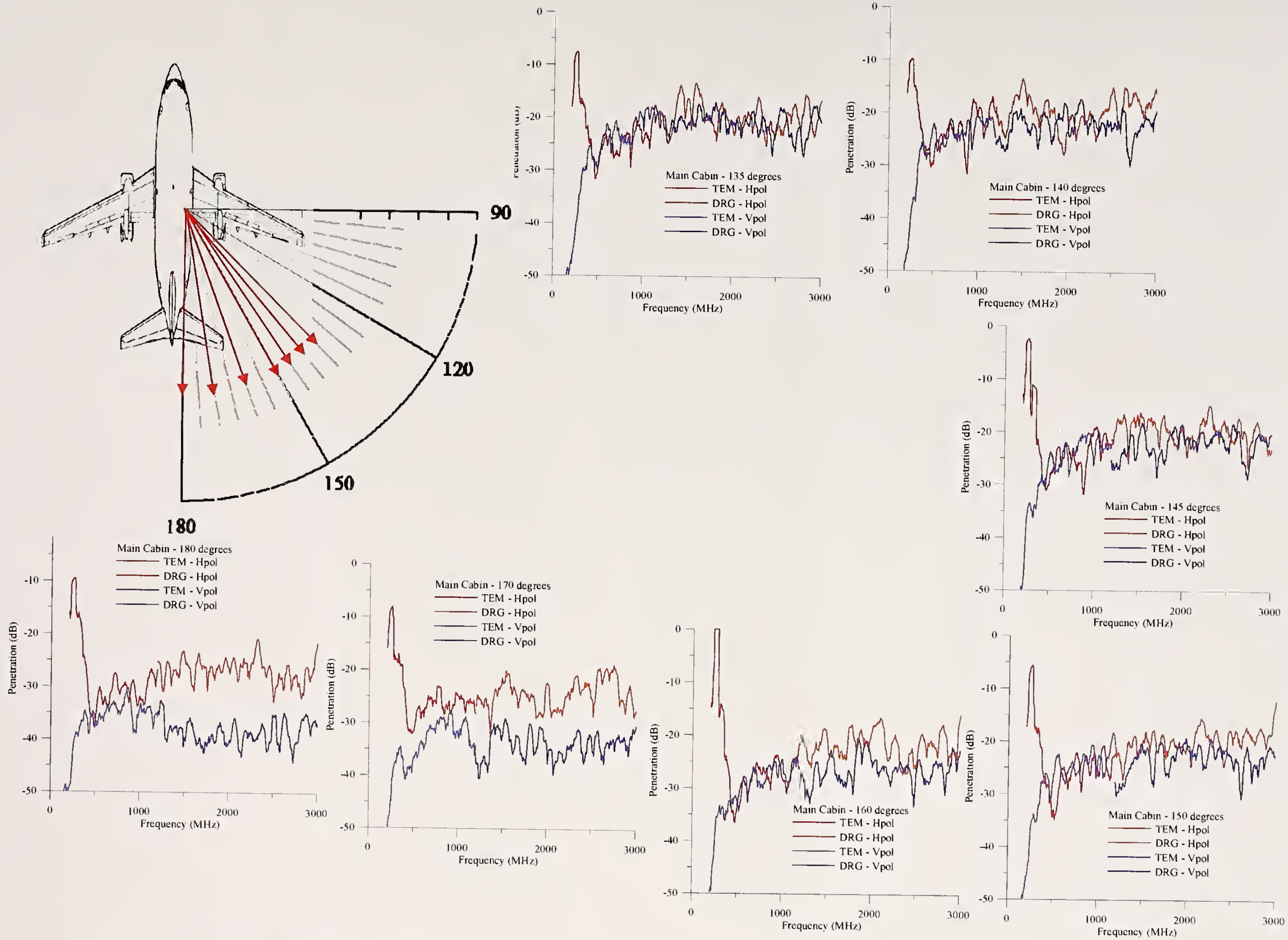


Figure 74. Penetration versus frequency for all antennas and polarizations for the transmitting tower moved to angular positions, 135°, 140°, 145°, 150°, 160°, and 170°, 180°. The receiving antenna is in the mid-passenger cabin.

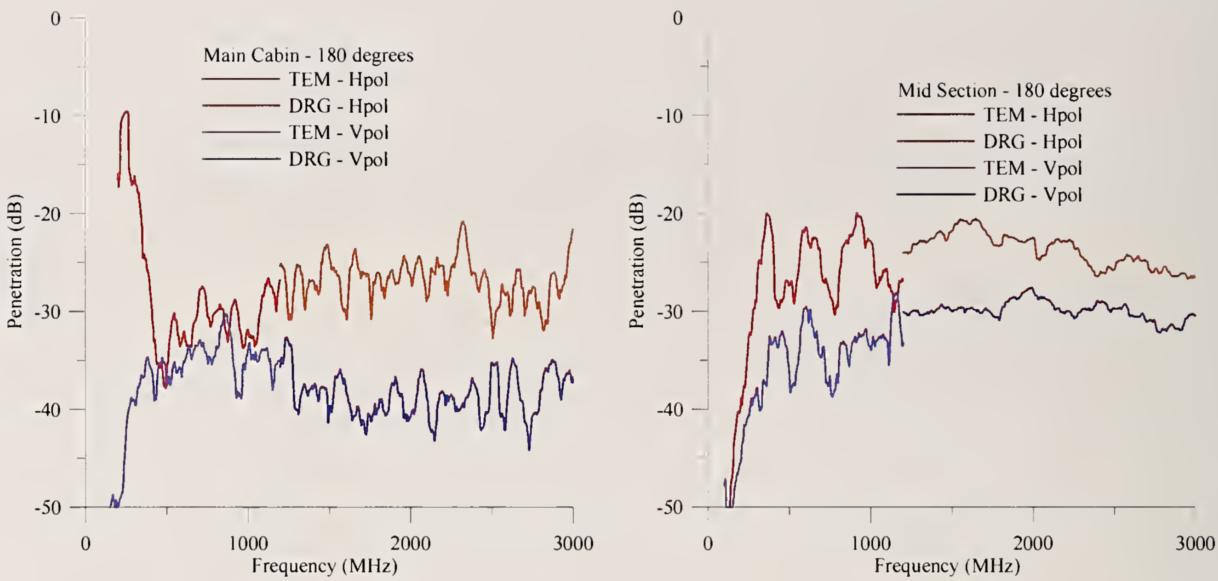


Figure 75. Comparison between Oct 2004 tests (left) and October 2005 tests (right) at the 180° position. The tests on the left were taken with a system having a bandwidth of 6000 MHz and the tests on the right were taken with a system having a bandwidth of 18,000 MHz.

## 6.4 Intercompartmental Insertion Loss Measurements

Aircraft manufacturers are concerned with high-level RF signals entering aircraft compartments where flight-sensitive equipment is installed. They will typically measure the penetration of high-level fields into these compartments where aircraft control systems exist. Usually, the receiving antenna is placed into the cavity along with a small stirrer and then the reverberant fields are measured to obtain a time and spatial average of the fields over the volume of the cavity. Because aircraft testing is time-consuming and expensive, typically only a few positions are measured, and the cavity is assumed to exhibit reverberant behavior. If the cavity is assumed to be reverberant, then statistically the electric field is uniform over the volume of that cavity. To verify this assumption, NIST decided to measure the insertion loss between aircraft cavities for several different positions without the use of mode-stirring/mode-tuning. The results are presented here. We have also included more information on statistics for the Bombardier Global 5000 and the Premier IA in Appendix C and numerical simulations for interior propagation measurements for the 737-200 in Appendix D.

### 6.4.1 Main Cabin to Main Cabin

The DRG and TEM horn antennas were measured at various positions around the main cabin. The DRG antenna positions were not measured at the same time as the TEM horn antenna positions because only two channels were available from the VNA at any one time for the internal configurations. In general, for each compartment-to-compartment measurement we tried to position them in approximately the same position for each of these runs.

#### 6.4.1.1 Combined TEM horn antenna positions

Six positions were measured by use of the TEM horn antennas. For setup 1, the measurement was taken twice without repositioning antennas with the main cabin door open and closed. Figure 76 shows all measurement results in the main cabin for the TEM horn antenna showing a maximum insertion loss of around −35 dB and a minimum insertion loss of around −75 dB. Figures 77 shows the results for the measurement having maximum cabin insertion loss, minimum insertion loss and two system noise-floor measurements. The first noise-floor measurement was taken with the aircraft's Auxiliary Power Unit (APU) on and the second was taken with the APU off.

Whisker-box plots are shown in Figure 78 for the following center frequencies, (1) 100 MHz, (2) 500 MHz, (3) 1000 MHz, (4) 1500 MHz, (5) 2000 MHz, and (6) 2500 MHz. Data in these plots are from a 200 MHz bandwidth around each center frequency. These plots show that the median insertion loss for these frequencies have values from about −45 dB to −85 dB. The maximum insertion loss for these frequencies is approximately −30 dB in a 200 MHz bandwidth around a center frequency of 1500 MHz, and the minimum insertion loss is −118 dB in a 200 MHz bandwidth around a center frequency of 100 MHz. Fifty percent of the data occurs in the light blue and dark blue boxes in the $25^{th}$ and $75^{th}$ percent quartiles. The program used to process this data does not give the distribution of points in the upper and lower tails of this data.

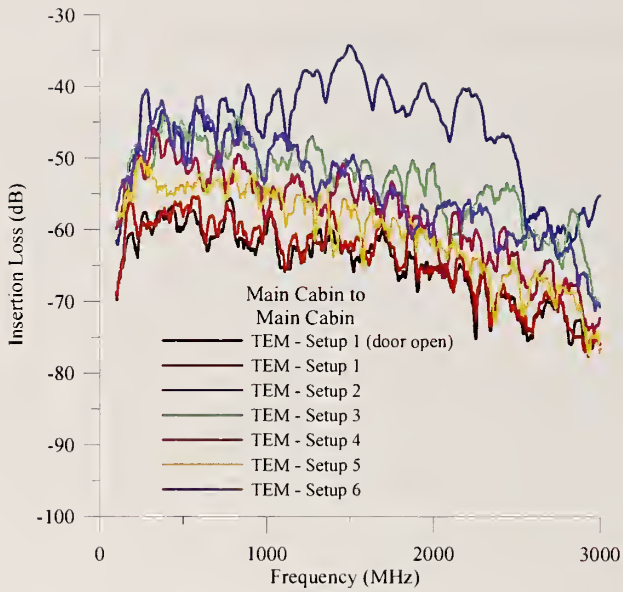


Figure 76. Main cabin to main cabin TEM antenna data insertion loss data at each of the six positions and one repeat position.

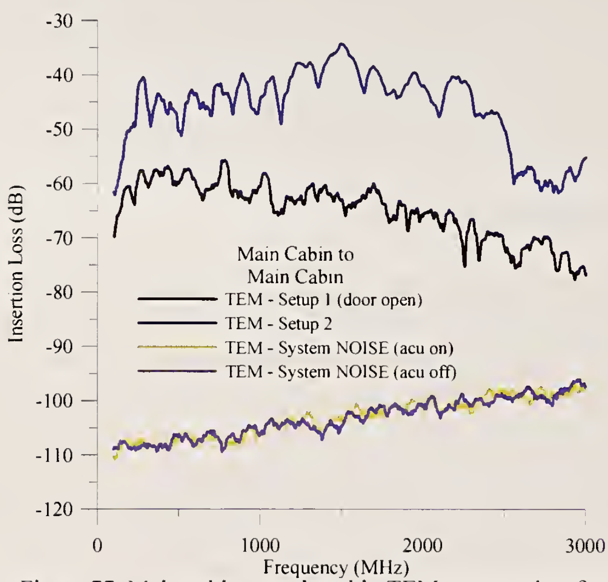


Figure 77. Main cabin to main cabin TEM antenna data for the maximum insertion loss, the minimum insertion loss and two noise measurements.

In reverberation chambers, common statistical distributions used to evaluate the cavity are the chi-squared probability density function ($\chi^2$ *pdf*) and the chi-squared cumulative distribution function ($\chi^2$ *cdf*). The $\chi^2$ *pdf* for all TEM horn antenna measurements is shown in Figure 79 and the $\chi^2$ *cdf* for all TEM horn antenna measurements is shown in Figure 80. The histogram in Figure 79 consists of all points binned into 1 dB bins (light-blue bins) and plotted against the theoretical probability density function (dark-blue trace) and the average value of the theoretical data (pink trace). The theoretical average value is around −38 dB. Figure 80 is the data (dark-

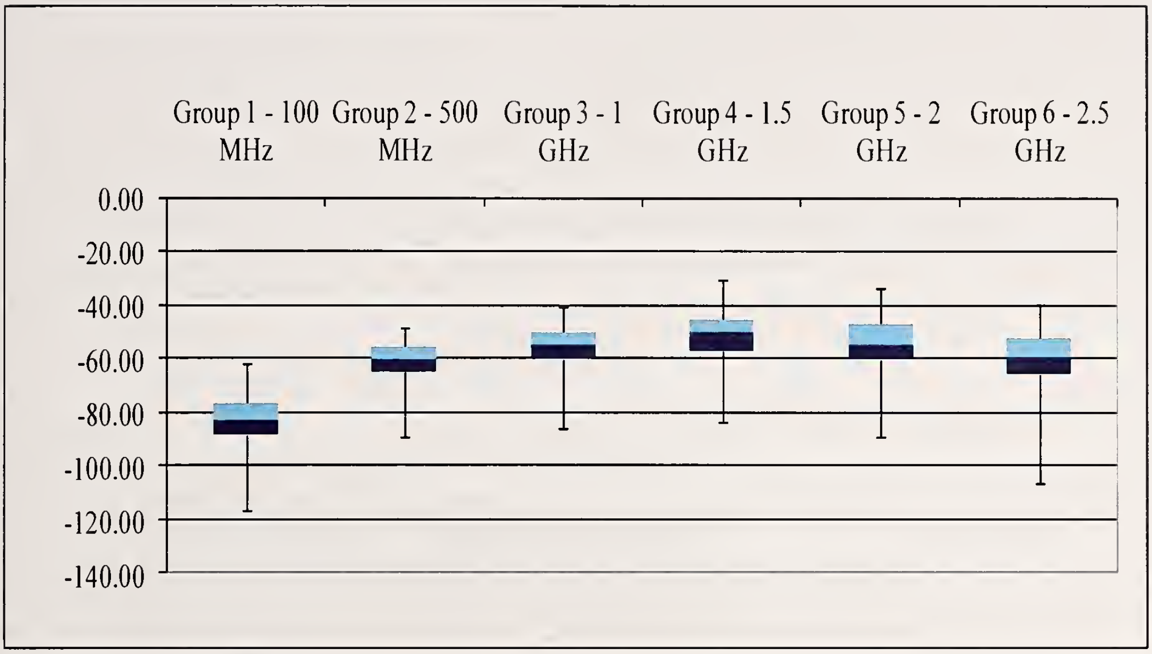


Figure 78. Whisker-box plots for all main cabin to main cabin insertion loss measurements of the TEM horn antennas at several frequencies.

blue, solid trace) plotted against the theoretical cumulative distribution function. This plot shows that the data does not tightly follow the theoretical cumulative distribution function. This does not typically seem to be the case for the individual positions.

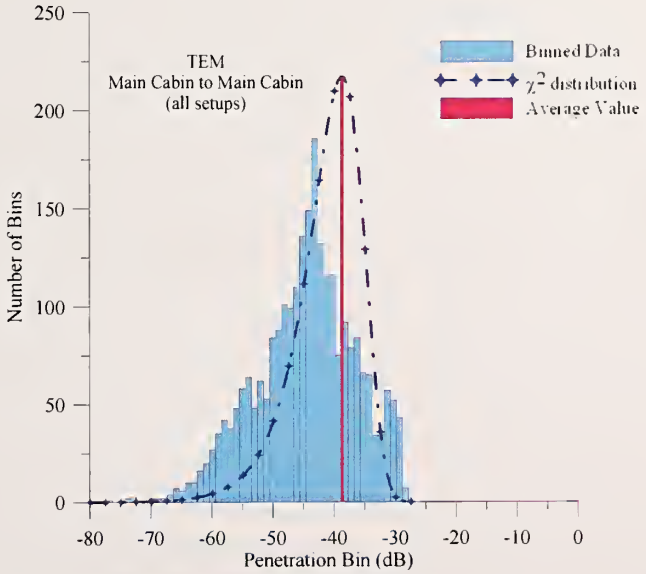


Figure 79. Chi-squared probability density function for all measurements in the main cabin to main cabin insertion loss measurements.

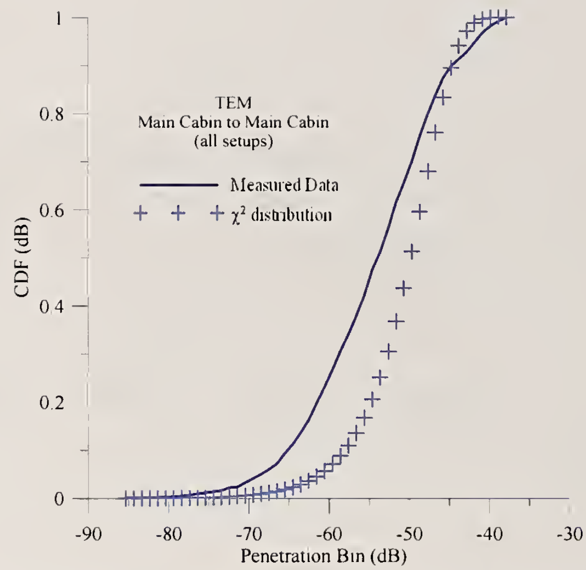


Figure 80. Chi-squared cumulative density function for all measurements in the main cabin to main cabin insertion loss measurements.

### 6.4.1.1 Individual TEM horn antenna measurement positions

In this section each measurement position is individually analyzed. Figures 81 to 92 show a photograph of the measurement positions, a time-domain plot and a schematic of the inside of the737-200 that indicates where the antennas were placed.

Figure 81 shows the placement for the transmitting and receiving TEM horn antennas in the main cabin for setup 1 and measurements 1 and 2. The horizontally polarized 1.2 m TEM horn antenna was located in the rear of the aircraft on a piece of closed-cell foam and pointed toward the back of the aircraft. The vertically polarized 36 cm antenna was located in the first-class section of the aircraft and pointed toward the front of the aircraft. The antennas were not boresighted and therefore no direct components exist in this measurement, as shown in the time-domain graph of Figure 82. Two measurements were taken, one with the main cabin passenger door open and one with it closed. The graph in Figure 82 shows only minor differences exist between having the door open or closed.

Figure 81. Main cabin to main cabin TEM horn antenna setup 1.

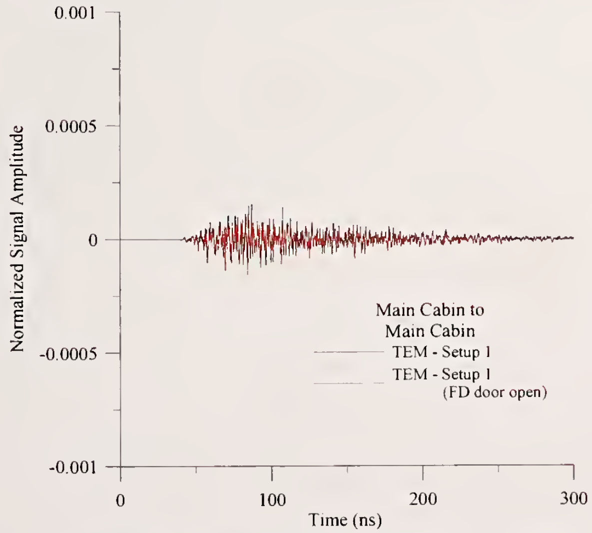


Figure 82. Main cabin to main cabin TEM horn antenna setup 1, time-domain response.

Figure 83 shows the placement of the transmitting and receiving TEM horn antennas in the main cabin for setup 2, measurements 1 and 2. The vertically polarized 1.2 m TEM horn antenna was located in the rear of the aircraft on a piece of closed-cell foam centered over the aisle. The vertically polarized 36 cm antenna was located in the first-class section of the aircraft toward the front and was also placed on a piece of closed-cell foam centered over the aisle. The antennas were intentionally boresighted in this setup to help us understand how the direct component can influence the statistics. A time-domain graph of this measurement is shown in Figure 84. The time domain is used to help us understand relationship between the direct component and reverberant fields. Figure 84 shows the waveform including the direct component (black trace), and another waveform with the direct component gated out (red trace).

Figure 83. Main cabin to main cabin TEM horn antenna setup.

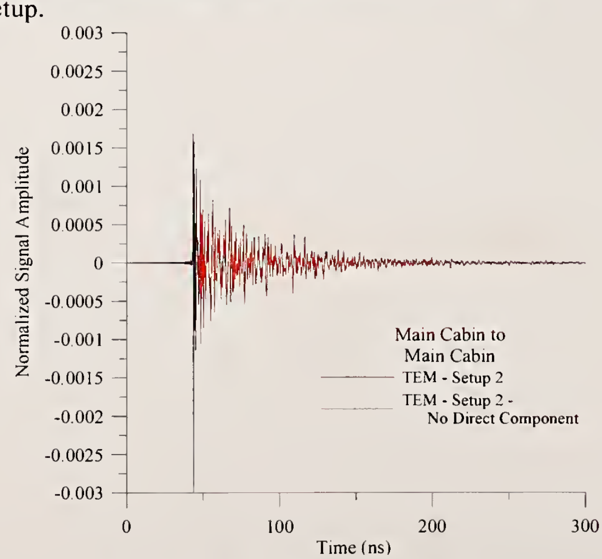


Figure 84. Main cabin to main cabin TEM horn antenna setup 2,time-domain response.

Figure 85 shows the placement of the transmitting and receiving TEM horn antennas in the main cabin for setup 3, measurements 1 and 2. The vertically polarized 1.2 m TEM horn antenna was left in the same location as for setup 2, which was on a piece of closed-cell foam centered over the aisle at the rear of the aircraft. The 36 cm TEM horn antenna was located in an overhead compartment in the first-class section of the aircraft and pointed toward the front of the aircraft. The overhead compartment door was open. The time-domain waveform is shown in Figure 86.

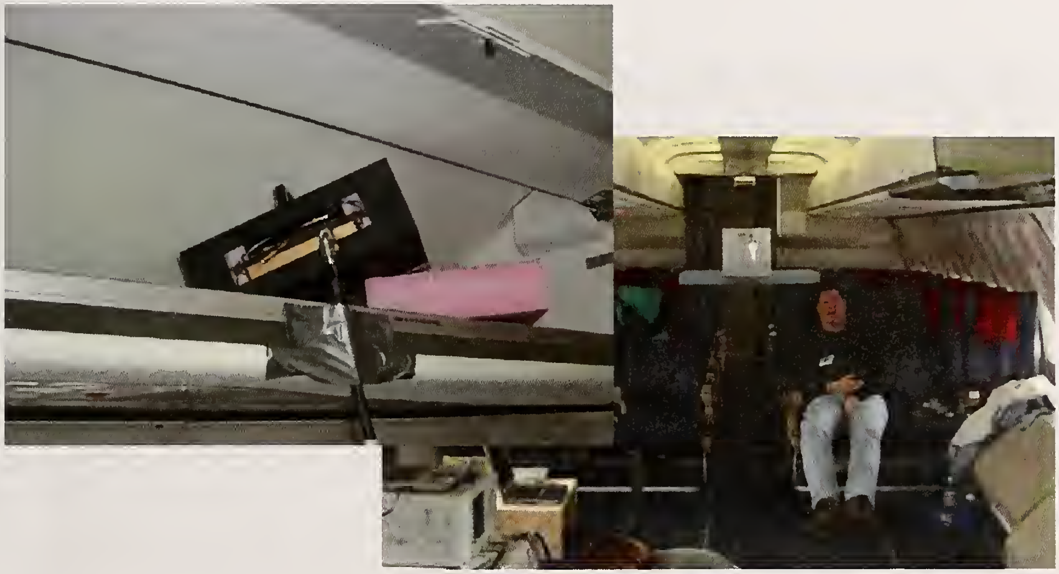

Figure 85. Main cabin to main cabin TEM horn antenna setup 3.

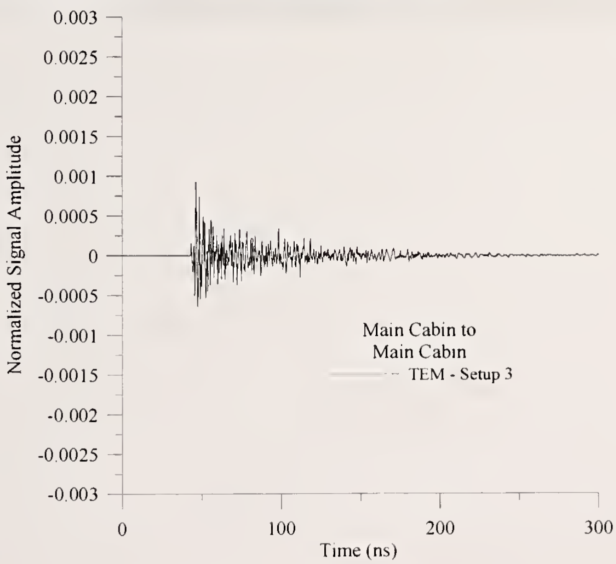


Figure 86. Main cabin to main cabin TEM horn antenna setup 3, time-domain response.

Figure 87 shows the placement of the transmitting and receiving DRG horn antennas in the main cabin for setup 4. The 1.2 m TEM horn antenna was located in the rear of the aircraft on a piece of closed-cell foam facing the passenger windows toward the front of the aircraft. The 36 cm antenna was located in an overhead compartment in the first-class section of the aircraft and pointed toward the front of the aircraft, as in setup 3. The compartment was partially closed. The time-domain waveform is shown in Figure 88.

Figure 87. Main cabin to main cabin TEM horn antenna setup 4.

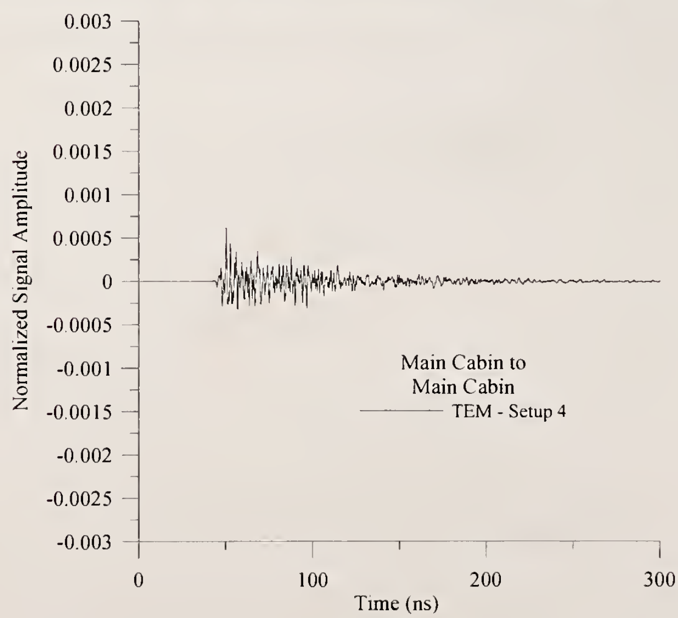


Figure 88. Main cabin to main cabin TEM horn antenna setup 4, time-domain response.

Figure 89 shows the placement of the transmitting and receiving TEM horn antennas in the main cabin for setup 5. The 1.2 m TEM horn antenna was on a piece of closed-cell foam the rear of the aircraft in the same configuration as for Setup 4. The vertically polarized 36 cm TEM horn antenna was located on the floor the first-class section of the aircraft and pointed toward the side of the aircraft. The time-domain waveform is shown in Figure 90.

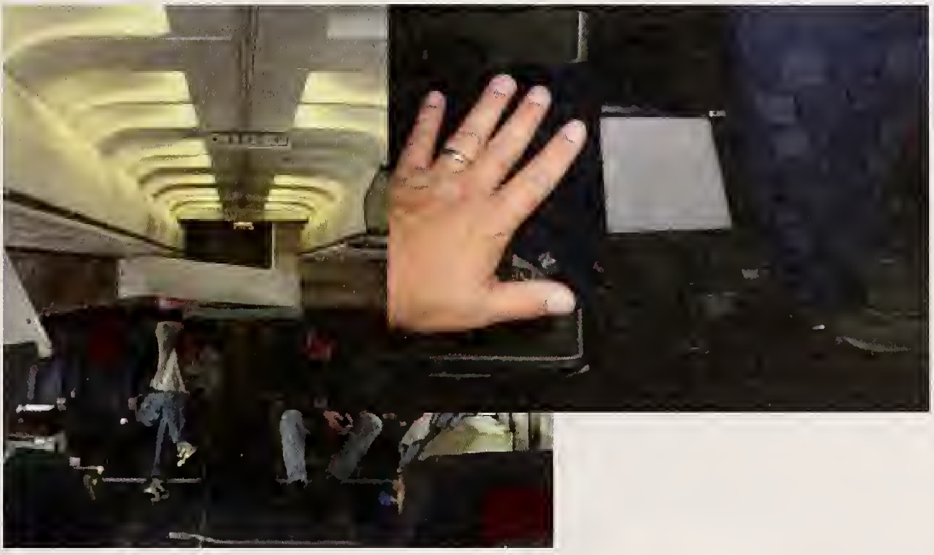

Figure 89. Main cabin to main cabin TEM horn antenna setup 5.

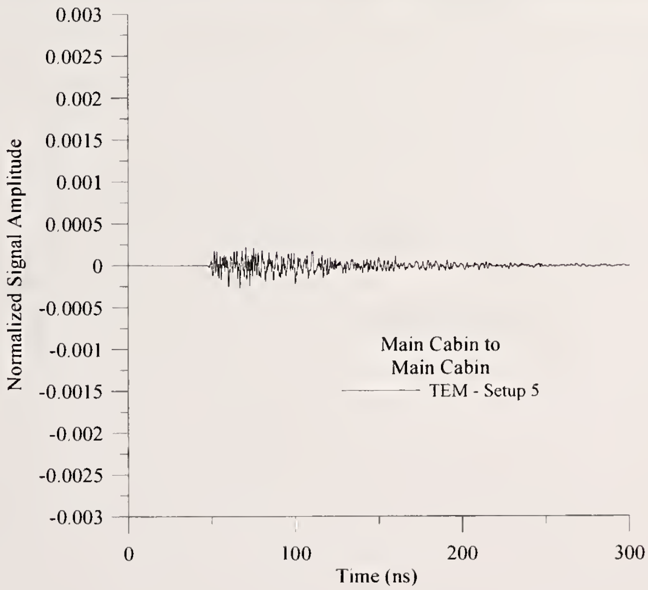


Figure 90. Main cabin to main cabin TEM horn antenna setup 5, time-domain response.

Figure 91 shows the placement of the transmitting and receiving TEM horn antennas in the main cabin for setup 6, measurements 1 and 2. Both antennas were placed on the floor of the main cabin. The horizontally polarized 1.2 m TEM horn antenna was located in the rear of the aircraft and pointed toward the front of the aircraft along the aisle. The vertically polarized 36 cm TEM horn antenna was located on the floor just behind the first-class section of the aircraft and pointed toward the rear of the aircraft. The time-domain waveform is shown in Figure 92.

Figure 91. Main cabin to main cabin TEM horn antenna setup 6.

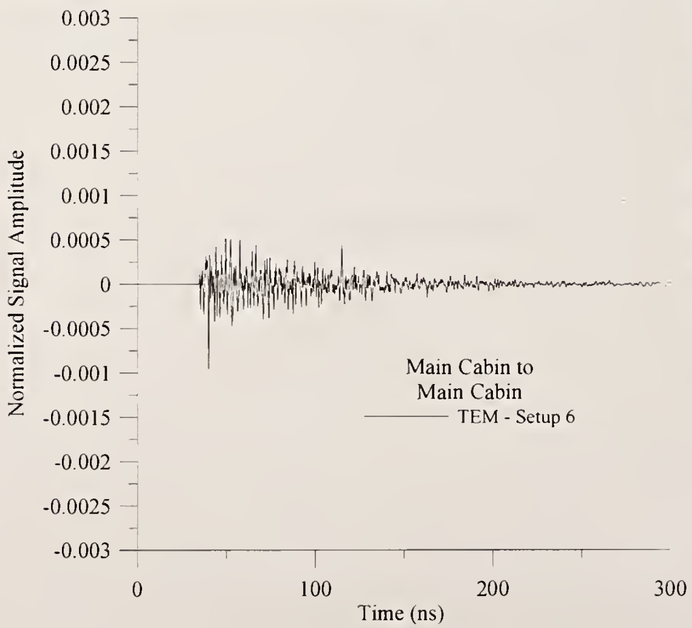


Figure 92 Main cabin to main cabin TEM horn antenna setup 6, time-domain response.

Figure 93 shows whisker-box plots of each individual setup. The group of data was analyzed around a center frequency of 1000 MHz over a 200 MHz bandwidth containing 321 points. Table 1 summarizes the statistics of each setup for the whisker-box plots, and includes the mean value, the median value, the standard deviation, the maximum value in the group, and the minimum value in the group. Table 2 summarizes the differences between the mean value for the whisker-box plot analysis and the mean value for the $\chi^2$ statistic. The difference between the two means is also displayed. Finally, the $\chi^2$ *pdf* and the $\chi^2$ *cdf* are plotted for each setup from Figure 94 to Figure 97.

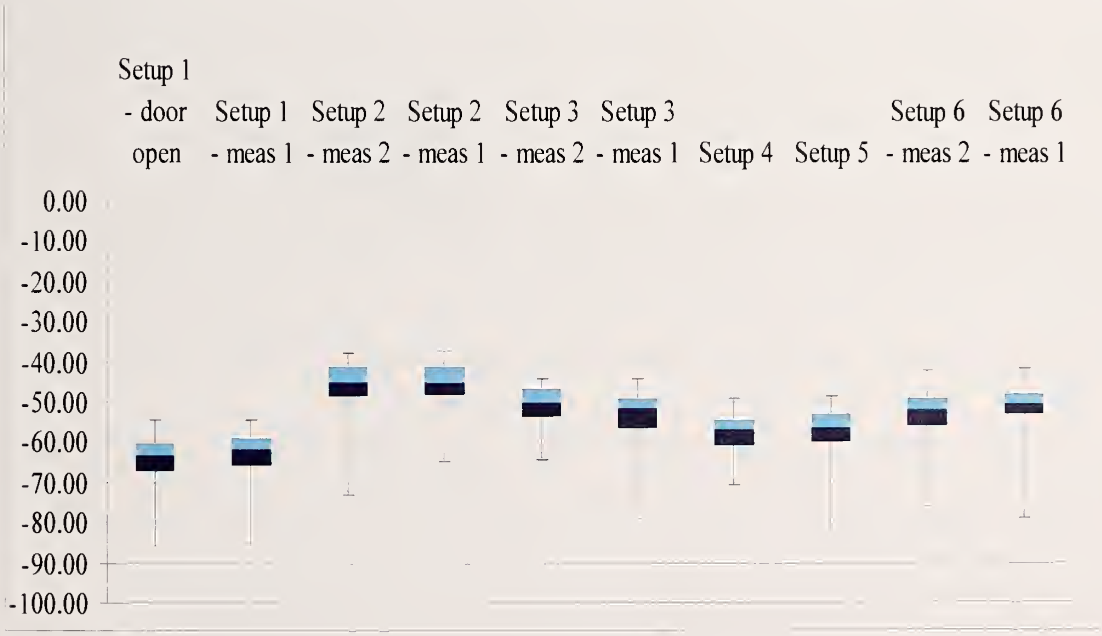


Figure 93. Whisker-box plots for the TEM horn antennas for main cabin to main cabin insertion loss.

Table 1. TEM horn internal cabin statistics for measurements from the main cabin to the main cabin. The sample size was 321 points which were in a 200 MHz bandwidth around a center frequency of 1 GHz.

| | Setup 1 door open | Setup1 door closed | Setup 2 meas 1 | Setup 2 meas 2 | Setup 3 meas 1 | Setup 3 meas 2 | Setup 4 | Setup 5 | Setup 6 meas 1 | Setup 6 meas 2 |
|---|---|---|---|---|---|---|---|---|---|---|
| Mean (dB) | −63.99 | −63.08 | −44.98 | −45.62 | −53.09 | −50.75 | −57.75 | −57.15 | −51.08 | −53.24 |
| Median (dB) | −63.11 | −61.79 | −45.12 | −45.19 | −51.43 | −50.10 | -57.09 | −56.40 | −50.51 | −52.07 |
| Standard Deviation (dB) | 5.28 | 5.98 | 4.64 | 5.60 | 5.58 | 4.65 | 4.53 | 5.04 | 5.15 | 6.08 |
| Minimum (dB) | −85.79 | −85.47 | −64.56 | −73.12 | −78.71 | −64.27 | −70.59 | −82.58 | −78.92 | −78.78 |
| Maximum (dB) | −54.35 | −54.47 | −37.31 | −37.69 | −44.19 | −43.88 | −48.90 | −48.47 | −41.73 | −42.07 |

Table 2. TEM horn antenna internal cabin $X^2$-distribution statistics for measurements from the main cabin to the main cabin.

| | Setup 1 door open | Setup1 door closed | Setup 2 meas 1 | Setup 2 meas 2 | Setup 3 meas 1 | Setup 3 meas 2 | Setup 4 | Setup 5 | Setup 6 meas 1 | Setup 6 meas 2 |
|---|---|---|---|---|---|---|---|---|---|---|
| Whisker-Box Plot Mean (dB) | -63.99 | -63.08 | -44.92 | -45.62 | -53.09 | - 50.75 | -57.75 | -57.15 | -51.08 | -53.24 |
| $X^2$ Mean (dB) | -62.00 | -61.00 | -35.00 | -34.00 | -50.00 | -47.00 | -56.00 | -62.00 | -63.00 | -59.00 |
| Δ (dB) | -1.00 | -2.00 | -10.00 | -11.00 | -3.00 | -3.00 | -2.00 | +5.00 | +13.00 | +6.00 |

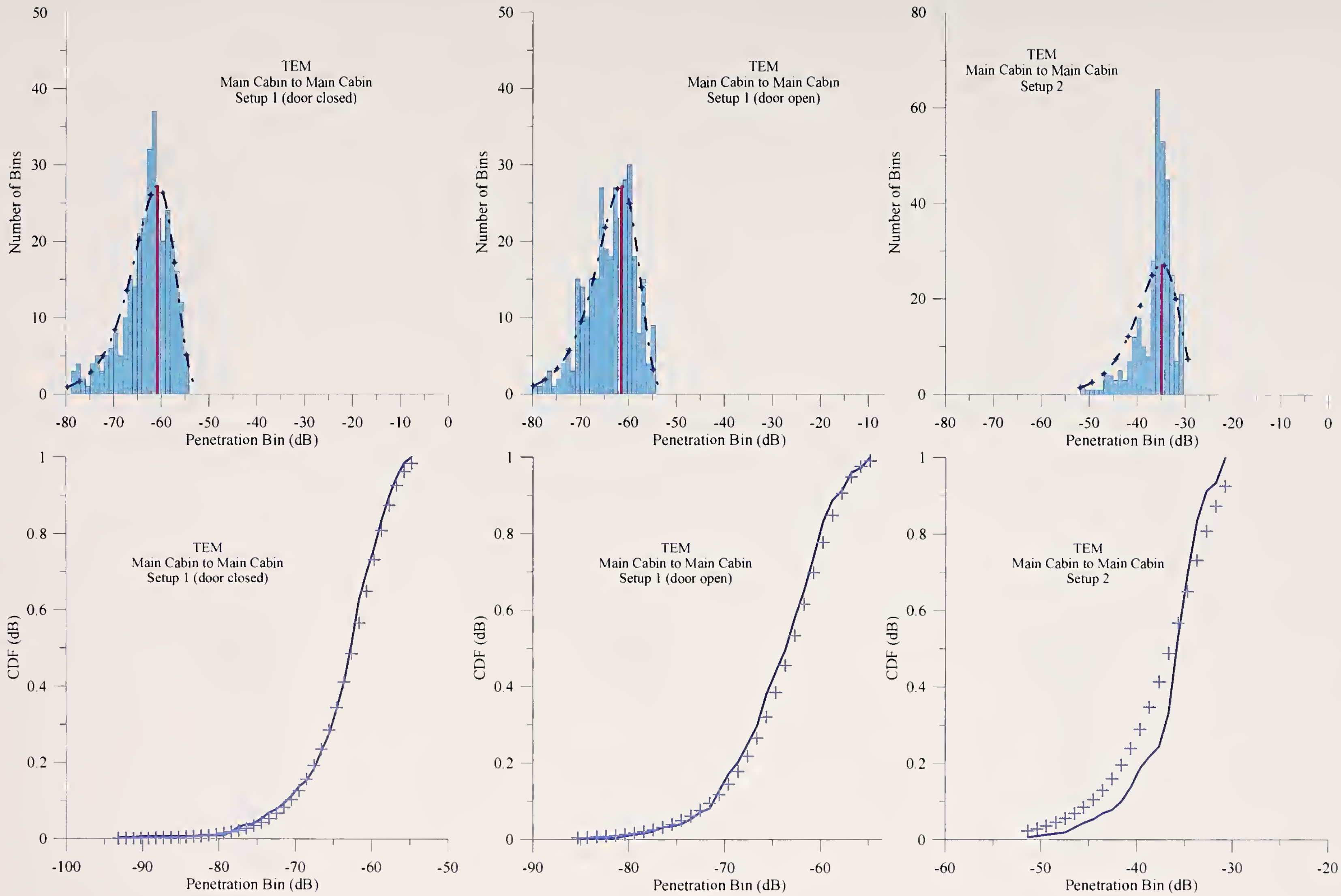


Figure 94. Chi-squared plots for TEM horn antenna, setup 1, measurement 1 (door open and closed),and setup 2, measurement 1, for the main cabin to main cabin insertion loss.

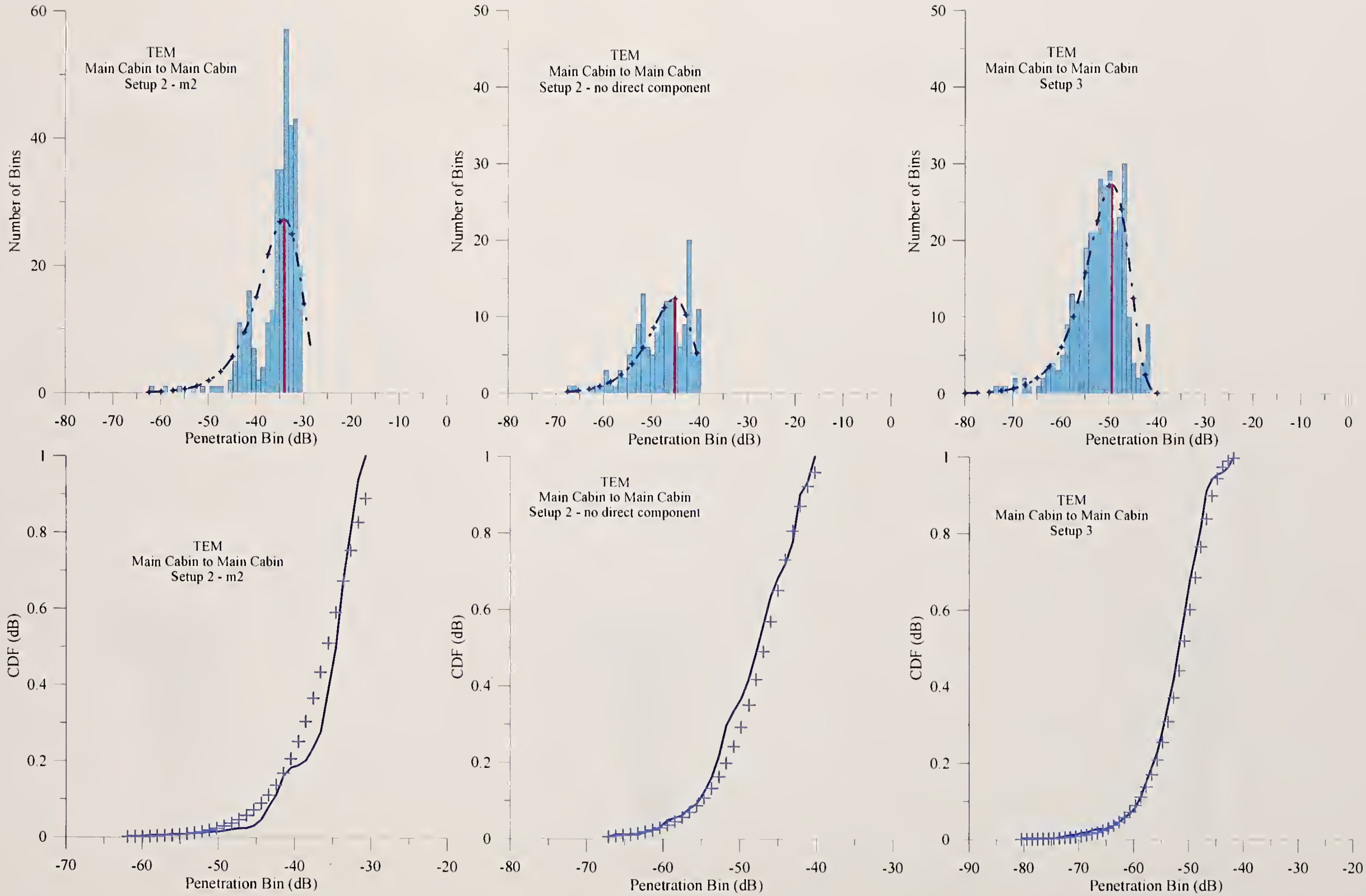


Figure 95. Chi-squared plots for TEM horn antenna, setup 2, measurement 2, setup 2, no direct component, and setup 3, measurement 1 for the main cabin to main cabin insertion loss.

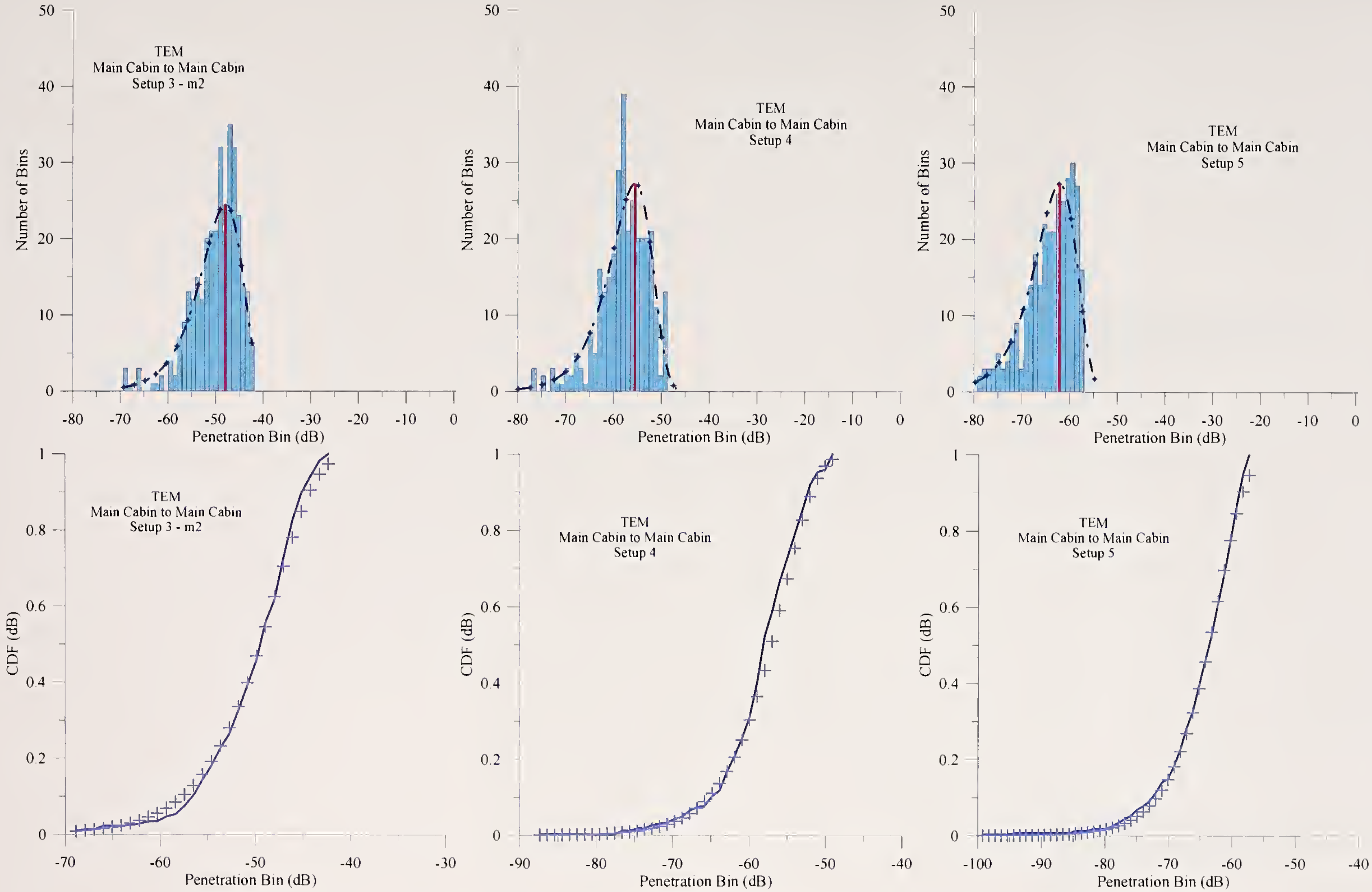


Figure 96. Chi-squared plots for TEM horn antenna, setup 3, measurement 2, setup 4, and setup 5, for the main cabin to main cabin insertion loss.

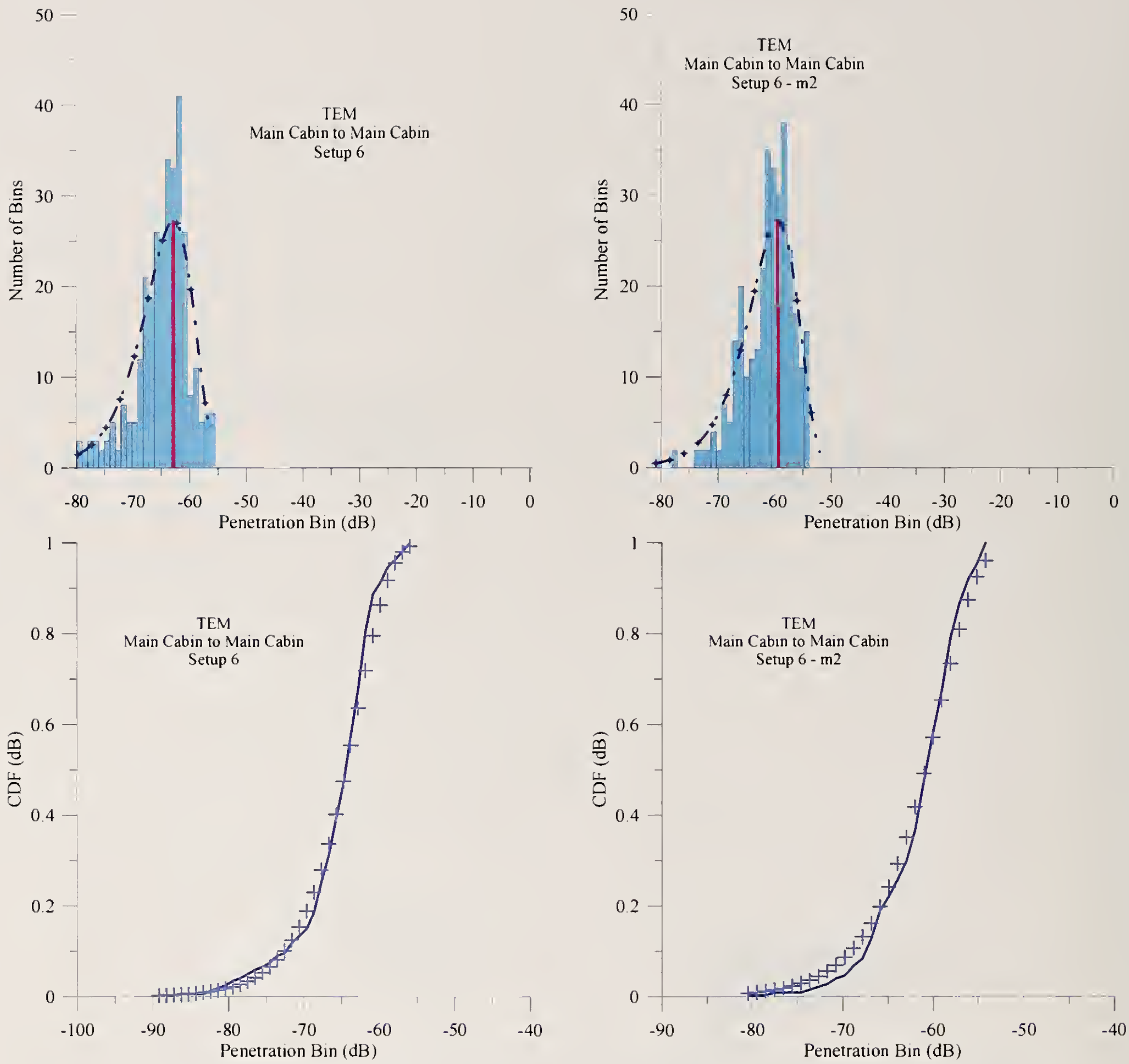


Figure 97. Statistical analysis for TEM horn antenna, setup 6-measurement 1, and setup 6, measurement 2, for main cabin to main cabin insertion loss.

#### 6.4.1.3 Combined DRG horn antenna positions

Six positions were measured, with one repeat measurement for two of the positions. The antennas were not moved for the reposition, the data were just retaken. Figure 98 shows results for all measurements in the main cabin for the TEM horn antenna showing a maximum insertion loss of around −30 dB and a minimum insertion loss of around −65 dB. Figure 99 show results for the measurement of maximum cabin insertion loss, the minimum insertion loss, and two system noise floors. One noise-floor measurement was taken with the DRG antennas positioned in setup 1, and the other noise-floor measurement was taken with the antennas positioned in setup 4.

For the DRG horn antennas, statistics are given for a 200 MHz bandwidth around 900 MHz, 1000 MHz, 1500 MHz, 2000 MHz, and 2500 MHz over all measurement positions, as shown in Figure 97. In a 200 MHz bandwidth there are 321 points, so for six measurement positions a total of 2247 points will be in the statistical bandwidth. The results from the 900 MHz set and the 1000 MHz for the DRG horn antenna sets may not be completely statistically independent but it was important to stay away from the band edges of the measurement; and it was also important to include enough information for reliable processing. Figure 100 shows the median insertion loss across the frequency bandwidth range from about −40 dB to −50 dB. The maximum insertion loss for these frequencies is approximately −21 dB in a 200 MHz bandwidth around a center frequency of 1500 MHz; and the minimum insertion loss is −100 dB in a 200 MHz bandwidth around a center frequency of 1000 MHz.

The $\chi^2$ *pdf* for all TEM horn antenna measurements is shown in Figure 101, and the $\chi^2$ *cdf* for all TEM horn antenna measurements is shown in Figure 102. The histogram in Figure 101 consists of all points binned into 1 dB bins (light-blue bins) and plotted against the theoretical probability density function (dark-blue trace) and the average value of the theoretical data (pink trace). The theoretical average value is around −38 dB. Figure 102 is the data (dark-blue, solid trace) plotted against the theoretical cumulative distribution function.

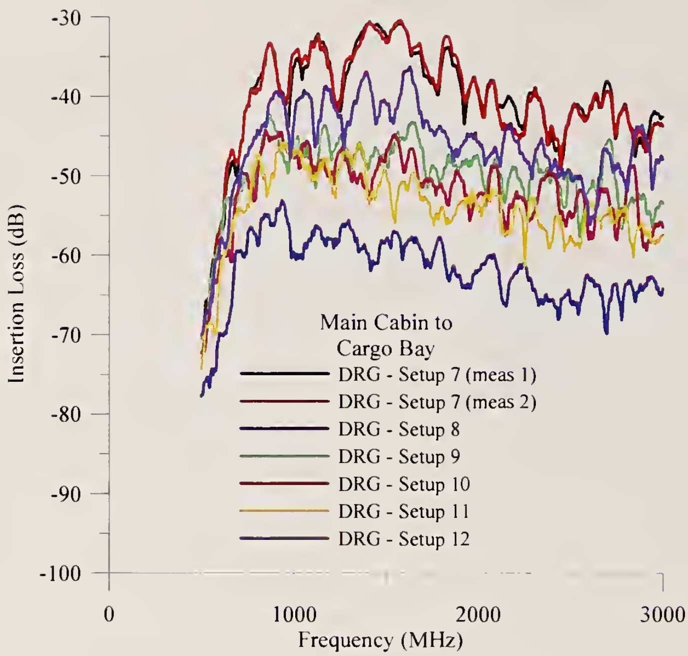


Figure 98. Main cabin to main cabin DRG antenna insertion loss data at each of the six positions and one repeat position.

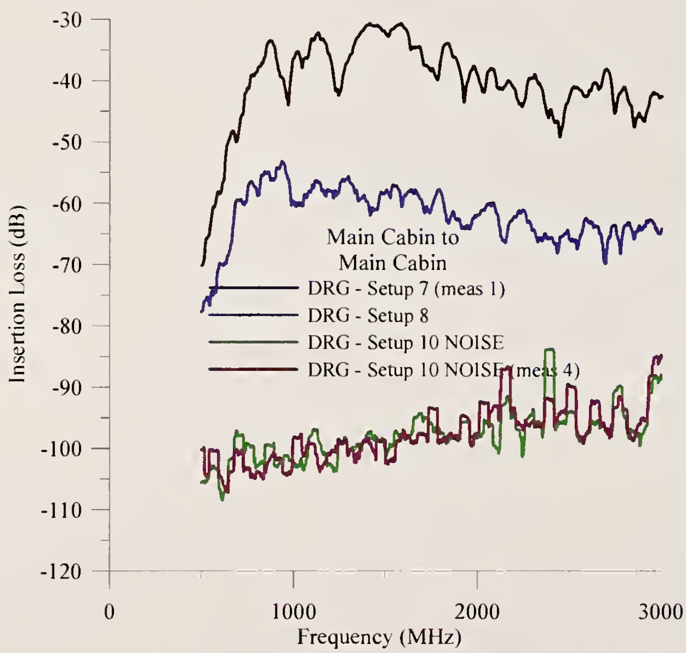


Figure 99. Main cabin to main cabin DRG antenna data for the maximum insertion loss, the minimum insertion loss, and two noise measurements.

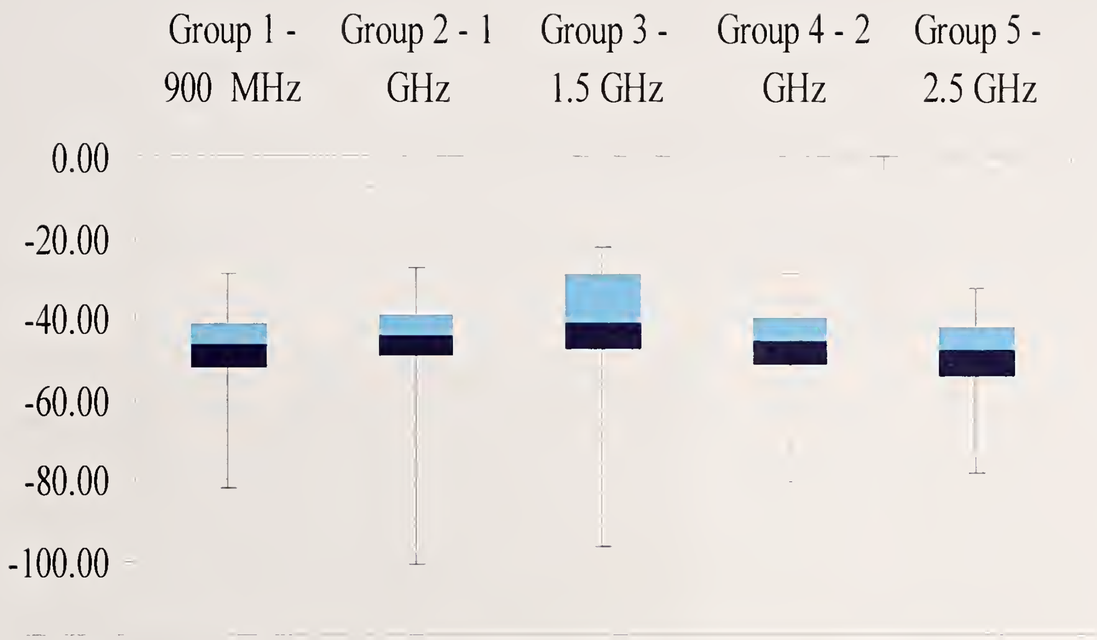


Figure 100. Whisker-box plots for all main cabin to main cabin insertion loss measurements of the DRG horn antennas at several frequencies.

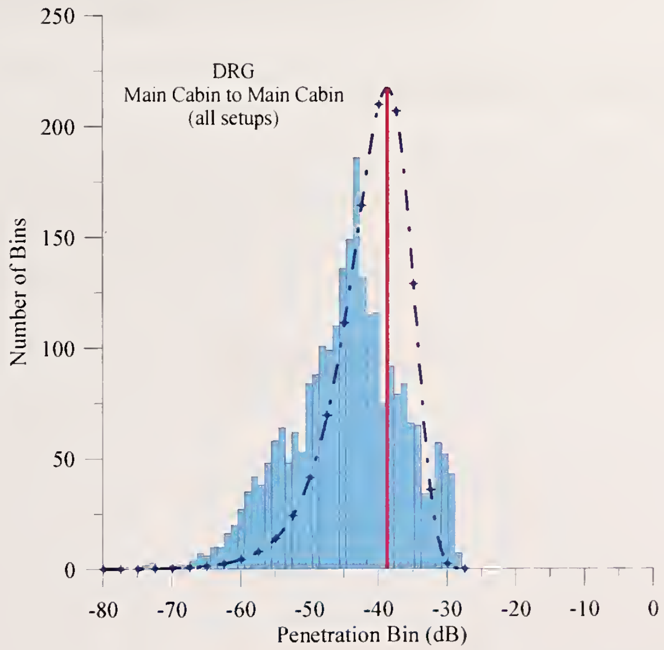


Figure 101. Chi-squared probability density function for all setups in the main cabin to main cabin insertion loss measurements.

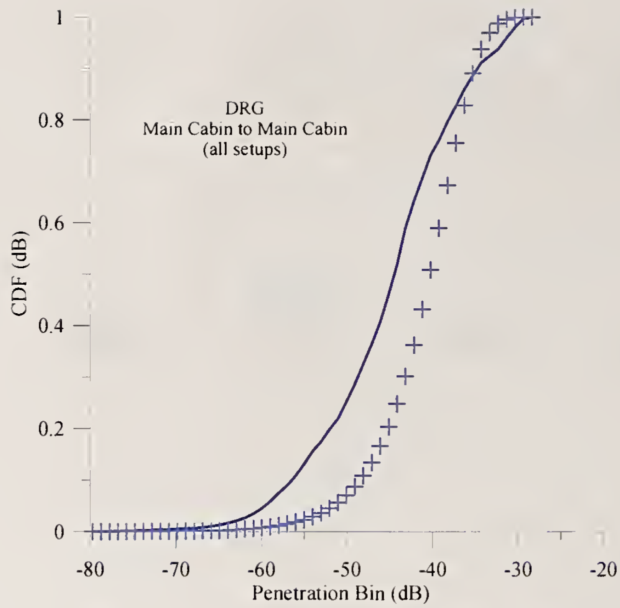


Figure 102. Chi-squared cumulative density function for all setups in the main cabin to main cabin insertion loss measurements.

### 6.4.1.4 Individual DRG horn antenna positions

A photograph for each DRG antenna to DRG antenna measurement position, its associated time-domain waveform, and a schematic showing the antenna positions inside the aircraft is shown from Figure 103 to Figure 114. The time-domain waveforms provide information for any direct antenna coupling components that may exist and the reverberant decay characteristics of the cavity-to-cavity interaction.

Figure 103 shows the placement of the transmitting and receiving DRG horn antennas in the main cabin for setup 7, measurements 1 and 2. Measurement 2 is a repeat measurement; the antennas were not moved. Unfortunately, this is the only photograph we have and it is out of focus. One antenna was vertically polarized and located in the rear of the aircraft on a piece of closed-cell foam centered over the aisle. The other antenna was located in the first-class section of the aircraft toward the front and was also placed on a piece of closed-cell foam centered over the aisle in the vertical polarization. The antennas were intentionally boresighted in this setup to help us understand how the direct component can influence the statistics. Figure 104 is a time-domain graph showing a measurement with the direct antenna coupling component (black trace) and without the direct antenna coupling component with only the reverberant fields (red trace).

Figure 103. Main cabin to main cabin DRG horn antenna setup 7.

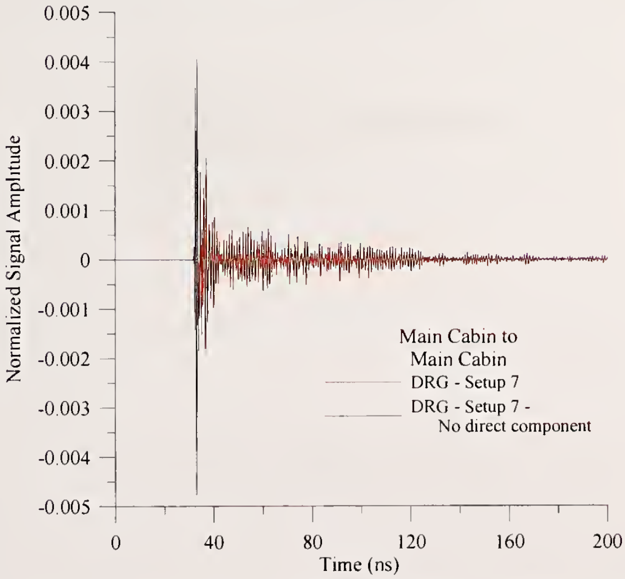


Figure 104. Main cabin to main cabin DRG horn antenna setup 7, time-domain response.

Figure 105 shows the placement of the transmitting and receiving DRG horn antennas in the main cabin for setup 8. One antenna was horizontally polarized and located in the rear of the aircraft on a piece of closed-cell foam pointing toward the back of the aircraft. The other, vertically polarized antenna was located in the first-class section of the aircraft and pointed toward the front of the aircraft. The antennas were not boresighted, and therefore no direct components exist in this measurement, as shown in the time-domain graph of Figure 106.

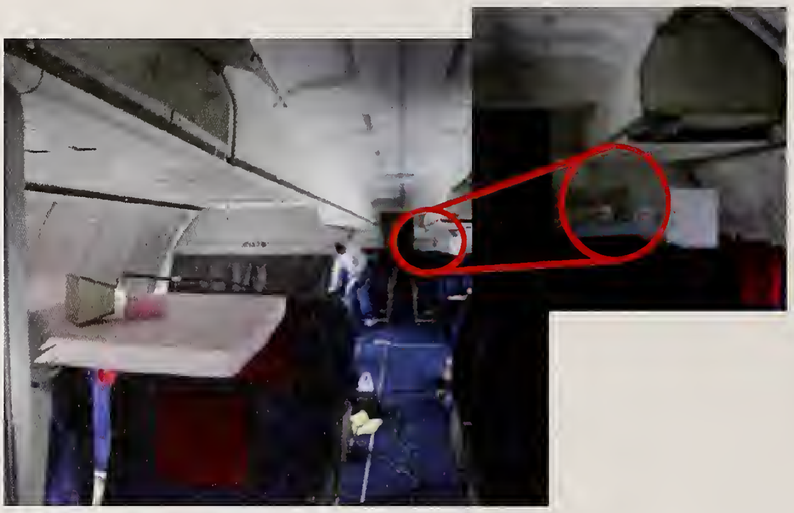

Figure 105. Main cabin to main cabin DRG horn antenna setup 8.

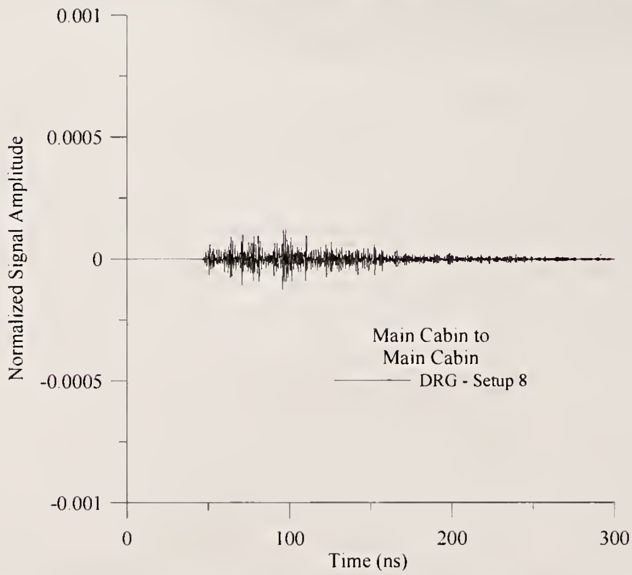


Figure 106. Main cabin to main cabin DRG horn antenna setup 8, time-domain response.

Figure 107 shows the placement of the transmitting and receiving DRG horn antennas in the main cabin for setup 9. One vertically polarized antenna was located in the rear of the aircraft on a piece of closed-cell foam centered over the aisle in the same position as in setup 7. The other antenna was located in an overhead compartment in the first-class section of the aircraft and pointed toward the front of the aircraft. The compartment was left open. The time-domain graph is shown in Figure 108.

Figure107. Main cabin to main cabin DRG horn antenna setup. 9

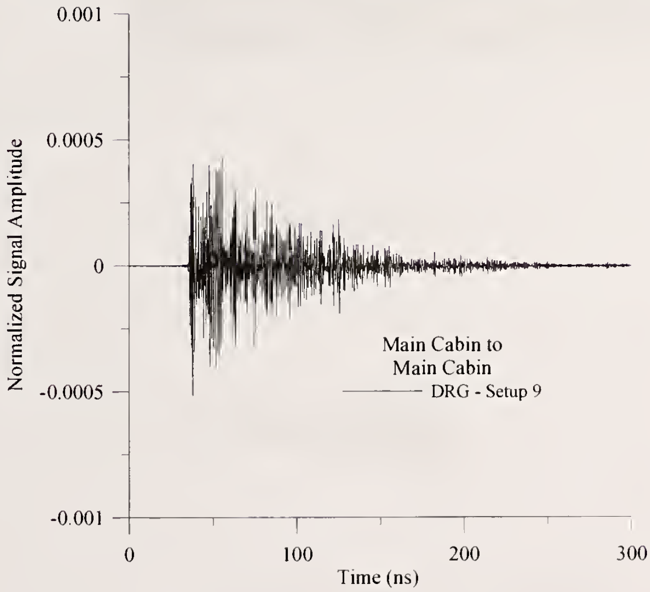


Figure 108. Main cabin to main cabin DRG horn

Figure 109 shows the placement of the transmitting and receiving DRG horn antennas in the main cabin for setup 10, measurements 1 and 2. One vertically polarized antenna was located in the rear of the aircraft on a piece of closed-cell foam centered over the aisle, as in setup 9. The other antenna was located in an overhead compartment in the first-class section of the aircraft and pointed toward the front of the aircraft, but the overhead compartment door was then closed. The time-domain graph is shown in Figure 110. By comparing Figure 108 and Figure 110 we can see there is little difference in amplitude between closing the overhead compartment and leaving it open.

Figure 109. Main cabin to main cabin DRG horn antenna setup 10.

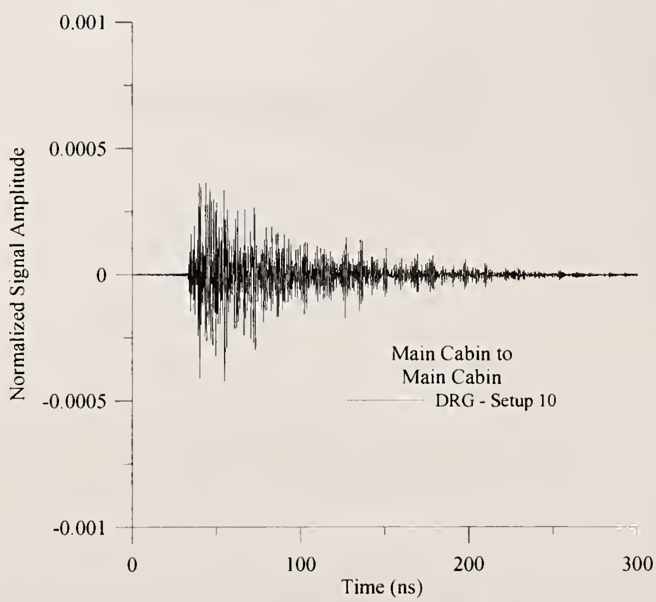


Figure 110. Main cabin to main cabin DRG horn antenna setup 10, time-domain response.

Figure 111 shows the placement of the transmitting and receiving DRG horn antennas in the main cabin for setup 11. One vertically polarized antenna was located in the rear of the aircraft on a piece of closed-cell foam pointing toward the center and outside of the aircraft. The other vertically polarized antenna was located on the floor the first-class section of the aircraft and pointed toward the outside of the aircraft. The time-domain graph is shown in Figure 112.

Figure 111. Main cabin to main cabin DRG horn antenna setup 11.

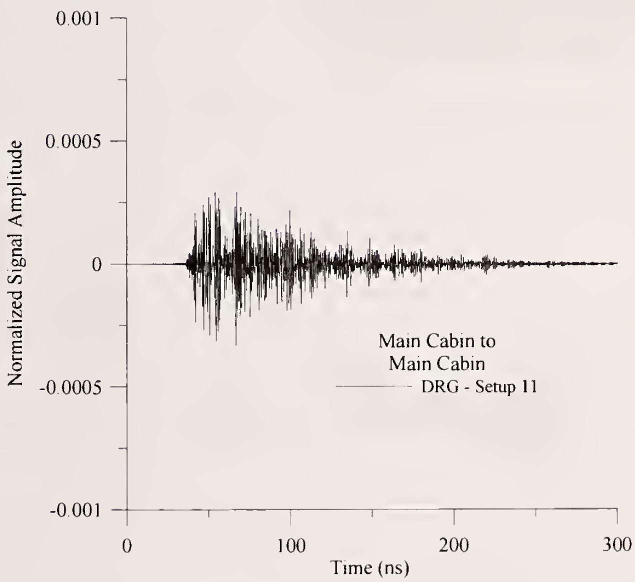


Figure 112. Main cabin to main cabin DRG horn antenna setup 11, time-domain response.

Figure 113 shows the placement of the transmitting and receiving DRG horn antennas in the main cabin for setup 12. Both antennas were placed on the floor of the main cabin. One horizontally polarized antenna was located in the rear of the aircraft and pointed toward the front of the aircraft along the aisle. The other vertically polarized antenna was located on the floor just behind the first class section of the aircraft and pointed toward the rear of the aircraft. The antennas were not boresighted, and therefore no direct components exist in this measurement as shown in the time-domain graph of Figure 114.

Figure 113. Main cabin to main cabin DRG horn antenna setup 12.

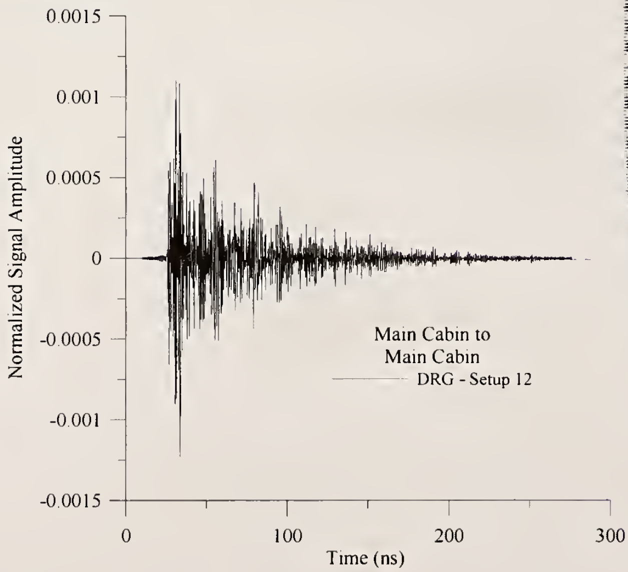


Figure 114. Main cabin to main cabin DRG horn antenna setup 12, time-domain response.

A statistical analysis is presented in the next few graphs. A whisker-box plot is shown for each DRG horn antenna in Figure 115, and Table 3 shows the mean value, the median value, the standard deviation, the maximum value, and the minimum value. The statistics for each setup were taken over a 200 MHz bandwidth (equivalent to 321 data points) centered around a frequency of 1000 MHz. The chi-squared $\chi^2$ *pdf* and the $\chi^2$ *cdf* statistical descriptions are shown in Figures 116 to Figure 117, and Table 4 compares the mean of general statistical analysis, the mean from the analysis of the $\chi^2$ distribution, and the difference between these two means.

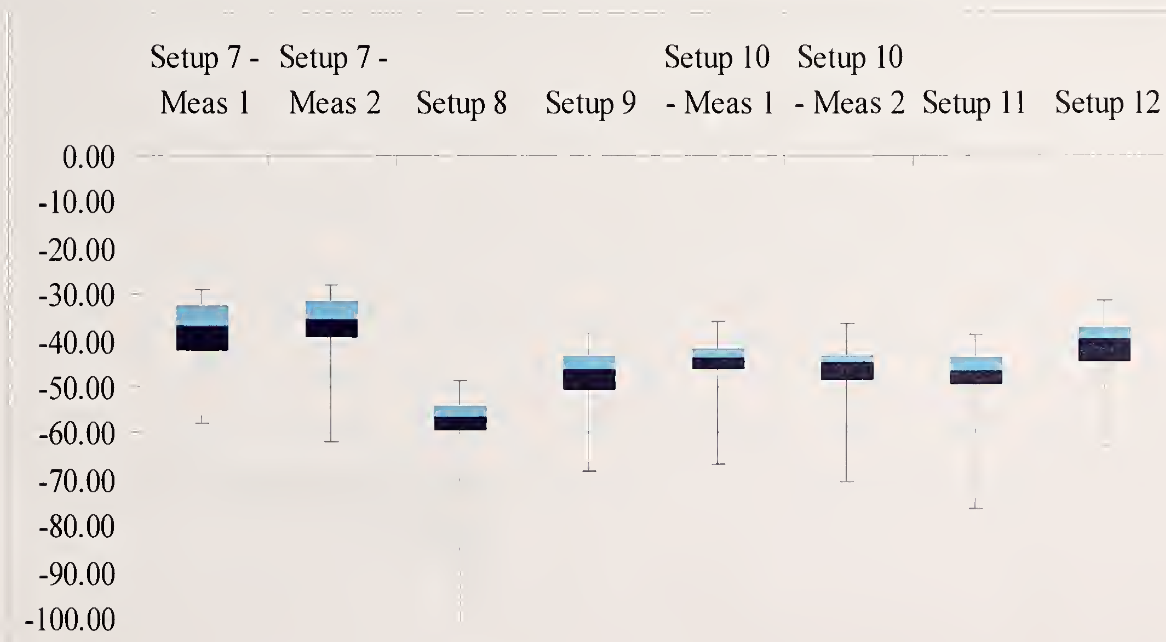


Figure 115. Whisker-box plots for the DRG horn antennas for setups 7 to 10. These data are from measurements of main cabin to main cabin insertion loss.

Table 3. DRG horn internal cabin statistics for measurements from the main cabin to the main cabin. The sample size was 321 points in a 200 MHz bandwidth around a center frequency of 1 GHz.

| | Setup 7 meas 1 | Setup7 meas 2 | Setup 7 no direct | Setup 8 | Setup 9 | Setup 10 | Setup 10 redo | Setup 11 | Setup 12 |
|---|---|---|---|---|---|---|---|---|---|
| Mean (dB) | -37.85 | -36.40 | -42.44 | -56.92 | -46.98 | -46.25 | -44.46 | -47.41 | -41.10 |
| Median (dB) | -36.69 | -35.12 | -40.71 | -56.47 | -45.89 | -44.76 | -43.76 | -46.72 | -39.90 |
| Standard Deviation (dB) | 6.25 | 6.19 | 5.07 | 5.19 | 5.63 | 5.42 | 5.03 | 5.50 | 5.73 |
| Minimum (dB) | -57.95 | -61.68 | -66.28 | -100.92 | -68.21 | -70.77 | -66.72 | -76.71 | -62.97 |
| Maximum (dB) | -29.15 | -27.83 | -36.44 | -48.30 | -38.34 | -36.37 | -35.71 | -38.49 | -31.16 |

Table 4. DRG horn antenna internal cabin $X^2$-distribution statistics for measurements from the main cabin to the main cabin.

| | Setup 7 meas 1 | Setup7 meas 2 | Setup 7 no direct | Setup 8 | Setup 9 | Setup 10 | Setup 10 redo | Setup 11 | Setup 12 |
|---|---|---|---|---|---|---|---|---|---|
| Whisker-Box Plot Mean (dB) | −37.85 | −36.40 | − 42.44 | −56.92 | − 46.98 | − 46.25 | − 44.46 | − 47.41 | − 41.10 |
| $X^2$ Mean (dB) | −35.00 | −31.00 | −41.00 | −57.00 | − 44.00 | − 43.00 | − 43.00 | − 44.00 | − 33.00 |
| Δ (dB) | − 3.00 | − 4.00 | − 1.00 | > +1.00 | − 3.00 | − 2.00 | − 1.50 | − 3.00 | − 7.00 |

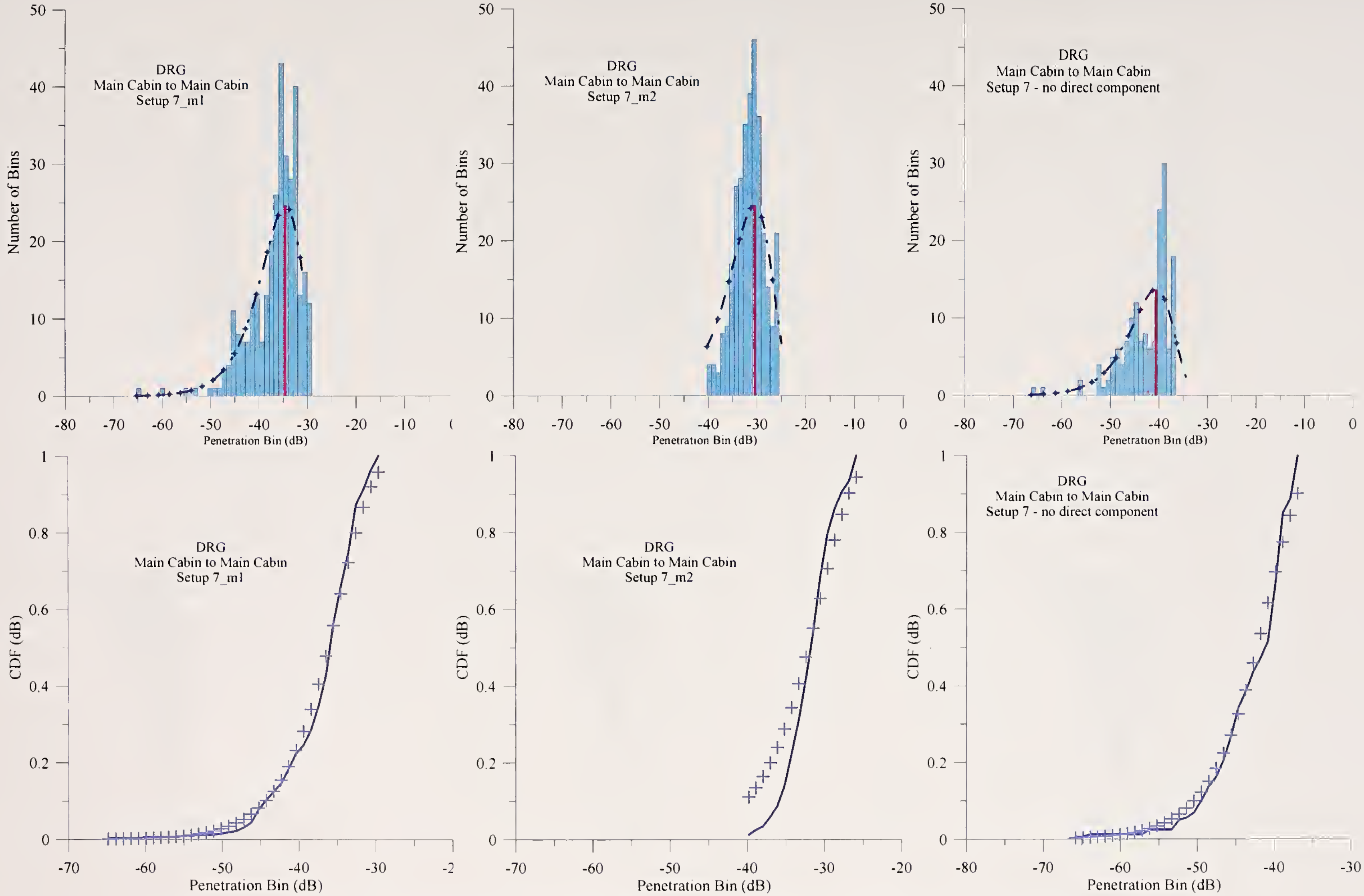


Figure 116. Chi-squared plots for DRG horn antenna, setup 7, measurement 1, measurement 2, and statistics with no direct component for the main cabin to main cabin insertion loss.

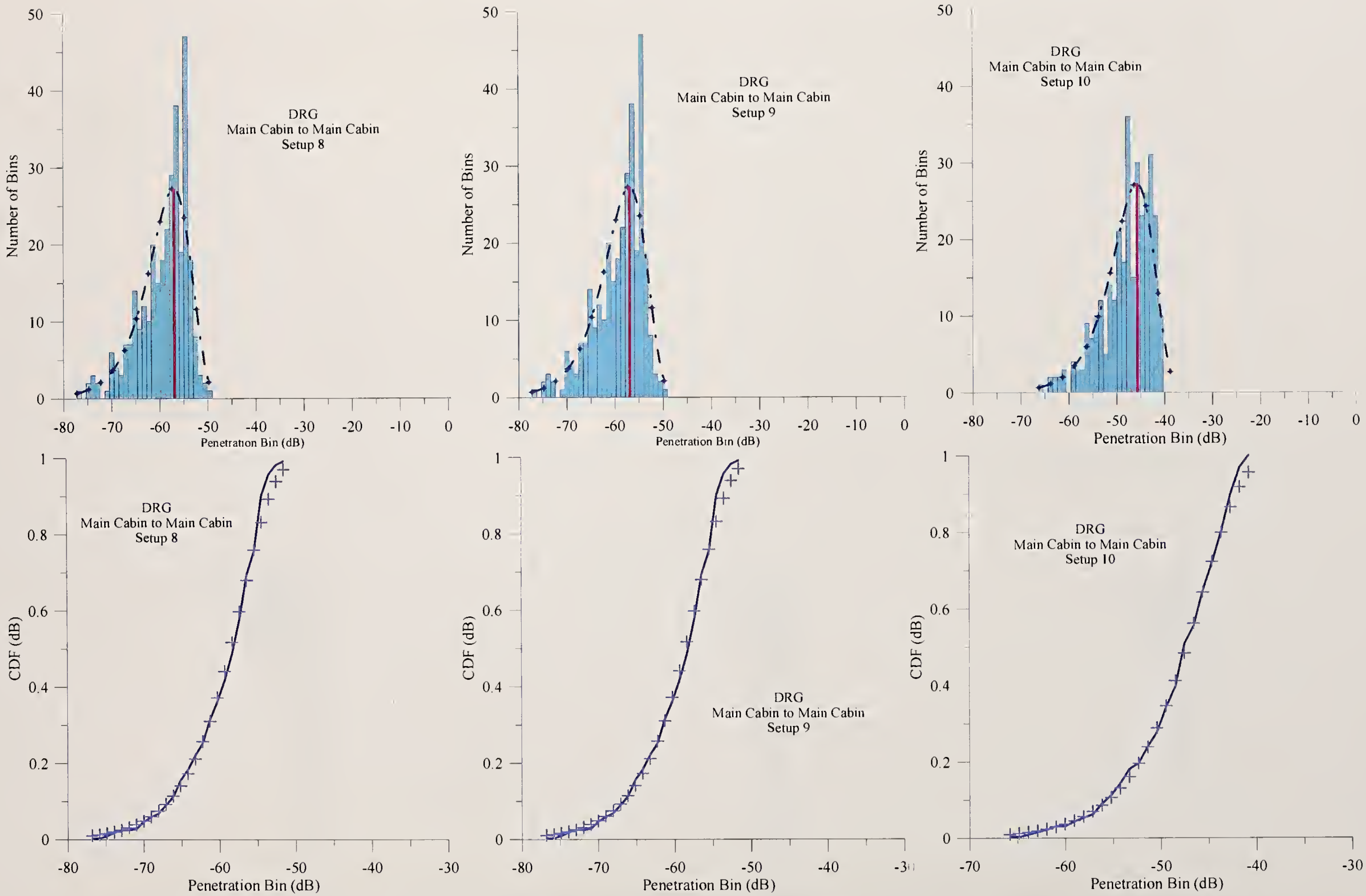


Figure 117. Statistical analysis for DRG horn antenna, setups 8, 9, and 10 (measurement 1) for the main cabin to main cabin insertion loss.

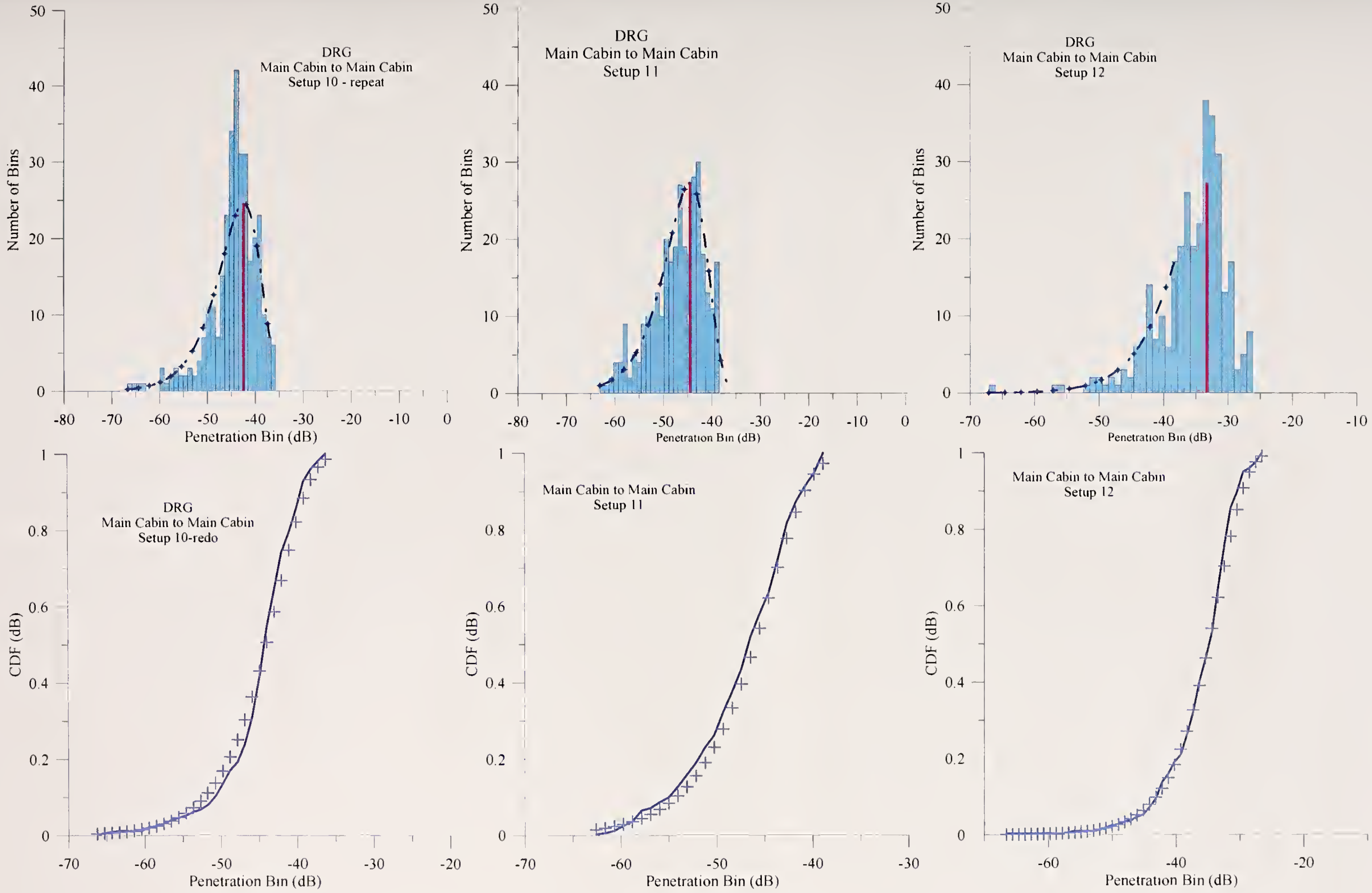


Figure 118. Statistical analysis for DRG horn antenna, setups 10 (measurement 2), 11, and 12 for the main cabin to main cabin insertion loss.

### 6.4.2 Main Cabin to Flight Deck

The DRG and TEM horn antennas were measured at various positions between the main cabin and flight deck. In general, for each compartment-to-compartment measurement, we tried to position them in approximately the same position for each of these runs.

#### 6.4.2.1 Combined DRG horn antenna positions

Four positions were measured for the DRG antenna type with a repeat measurement with the flight deck to main cabin door closed for positions 1 and 3. Figure 119 shows all measurement results for the DRG horn antenna showing a maximum insertion loss of around −50 dB and minimum insertion loss of around −65 dB. Figure 120 shows the results for the measurement having maximum cabin insertion loss, minimum insertion loss, and two system noise floor measurements. There were no noise-floor measurements taken with the DRG horn antennas; the TEM horn antenna data were used for the noise floor. The noise-floor measurement shown by the gold trace was the system noise floor taken by putting a 50 ohm load on the receiving side of the system. The purple trace is the ambient noise floor taken by putting the 50 ohm load on the transmitting side and looking for the ambient that enters the receiving antenna. Both were averaged over a 200 MHz bandwidth.

Whisker-box plots are shown in Figure 121 for the following center frequencies, (1) 100 MHz, (2) 500 MHz, (3) 1000 MHz, (4) 1500 MHz, (5) 2000 MHz, and (6) 2500 MHz. Data in these plots are from a 200 MHz bandwidth around each center frequency. These plots show that the median insertion loss for these frequencies has values from about −50 dB to −60 dB. The maximum insertion loss for these frequencies is approximately −44 dB in a 200 MHz bandwidth around a center frequency of 1500 MHz, and the minimum insertion loss is −100 dB dB in a 200 MHz bandwidth around a center frequency of 100 MHz.

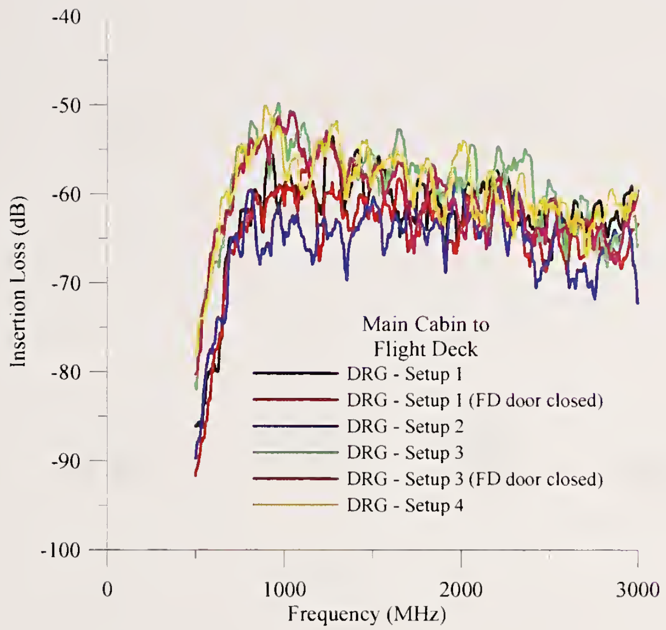


Figure 119. Main cabin to flight deck DRG antenna insertion loss data at each of the four positions, and two repeat measurements with the flight deck door closed.

The $\chi^2$ *pdf* for all DRG horn antenna measurements is shown in Figure 122, and the $\chi^2$ *cdf* for all TEM horn antenna measurements is shown in Figure 123. The histogram in Figure 122 consists of all points binned into 1 dB bins (light-blue bins) and plotted against the theoretical probability density function (dark-blue trace) and the average value of the theoretical data (pink trace). The theoretical average value is around −53 dB. Figure 123 is the data (dark-blue, solid trace) plotted

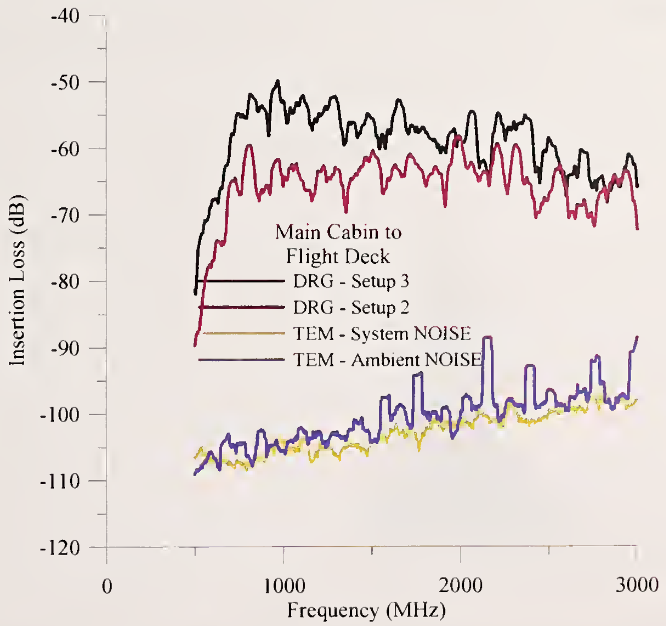


Figure 120. Main cabin to flight deck DRG horn antenna data for the maximum and minimum insertion loss, and two TEM horn antenna noise measurements.

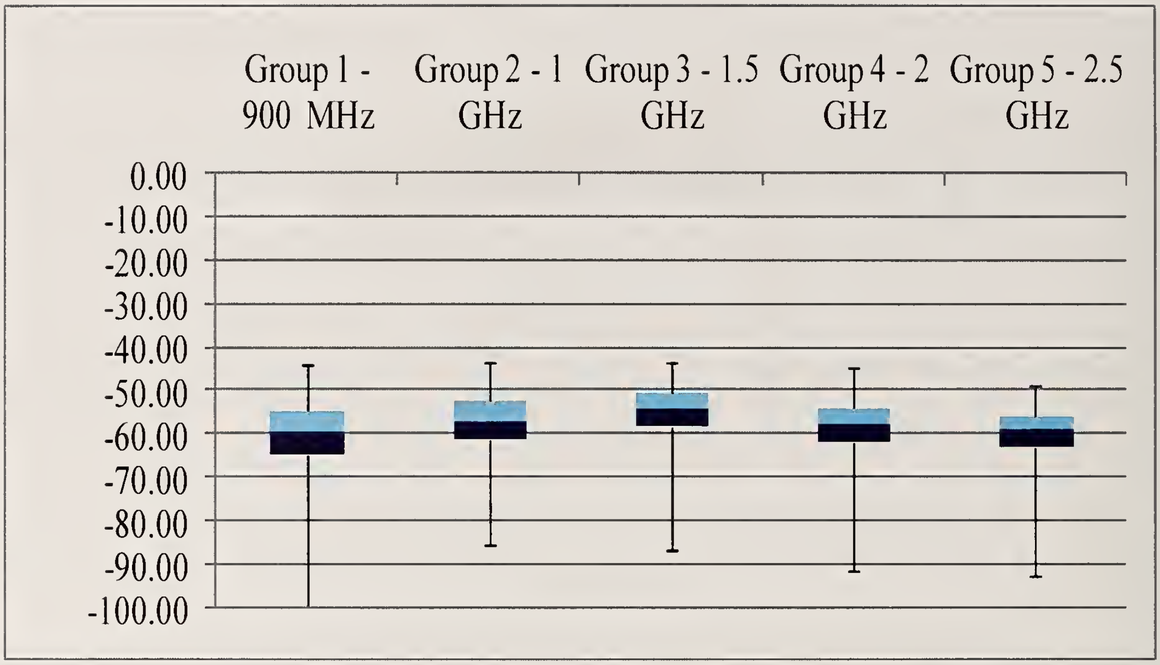


Figure 121. Whisker-box plots of all main cabin to flight deck insertion-loss measurements for the DRG horn antennas at several frequencies.

against the theoretical cumulative distribution function. This plot shows that the data do not tightly follow the theoretical cumulative distribution function. This does not typically seem to be the case for the individual positions.

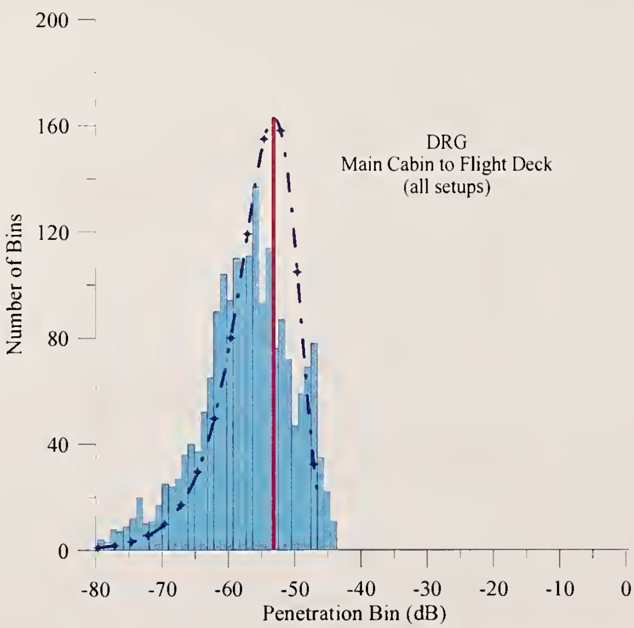


Figure 122. Chi-squared probability density function for all setups in the main cabin to flight deck insertion-loss measurements.

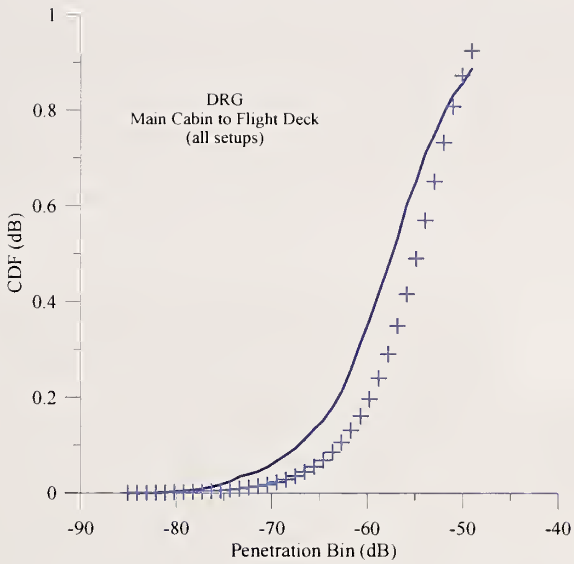


Figure 123. Chi-squared cumulative density function for all setups in the main cabin to flight deck insertion loss measurements.

### 6.4.2.2 Individual DRG horn antenna measurement positions

In this section each measurement position from the main cabin to the flight deck is individually analyzed. Figures 124 to 131 show photographs of the locations of the antennas in the flight deck and the main cabin, a time-domain plot, and a schematic of the inside of the 737-200 that indicates where the antennas were placed.

Figure 124 shows the placement for the transmitting and receiving DRG horn antennas in the main cabin for setup 1, measurements 1 and 2. The flight deck door was open for measurement 1 and closed for measurement 2. One horizontally polarized antenna was located in the rear of the aircraft on the floor of the main passenger cabin. The other antenna was located in the pilot's seat in the flight deck of the aircraft and pointed toward the ceiling. The graph in Figure 125 shows there is a slight difference between having the door open or closed, noticeable at the beginning of the waveform; however, the decay of the fields seem to be the same.

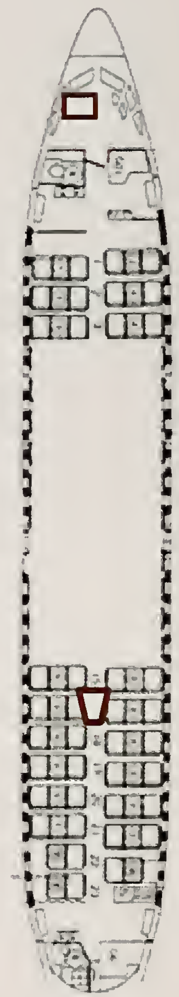

Figure 124. Main cabin to flight deck DRG horn antenna setup.

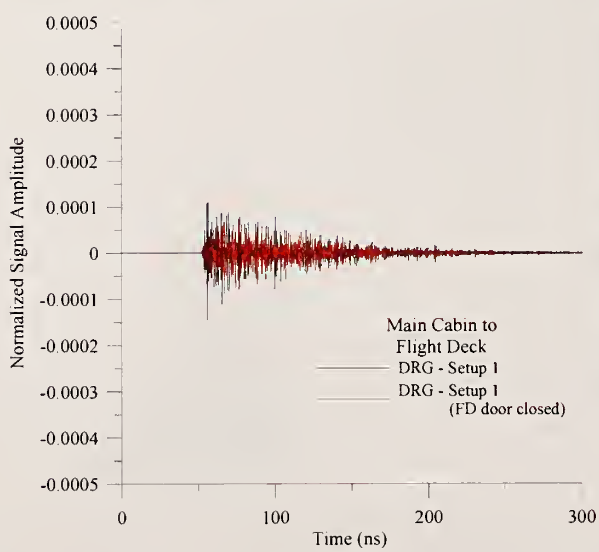


Figure 125. Main cabin to flight deck DRG horn antenna setup 1, time-domain response.

Figure 126 shows the placements of the transmitting and receiving DRG horn antennas in the main cabin for setup 2, measurements 1 and 2. One horizontally polarized antenna was located in the rear of the aircraft on the floor of the main passenger cabin. The other horizontally polarized antenna was located in the co-pilot's seat in the flight deck of the aircraft and pointed toward the left side. A time-domain graph of this measurement is shown in Figure 127.

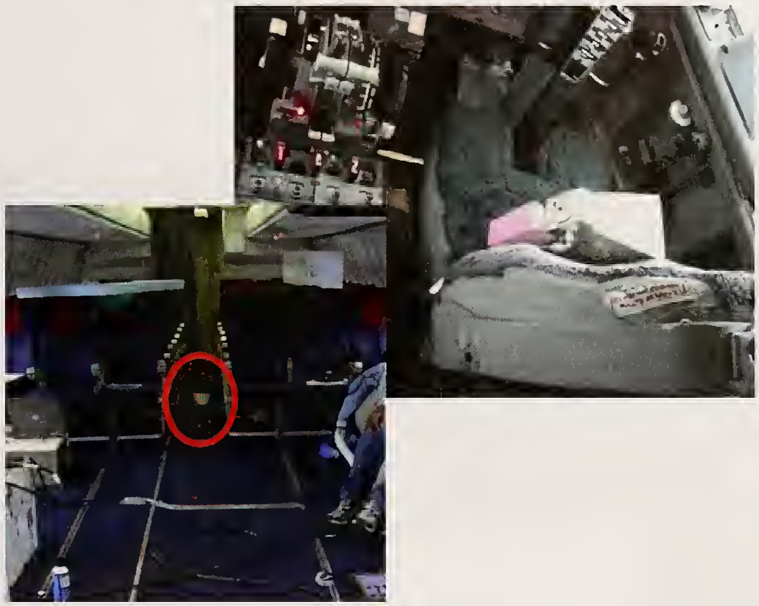

Figure 126. Main cabin to flight deck DRG horn antenna setup 2.

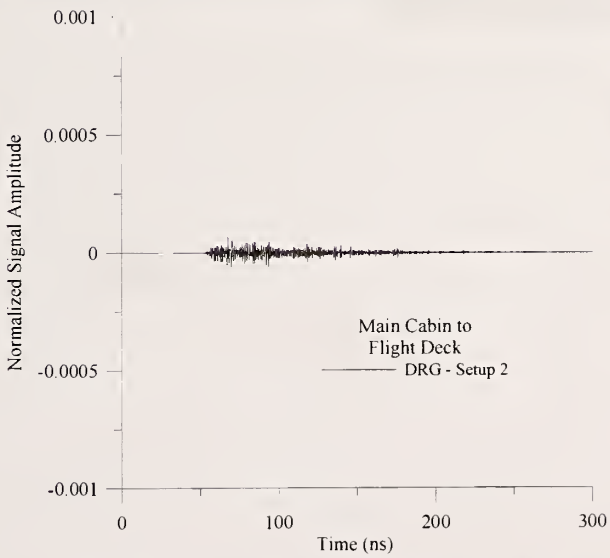


Figure 127. Main cabin to flight deck DRG horn antenna setup 2, time-domain response.

Figure 128 shows the placement of the transmitting and receiving DRG horn antennas in the main cabin for setup 3, measurements 1 and 2. For this position we also took one measurement with the flight deck door open and one with the flight deck door closed. One vertically polarized antenna was located in the first class section over a seat. The other horizontally polarized antenna was located in the co-pilot's seat in the flight deck of the aircraft and pointed toward the left side. The time-domain waveform is shown in Figure 129. The time-domain graphs show only slight differences between the two measurements.

Figure 128. Main cabin to flight deck DRG horn antenna setup 3.

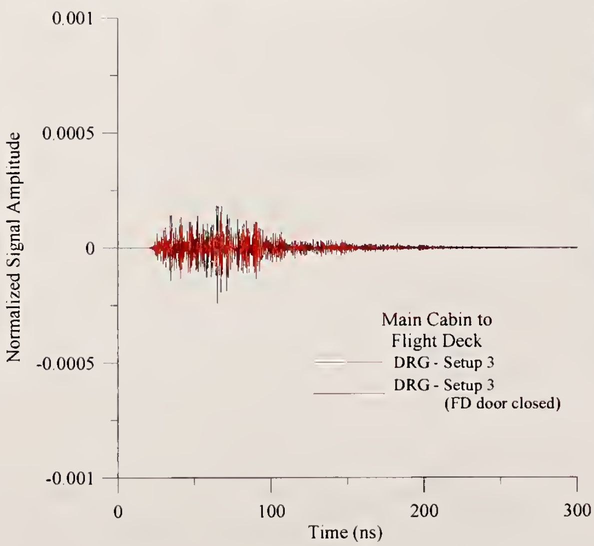


Figure 129. Main cabin to flight deck DRG horn antenna setup 3, time-domain response.

Figure 130 shows the placements of the transmitting and receiving DRG horn antennas in the main cabin for setup 4. One vertically polarized antenna was located in the first class section over a seat. The other horizontally polarized antenna was located on the floor by the co-pilot's seat and pointed toward the front of the aircraft. The compartment was partially closed. The time-domain waveform is shown in Figure 131.

Figure 130. Main cabin to flight deck DRG horn antenna setup 4.

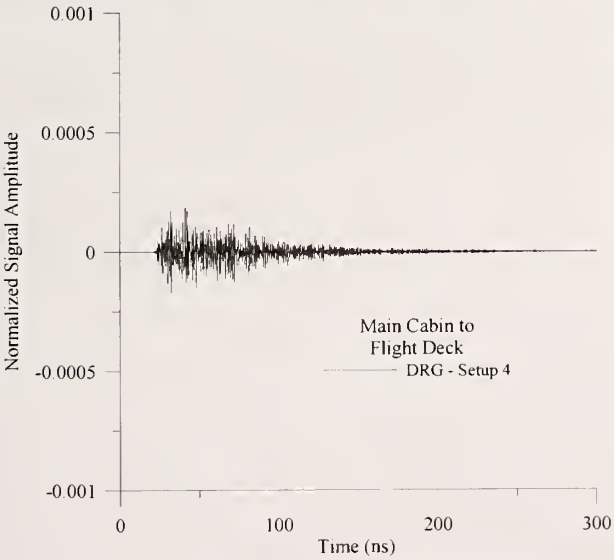


Figure 131. Main cabin to flight deck DRG horn antenna setup 4, time-domain response.

Figure 132 shows whisker-box plots of each individual setup. The group of data was analyzed around a center frequency of 1000 MHz over a 200 MHz bandwidth containing 321 points. Table 5 summarizes the statistics of each setup for the whisker-box plots, including the mean value, the median value, the standard deviation, the maximum value in the group, and the minimum value in the group. Table 6 summarizes the differences between the mean value for the whisker-box plot analysis and the mean value for the $\chi^2$ statistic. The difference between the two means is also displayed. Finally, the $\chi^2$ *pdf* and the $\chi^2$ *cdf* are plotted for each setup in Figure 133 and Figure 134.

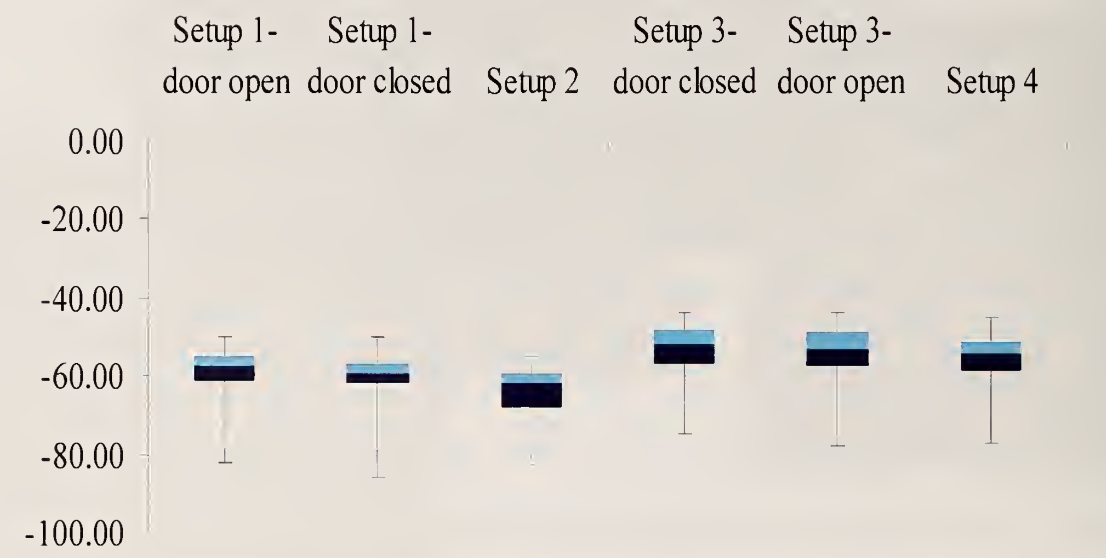


Figure 132. Whisker-box plots for the DRG horn antennas for main cabin to flight deck insertion loss.

Table 5. DRG horn internal cabin statistics for measurements from the main cabin to the flight deck. The sample size was 321 points in a 200 MHz bandwidth around a center frequency of 1 GHz.

| | Setup 1 door open | Setup1 door closed | Setup 2 meas 1 | Setup 3 door open | Setup 3 door closed | Setup 4 |
|---|---|---|---|---|---|---|
| Mean (dB) | −58.37 | −59.78 | −63.98 | −54.08 | −53.07 | −55.21 |
| Median (dB) | −57.11 | −59.02 | −62.06 | −52.87 | −51.89 | −53.95 |
| Standard Deviation (dB) | 5.28 | 4.88 | 6.25 | 6.70 | 6.08 | 6.35 |
| Minimum (dB) | −81.94 | −85.55 | −82.42 | −77.53 | −74.91 | −77.17 |
| Maximum (dB) | −50.31 | −49.82 | −54.90 | −44.03 | −43.64 | −44.83 |

Table 6. DRG horn antenna internal cabin $X^2$ - distribution statistics for measurements from the main cabin to the flight deck.

| | Setup 1 door open | Setup1 door closed | Setup 2 meas 1 | Setup 3 door open | Setup 3 door closed | Setup 4 |
|---|---|---|---|---|---|---|
| Whisker-Box Plot Mean (dB) | −58.37 | −59.78 | −63.98 | −54.08 | −53.07 | −55.21 |
| $X^2$ Mean (dB) | −57.00 | −55.00 | −58.00 | −54.00 | −52.00 | −52.00 |
| Δ (dB) | −1.00 | −5.00 | − 6.00 | < −1.00 | − 1.00 | − 3.00 |

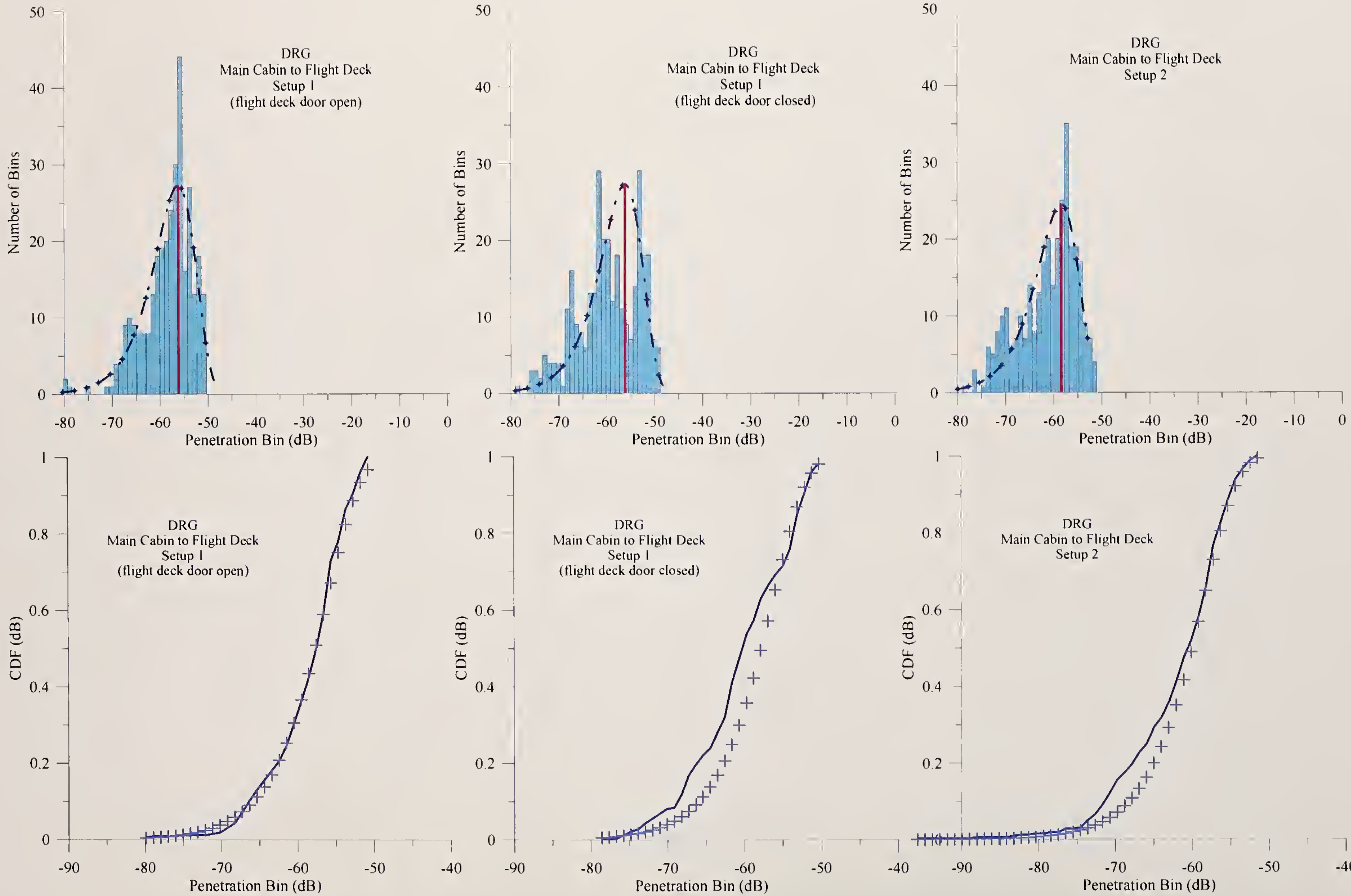


Figure 133. Chi-squared plots for TEM horn antenna, setup 1, flight deck door open and closed, and setup 2, for the main cabin to flight deck insertion loss.

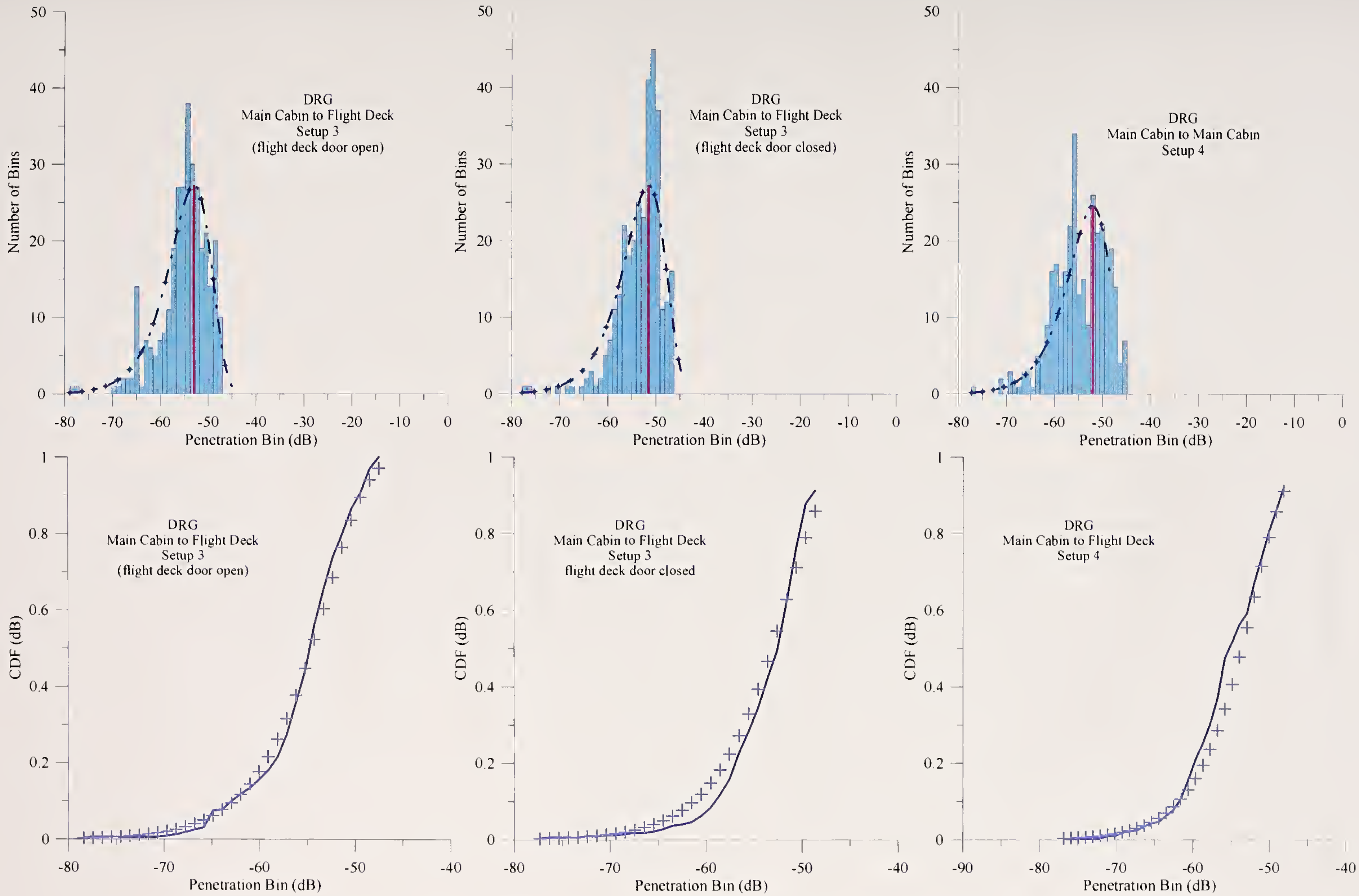


Figure 134. Chi-squared plots for TEM horn antenna, setup 3, flight deck door open and closed, and setup 4, for the main cabin to flight deck insertion loss.

### 6.4.2.3 Combined TEM horn antenna positions

Six positions were measured for the TEM horn antenna type, with a repeat measurement for position 8. The antennas were not moved for the reposition, the data were just retaken. Figure 135 shows results for all measurement results in the main cabin for the TEM horn antenna showing a maximum insertion loss of around −50 dB and a minimum insertion loss of around −75 dB. Figure 136 show results for the maximum cabin insertion loss measurement, the minimum insertion loss measurement, and two system noise floors.

For the TEM horn antennas, statistics are given for a 200 MHz bandwidth around 900 MHz, 1000 MHz, 1500 MHz, 2000 MHz, and 2500 MHz over all measurement positions, as shown in Figure 97. In a 200 MHz bandwidth there are 321 points, so for six measurement positions a total of 2247 points will be in the statistical bandwidth. The results from the 900 MHz set and the 1000 MHz for the TEM horn antenna sets may not be completely statistically independent, but it was important to stay away from the band edges of the measurement, and it was also important to include enough information for reliable processing. Figure 137 shows the median insertion loss across the frequency bandwidth range from about −65 dB to −90 dB. The maximum insertion loss for these frequencies is approximately −50 dB in a 200 MHz bandwidth around a center frequency of 1500 MHz, and the minimum insertion loss is −140 dB in a 200 MHz bandwidth around a center frequency of 1000 MHz.

The $\chi^2$ *pdf* for all TEM horn antenna measurements is shown in Figure 138, and the $\chi^2$ *cdf* for all TEM horn antenna measurements is shown in Figure 139. The histogram in Figure 138 consists of all points binned into 1 dB bins (light-blue bins) and plotted against the theoretical probability density function (dark-blue trace) and the average value of the theoretical data (pink trace). The theoretical average value is around −62 dB. Figure 139 is the data (dark-blue, solid trace) plotted against the theoretical cumulative distribution function.

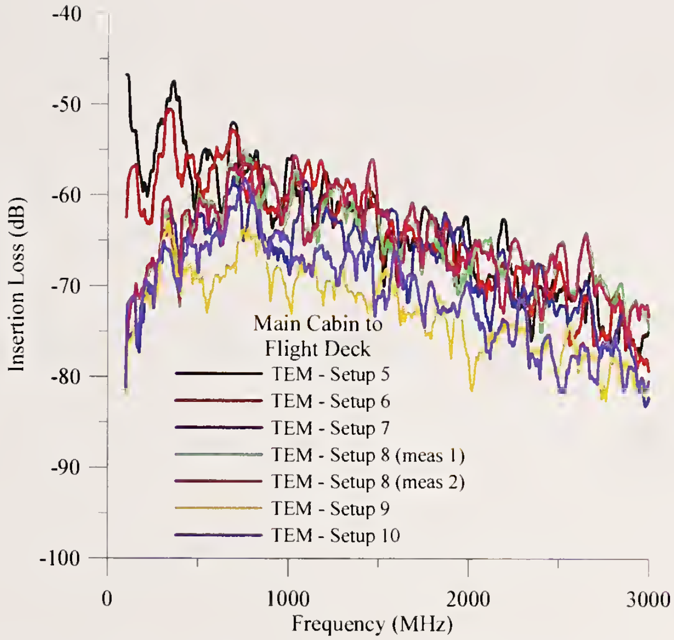


Figure 135. Main cabin to flight deck TEM antenna insertion loss data at each of the six positions and one repeat measurement at position 8.

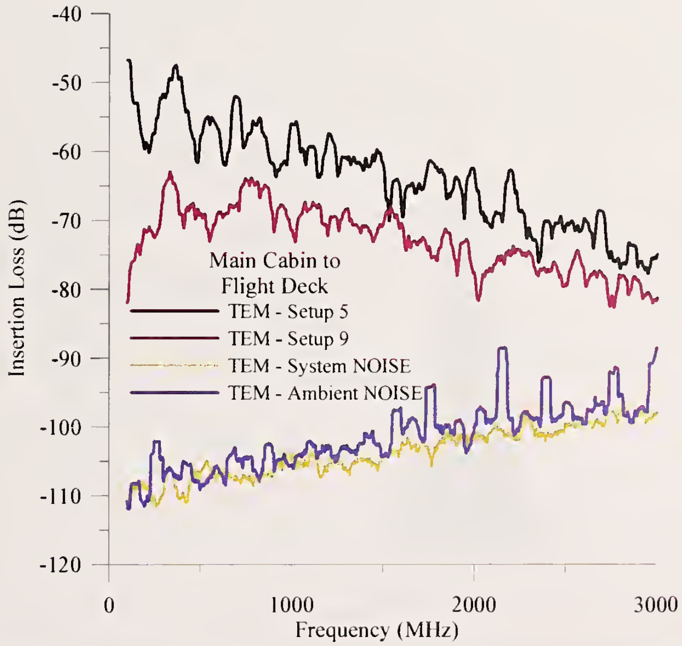


Figure 136. Main cabin to flight deck TEM horn antenna data for the maximum insertion loss, the minimum insertion loss, and two noise measurements.

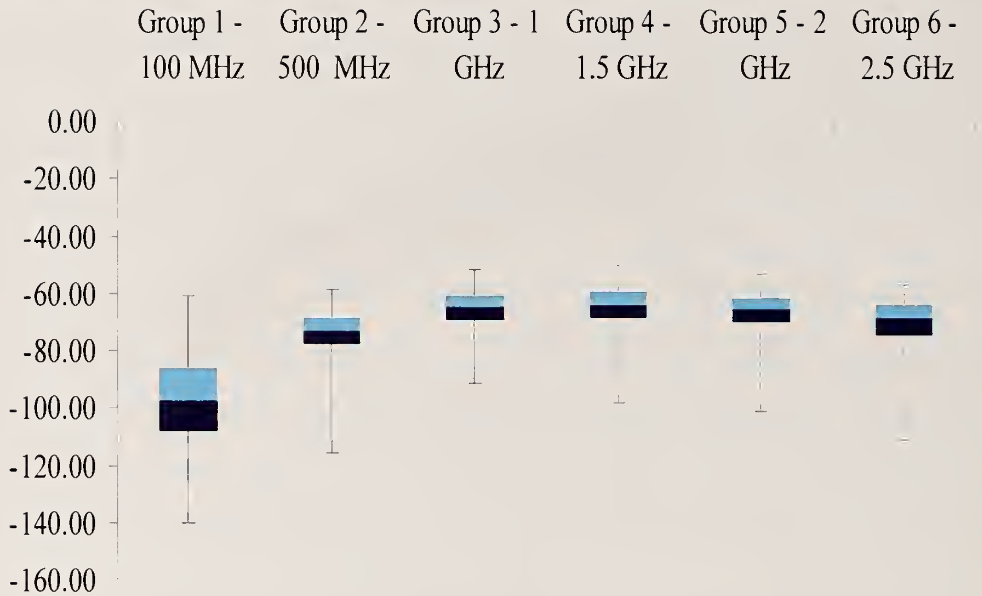


Figure 137. Whisker-box plots for all main cabin to flight deck insertion loss measurements of the TEM horn antennas at several frequencies.

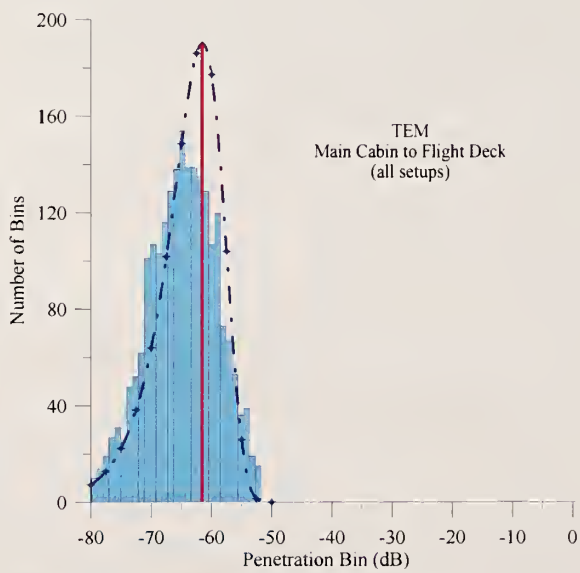


Figure 138. Chi-squared probability density function for all setups in the main cabin to flight deck insertion loss measurements.

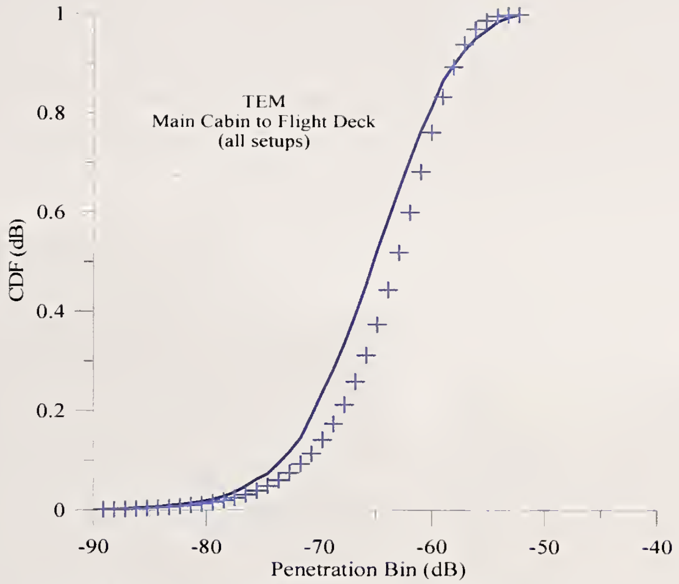

Figure 139. Chi-squared cumulative density function for all setups in the main cabin to flight deck insertion loss measurements.

### 6.4.2.4 Individual TEM horn antenna positions

Figures 140 to Figure 149 include a photograph for each TEM antenna measurement location from the main cabin to the flight deck, its associated time-domain waveform, and a schematic showing the antenna positions inside the aircraft.

Figure 140 shows the placement of a transmitting 1.2 m TEM horn antenna in the main passenger cabin and a receiving 36 cm TEM horn antenna in the flight deck for setup 5. The vertically polarized 1.2 m TEM horn antenna was located in the rear of the aircraft across the center aisle. The horizontally polarized 36 cm TEM horn antenna was located on the floor by the co-pilot's seat and pointed toward the front of the aircraft. Figure 141 is a time-domain graph showing a measurement with the direct antenna coupling component (black trace) and without the direct antenna coupling component with only the reverberant fields (red trace).

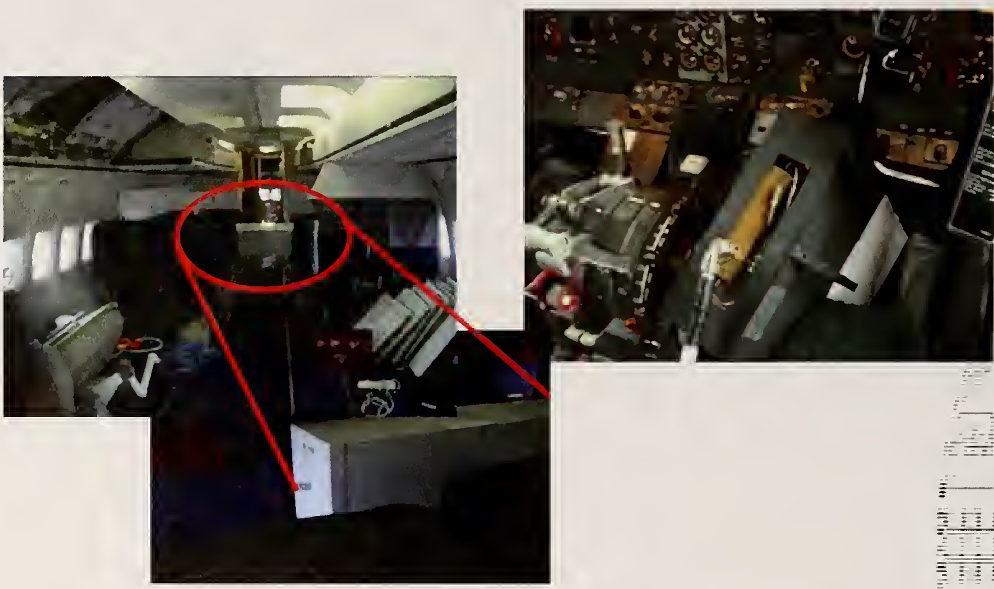

Figure 140. Main cabin to flight deck TEM horn antenna setup 5.

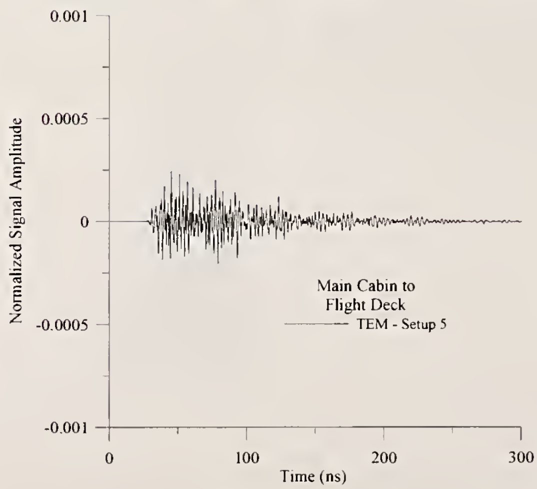


Figure 141. Main cabin to flight deck TEM horn antenna setup 5, time-domain response.

Figure 142 shows the placement of a transmitting 1.2 m TEM horn antenna in the main passenger cabin and a receiving 36 cm TEM horn antenna in the flight deck for setup 6. The vertically polarized 1.2 m TEM horn antenna was located in the rear of the aircraft across the center aisle. The horizontally polarized 36 cm TEM horn antenna was located in the co-pilot's seat and pointed toward the left side of the aircraft. Figure 143 is a time-domain graph of the measurement.

Figure 142. Main cabin to flight deck TEM horn antenna setup 6.

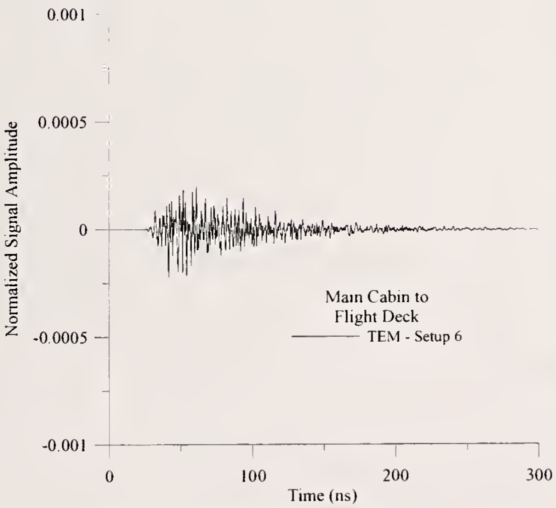


Figure 143. Main cabin to flight deck TEM horn antenna setup 6, time-domain response.

Figure 144 shows the placement of a transmitting 1.2 m TEM horn antenna in the main passenger cabin and a receiving 36 cm TEM horn antenna in the flight deck for setup 7. The horizontally polarized 1.2 m TEM horn antenna was placed on the floor in the aisle at the rear of the aircraft. The vertically polarized 36 cm TEM horn antenna was located in the co-pilot's seat and pointed toward the left side of the aircraft. Figure 145 is a time-domain graph of the measurement.

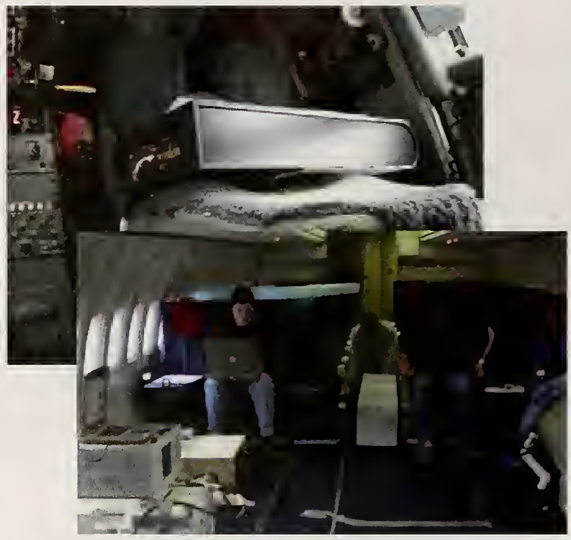

Figure 144. Main cabin to flight deck TEM horn antenna setup 7.

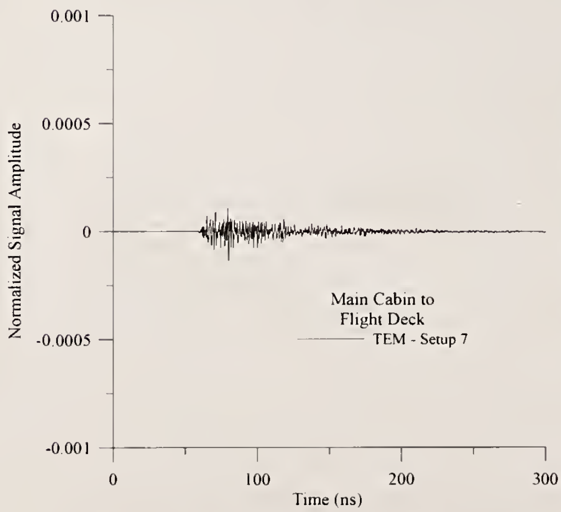


Figure 145. Main cabin to flight deck TEM horn antenna setup 7, time-domain response.

Figure 146 shows the placement of a transmitting 1.2 m TEM horn antenna in the main passenger cabin and a receiving 36 cm TEM horn antenna in the flight deck for setup 8, measurements 1 and 2. The horizontally polarized 1.2 m TEM horn antenna was placed on the floor in the aisle at the rear of the aircraft. The horizontally polarized 36 cm TEM horn antenna was located in the co-pilot's seat and pointed toward the ceiling of the aircraft. Figure 147 is a time-domain graph of the measurement and a repeat measurement for the flight deck.

Figure 146. Main cabin to flight deck TEM horn antenna setup 8.

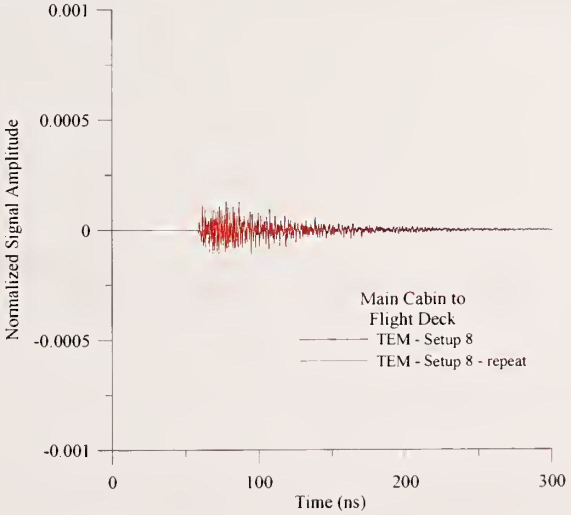


Figure 147. Main cabin to flight deck TEM horn antenna setup 8, time-domain response.

Figure 148 shows the placement of a transmitting 1.2 m TEM horn antenna in the main passenger cabin and a receiving 36 cm TEM horn antenna in the flight deck for setup 9. The horizontally polarized 1.2 m TEM horn antenna was placed facing into the floor in the aisle at the rear of the aircraft. The 36 cm TEM horn antenna was located in the pilot's seat and pointed upward toward the ceiling. Figure 149 is a time-domain graph of the measurement.

Figure 148. Main cabin to flight deck TEM horn antenna setup 9 and setup 10. The 1.2 m TEM horn antenna was in the horizontal polarization for setup 9 and in the vertical polarization for setup 10.

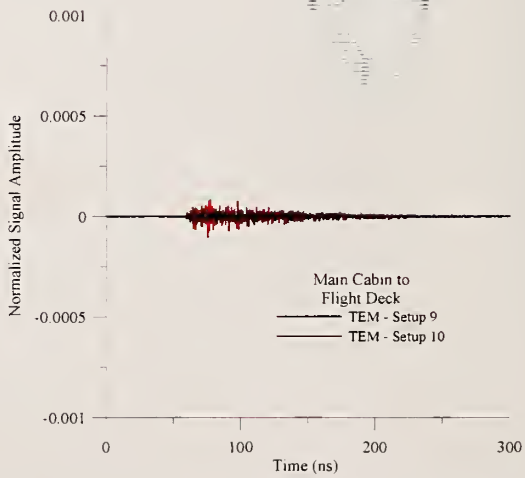


Figure 149. Main cabin to flight deck TEM horn antenna setup 9 and setup 10, time-domain response.

Figure 150 shows whisker-box plots of each individual setup. The group of data was analyzed around a center frequency of 1000 MHz over a 200 MHz bandwidth containing 321 points. Table 7 summarizes the statistics of each setup for the whisker-box plots, and includes the mean value, the median value, the standard deviation, the maximum value in the group, and the minimum value in the group. Table 8 summarizes the differences between the mean value for the whisker-box plot analysis and the mean value for the $\chi^2$ statistic. The difference between the two means is also displayed. Finally, the $\chi^2$ *pdf* and the $\chi^2$ *cdf* are plotted for each setup in Figure 148, Figure 149, and Figure 150.

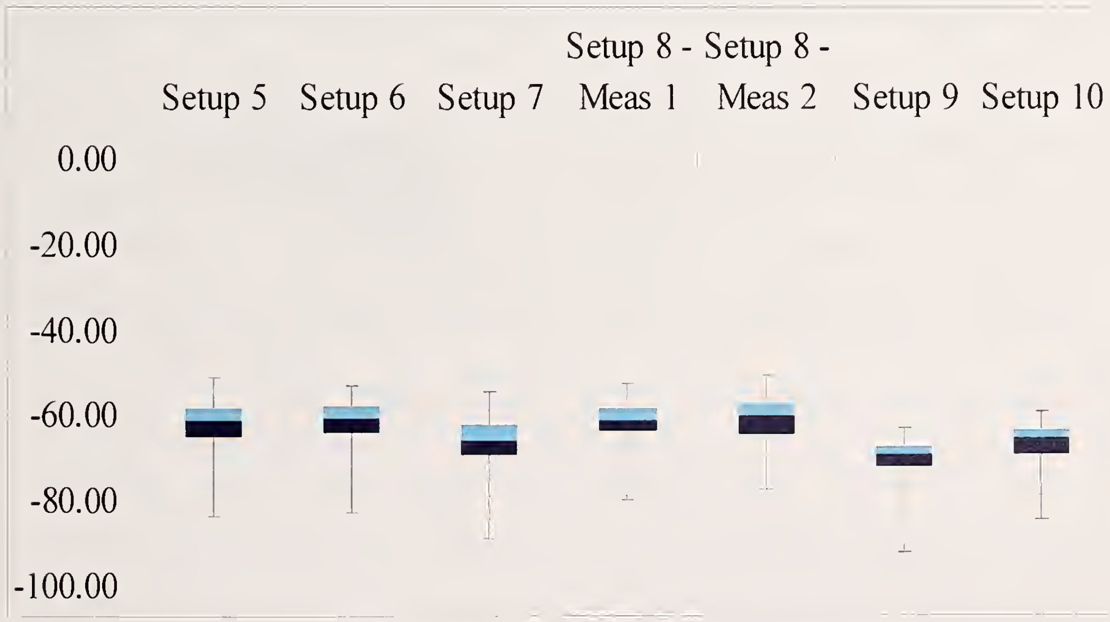


Figure 150. Whisker-box plots for the TEM horn antennas for main cabin to flight deck insertion loss.

Table 7. TEM horn internal cabin statistics for measurements from the main cabin to the flight deck. The sample size was 321 points in a 200 MHz bandwidth around a center frequency of 1 GHz.

| | Setup 5 | Setup 6 | Setup 7 | Setup 8 meas 1 | Setup 8 meas 2 | Setup 9 | Setup 10 |
|---|---|---|---|---|---|---|---|
| Mean (dB) | −62.60 | −62.22 | −67.16 | −62.26 | −62.15 | −71.29 | −67.83 |
| Median (dB) | −62.12 | −61.94 | −67.22 | −62.13 | −61.45 | −70.40 | −66.61 |
| Standard Deviation (dB) | 5.36 | 4.74 | 6.06 | 4.61 | 5.36 | 4.92 | 4.89 |
| Minimum (dB) | −84.56 | −83.75 | −90.19 | −80.67 | −78.64 | −93.48 | −85.75 |
| Maximum (dB) | −52.30 | −54.00 | −55.35 | −53.65 | −51.72 | −64.00 | −60.19 |

Table 8. TEM horn antenna internal cabin $X^2$ - distribution statistics for measurements from the main cabin to the flight deck.

| | Setup 5 | Setup 6 | Setup 7 | Setup 8 meas 1 | Setup 8 meas 2 | Setup 9 | Setup 10 |
|---|---|---|---|---|---|---|---|
| Whisker-Box Plot Mean (dB) | − 62.60 | − 62.22 | − 67.16 | − 62.26 | − 62.15 | − 71.29 | − 67.83 |
| $X^2$ Mean (dB) | − 60.00 | − 57.00 | − 63.00 | − 62.00 | − 60.00 | − 71.00 | − 69.00 |
| Δ (dB) | − 2.00 | − 5.00 | − 4.00 | > − 1.00 | − 2.00 | > − 1.00 | + 2.00 |

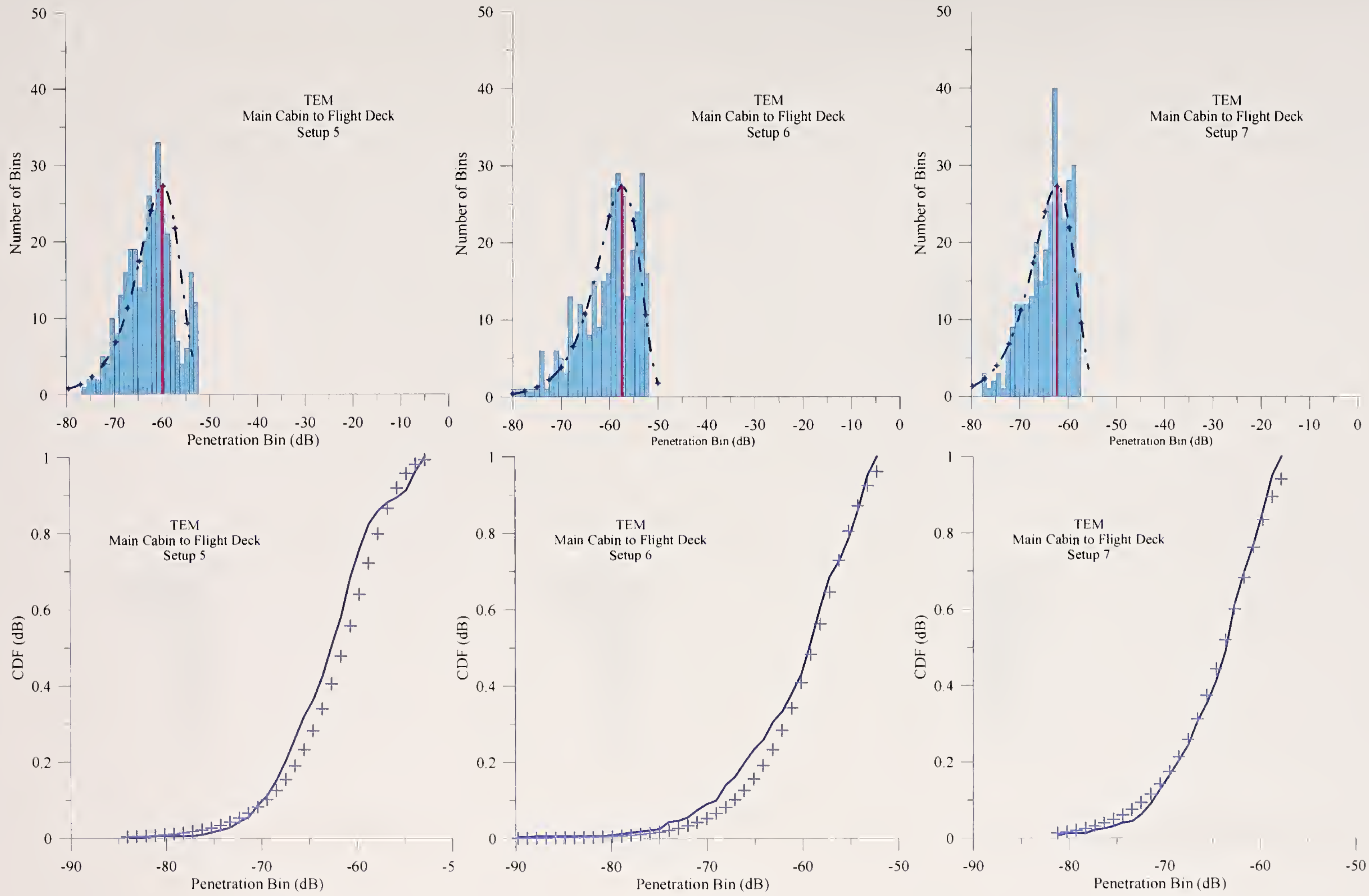


Figure 151. Chi-squared plots for TEM horn antenna, setup 5, setup 6, and setup 7, for the main cabin to flight deck insertion loss.

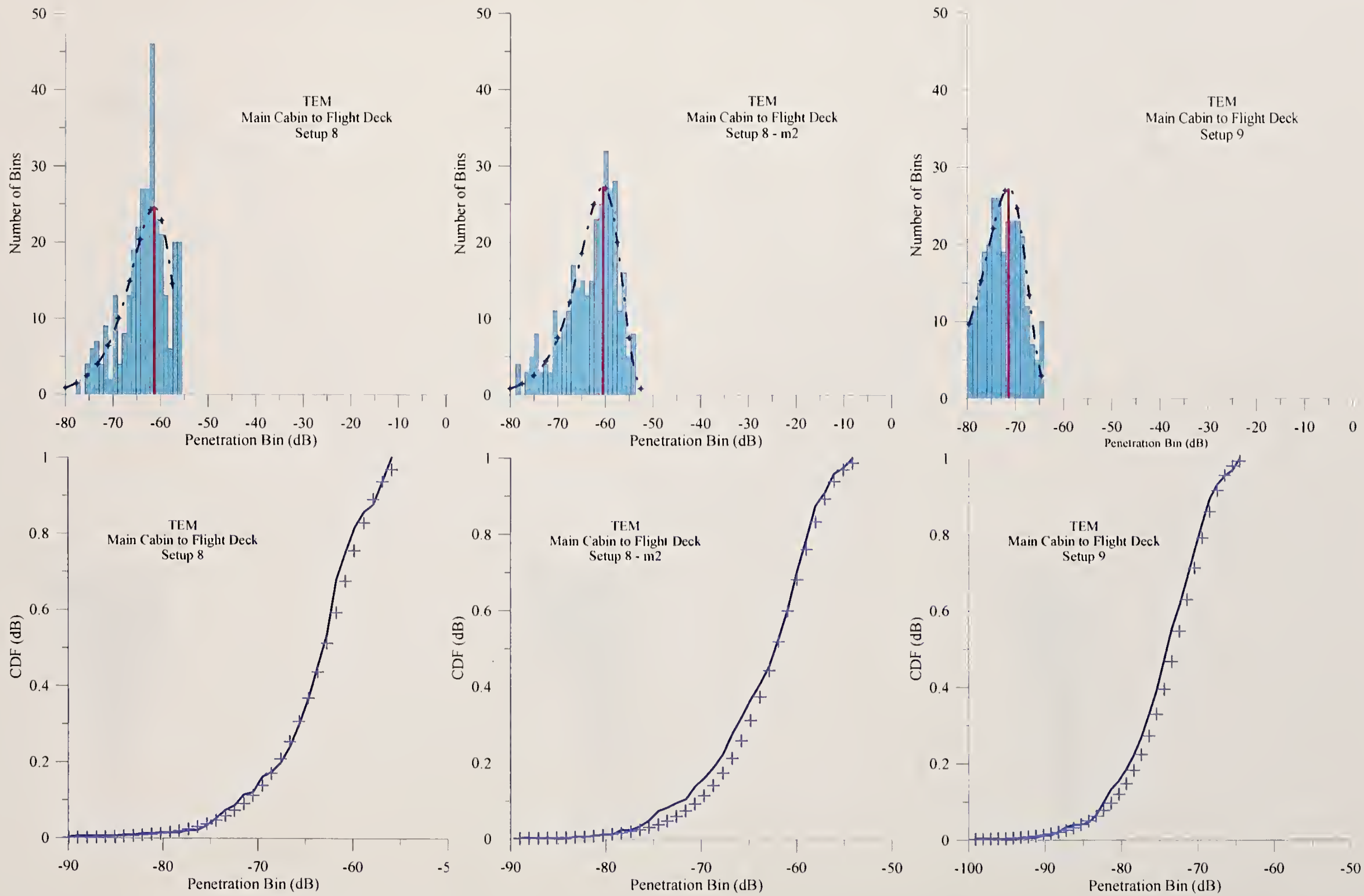


Figure 152. Chi-squared plots for TEM horn antenna, setup 8, measurements 1 and 2, and setup 9, for the main cabin to flight deck insertion loss.

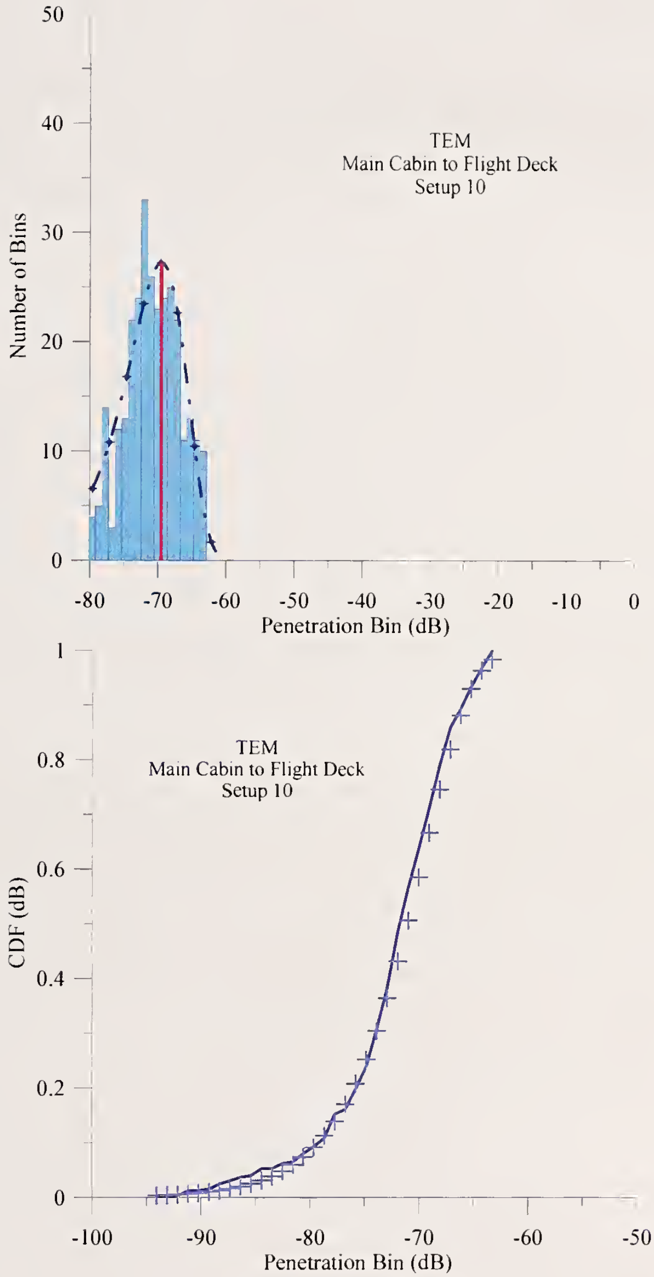


Figure 153. Statistical analysis for TEM horn antenna, setup 10, for main cabin to flight deck insertion loss.

### 6.4.3 Main Cabin to Cargo Bay

The DRG and TEM horn antennas were measured at various positions between the main cabin and cargo bay. An RF cable was run from the VNA in the main cabin through a hole drilled into the floor of the main passenger cabin into the cargo bay. In general, for each compartment-to-compartment measurement we tried to position them in approximately the same position for each of these runs.

#### 6.4.3.1 Combined DRG horn antenna positions

Four positions were measured for the DRG antenna type. No repeat measurements were completed in this compartment-to-compartment measurement. Figure 154 shows all measurement results for the DRG horn antenna showing a maximum insertion loss of around −30 dB and minimum insertion loss of around −55 dB. Figure 155 shows the results for the measurement having maximum cabin insertion loss, minimum insertion loss and two system noise-floor measurements. The noise-floor measurement shown by the brown trace was the system noise floor taken by putting a 50 ohm load on the receiving side of the system. The green trace is the ambient noise floor taken by putting the 50 ohm load on the transmitting side and looking for the ambient signals that enter the receiving antenna. Both results were averaged by se of a 200 MHz bandwidth.

Whisker-box plots are shown in Figure 156 for the following center frequencies, (1) 100 MHz, (2) 500 MHz, (3) 1000 MHz, (4) 1500 MHz, (5) 2000 MHz, and (6) 2500 MHz. Data in these plots are from a 200 MHz bandwidth around each center frequency. The plots show the median insertion loss for these frequencies range from about −41 dB to −48 dB. The maximum value for these frequencies is approximately −26 dB in a 200 MHz bandwidth around a center frequency of 1000 MHz, and the minimum insertion loss is −89 dB in a 200 MHz bandwidth around a center frequency of 900 MHz.

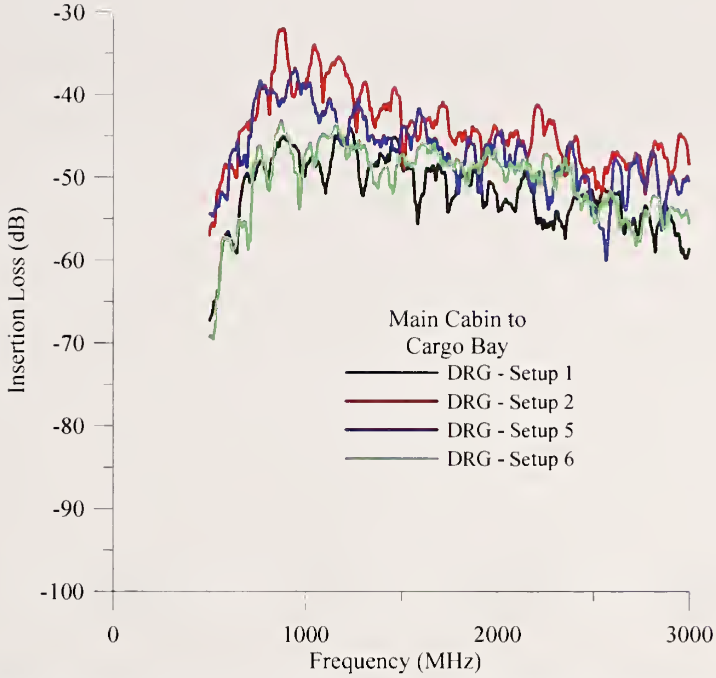


Figure 154. Main cabin to cargo bay DRG antenna insertion loss data at each of the four positions.

The $\chi^2$ *pdf* for all DRG horn antenna measurements is shown in Figure 157 and the $\chi^2$ *cdf* for all DRG horn antenna measurements is shown in Figure 158. The histogram in Figure 157 consists of all points binned into 1 dB bins (light-blue bins) and plotted against the theoretical probability density function (dark-blue trace) and the average value of the theoretical data (pink trace). The

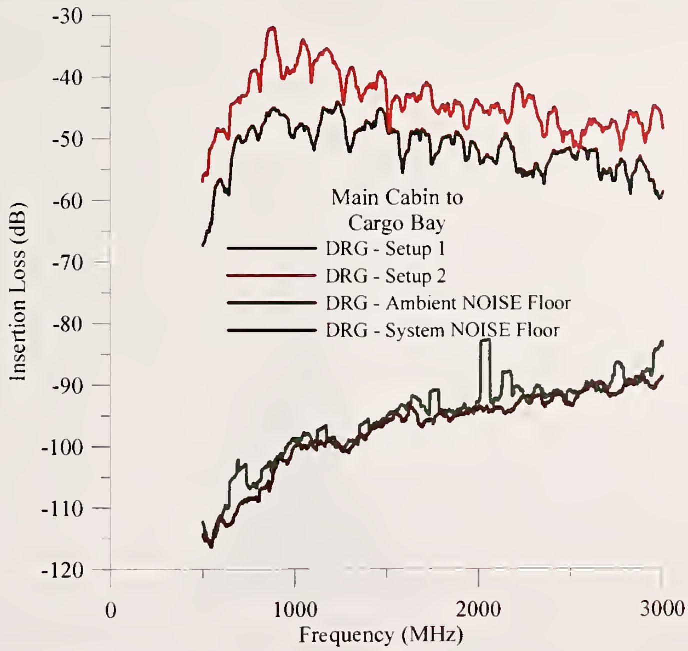


Figure 155. Main cabin to cargo bay DRG antenna data for the maximum insertion loss, the minimum insertion loss, and two noise measurements.

theoretical average value is around −39 dB. Figure 158 is the data (dark-blue, solid trace) plotted against the theoretical cumulative distribution function. This plot shows that the data do not tightly follow the theoretical cumulative distribution function. This does not typically seem to be the case for the individual positions.

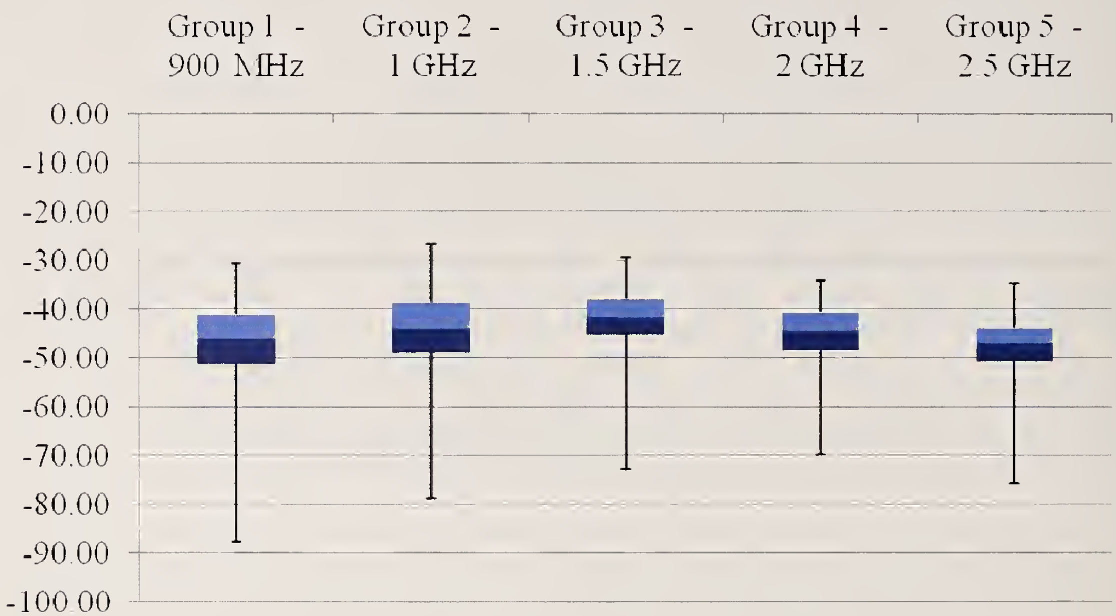


Figure 156. Whisker-box plots of all main cabin to cargo bay insertion loss measurements for the DRG horn antennas at several frequencies.

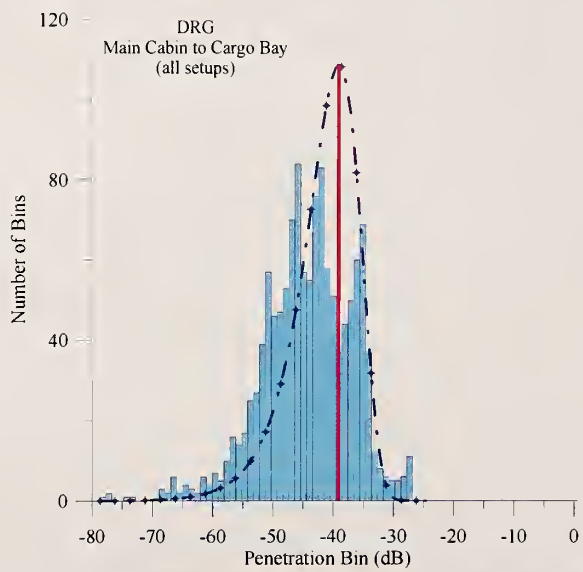


Figure 157. Chi-squared probability density function for all measurements of insertion loss in the main cabin to cargo bay.

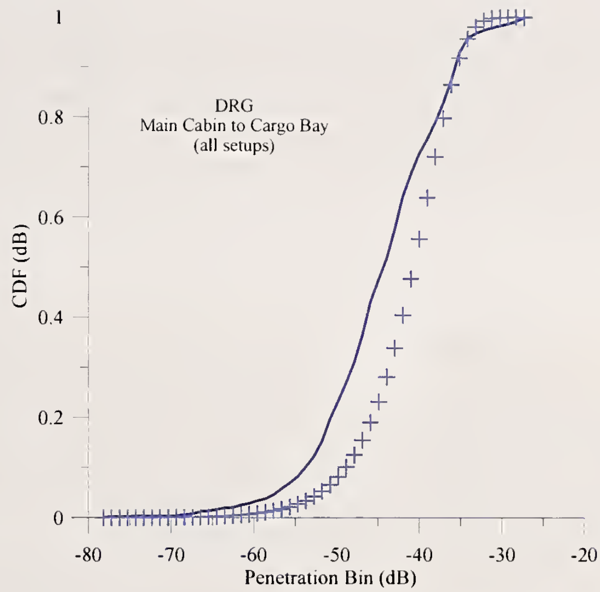


Figure 158. Chi-squared cumulative density function for all measurements of insertion loss in the main cabin to cargo bay.

#### 6.4.3.2 Individual DRG horn antenna measurement positions

In this section each measurement position from the main cabin to the cargo bay is individually analyzed. Figures 159 to 166 show a photograph of the locations of the antennas in the flight deck and the main cabin, a time-domain plot, and a schematic of the inside of the 737-200 that indicates where the antennas were placed.

Figure 159 shows the placement of a transmitting DRG horn antenna in the main passenger cabin and a receiving DRG horn antenna in the cargo bay for setup 1. One vertically polarized antenna was located in the rear of the aircraft on top of the seats of the main passenger and pointed toward the front of the aircraft. The other vertically polarized antenna was located on an insulated cooler and pointed toward the avionics bay. Figure 160 is a time-domain graph of the measurement for the cargo bay.


Figure 159. Main cabin to cargo bay DRG horn antenna setup 1.

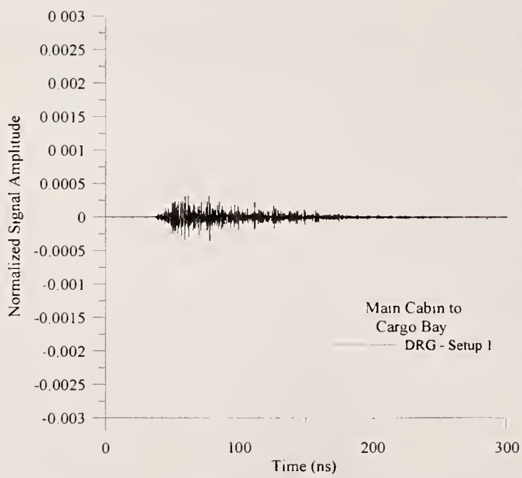


Figure 160. Main cabin to cargo bay DRG horn antenna setup 1, time-domain response.

Figure 161 shows the placement of a transmitting DRG horn antenna in the main passenger cabin and a receiving DRG horn antenna in the cargo bay for setup 2. One vertically polarized antenna was located in the in the first-class section on top of the seats of the main passenger cabin and pointed toward the front of the aircraft. The other, vertically polarized, antenna was located on an insulated cooler and pointed toward the avionics bay. Figure 162 is a time-domain graph of the measurement for the cargo bay.


Figure 161. Main cabin to cargo bay DRG horn antenna setup 2.

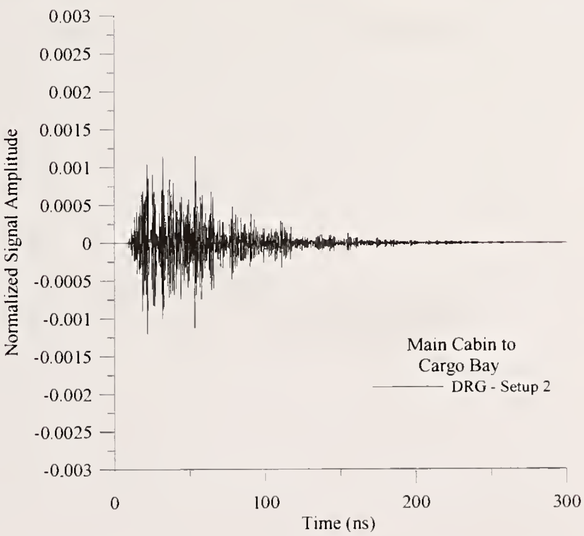


Figure 162. Main cabin to cargo bay DRG horn antenna setup 2, time-domain response.

Figure 163 shows the placement of a transmitting DRG horn antenna in the main passenger cabin and a receiving DRG horn antenna in the cargo bay for setup 5. One vertically polarized antenna was located in the in the first class section on top of the seats of the main passenger cabin and pointed toward the front of the aircraft. The other horizontally polarized antenna was located on an insulated cooler and pointed toward the avionics bay. Figure 164 is a time-domain graph of the measurement for the cargo bay.


Figure 163. Main cabin to cargo bay DRG horn antenna setup 5.

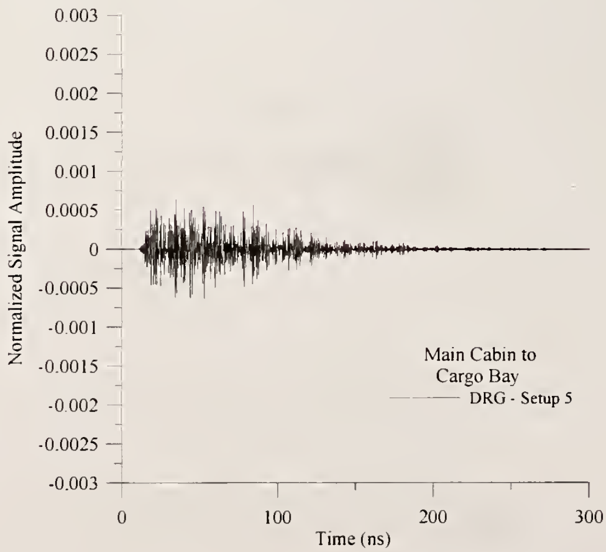


Figure 164. Main cabin to cargo bay DRG horn antenna setup 5, time-domain response.

Figure 165 shows the placement of a transmitting DRG horn antenna in the main passenger cabin and a receiving DRG horn antenna in the cargo bay for setup 6. One vertically polarized antenna was located in the rear of the aircraft on top of the seats of the main passenger cabin and pointed toward the front of the aircraft. The other, horizontally polarized, antenna was located on an insulated cooler pointing toward the avionics bay. A time-domain graph of the measurement for the cargo bay is shown in Figure 166.


Figure 165. Main cabin to cargo bay DRG horn antenna setup 6.

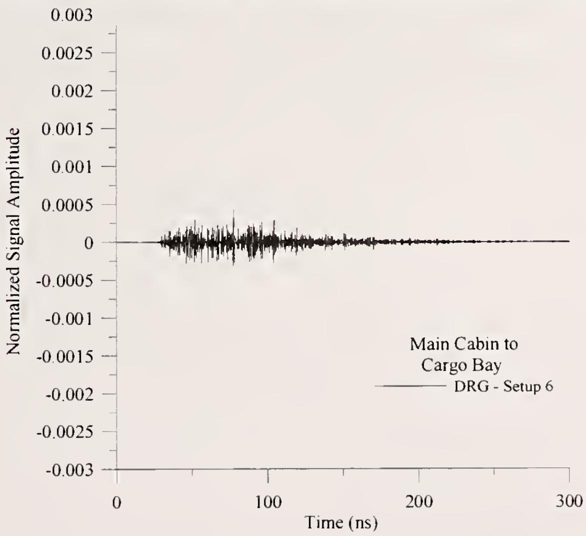


Figure 166. Main cabin to cargo bay DRG horn antenna setup 6, time-domain response.

Figure 167 shows whisker-box plots of each individual setup. The group of data was analyzed around a center frequency of 1000 MHz over a 200 MHz bandwidth containing 321 points. Table 9 summarizes the statistics of each setup for the whisker-box plots, and includes the mean value, the median value, the standard deviation, the maximum value in the group, and the minimum value in the group. Table 10 summarizes the differences between the mean value for the whisker-box plot analysis and the mean value for the $\chi^2$ statistic. The difference between the two means is also displayed. Finally, the $\chi^2$ *pdf* and the $\chi^2$ *cdf* are plotted for each setup in Figure 168 and Figure 169.

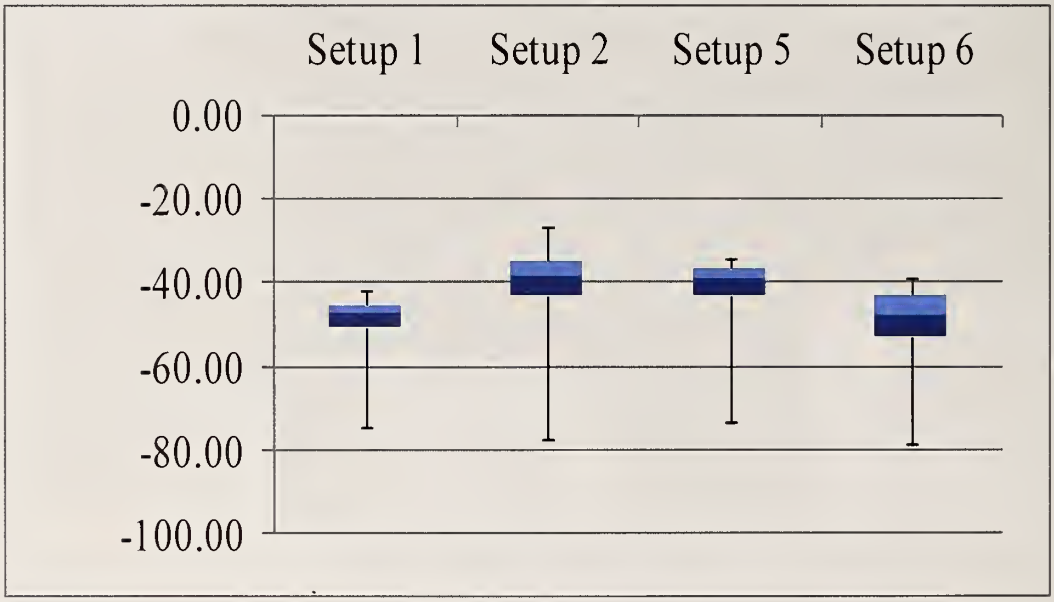


Figure 167. Whisker-box plots for the DRG horn antennas for main cabin to cargo bay insertion loss.

Table 9. DRG Horn internal cabin statistics for measurements from the main cabin to the cargo bay. The sample size was 321 points in a 200 MHz bandwidth around a center frequency of 1 GHz.

| | Setup 1 | Setup 2 | Setup 5 | Setup 6 |
|---|---|---|---|---|
| Mean (dB) | - 48.06 | - 39.46 | - 40.68 | - 48.83 |
| Median (dB) | - 47.31 | - 38.62 | - 38.71 | - 47.45 |
| Standard Deviation (dB) | 4.10 | 7.13 | 6.01 | 7.20 |
| Minimum (dB) | - 74.68 | - 77.41 | - 73.48 | - 78.66 |
| Maximum (dB) | - 41.62 | - 26.80 | - 34.17 | - 38.63 |

Table 10. DRG horn antenna internal cabin $X^2$ - distribution statistics for measurements from the main cabin to the cargo bay.

| | Setup 1 | Setup 2 | Setup 5 | Setup 6 |
|---|---|---|---|---|
| Whisker-Box Plot Mean (dB) | - 48.06 | - 39.46 | - 40.68 | - 48.83 |
| $X^2$ Mean (dB) | - 45.00 | - 35.00 | - 38.00 | - 45.00 |
| $\Delta$ (dB) | - 3.00 | - 4.00 | - 1.00 | - 3.00 |

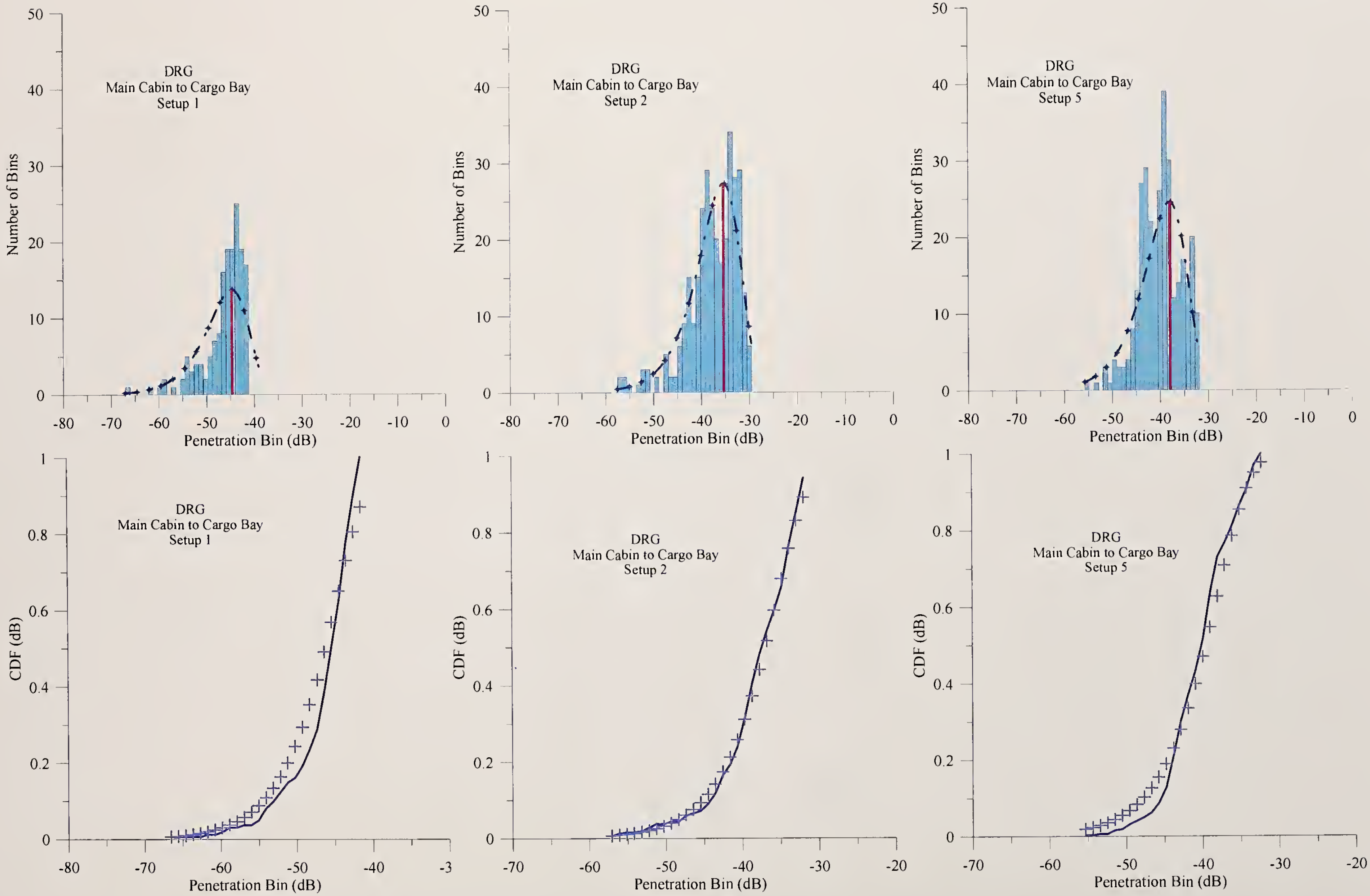


Figure 168. Statistical analysis for DRG horn antenna, setup 1, setup 2, and setup 5 for main cabin to cargo bay insertion loss.

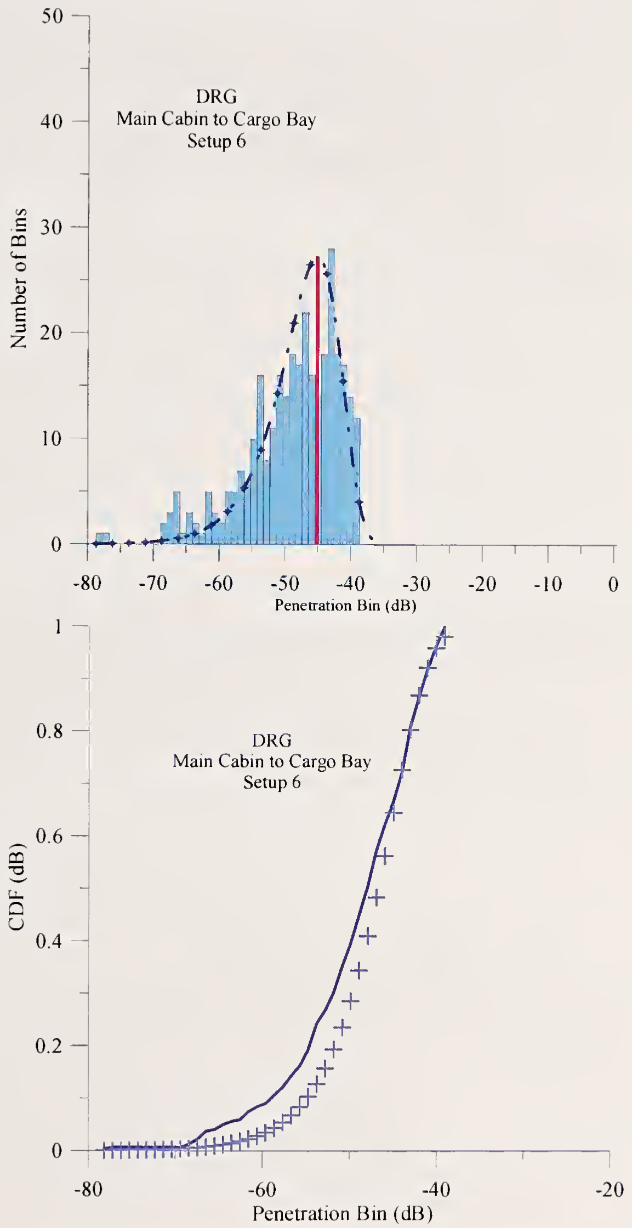


Figure 169. Statistical analysis for DRG horn antenna, setup 6, for main cabin to cargo bay insertion loss.

### 6.4.3.3 Combined TEM horn antenna positions

Six positions were measured for the TEM horn antenna. Figure 170 show results for all measurements in the main cabin for the TEM horn antenna showing a maximum insertion loss of around −35 dB and a minimum insertion loss of around −60 dB. Figure 171 shows a measurement of the maximum cabin insertion loss, the minimum insertion loss, and two system noise floors.

For the TEM horn antennas, statistics are given for a 200 MHz bandwidth around 900 MHz, 1000 MHz, 1500 MHz, 2000 MHz, and 2500 MHz over all measurement positions, as shown in Figure 172. In a 200 MHz bandwidth there are 321 points, so for six measurement positions a total of 2247 points will be in the statistical bandwidth. These plots show the average insertion loss for these frequencies range from about −45 dB to −90 dB. The maximum insertion loss for these frequencies is approximately −35 dB in a 200 MHz bandwidth around center frequencies of 1000 and 2000 MHz, and the minimum insertion loss is −135 dB in a 200 MHz bandwidth around a center frequency of 100 MHz.

The $\chi^2$ *pdf* for all TEM horn antenna measurements is shown in Figure 173, and the $\chi^2$ *cdf* for all TEM horn antenna measurements is shown in Figure 174. The histogram in Figure 173 consists of all points binned into 1 dB bins (light-blue bins) and plotted against the theoretical probability density function (dark-blue trace) and the average value of the theoretical data (pink trace). The theoretical average value is around −46 dB. Figure 174 is the data (dark-blue, solid trace) plotted against the theoretical cumulative distribution function.

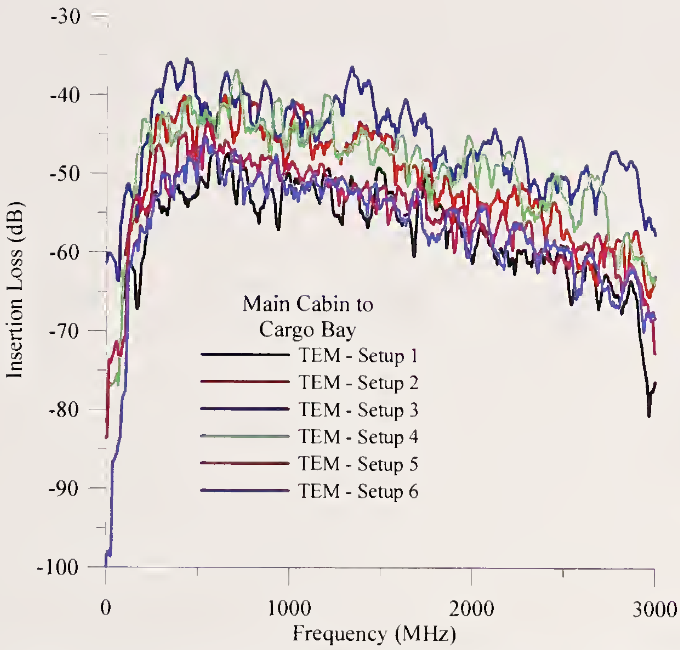


Figure 170. Main cabin to cargo bay TEM antenna insertion loss data at each of the six positions.

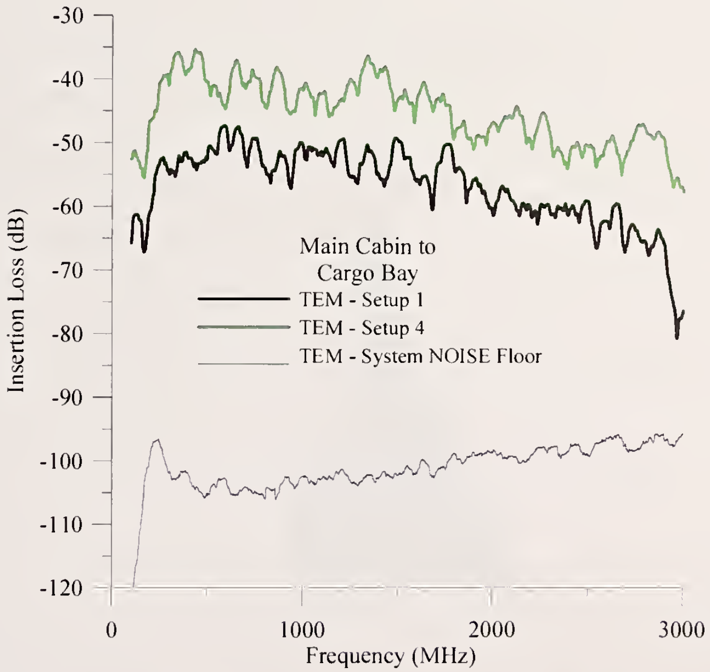


Figure 171. Main cabin to cargo bay TEM antenna data for the maximum insertion loss, the minimumt insertion loss, and a noise measurement.

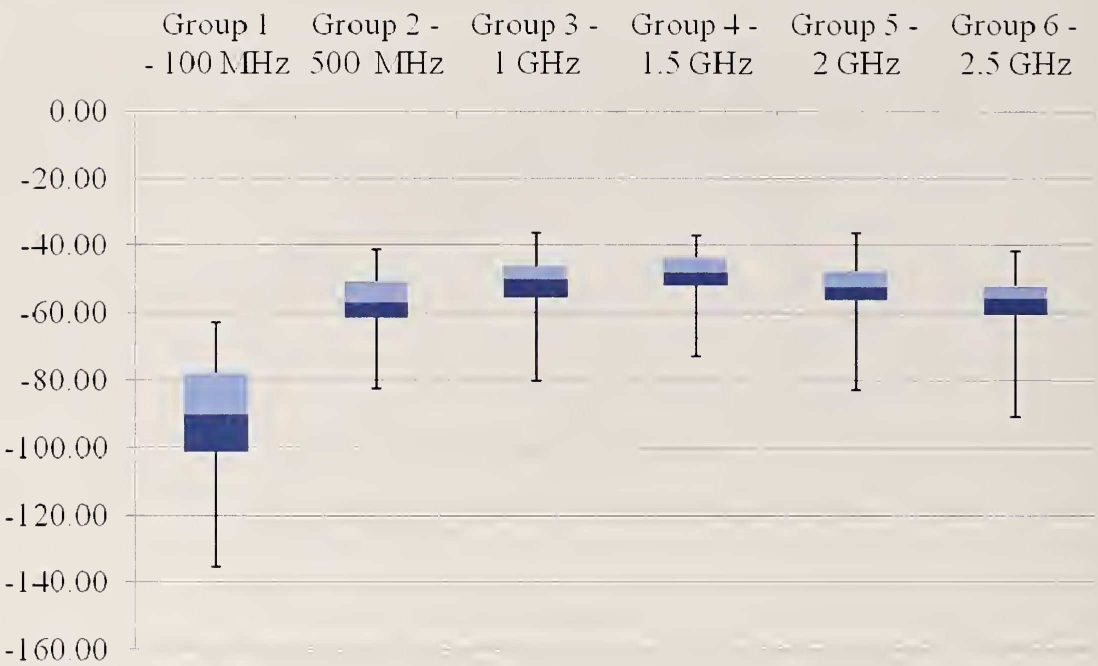


Figure 172. Whisker-box plots of all main cabin to cargo bay insertion-loss measurements for the TEM horn antennas at several frequencies.

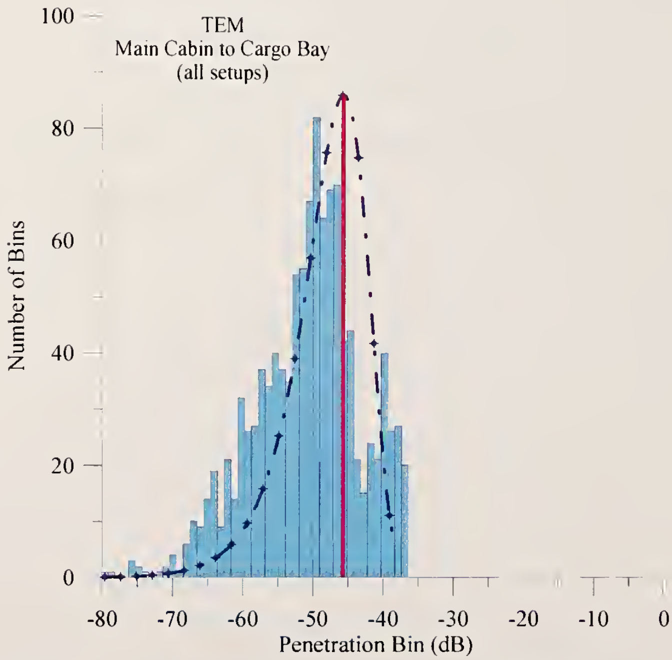


Figure 173. Chi-squared probability density function for all measurements of insertion loss in the main cabin to cargo bay.

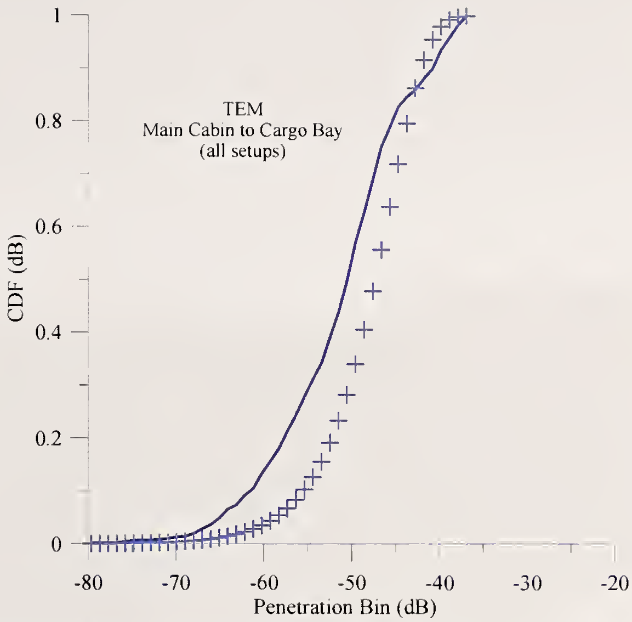


Figure 174. Chi-squared cumulative density function for all measurements of insertion loss in the main cabin to cargo bay.

### 6.4.3.4 Individual TEM horn antenna positions

A photograph for each TEM antenna measurement location from the main cabin to the cargo bay, its associated time-domain waveform, and a schematic showing the antenna positions inside the aircraft is shown from Figure 175 to Figure 186.

Figure 175 shows the placement of a transmitting 1.2 m TEM horn antenna in the main passenger cabin and a receiving 36 cm TEM horn antenna in the cargo bay for setup 1, measurements 1 and 2. The vertically polarized 1.2 m TEM horn antenna was located in the rear of the aircraft positioned across the seats, and pointed toward the front of the aircraft and out the windows. The vertically polarized 36 cm TEM horn antenna was located on an insulated cooler and pointed toward the avionics bay. A time-domain graph is shown in Figure 176.


Figure 175. Main cabin to cargo bay TEM horn antenna setup 1.

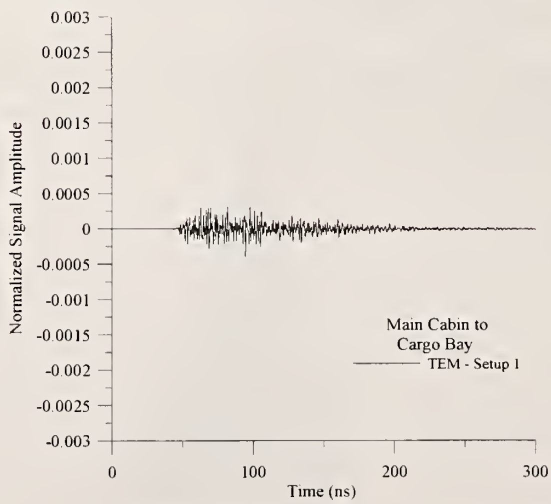


Figure 176. Main cabin to cargo bay TEM horn antenna setup 1, time-domain response.

Figure 177 shows the placement of a transmitting 1.2 m TEM horn antenna in the main passenger cabin and a receiving 36 cm TEM horn antenna in the cargo bay for setup 2. The vertically polarized 1.2 m TEM horn antenna was located in the first-class section of the aircraft positioned across the seats, and pointed toward the front of the aircraft. The vertically polarized 36 cm TEM horn antenna was located on an insulated cooler and pointed toward the avionics bay. A time-domain graph is shown in Figures 178.


Figure 177. Main cabin to cargo bay TEM horn antenna setup 2.

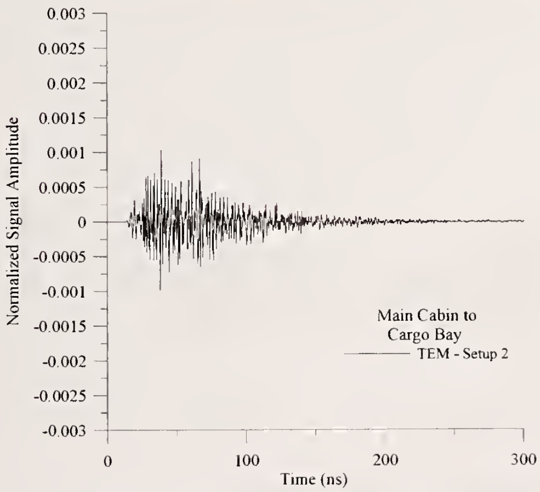


Figure 178. Main cabin to cargo bay TEM horn antenna setup 2, time-domain response.

Figure 179 shows the placement of a transmitting 1.2 m TEM horn antenna in the main passenger cabin and a receiving 36 cm TEM horn antenna in the cargo bay for setup 3. The vertically polarized 1.2 m TEM horn antenna was located in the first-class section of the aircraft and pointed down into the cargo bay. This was to see whether there was strong coupling with a directed measurement. The vertically polarized 36 cm TEM horn antenna was located on an insulated cooler and pointed toward the avionics bay. A time-domain graph is shown in Figure 180.


Figure 179. Main cabin to cargo bay TEM horn antenna setup 3.

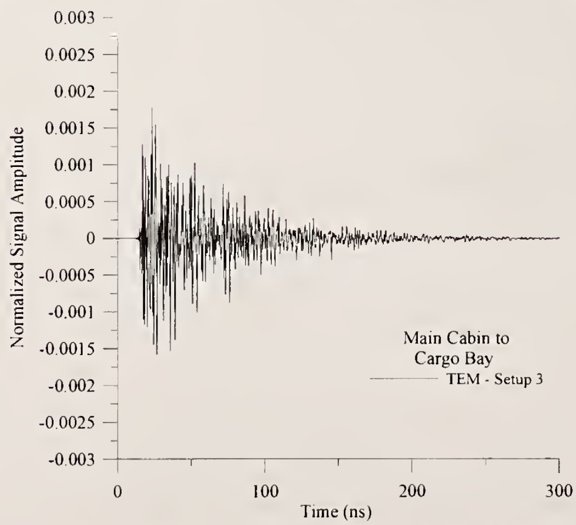


Figure 180. Main cabin to cargo bay TEM horn antenna setup 3, time-domain response.

Figure 181 shows the placement of a transmitting 1.2 m TEM horn antenna in the main passenger cabin and a receiving 36 cm TEM horn antenna in the cargo bay for setup 4. The vertically polarized 1.2 m TEM horn antenna was located in the first-class section of the aircraft and pointed down into the cargo bay. This was to see whether there was strong coupling with a directed measurement. The horizontally polarized 36 cm TEM horn antenna was located on an insulated cooler and pointed toward the avionics bay. A time-domain graph is shown in Figure 182.


Figure 181. Main cabin to cargo bay TEM horn antenna setup 4.

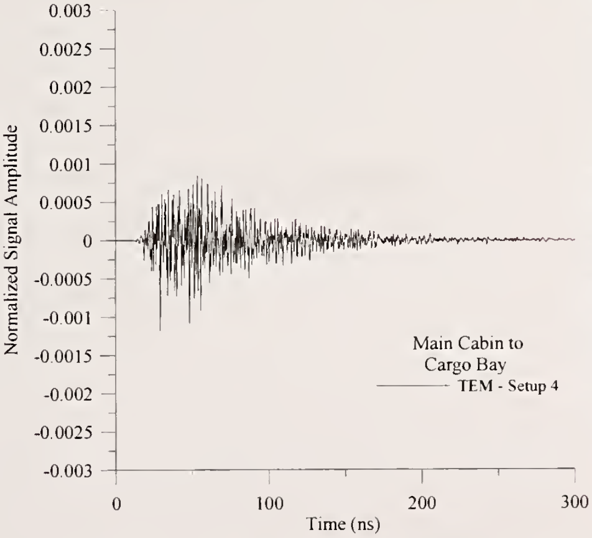


Figure 182. Main cabin to cargo bay TEM horn antenna setup 4, time-domain response.

Figure 183 shows the placement of a transmitting 1.2 m TEM horn antenna in the main passenger cabin and a receiving 36 cm TEM horn antenna in the cargo bay for setup 5. The horizontally polarized 1.2 m TEM horn antenna was located in the first-class section of the aircraft and pointed down into the cargo bay. The horizontally polarized 36 cm TEM horn antenna was located on an insulated cooler and pointed toward the avionics bay. A time-domain graph is shown in Figure 184.


Figure 183. Main cabin to cargo bay TEM horn antenna setup 5.

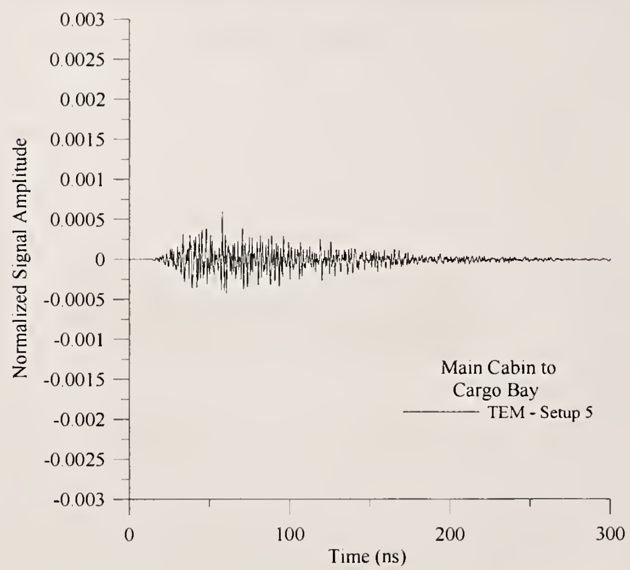


Figure 184. Main cabin to cargo bay TEM horn antenna setup 5, time-domain response.

Figure 185 shows the placement of a transmitting 1.2 m TEM horn antenna in the main passenger cabin and a receiving 36 cm TEM horn antenna in the cargo bay for setup 6. The vertically polarized 1.2 m TEM horn antenna was located in the rear of the aircraft positioned across the seats, and pointed toward the front of the aircraft and out the windows. The horizontally polarized 36 cm TEM horn antenna was located on an insulated cooler and pointed toward the avionics bay. A time-domain graph is shown in Figure 186.


Figure 185. Main cabin to cargo bay TEM horn antenna setup 6.

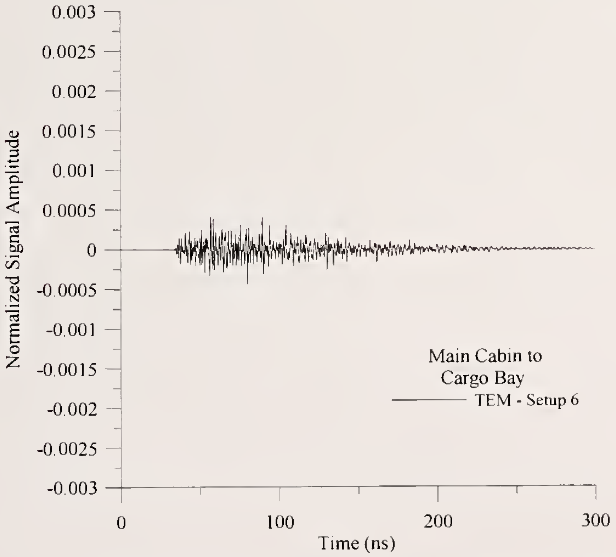


Figure 186. Main cabin to cargo bay TEM horn antenna setup 6, time-domain response.

Figure 187 shows whisker-box plots of each individual setup. The group of data was analyzed around a center frequency of 1000 MHz over a 200 MHz bandwidth containing 321 points. Table 11 summarizes the statistics of each setup for the whisker-box plots, and includes the mean value, the median value, the standard deviation, the maximum value in the group, and the minimum value in the group. Table 12 summarizes the differences between the mean value for the whisker-box plot analysis and the mean value for the $\chi^2$ statistic. The difference between the two means is also displayed. Finally, the $\chi^2$ *pdf* and the $\chi^2$ *cdf* are plotted for each setup in Figure 188, Figure 189, and Figure 190.

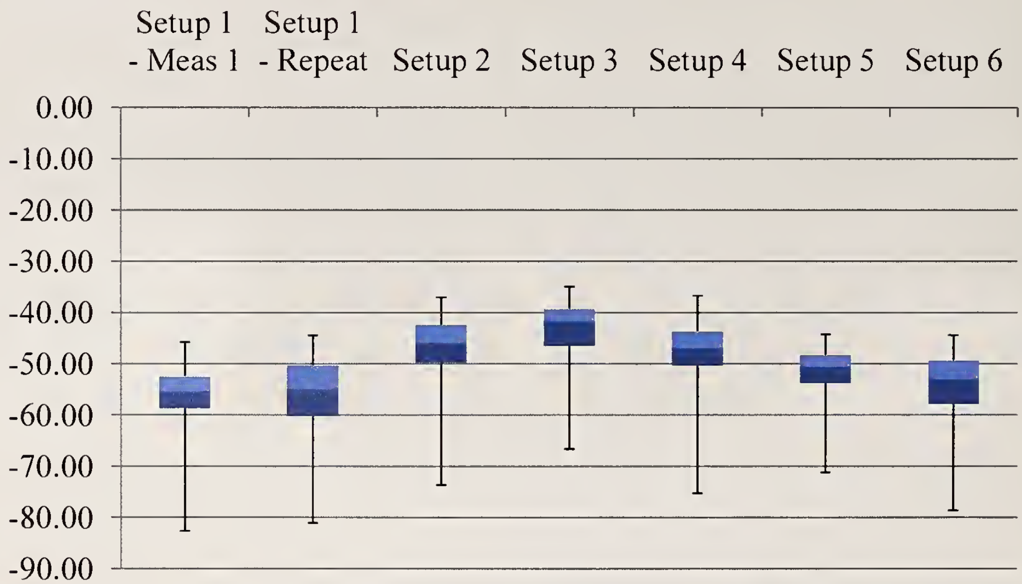


Figure 187. Whisker-box plots for the TEM horn antennas for main cabin to cargo bay insertion loss for individual setups.

Table 11. TEM Horn internal cabin statistics for measurements from the main cabin to the cargo bay. The sample size was 321 points in a 200 MHz bandwidth around a center frequency of 1 GHz.

| | Setup 1 | Setup 1 repeat | Setup 2 | Setup 3 | Setup 4 | Setup 5 | Setup 6 |
|---|---|---|---|---|---|---|---|
| Mean (dB) | - 56.03 | - 56.17 | - 46.94 | - 43.05 | - 47.12 | - 40.68 | - 53.88 |
| Median (dB) | - 54.99 | - 55.47 | - 45.88 | - 41.45 | - 46.52 | - 38.71 | - 52.80 |
| Standard Deviation (dB) | 6.78 | 5.55 | 6.41 | 5.22 | 6.01 | 6.01 | 6.04 |
| Minimum (dB) | - 81.06 | - 82.68 | - 73.65 | - 66.62 | - 75.27 | - 73.48 | - 78.61 |
| Maximum (dB) | - 44.43 | - 45.74 | - 37.02 | - 34.91 | - 36.68 | - 34.17 | - 44.39 |

Table 12. TEM horn antenna internal cabin $X^2$ - distribution statistics for measurements from the main cabin to the cargo bay.

| | Setup 1 | Setup 1 repeat | Setup 2 | Setup 3 | Setup 4 | Setup 5 | Setup 6 |
|---|---|---|---|---|---|---|---|
| Whisker-Box Plot Mean (dB) | - 56.03 | - 56.17 | - 46.94 | - 43.05 | - 47.12 | - 40.68 | - 53.88 |
| $X^2$ Mean (dB) | - 51.00 | - 45.00 | - 36.00 | - 44.00 | - 50.00 | - 38.00 | - 54.00 |
| $\Delta$ (dB) | -5.00 | -11.00 | -11.00 | + 1.00 | + 3.00 | -3.00 | < 1.00 |

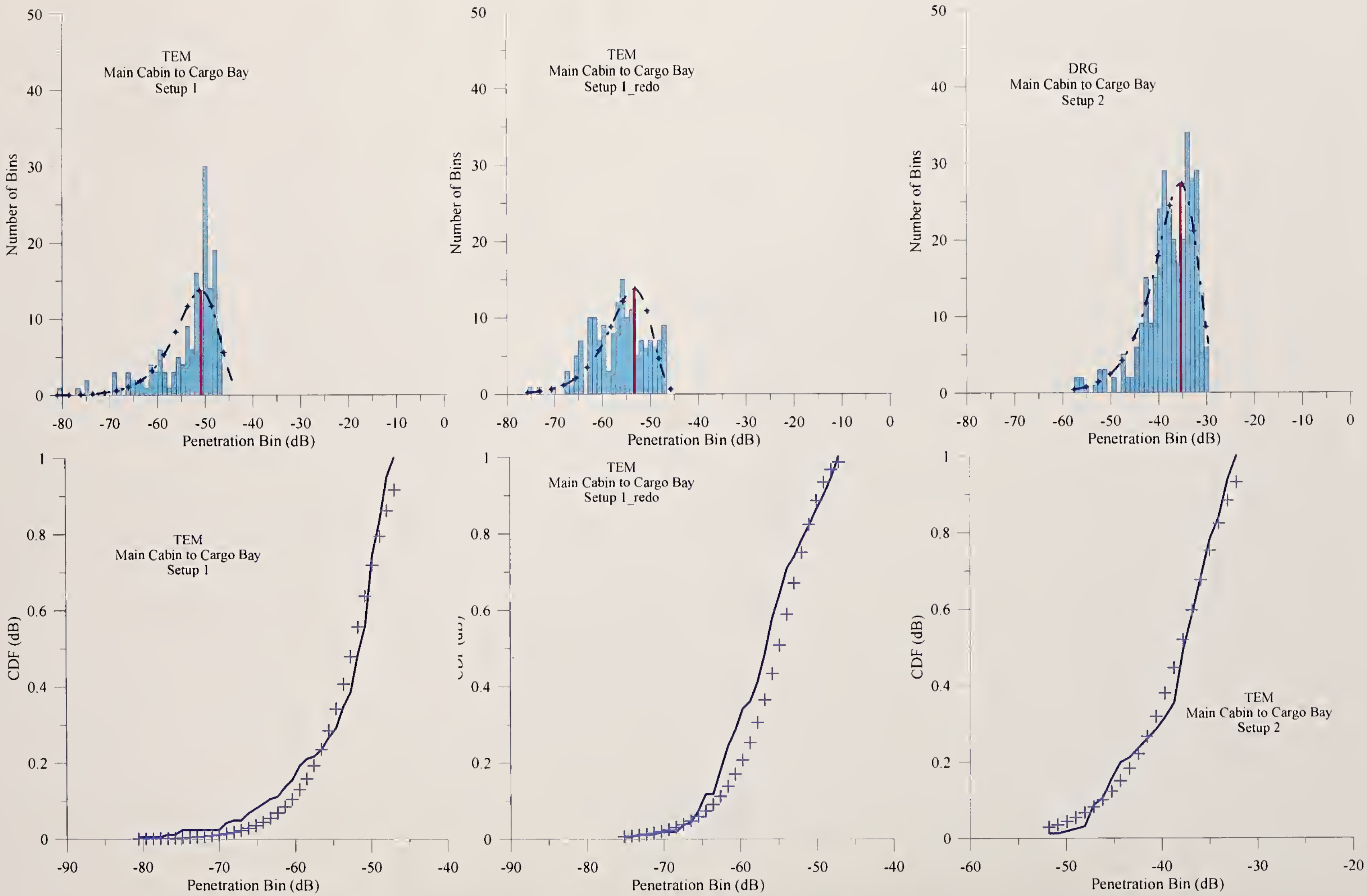


Figure 188. Statistical analysis for TEM horn antenna, setup 1 and a repeat measurement for setup 1, and setup 2 for main cabin to cargo bay insertion loss.

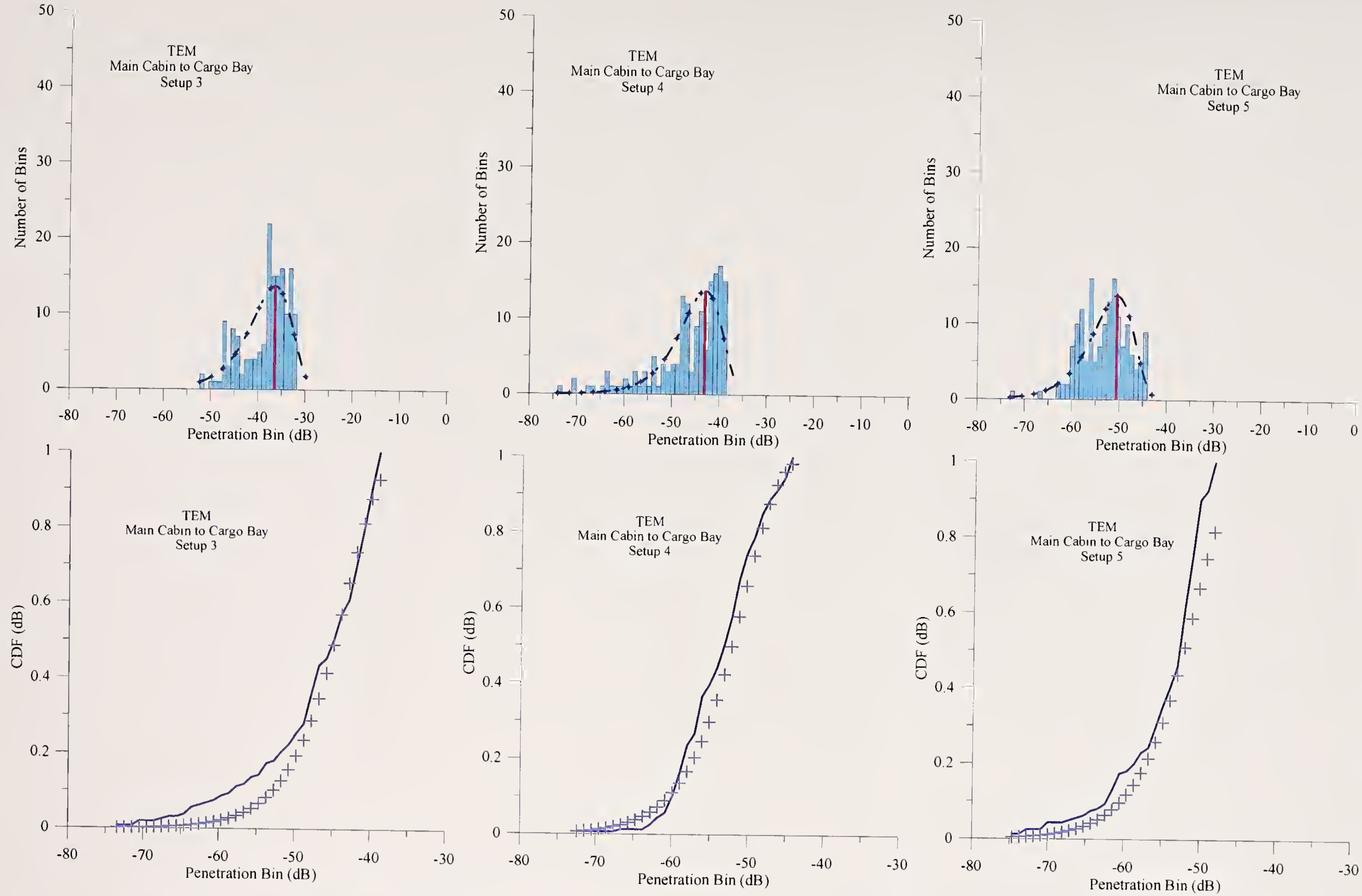


Figure 189. Statistical analysis for TEM horn antenna, setup 3, setup 4, and setup 5 for main cabin to cargo bay insertion loss.

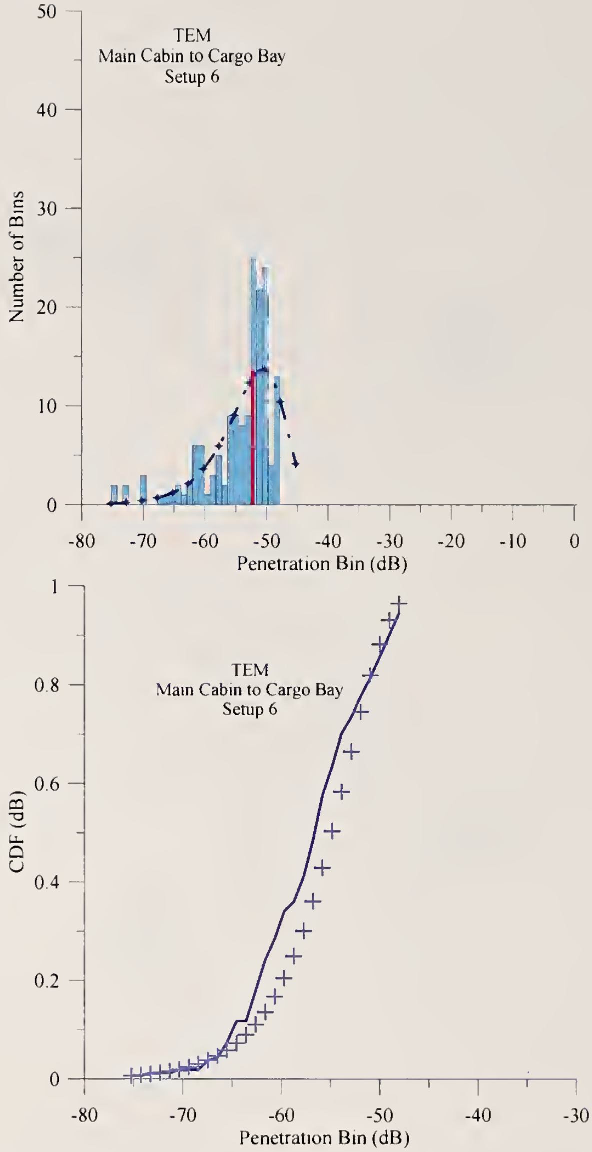


Figure 190. Statistical analysis for TEM horn antenna, setup 6, for main cabin to cargo bay insertion loss.

### 6.4.4 Main Cabin to Avionics Bay

The DRG and TEM horn antennas were measured at various positions between the main cabin and cargo bay. An RF cable was run from the main passenger cabin through the hole in the floor of the main passenger cabin and through a hole in the wall from the cargo bay to the avionics bay. In general, for each compartment-to-compartment measurement we tried to position the antennas in approximately the same position for each of these runs.

#### 6.4.4.1 Combined DRG horn antenna positions

Four positions were measured for the DRG antenna type. No repeat measurements were completed in this compartment-to-compartment measurement. Figure 191 shows all measurement results for the DRG horn antenna showing a maximum insertion loss of around −30 dB and and minimum insertion loss of around −55 dB. Figure 192 shows the results for the measurement having maximum cabin insertion loss, minimum insertion loss and two system noise-floor measurements. The noise-floor measurement was averaged by use of a 200 MHz bandwidth.

Whisker-box plots are shown in Figure 193 for the following center frequencies, (1) 100 MHz, (2) 500 MHz, (3) 1000 MHz, (4) 1500 MHz, (5) 2000 MHz, and (6) 2500 MHz. Data in these plots are from a 200 MHz bandwidth around each center frequency. The plots show the median insertion loss for these frequencies have values from about −55 dB to −59 dB. The maximum value for these frequencies is approximately −32 dB in a 200 MHz bandwidth around center frequencies of 1000 MHz and 1500 MHz, and the minimum insertion loss is −98 dB in a 200 MHz bandwidth around center frequencies of 1500 MHz and 2500 MHz.

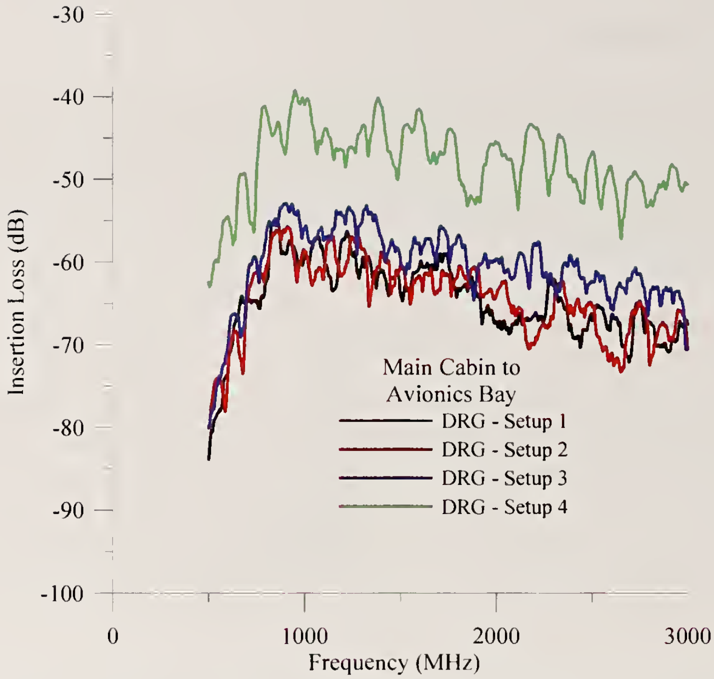


Figure 191. Main cabin to avionics bay DRG antenna insertion loss data at each of the four positions.

The $\chi^2$ *pdf* for all DRG horn antenna measurements is shown in Figure 194 and the $\chi^2$ *cdf* for all DRG horn antenna measurements is shown in Figure 195. The histogram in Figure 194 contains all points binned into 1 dB bins (light-blue bins) and plotted against the theoretical probability density function (dark-blue trace) and the average value of the theoretical data (pink trace). The theoretical average value is around −39 dB. Figure 195 is the data (dark-blue, solid trace) plotted against the theoretical cumulative distribution function. This plot shows that the data do not

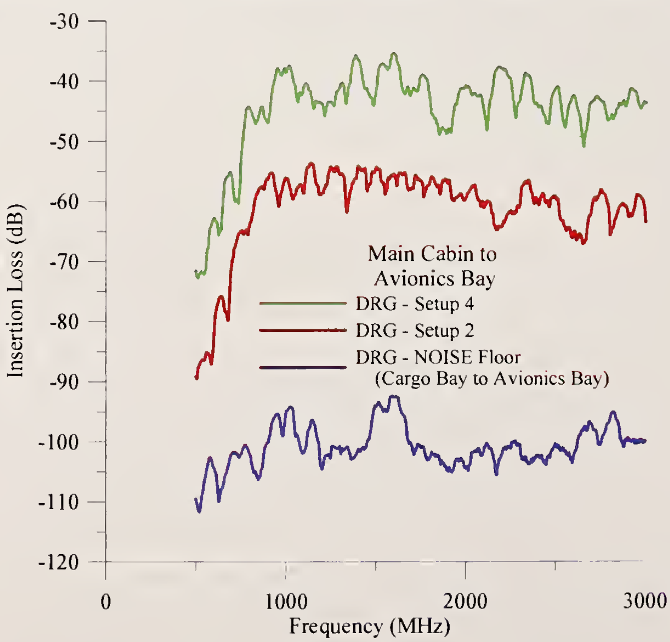


Figure 192. Main cabin to avionics bay DRG horn antenna data for the maximum insertion loss, the minimum insertion loss, and two noise measurements.

tightly follow the theoretical cumulative distribution function. This does not typically seem to be the case for the individual positions.

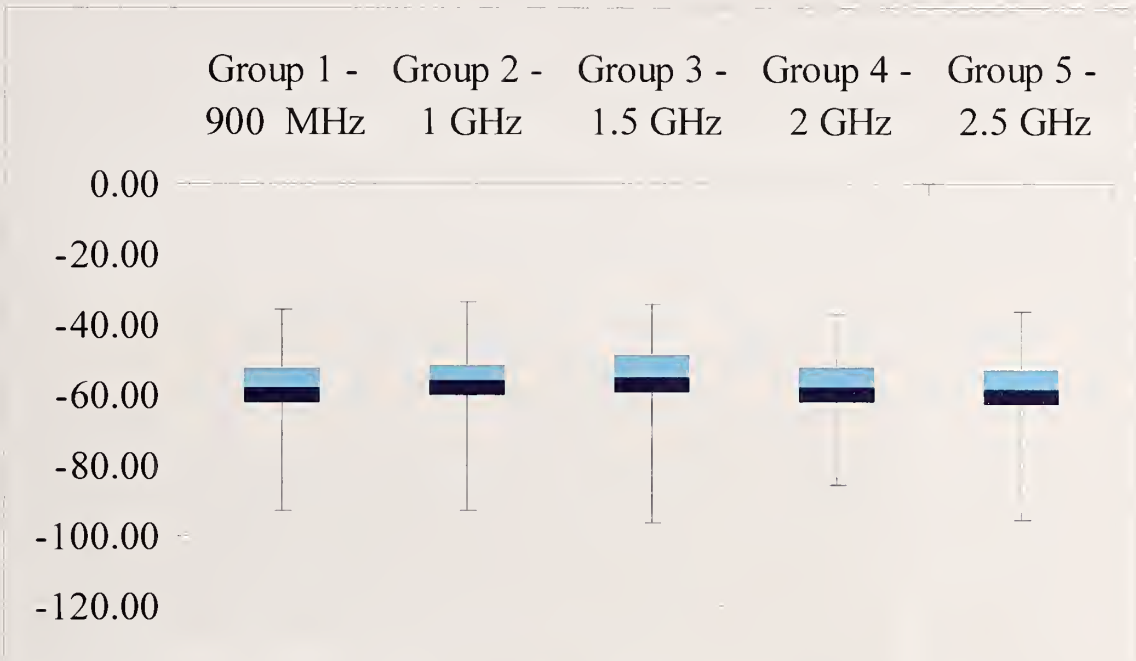


Figure 193. Whisker-box plots of all main cabin to avionics bay insertion loss measurements for the DRG horn antennas at several frequencies.

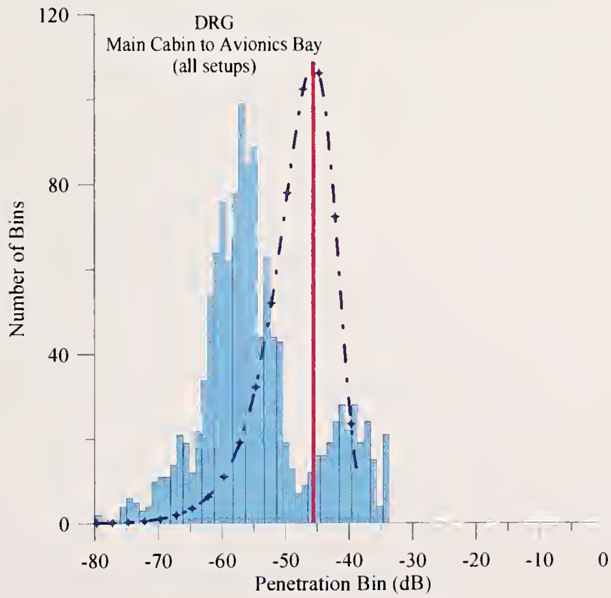


Figure 194. Chi-squared probability density function for all DRG measurements of insertion loss in the main cabin to avionics bay.

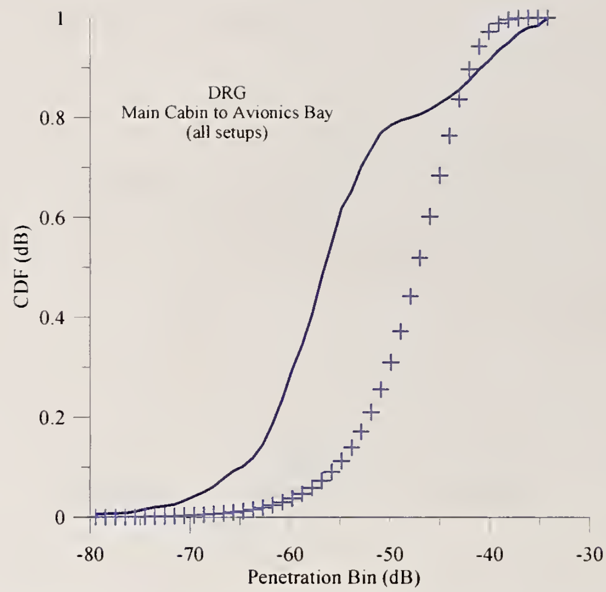


Figure 195. Chi-squared cumulative density function for all DRG measurements of insertion loss in the main cabin to avionics bay.

### 6.4.4.2 Individual DRG horn antenna measurement positions

In this section each measurement position from the main cabin to the avionics bay is individually analyzed. Figures 196 to 203 show a photograph of the locations of the antennas in the flight deck and the main cabin, a time-domain plot, and a schematic of the inside of the 737-200 that indicates where the antennas were placed.

Figure 196 shows the placement of a transmitting DRG horn antenna in the main passenger cabin and a receiving DRG horn antenna in the avionics bay for setup 1, measurements with the avionics bay door open and closed. One vertically polarized antenna was located in the rear of the aircraft on top of the seats of the main passenger cabin and pointed toward the front of the aircraft. The other vertically polarized antenna was located on an insulated cooler and pointed toward the front of the aircraft. A time-domain graph of the measurement for the cargo bay is shown in Figure 197.


Figure 196. Main cabin to avionics bay DRG horn antenna setup 1.

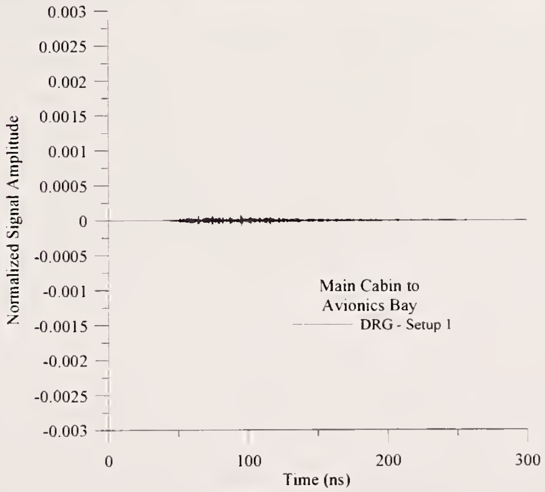


Figure 197. Main cabin to avionics bay DRG horn antenna setup 1, time-domain response.

Figure 198 shows the placement of a transmitting DRG horn antenna in the main passenger cabin and a receiving DRG horn antenna in the avionics bay for setup 2, measurements with the avionics bay door open and closed. One vertically polarized antenna was located in the rear of the aircraft on top of the seats of the main passenger cabin and pointed toward the front of the aircraft. The horizontally polarized other antenna was located on an insulated cooler and pointed toward the front of the aircraft. A time-domain graph of the measurement for the cargo bay is shown in Figure 199.

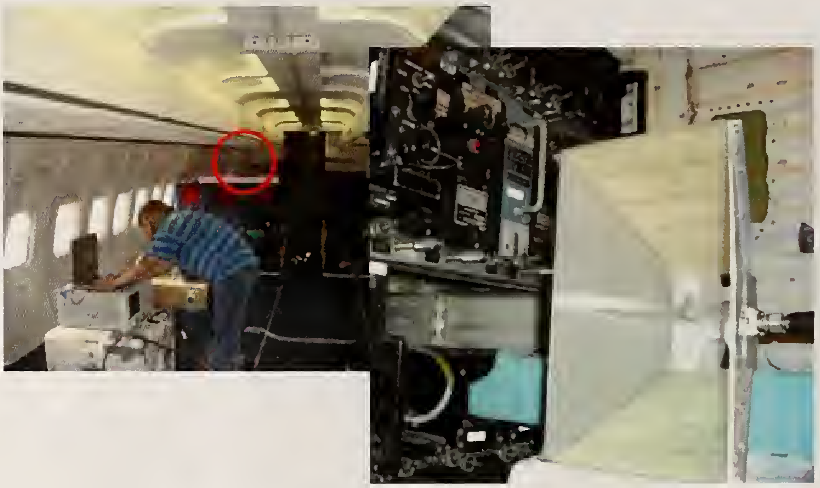

Figure 198. Main cabin to avionics bay DRG horn antenna setup 2.


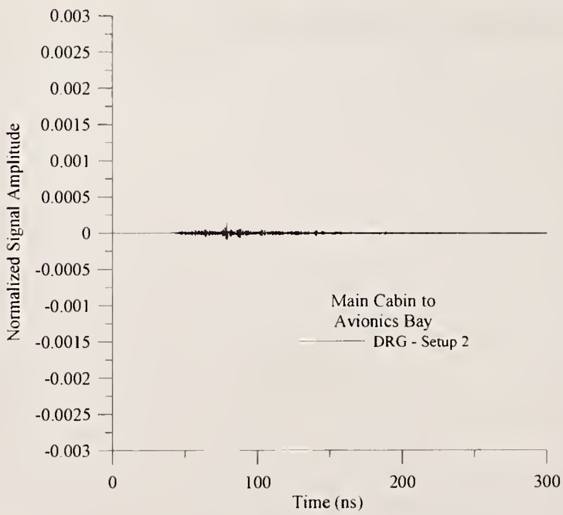


Figure 199. Main cabin to avionics bay DRG horn antenna setup 2, time-domain response.

Figure 200 shows the placement of a transmitting DRG horn antenna in the main passenger cabin and a receiving DRG horn antenna in the avionics bay for setup 3, measurements with the avionics bay door open and closed. One vertically polarized antenna was located in the rear of the aircraft on top of the seats of the main passenger cabin and pointed toward the front of the aircraft. The other antenna was located on an insulated cooler and pointed upward toward avionics bay door. A time-domain graph of the measurement for the cargo bay is shown in Figure 201.

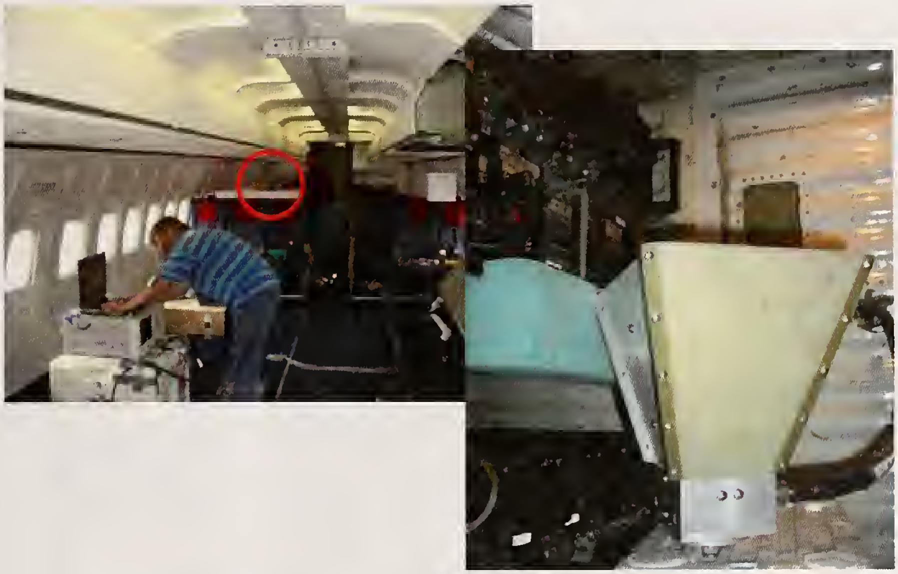


Figure 200. Main cabin to avionics bay DRG horn antenna setup 3.

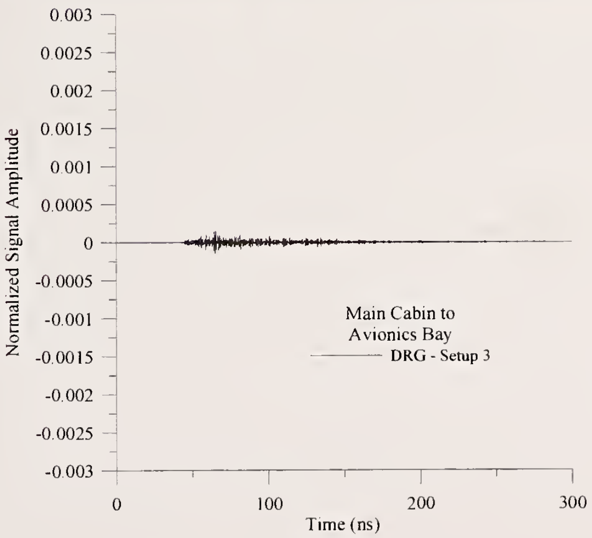


Figure 201. Main cabin to avionics bay DRG horn antenna setup 3, time-domain response.

Figure 202 shows the placement of a transmitting DRG horn antenna in the main passenger cabin and a receiving DRG horn antenna in the avionics bay for setup 4, measurements with the avionics bay door open and closed. One horizontally polarized antenna was located in the first class section on top of the main passenger seats. The antenna pointed toward the front of the aircraft. The other antenna was located on an insulated cooler and pointed upward toward avionics bay door. A time-domain graph of the measurement for the cargo bay is shown in Figure 203.


Figure 202. Main cabin to avionics bay DRG horn antenna setup 4.

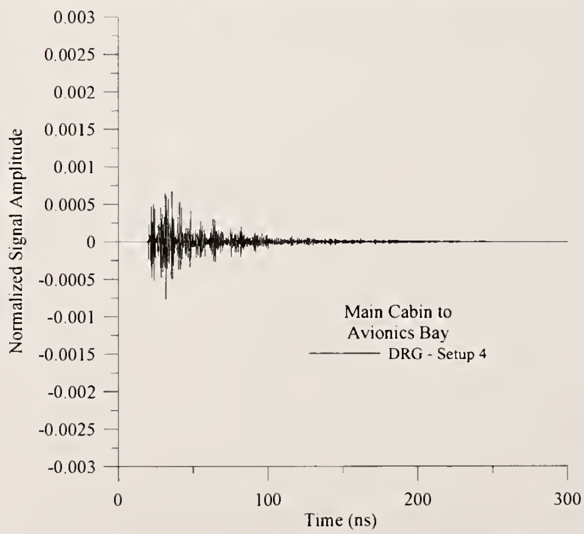


Figure 203. Main cabin to avionics bay DRG horn antenna setup 4, time-domain response.

Figure 204 shows whisker-box plots of each individual setup. The group of data was analyzed around a center frequency of 1000 MHz over a 200 MHz bandwidth containing 321 points. Table 13 summarizes the statistics of each setup for the whisker-box plots, and includes the mean value, the median value, the standard deviation, the maximum value in the group, and the minimum value in the group. Table 14 summarizes the differences between the mean value for the whisker-box plot analysis and the mean value for the $\chi^2$ statistic. The difference between the two means is also displayed. Finally, the $\chi^2$ *pdf* and the $\chi^2$ *cdf* are plotted for each setup in Figure 202.

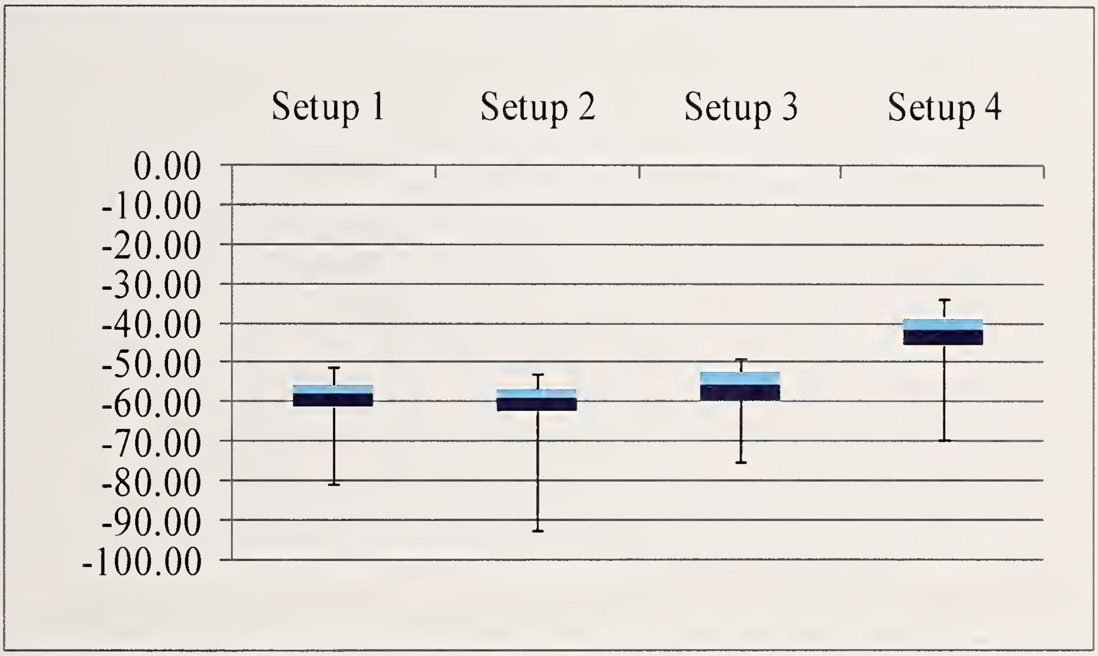


Figure 204. Statistical analysis for DRG horn antenna for main cabin to avionics bay insertion loss for individual setups.

Table 13. DRG Horn internal cabin statistics for measurements from the main cabin to the avionics bay. The sample size was 321 points in a 200 MHz bandwidth around a center frequency of 1 GHz.

| | Setup 1 | Setup 2 | Setup 3 | Setup 4 |
|---|---|---|---|---|
| Mean (dB) | - 59.00 | - 60.41 | - 56.53 | - 42.89 |
| Median (dB) | - 57.86 | - 59.25 | - 55.37 | - 41.51 |
| Standard Deviation (dB) | 5.16 | 5.78 | 5.23 | 6.43 |
| Minimum (dB) | - 80.88 | - 92.70 | - 75.04 | - 69.71 |
| Maximum (dB) | - 51.04 | - 53.00 | - 48.70 | - 33.68 |

Table 14. DRG horn antenna internal cabin $X^2$ - distribution statistics for measurements from the main cabin to the avionics bay.

| | Setup 1 | Setup 2 | Setup 3 | Setup 4 |
|---|---|---|---|---|
| Whisker-Box Plot Mean (dB) | - 59.00 | - 60.41 | - 56.53 | - 42.89 |
| $X^2$ Mean (dB) | - 62.00 | - 57.00 | - 52.00 | - 37.00 |
| $\Delta$ (dB) | + 3.00 | - 3.00 | - 4.00 | - 6.00 |

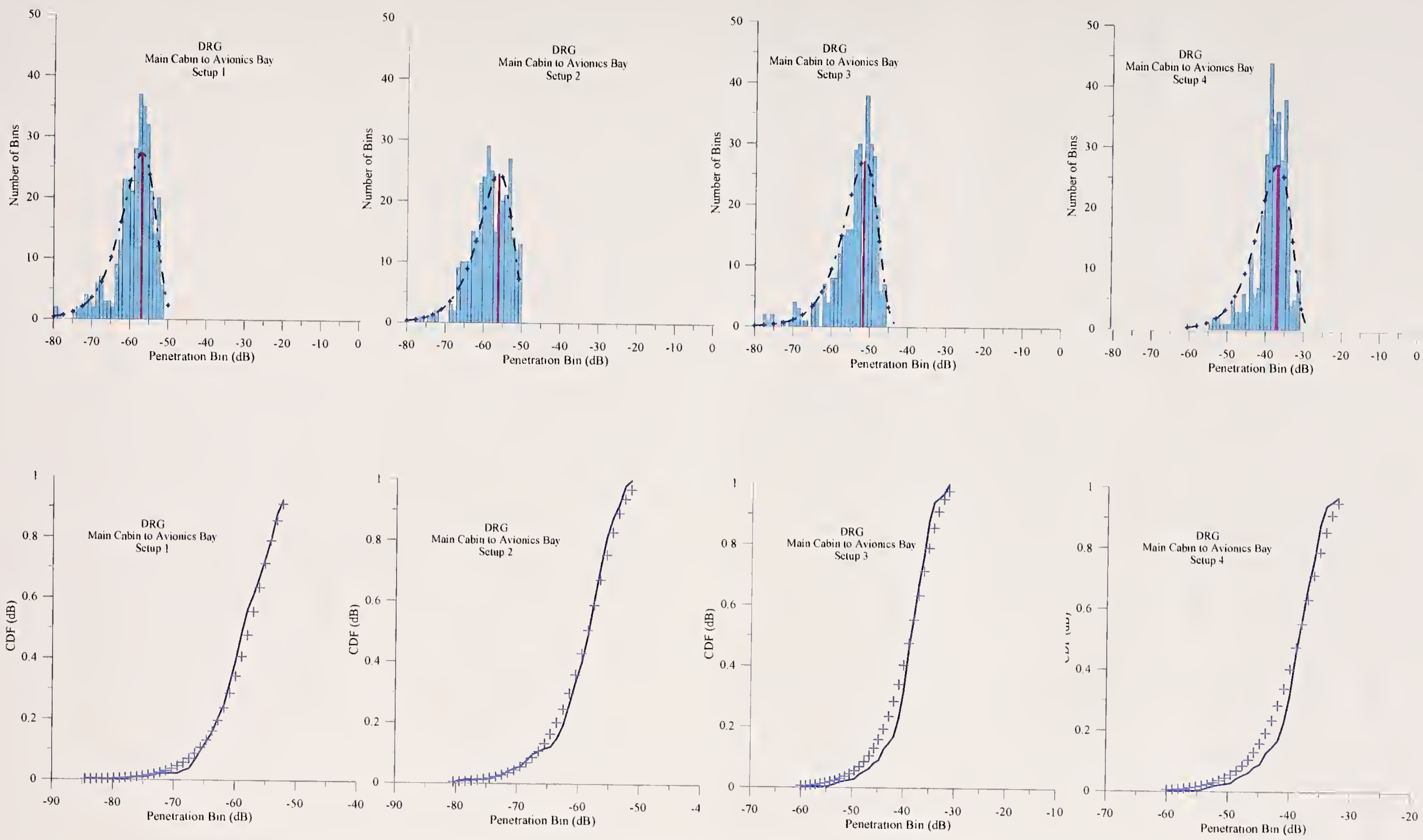


Figure 205. Statistical analysis for DRG horn antenna, for setup1, setup 2, setup 3, and setup 4 for main cabin to avionics bay insertion loss.

### 6.4.4.3 Combined TEM horn antenna positions

Three positions were measured for the TEM horn antenna type. Figure 206 shows results for all measurement results in the main cabin for the TEM horn antenna showing a maximum insertion loss of around −35 dB and a minimum insertion loss of around −60 dB. Figure 207 show results for the maximum cabin insertion loss measurement, the minimum insertion loss measurement, and a system noise floor taken from the cargo bay to the avionics bay.

For the TEM horn antennas, statistics are given for a 200 MHz bandwidth around 900 MHz, 1000 MHz, 1500 MHz, 2000 MHz, and 2500 MHz over all measurement positions as shown in Figure 208. In a 200 MHz bandwidth there are 321 points, so for six measurement positions a total of 2247 points will be in the statistical bandwidth. The maximum insertion loss for these frequencies is approximately −41 dB in a 200 MHz bandwidth around a center frequency of 1000 MHz, and the minimum insertion loss is −156 dB in a 200 MHz bandwidth around a center frequency of 100 MHz.

The $\chi^2$ *pdf* for all TEM horn antenna measurements is shown in Figure 20, and the $\chi^2$ *cdf* for all TEM horn antenna measurements is shown in Figure 210. The histogram in Figure 209 consists of all points binned into 1 dB bins (light-blue bins) and plotted against the theoretical probability density function (dark-blue trace) and the average value of the theoretical data (pink trace). The theoretical average value is around −46 dB. Figure 210 is the data (dark-blue, solid trace) plotted against the theoretical cumulative distribution function.

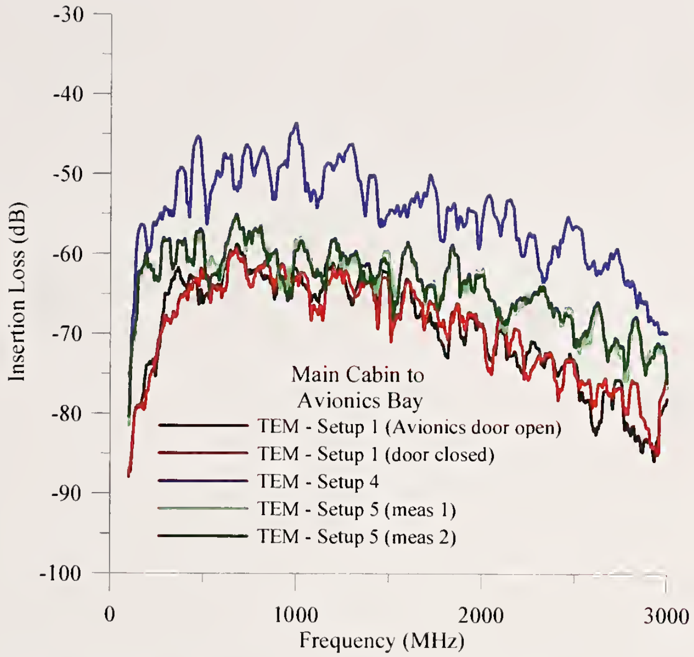


Figure 206. Main cabin to avionics bay TEM antenna insertion loss data at each of the three positions, with two additional measurements.

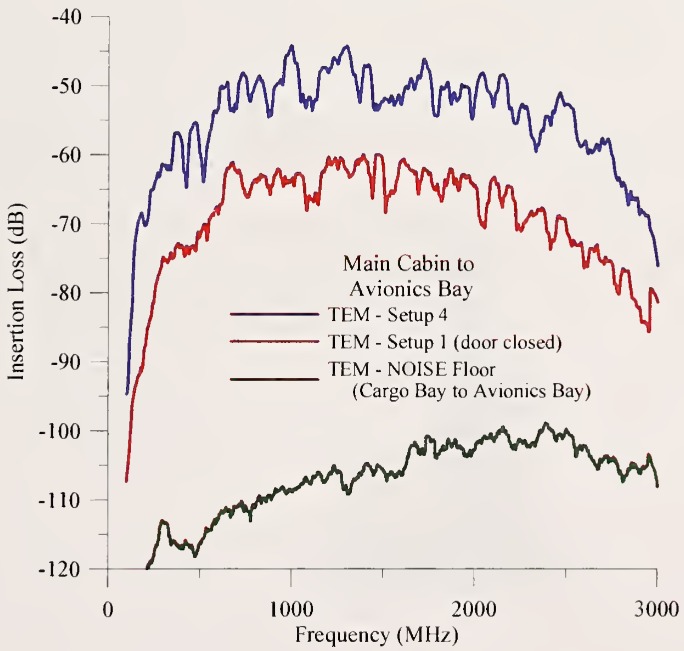


Figure 207. Main cabin to avionics bay TEM horn antenna data for the maximum insertion loss, the minimum insertion loss, and two noise measurements.

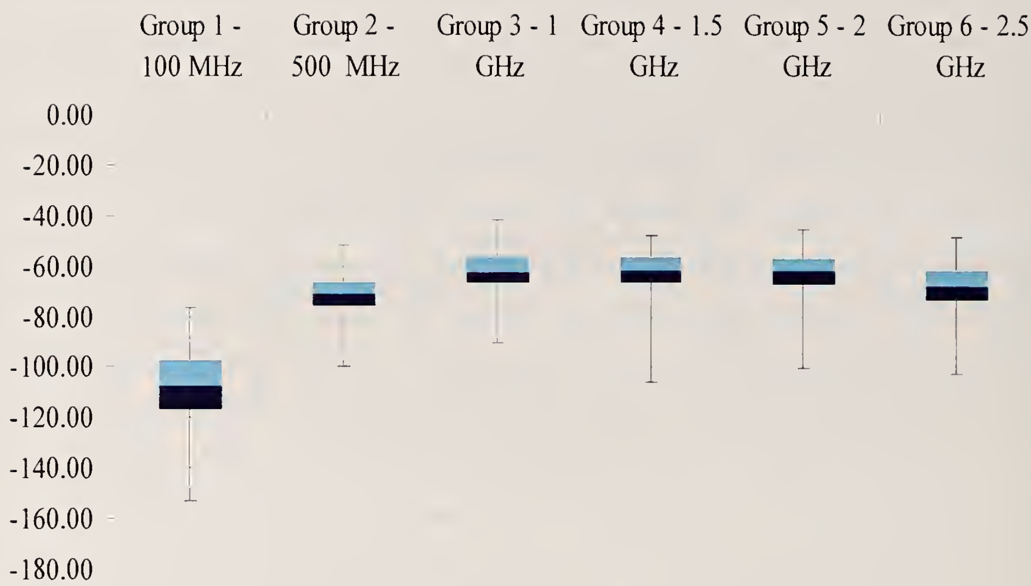


Figure 208. Whisker-box plots of all main cabin to avionics bay insertion loss measurements for the TEM horn antennas at several frequencies.

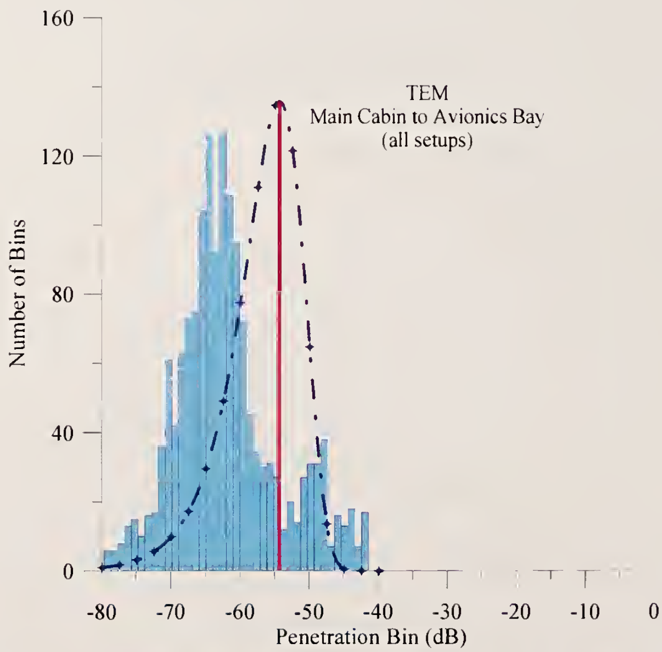


Figure 209. Chi-squared probability density function for all TEM measurements of insertion loss in the main cabin to avionics bay.

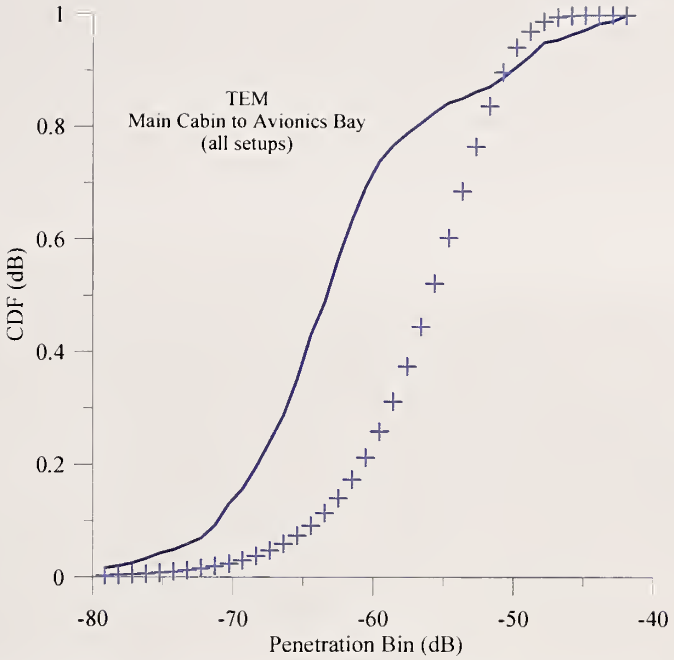


Figure 210. Chi-squared cumulative density function for all TEM measurements of insertion loss in the main cabin to avionics bay.

### 6.4.4.4 Individual TEM horn antenna positions

A photograph for each TEM antenna measurement location from the main cabin to the cargo bay, its associated time-domain waveform, and a schematic showing the antenna positions inside the aircraft is shown from Figure 211 to Figure 216.

Figure 211 shows the placement of a transmitting 1.2 m TEM horn antenna in the main passenger cabin and a receiving 36 cm TEM horn antenna in the avionics bay for setup 1, for measurements with the avionics bay door open and closed. The vertically polarized 1.2 m TEM horn antenna was located in the rear of the aircraft across the seats and pointed forward toward the windows. The vertically polarized 36 cm TEM horn antenna was located on an insulated cooler and pointed toward the front of the aircraft. A time-domain graph of the measurement is shown in Figure 212.

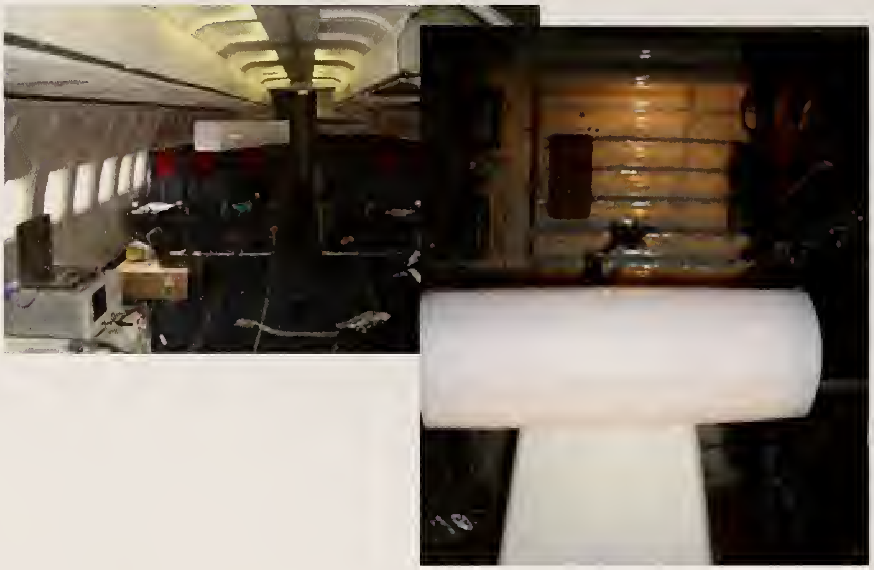


Figure 211. Main cabin to avionics bay TEM horn antenna setup 1.

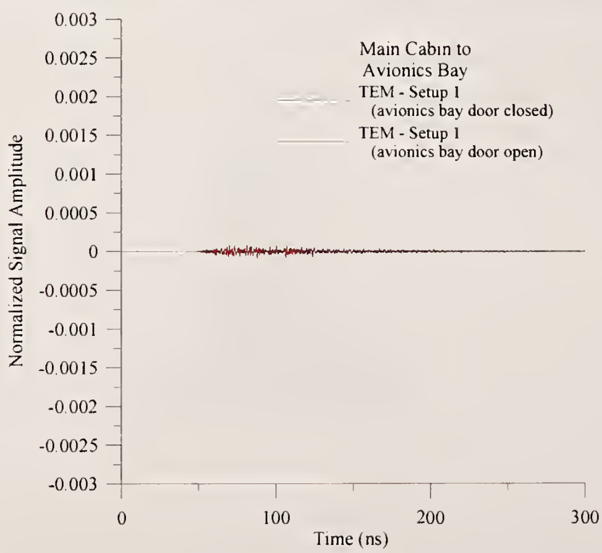


Figure 212. Main cabin to avionics bay TEM horn antenna setup 1, time-domain response.

Figure 213 shows the placement of a transmitting 1.2 m TEM horn antenna in the main passenger cabin and a receiving 36 cm TEM horn antenna in the avionics bay for setup 4. The horizontally polarized 1.2 m TEM horn antenna was located in the first-class section on top of the main passenger seats. The 36 cm TEM horn antenna was located on an insulated cooler and pointed upward toward avionics bay door. A time-domain graph of the measurement is shown in Figure 214.



Figure 213. Main cabin to avionics bay TEM horn antenna setup 4.

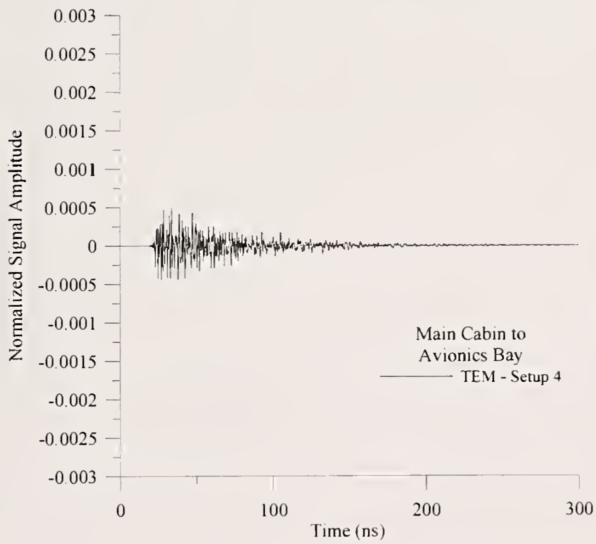


Figure 214. Main cabin to avionics bay TEM horn antenna setup 4, time-domain response.

Figure 215 shows the placement of a transmitting 1.2 m TEM horn antenna in the main passenger cabin and a receiving 36 cm TEM horn antenna in the avionics bay for setup 5, measurements 1 and 2. The 1.2 m TEM horn antenna was located on the floor in the rear of the aircraft and pointed forward down the aisle. The 36 cm TEM horn antenna was located on an insulated cooler and pointed upward toward the avionics bay door. A time-domain graph of the measurement is shown in Figure 216.

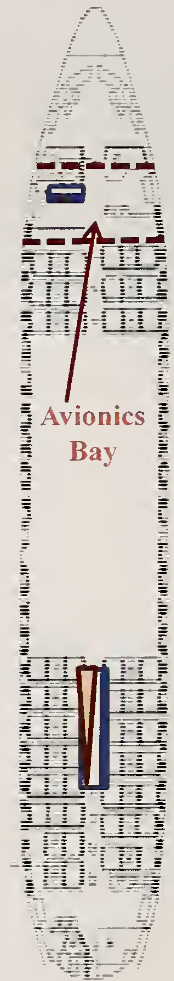


Figure 215. Main cabin to avionics bay TEM horn antenna setup 5.

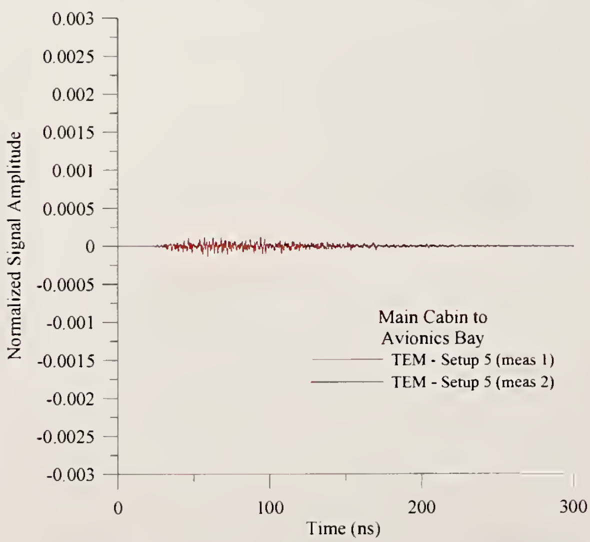


Figure 216. Main cabin to avionics bay TEM horn antenna setup 5, time-domain response.

Figure 217 shows whisker-box plots of each individual setup. The group of data was analyzed around a center frequency of 1000 MHz over a 200 MHz bandwidth containing 321 points. Table 15 summarizes the statistics of each setup for the whisker-box plots, and includes the mean value, the median value, the standard deviation, the maximum value in the group, and the minimum value in the group. Table 16 summarizes the differences between the mean value for the whisker-box plot analysis and the mean value for the $\chi^2$ statistic. The difference between the two means is also displayed. Finally, the $\chi^2$ *pdf* and the $\chi^2$ *cdf* are plotted for each setup in Figure 218 and Figure 219.

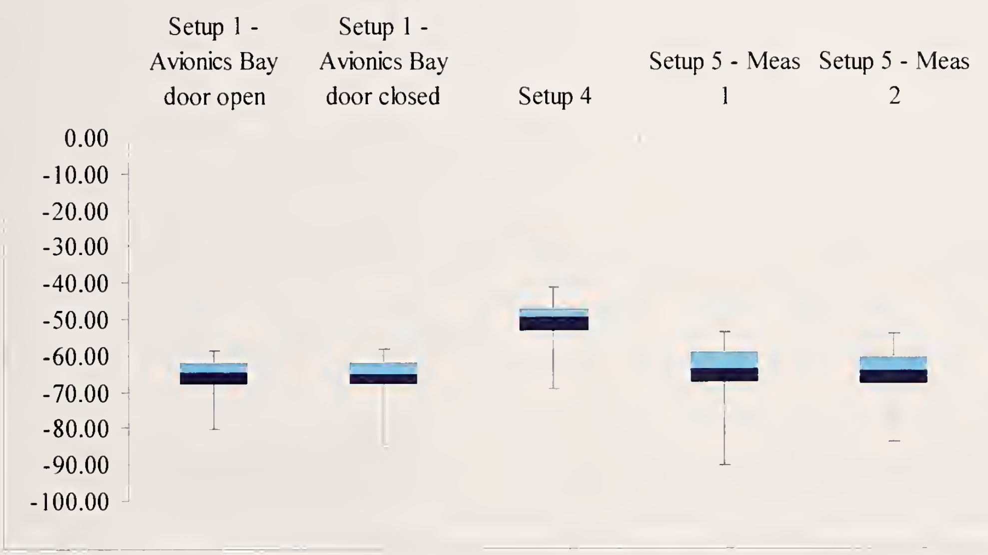


Figure 217. Statistical analysis for TEM horn antennas for main cabin to avionics bay insertion loss for individual setups.

Table 15. TEM Horn internal cabin statistics for measurements from the main cabin to the avionics bay. The sample size was 321 points in a 200 MHz bandwidth around a center frequency of 1 GHz.

| | Setup 1 Avionics Bay door open | Setup 1 Avionics Bay door closed | Setup 4 | Setup 5 meas 1 | Setup 5 meas 2 |
|---|---|---|---|---|---|
| Mean (dB) | − 65.11 | − 65.47 | − 50.85 | − 63.93 | − 64.72 |
| Median (dB) | − 64.48 | − 64.98 | − 49.75 | − 63.66 | − 64.04 |
| Standard Deviation (dB) | 3.88 | 4.86 | 6.03 | 5.98 | 6.11 |
| Minimum (dB) | − 80.25 | − 85.51 | − 69.11 | − 90.38 | − 83.74 |
| Maximum (dB) | − 58.63 | − 58.29 | − 41.41 | − 53.59 | − 54.13 |

Table 16. TEM horn antenna internal cabin $X^2$ - distribution statistics for measurements from the main cabin to the avionics bay.

| | Setup 1 Avionics Bay door open | Setup 1 Avionics Bay door closed | Setup 4 | Setup 5 meas 1 | Setup 5 meas 2 |
|---|---|---|---|---|---|
| Whisker-Box Plot Mean (dB) | − 65.11 | − 65.47 | − 50.85 | − 63.93 | − 64.72 |
| $X^2$ Mean (dB) | − 62.00 | − 62.00 | − 51.00 | − 58.00 | − 62.00 |
| $\Delta$ (dB) | − 3.00 | − 3.00 | < 1.00 | − 6.00 | − 3.00 |

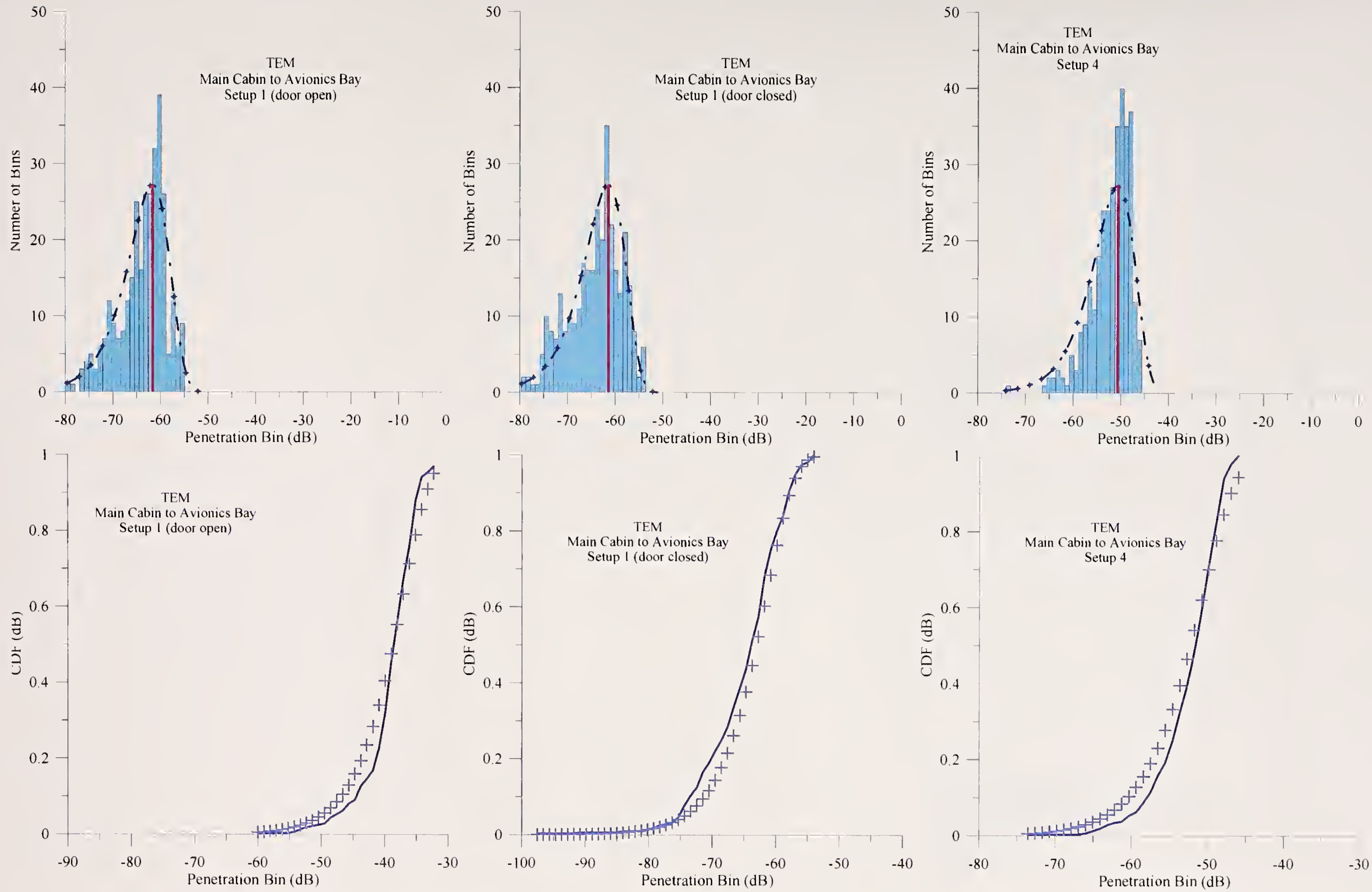


Figure 218. Statistical analysis for TEM horn antenna, setup 1 (avionics bay door open and closed), and setup 4 for main cabin to avionics bay insertion loss.

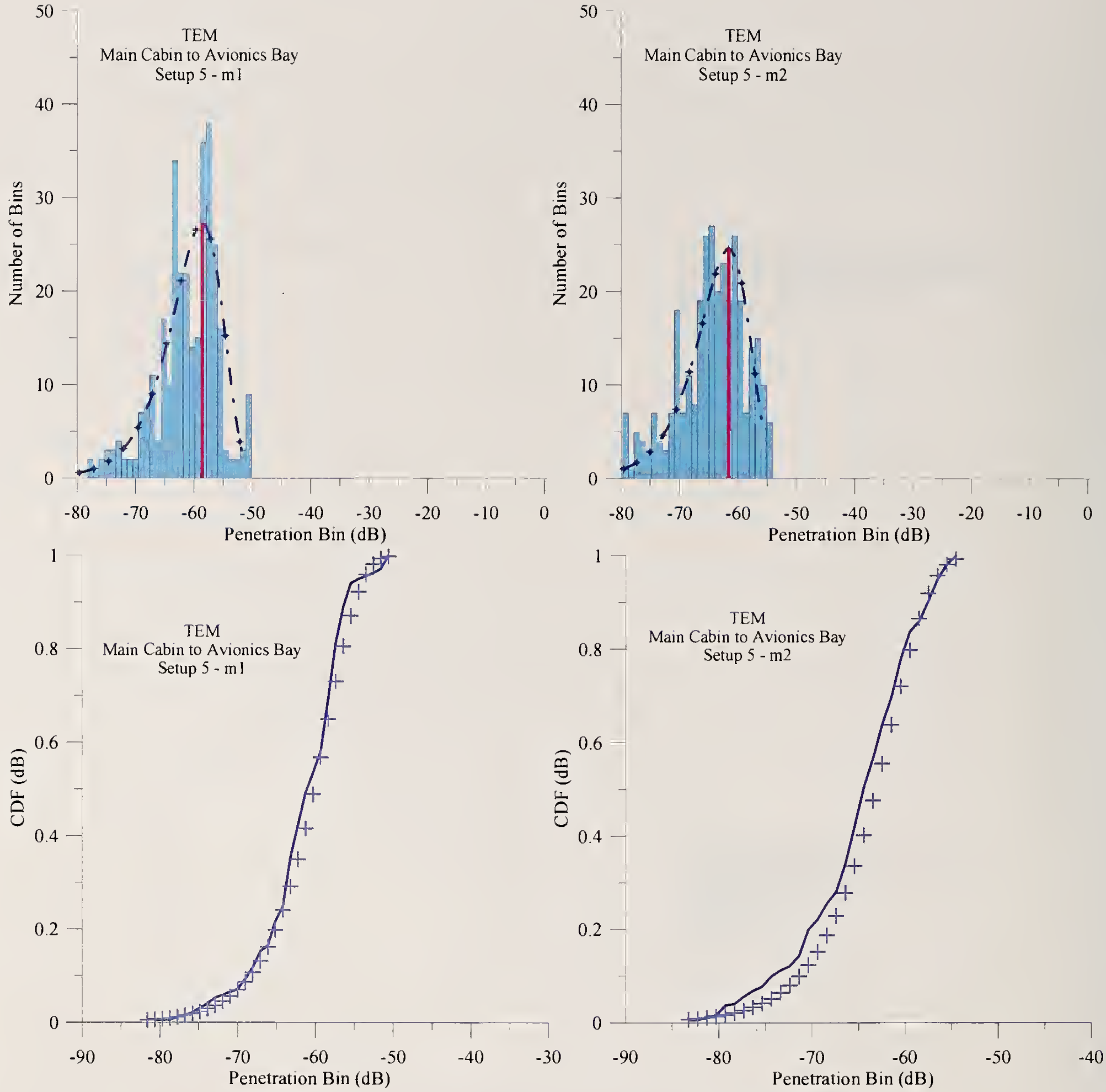


Figure 219. Statistical analysis for TEM horn antenna, setup 5-measurement 1 and 2, for main cabin to avionics bay insertion loss.

### 6.4.5 Cargo Bay to Avionics Bay

The DRG and TEM horn antennas were measured at various positions between the cargo bay and the avionics bay. The VNA was placed inside the cargo bay and an RF cable was run from the cargo bay to the avionics bay. In general, for each compartment-to-compartment measurement we tried to position the antennas in approximately the same position for each of these runs.

#### 6.4.5.1 Combined TEM horn antenna positions

Three positions were measured for the TEM horn antenna type and three repeat measurements were taken at one location. Figure 220 shows the data for the TEM horn antennas for the maximum cabin insertion loss and a system noise floor. Typically the noise floor drops when we place the antennas in compartments that have fewer leakage paths due to extra shielding that occurs from the outside environment. Figure 221 shows maximum insertion loss for the TEM horn antennas around −40 dB dropping to a minimum insertion loss of −80 dB. The TEM horn antennas were then left in one orientation and were remeasured three times to determine system variability as shown in Figure 221. Figure 222 shows the data for three different measurements at different orientations in the two compartments.

Whisker-box plots are shown in Figure 223 for the following center frequencies, (1) 100 MHz, (2) 500 MHz, (3) 1000 MHz, (4) 1500 MHz, (5) 2000 MHz, and (6) 2500 MHz. Data in these plots are from a 200 MHz bandwidth around each center frequency. The plots show that the median insertion loss for these frequencies have values from about −58 dB to −90 dB. The maximum value for these frequencies is approximately −50 dB in a 200 MHz bandwidth around a center frequency of 1500 MHz, and the minimum insertion loss is −118 dB in a 200 MHz bandwidth around center frequencies of 900 MHz.

The $\chi^2$ *pdf* for all DRG horn antenna measurements is shown in Figure 224 and the $\chi^2$ *cdf* for all TEM horn antenna measurements is shown in Figure 225. The histogram in Figure 224 consists of all points binned into 1 dB bins (light-blue bins) and plotted against the theoretical probability density function (dark-blue trace) and the average value of the theoretical data (pink trace). The theoretical average value is around −57 dB. Figure 225 is the data (dark-blue, solid trace) plotted against the theoretical cumulative distribution function.

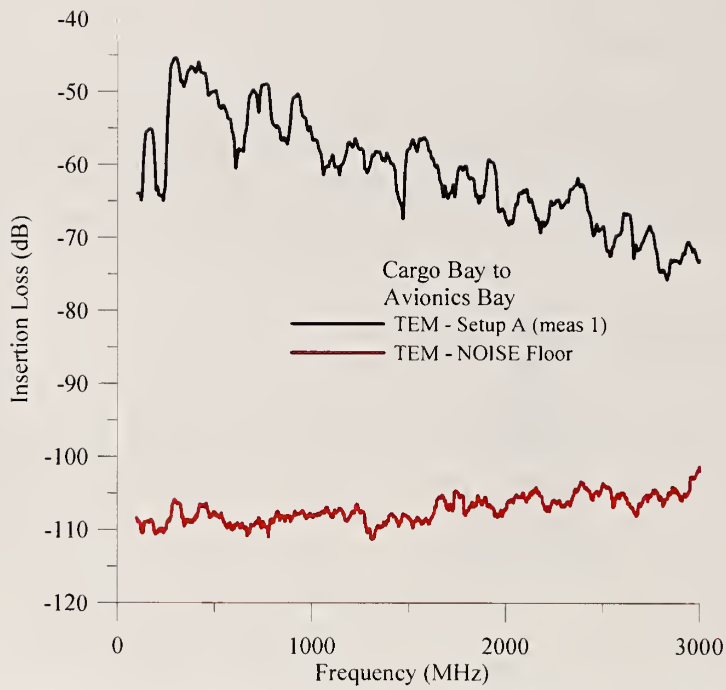


Figure 220. Cargo bay to avionics bay TEM antenna data for the maximum insertion loss and a system noise measurement.

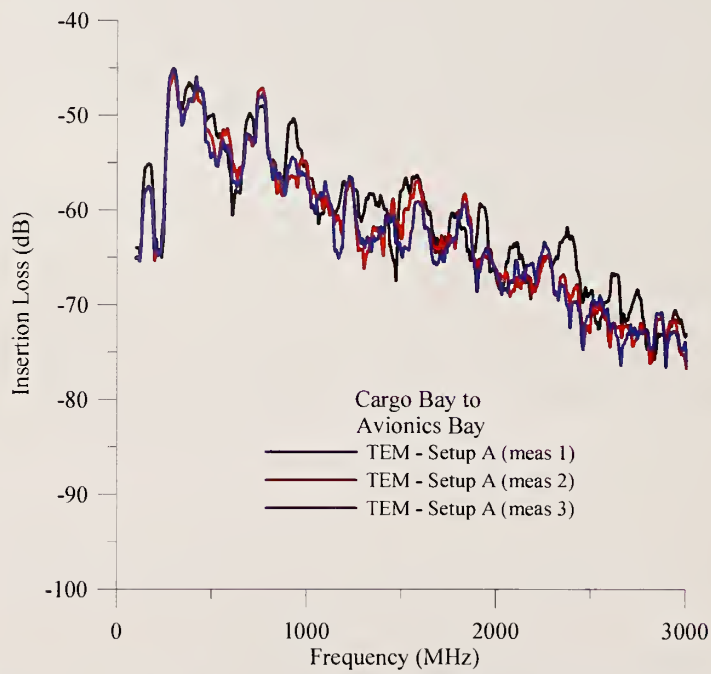


Figure 221. Cargo bay to avionics bay TEM horn antenna data insertion loss data at each of the three positions.

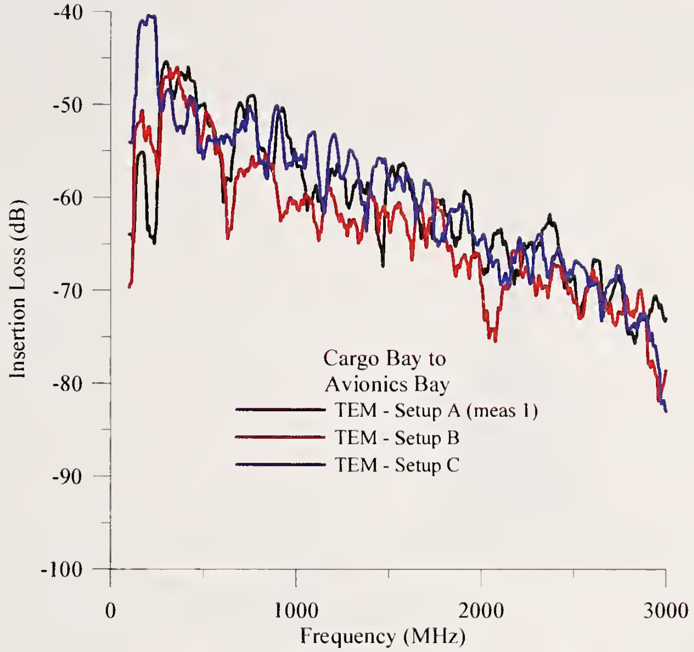


Figure 222. Cargo bay to avionics bay TEM horn antenna data insertion loss data at one position for three independent measurements.

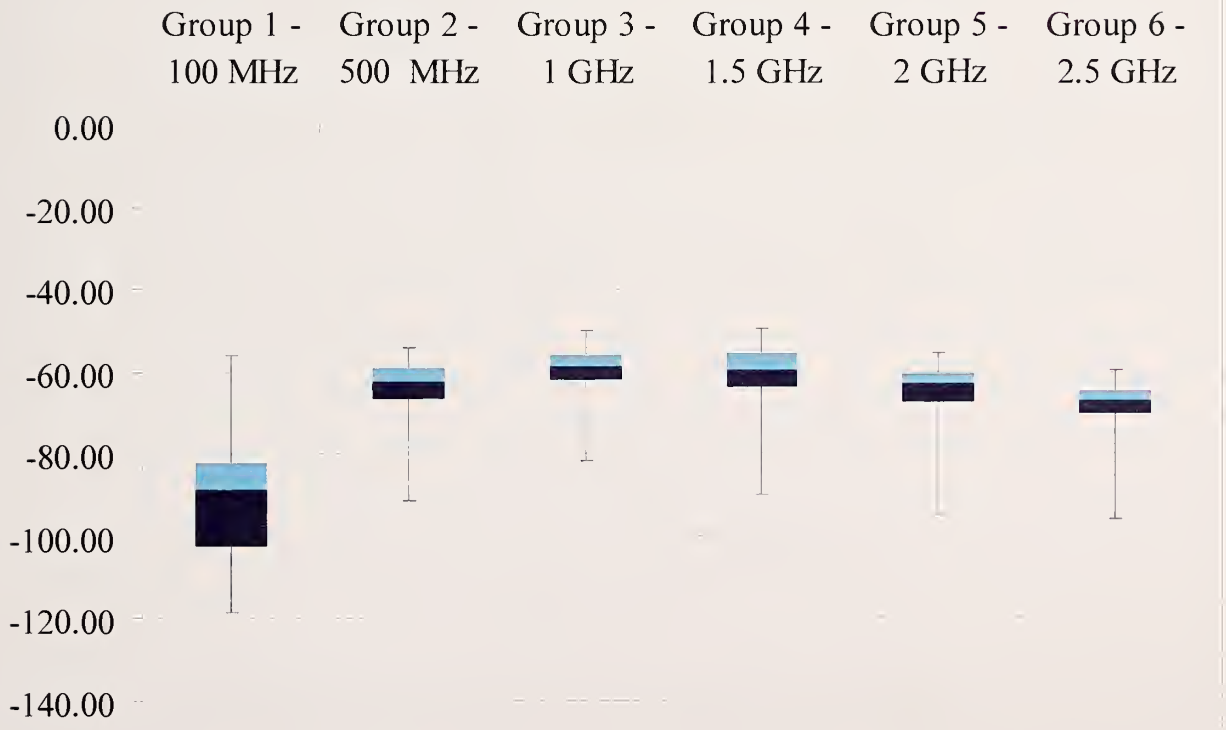


Figure 223. Whisker-box plots for all cargo bay to avionics bay insertion loss measurements of the TEM horn antennas at several frequencies.

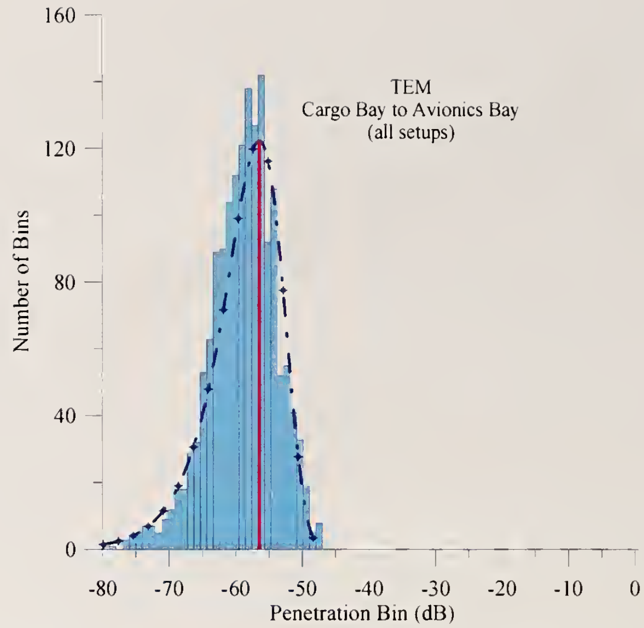


Figure 224. Chi-squared probability density function for all TEM measurements of insertion loss in the cargo bay to the avionics bay.

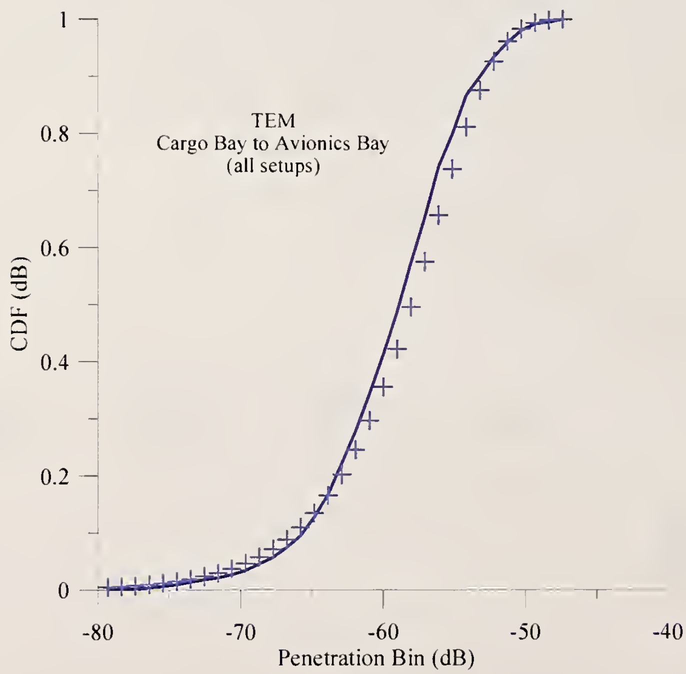


Figure 225. Chi-squared cumulative density function for all TEM measurements of insertion loss in the cargo bay to the avionics bay.

### 6.4.5.2 Individual TEM horn antenna positions

Photographs for each TEM antenna measurement location from the main cabin to the cargo bay, its associated time-domain waveform, and a schematic showing the antenna positions inside the aircraft are shown from Figure 226 to Figure 231.

Figure 226 shows the placement of a transmitting 1.2 m TEM horn antenna in the cargo bay and a receiving 36 cm horn antenna in the avionics bay for setup A, measurements 1, 2, and 3. The 1.2 m TEM horn antenna was located in the forward section of the cargo bay close to the avionics bay propped on a box pointed toward the rear back corner of the cargo bay with a mixed polarization. The vertically polarized 36 cm antenna was located on an insulated cooler pointing toward the front of the aircraft. A time-domain graph of all three measurements for position A for the cargo bay to avionics bay is shown in Figure 227. Traces 2 and 3 were offset, in the positive y-direction, from measurement 1 to compare differences between the repeat measurements.

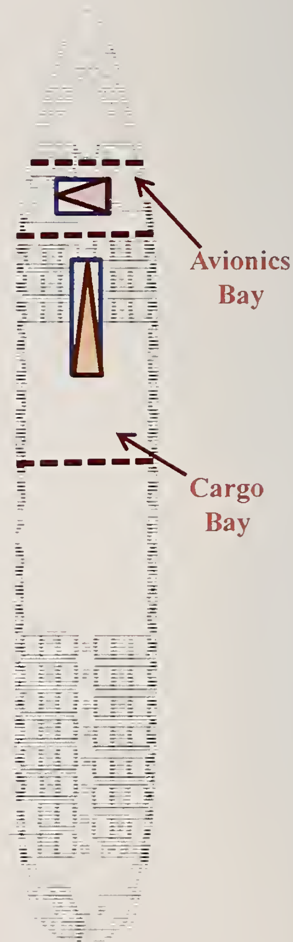


Figure 226. Cargo bay to avionics bay TEM horn antenna setup A.

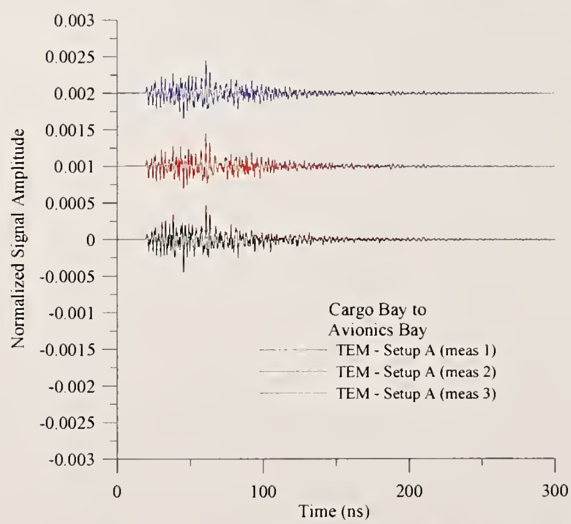


Figure 227. Cargo bay to avionics bay TEM horn antenna setup A, time-domain response.

Figure 228 shows the placement of a transmitting 1.2 m TEM horn antenna in the cargo bay and a receiving 36 cm TEM horn antenna in the avionics bay for setup B. The 1.2 m antenna was located in the forward section of the cargo bay close to the avionics bay and propped above the floor on a cargo net pointing toward the main passenger cabin floor. The horizontally polarized 36 cm antenna was located on the floor in the avionics bay. A time-domain graph of the measurement is shown in Figure 229.

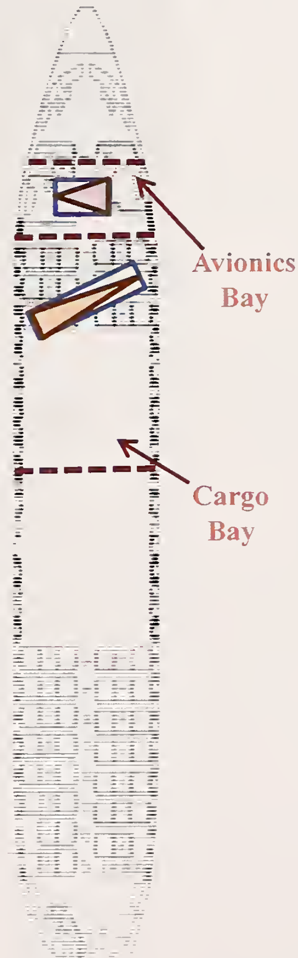


Figure 228. Cargo bay to avionics bay TEM horn antenna setup B.

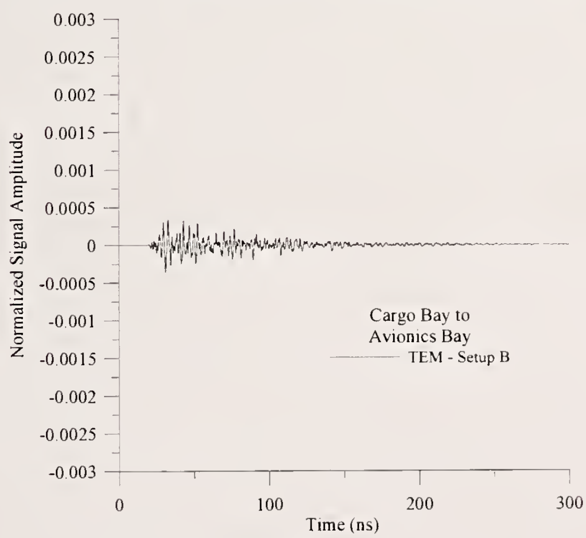


Figure 229. Cargo bay to avionics bay TEM horn antenna setup B, time-domain response.

Figure 230 shows the placement of a transmitting 1.2 m TEM horn antenna in the cargo bay and a receiving 36 cm TEM horn antenna in the avionics bay for setup C. The 1.2 m TEM horn antenna was located in the middle part of the cargo bay and pointed toward the avionics bay. The 36 cm TEM horn antenna was placed on the floor of the avionics bay and pointed down toward the floor. A time-domain graph of the measurement is shown in Figure 231.

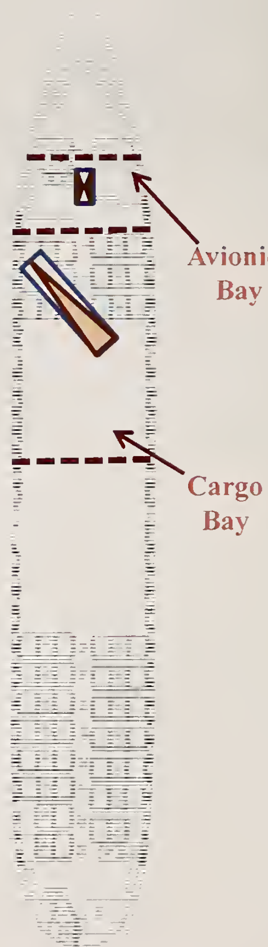


Figure 230. Cargo bay to avionics bay TEM horn antenna setup C.

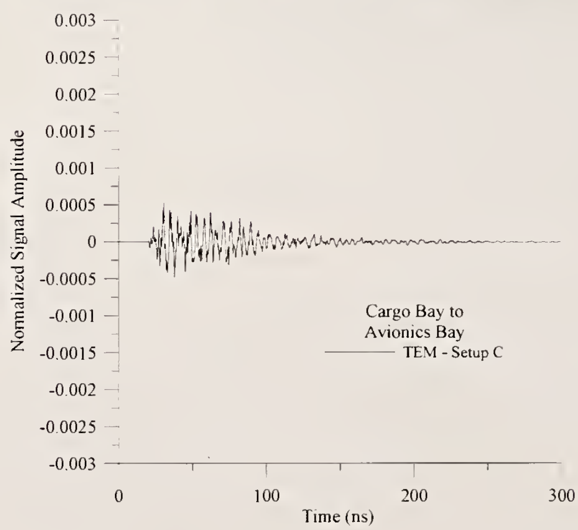


Figure 231. Cargo bay to avionics bay TEM horn antenna setup C, time-domain response.

Figure 232 shows whisker-box plots of each individual setup. The group of data was analyzed around a center frequency of 1000 MHz over a 200 MHz bandwidth containing 321 points. Table 17 summarizes the statistics of each setup for the whisker-box plots, and includes the mean value, the median value, the standard deviation, the maximum value in the group, and the minimum value in the group. Table 18 summarizes the differences between the mean value for the whisker-box plot analysis and the mean value for the $\chi^2$ statistic. The difference between the two means is also displayed. Finally, the $\chi^2$ *pdf* and the $\chi^2$ *cdf* are plotted for each setup in Figure 233 and Figure 234.

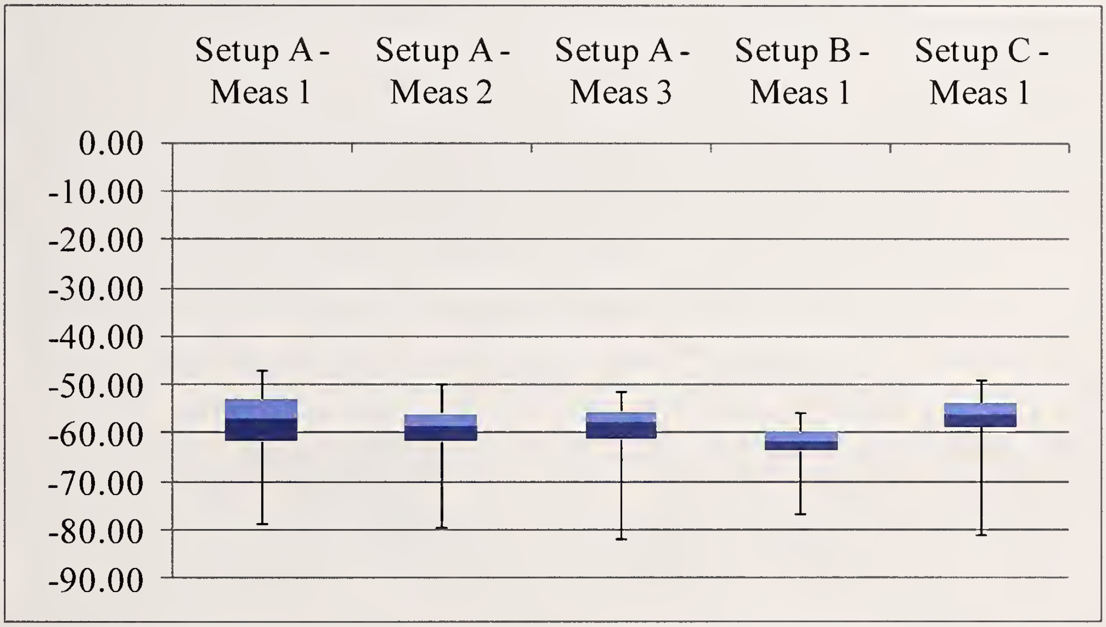


Figure 232. Statistical analysis for TEM horn antenna, setup A (measurements 1, 2, 3), setup B and setup C for cargo bay to avionics bay insertion loss.

Table 17. TEM Horn internal cabin statistics for measurements from the cargo bay to the avionics bay. The sample size was 321 points in a 200 MHz bandwidth around a center frequency of 1 GHz.

| | Setup A meas 1 | Setup A meas 2 | Setup A meas 3 | Setup B | Setup C |
|---|---|---|---|---|---|
| Mean (dB) | − 57.73 | − 59.10 | − 58.89 | − 61.12 | − 56.59 |
| Median (dB) | − 56.98 | − 58.53 | − 57.72 | − 61.67 | − 56.10 |
| Standard Deviation (dB) | 5.99 | 4.56 | 4.66 | 3.50 | 4.63 |
| Minimum (dB) | − 78.56 | − 79.57 | − 81.70 | − 76.72 | − 81.12 |
| Maximum (dB) | − 46.97 | − 49.85 | − 51.22 | − 55.94 | − 48.84 |

Table 18. TEM horn antenna internal cabin $X^2$-distribution statistics for measurements from the cargo bay to the avionics bay.

| | Setup A meas 1 | Setup A meas 2 | Setup A meas 3 | Setup B | Setup C |
|---|---|---|---|---|---|
| Whisker-Box Plot Mean (dB) | − 57.73 | − 59.10 | − 58.89 | − 61.12 | − 56.59 |
| $X^2$ Mean (dB) | − 55.00 | − 60.00 | − 59.00 | − 59.00 | − 57.00 |
| Δ (dB) | − 3.00 | + 1.00 | < 1.00 | − 2.00 | < 1.00 |

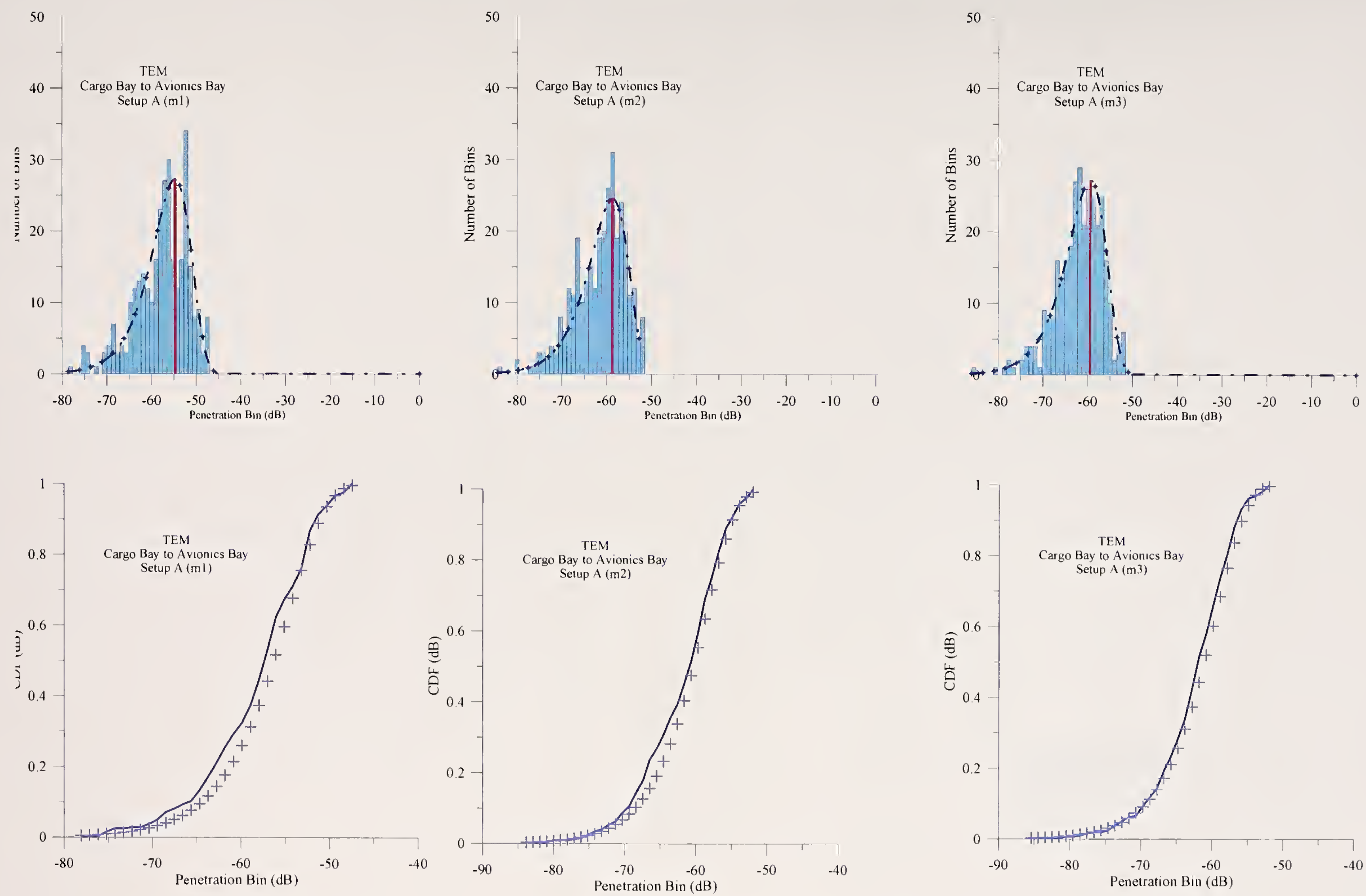


Figure 233. Statistical analysis for TEM horn antenna, setup A (measurements 1, 2, 3), for cargo bay to avionics bay insertion loss.

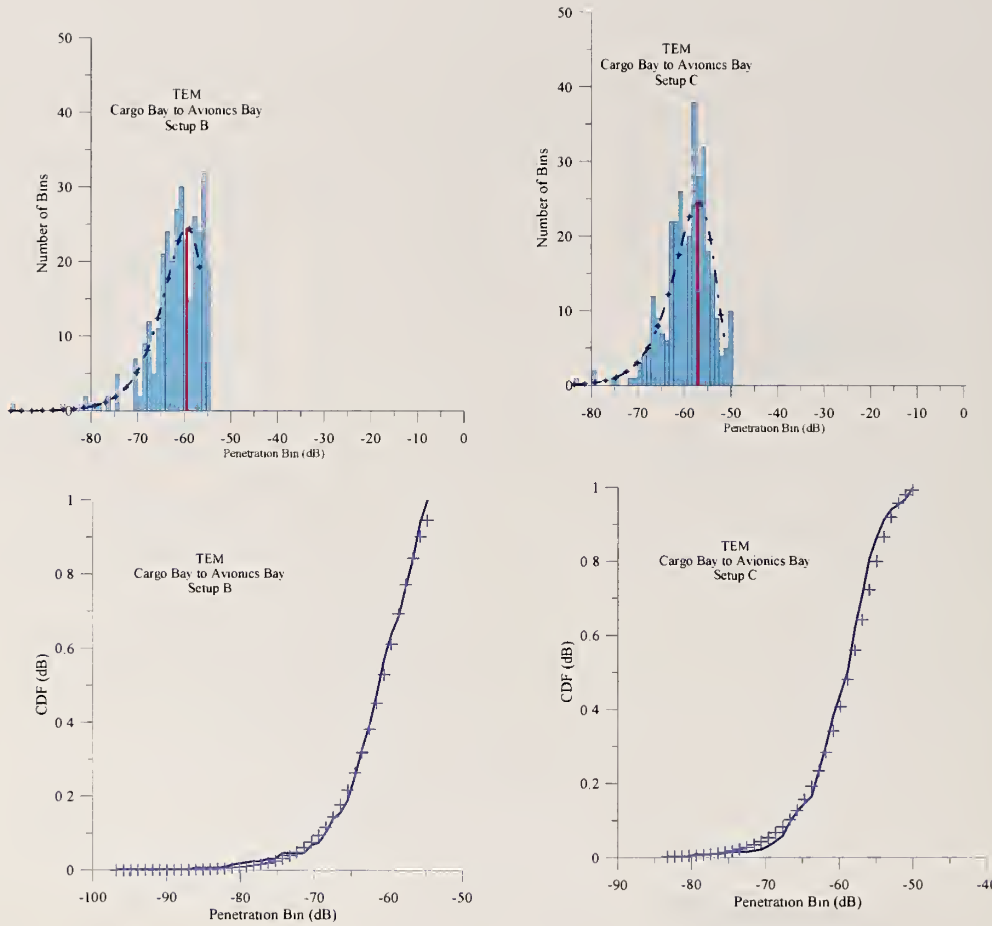


Figure 234. Statistical analysis for TEM horn antenna, setup B and setup C for cargo bay to avionics bay insertion loss.

#### 6.4.5.3 Combined DRG horn antenna positions

Three positions were measured for the DRG antenna and three repeat measurements were taken at one location. Figure 235 shows the data for the DRG horn antennas for the maximum cabin insertion loss and a system noise floor. Typically the noise floor drops when the antennas were placed in compartments that have fewer leakage paths due to extra shielding that occurs from the outside environment. Figure 236 shows maximum insertion loss for the DRG horn antennas around −45 dB dropping to minimum insertion loss of −65 dB. The DRG horn antennas were then left in one orientation and were remeasured three times to determine system variability, as shown in Figure 236. Figure 237 shows the data for three different measurements at different orientations in the two compartments.

Whisker-box plots are shown in Figure 238 for the following center frequencies, (1) 100 MHz, (2) 500 MHz, (3) 1000 MHz, (4) 1500 MHz, (5) 2000 MHz, and (6) 2500 MHz. Data in these plots are from a 200 MHz bandwidth around each center frequency. The plots show that the median insertion loss for these frequencies has values from about −50 dB to −55 dB. The maximum value for these frequencies is approximately −35 dB in a 200 MHz bandwidth around a center frequency of 1500 MHz, and the minimum insertion loss is −93 dB in a 200 MHz bandwidth around center frequencies of 900 MHz and 1000 MHz.

The $\chi^2$ *pdf* for all DRG horn antenna measurements is shown in Figure 239 and the $\chi^2$ *cdf* for all TEM horn antenna measurements is shown in Figure 240. The histogram in Figure 239 consists of all points binned into 1 dB bins (light-blue bins) and plotted against the theoretical probability density function (dark-blue trace) and the average value of the theoretical data (pink trace). The theoretical average value is around −47 dB. Figure 240 is the data (dark-blue, solid trace) plotted against the theoretical cumulative distribution function.

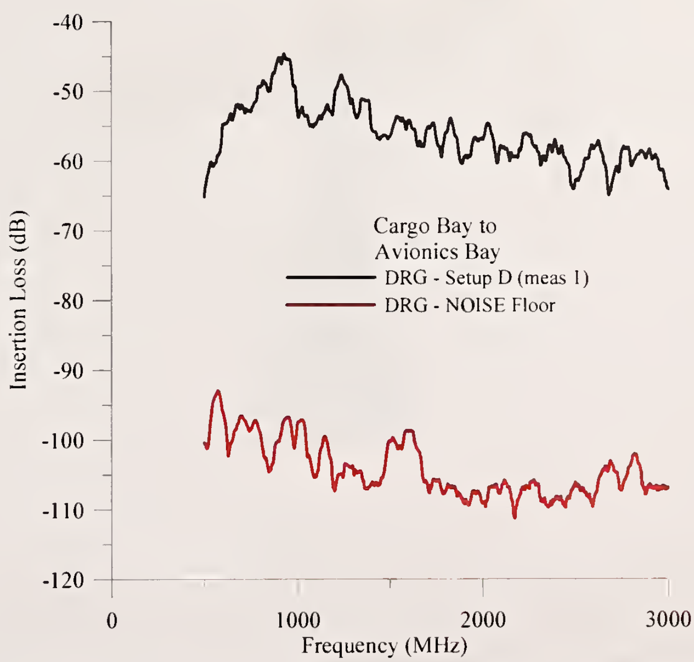


Figure 235. Cargo bay to avionics bay DRG antenna data for the maximum insertion loss and a system noise measurement.

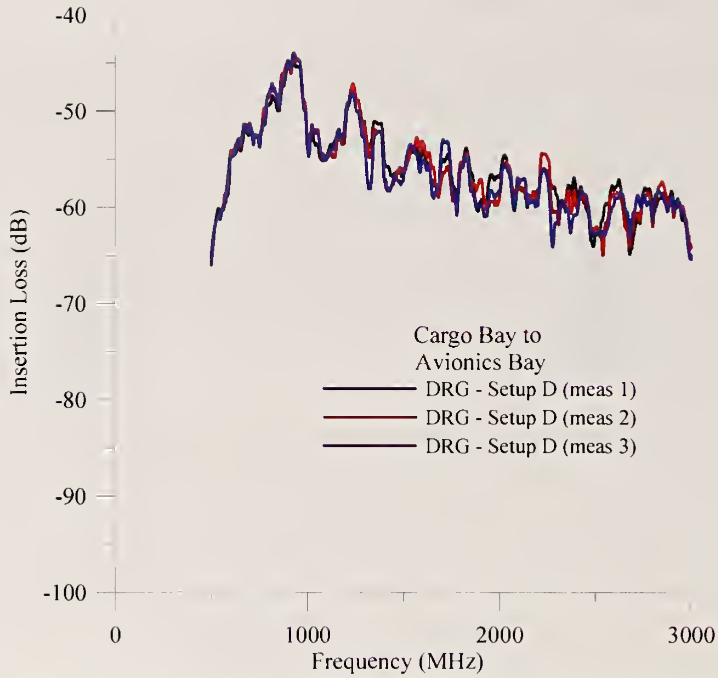


Figure 236. Cargo bay to avionics bay DRG antenna data insertion loss data at one position for three independent measurements.

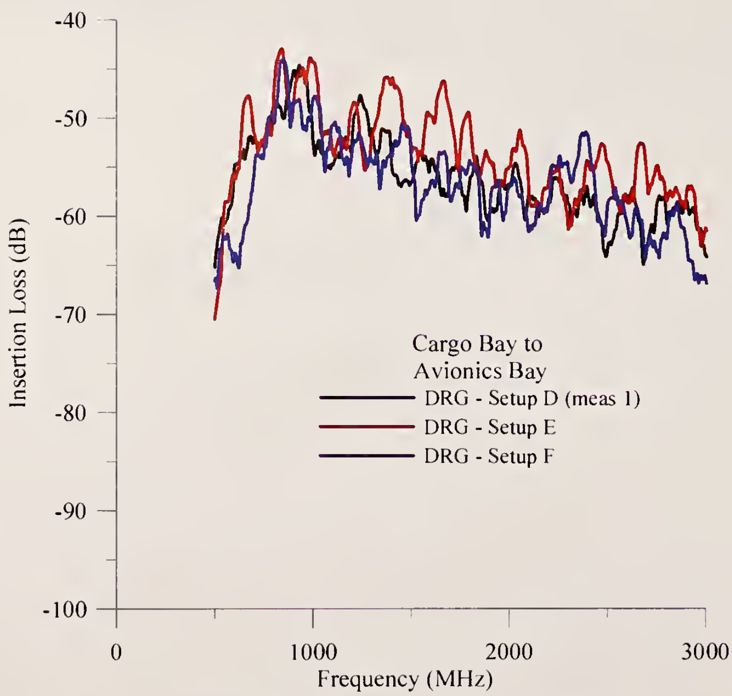


Figure 237. Cargo bay to avionics bay DRG antenna data insertion loss data at each of the three positions.

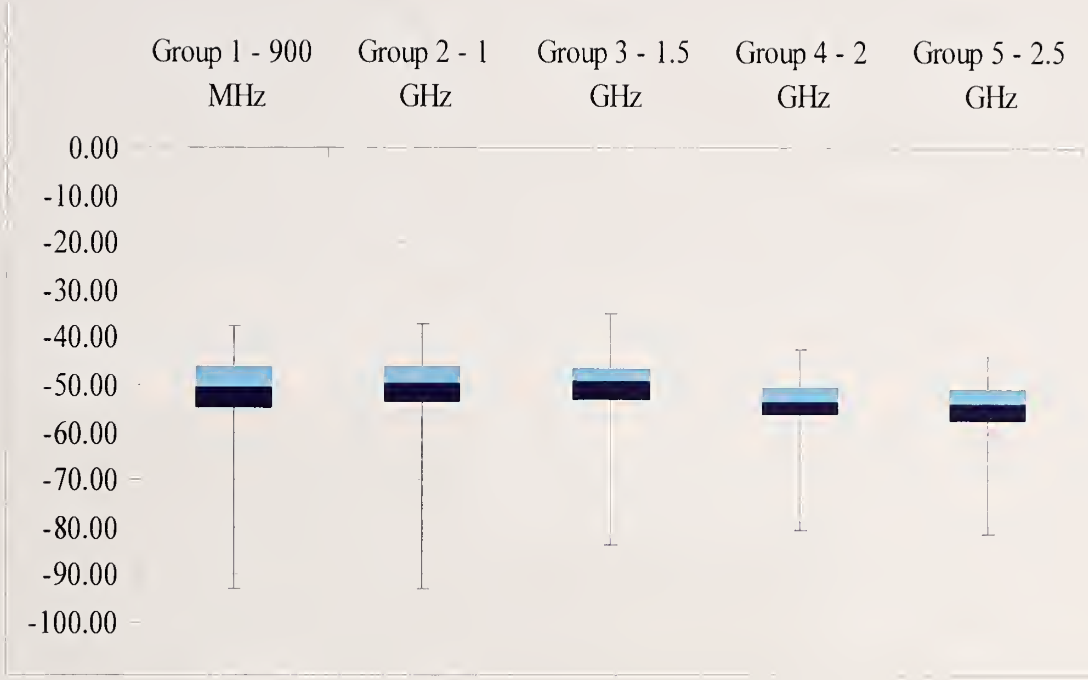


Figure 238. Whisker-box plots for all cargo bay to avionics bay insertion loss measurements of the DRG horn antennas at several frequencies.

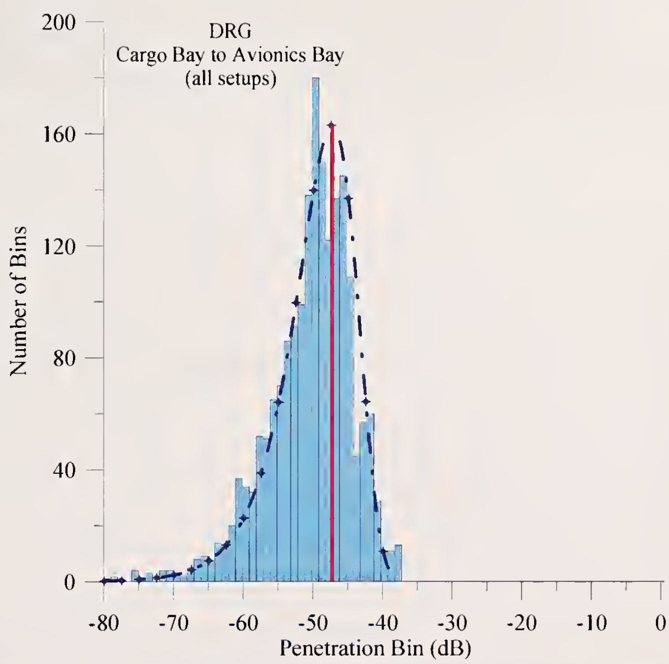


Figure 239. Chi-squared probability density function for all DRG measurements of insertion loss in the cargo bay to the avionics bay.

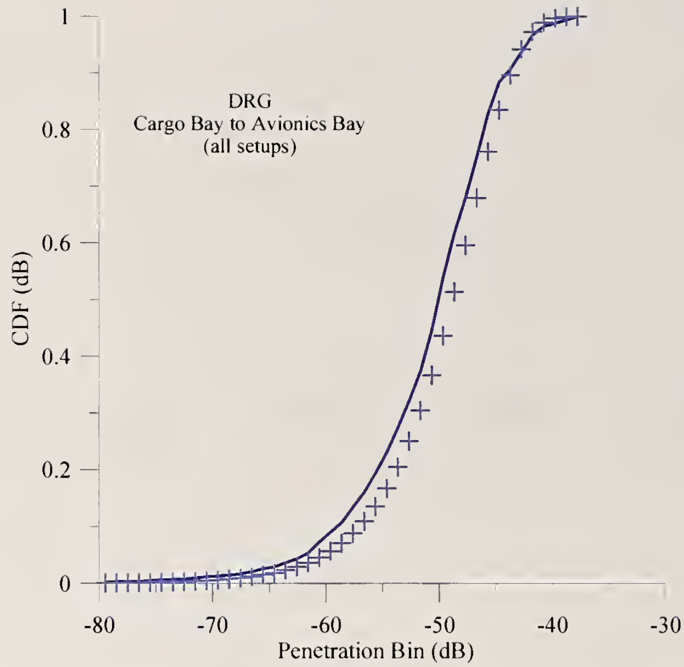

Figure 240. Chi-squared cumulative density function for all DRG measurements of insertion loss in the cargo bay to the avionics bay.

### 6.4.5.4 Individual TEM horn antenna positions

A photograph for each TEM antenna measurement location from the main cabin to the cargo bay, its associated time-domain waveform, and a schematic showing the antenna positions inside the aircraft is shown from Figure 241 to Figure 246.

Figure 241 shows the placement of a transmitting DRG horn antenna in the cargo bay and a receiving DRG horn antenna in the avionics bay for setup D, measurements 1, 2, and 3. One antenna was located in the forward section of the cargo bay close to the avionics bay and propped against a box pointed toward the rear back corner of the cargo bay with a mixed polarization. The other vertically polarized antenna was located on an insulated cooler pointing toward the front of the aircraft. A time-domain graph of all three measurements for position D for the cargo bay to avionics bay is shown in Figure 242. Traces 2 and 3 were offset, in the positive y-direction, from measurement 1 to compare differences between the repeat measurements.


Figure 241. Cargo bay to avionics bay DRG horn antenna setup D.

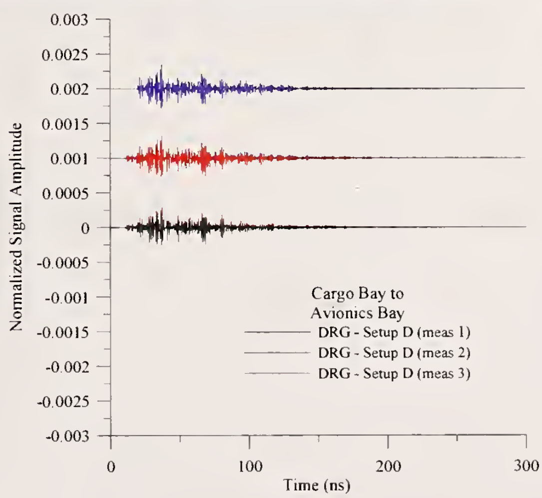


Figure 242. Cargo bay to avionics bay DRG horn antenna setup D, time-domain response.

Figure 243 shows the placement of a transmitting DRG horn antenna in the cargo bay and a receiving DRG horn antenna in the avionics bay for setup E. One antenna was located in the forward section of the cargo bay close to the avionics bay propped above the floor on a stack of insulation pointing toward the front corner of the cargo bay with a mixed polarization. The other antenna was located on an insulated cooler pointing down to the floor of the avionics bay. A time-domain graph of the measurement is shown in Figure 244.


Figure 243. Cargo bay to avionics bay DRG horn antenna setup E.

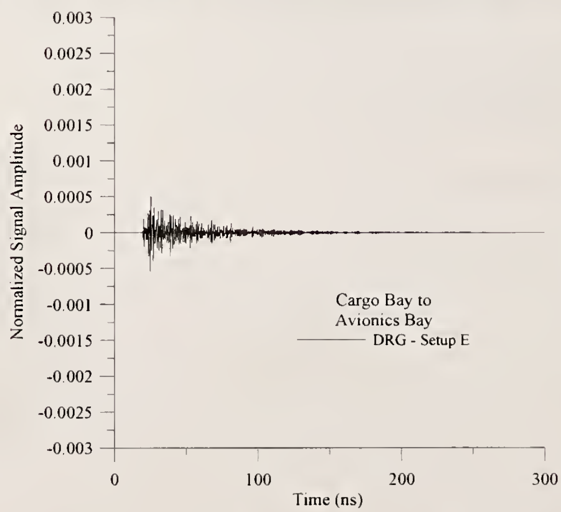


Figure 244. Cargo bay to avionics bay DRG horn antenna setup E, time-domain response.

Figure 245 shows the placement of a transmitting DRG horn antenna in the cargo bay and a receiving DRG horn antenna in the avionics bay for setup F, measurements 1 and 2. One antenna was located in the middle part of the cargo bay suspended from a support point toward the avionics bay. The other antenna was placed on the floor of the avionics bay pointing toward the front of the aircraft in a mixed polarization. A time-domain graph of the measurement is shown in Figure 246.


Figure 245. Cargo bay to avionics bay DRG horn antenna setup F.

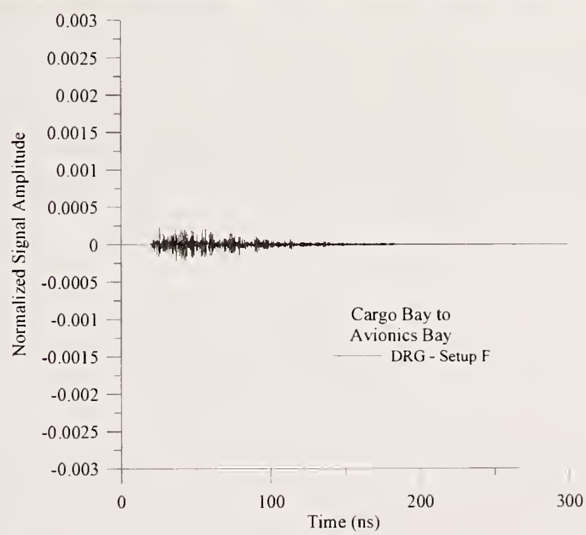


Figure 246. Cargo bay to avionics bay DRG horn antenna setup F, time-domain response.

Figure 247 shows whisker-box plots of each individual setup. The group of data was analyzed around a center frequency of 1000 MHz over a 200 MHz bandwidth containing 321 points. Table 19 summarizes the statistics of each setup for the whisker-box plots, and includes the mean value, the median value, the standard deviation, the maximum value in the group, and the minimum value in the group. Table 20 summarizes the differences between the mean value for the whisker-box plot analysis and the mean value for the $\chi^2$ statistic. The difference between the two means is also displayed. Finally, the $\chi^2$ *pdf* and the $\chi^2$ *cdf* are plotted for each setup in Figure 248 and Figure 249.

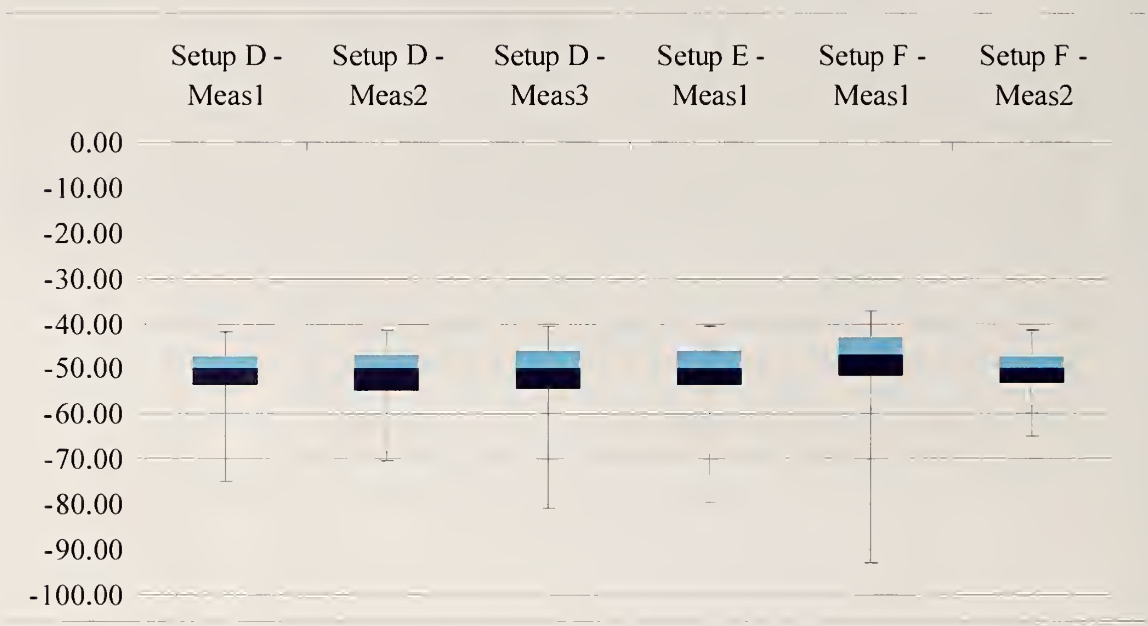


Figure 247. Statistical analysis for DRG horn antenna, setup D (measurements 1, 2, 3), setup E ( measurements 1 and 2), and setup F for cargo bay to avionics bay insertion loss.

Table 19. DRG Horn internal cabin statistics for measurements from the cargo bay to the avionics bay. The sample size was 321 points in a 200 MHz bandwidth around a center frequency of 1 GHz.

| | Setup D meas 1 | Setup D meas 2 | Setup D meas 3 | Setup E | Setup F meas 1 | Setup F meas 1 |
|---|---|---|---|---|---|---|
| Mean (dB) | − 50.75 | − 50.82 | − 50.65 | − 48.75 | − 50.70 | − 50.95 |
| Median (dB) | − 49.59 | − 49.70 | − 49.93 | − 46.67 | − 49.99 | − 49.88 |
| Standard Deviation (dB) | 5.37 | 6.13 | 6.41 | 8.38 | 4.77 | 5.46 |
| Minimum (dB) | − 70.22 | − 80.82 | − 79.69 | − 92.86 | − 65.06 | − 75.08 |
| Maximum (dB) | − 41.22 | − 40.55 | − 40.42 | − 37.24 | − 41.55 | − 41.80 |

Table 20. DRG horn antenna internal cabin $X^2$-distribution statistics for measurements from the cargo bay to the avionics bay.

| | Setup D meas 1 | Setup D meas 2 | Setup D meas 3 | Setup E | Setup F meas 1 | Setup F meas 1 |
|---|---|---|---|---|---|---|
| Whisker-Box Plot Mean (dB) | − 50.75 | − 50.82 | − 50.65 | − 48.75 | − 50.70 | − 50.95 |
| $X^2$ Mean (dB) | − 49.00 | − 51.00 | − 50.00 | − 47.00 | − 53.00 | − 49.00 |
| Δ (dB) | − 2.00 | < 1.00 | < 1.00 | − 2.00 | + 3.00 | − 1.00 |

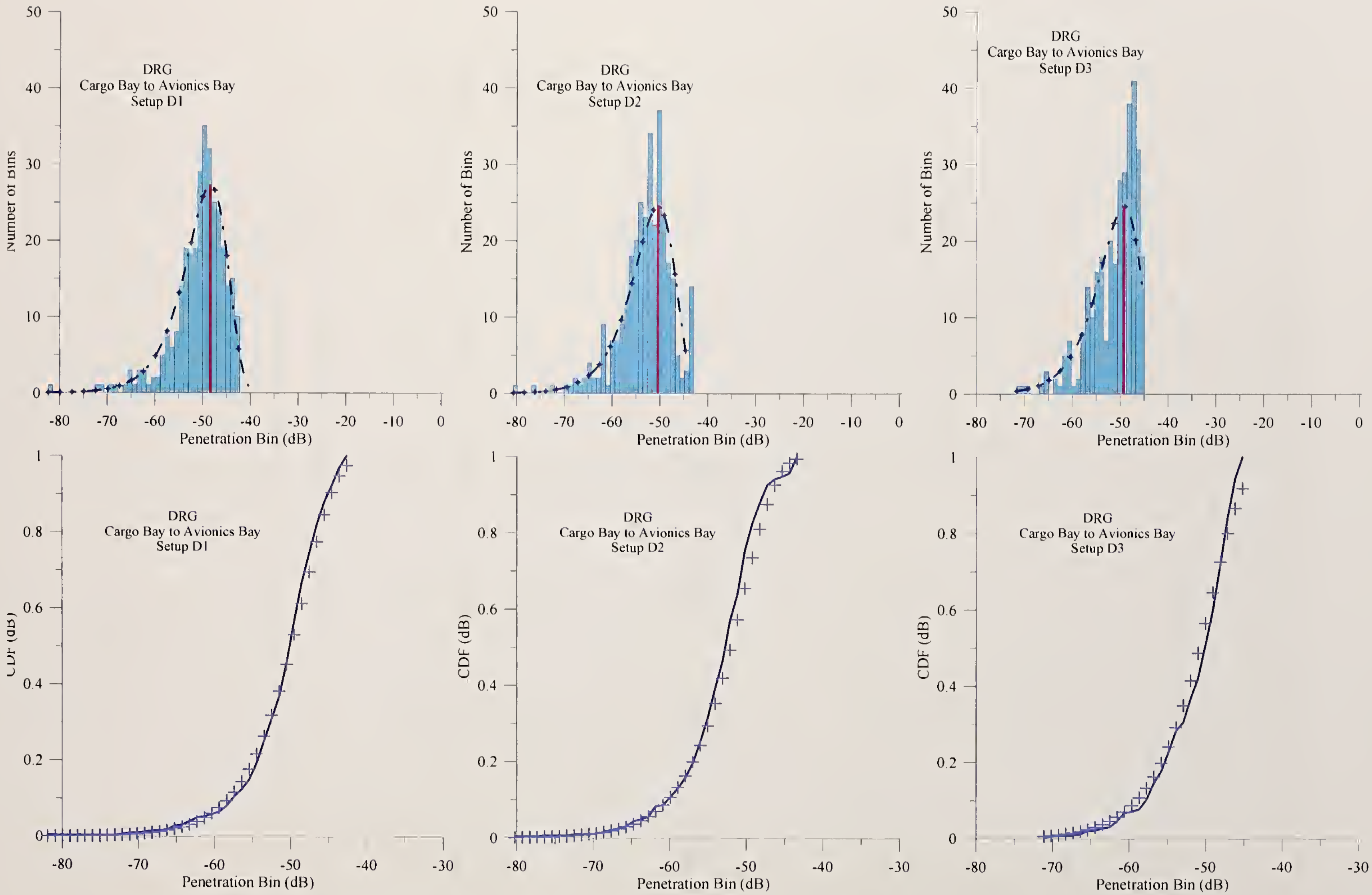


Figure 248. Statistical analysis for DRG horn antenna, setup D (measurements 1, 2, and 3), for cargo bay to avionics bay insertion loss.

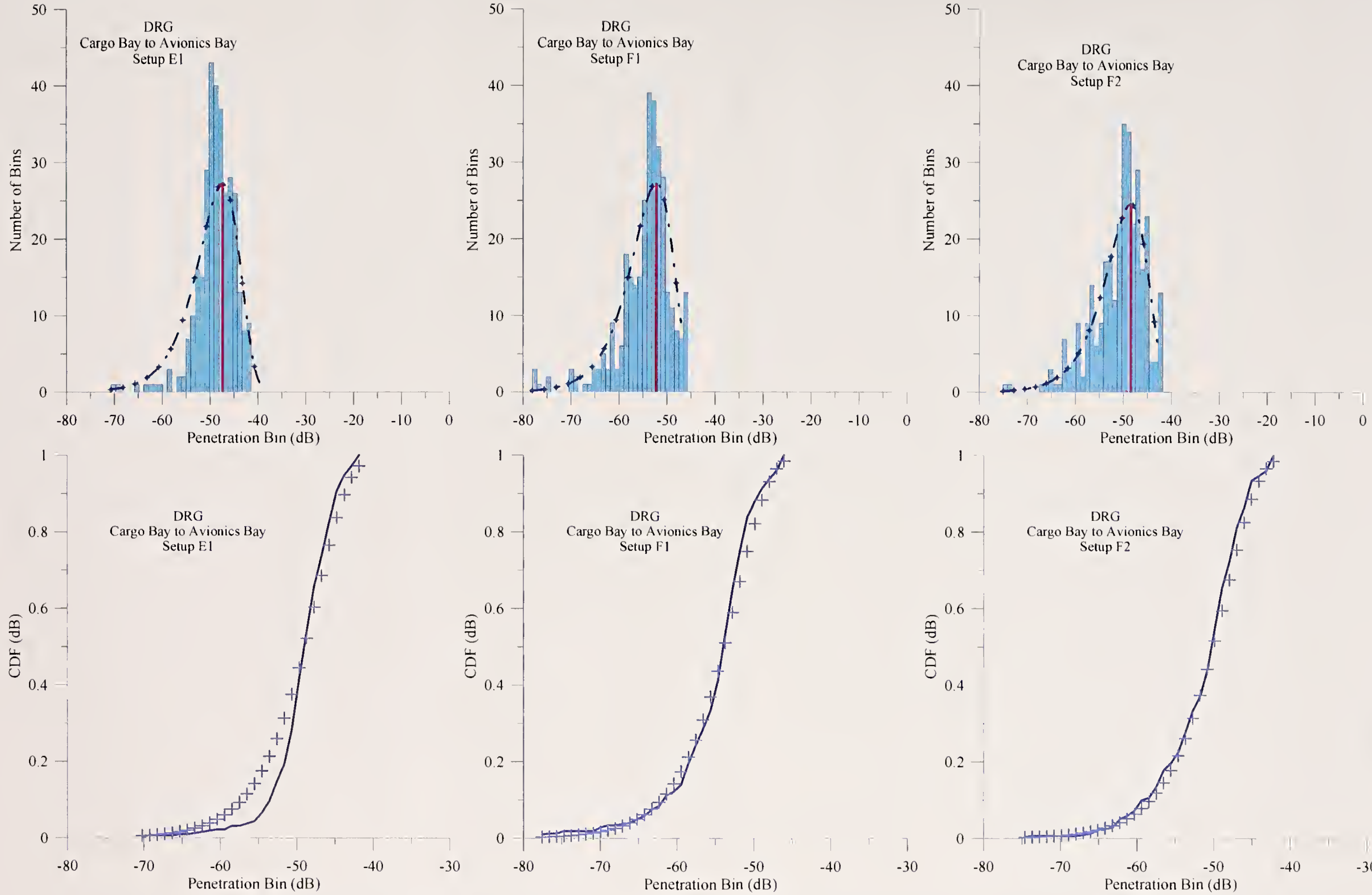


Figure 249. Statistical analysis for DRG horn antenna, setup E , and setup F, measurements 1 and 2 for cargo bay to avionics bay insertion loss.

## 7. Uncertainty Analysis

The sources of uncertainty are based on NISTIR 5019 [39], which provides a natural framework for the identification of source uncertainties encountered in aircraft shielding measurements, along with an efficient method for tracking and combining them.

Six sources of measurement uncertainty are considered in our analysis:

- Measurement Repeatability
- Range Uncertainties/Distance Correction
- Time Gating
- Drift
- Polarization Mismatch
- Signal-to-Noise Ratio

These sources of uncertainties (influence factors) were evaluated as follows:

1. Measurement Repeatability: For a given internal orientation, we took multiple data sets, in which we moved the external antennas to and from the same location.

2. Range Uncertainties: We used estimates of variations when positioning the antennas for both the reference and airframe measurements.

3. Time Gating: We determined time-gating uncertainties by varying the gate width and performing a statistical analysis on the resulting amplitude spectra; see Appendix A for further discussion.

4. Drift: The uncertainty due to instrumentation drift was small and was computed by use of the data obtained from system calibration checks done before and after circumnavigating the aircraft. The uncertainty was determined by calculating the difference and dividing that by the average of the two signals.

5. Polarization Mismatch: Polarization mismatch uncertainties occur because antennas could be misaligned for a given polarization. We calculated one uncertainty based on a possible misalignment of 5°. The other term comes from the possible leakage from one polarization to the other. The cross-polarization of our TEM horn antennas is approximately −20 dB, and for the DRG antennas it is approximately −15 dB. These two factors both contribute to the polarization mismatch uncertainty.

6. Signal-to-Noise Ratio: These uncertainties were calculated for the FAA 737-200 aircraft.

The effect of these six influence factors on the measured penetration is summarized in Table 21. This table lists the fractional uncertainties [40, 41] resulting from each influence factor. The signal-to-noise uncertainties were not calculated for specific signal-to-noise levels, but were determined for measurements that have a signal-to-noise ratio of 60 dB below 9 GHz and decreasing to approximately 40 dB at higher frequencies. The most significant errors are due to repeatability and time-gating uncertainties below 9 GHz, and above 9 GHz they are due to time-gating and extrapolation uncertainties. Signal-to-noise is the next largest uncertainty, followed by the range/distance correction uncertainties, polarization mismatch, and drift, respectively.

The combined standard uncertainty was computed by use of the procedure given in NIST Technical Note 1297 [41]. The six sources of uncertainties were combined by means of the root sum-of-squares of the linear fractional uncertainties averaged over a 400-point frequency window. The resulting uncertainties (in decibels) for penetration are plotted in Figure 250 for the frequency range from 800 MHz to 18000 MHz. The uncertainties were calculated as a function of frequency, and therefore we have listed an approximate average value in the table below. The rapid variation is due to the complex cavity environment where some frequencies penetrate into the aircraft and are absorbed by the environment, while others do not penetrate. We have broken the uncertainties into those below 9 GHz and those above 9 GHz because the noise floor resets itself there due to the internal configuration of both attenuators and mixers. We believe that a reasonable uncertainty bound would be at the 95 % level for the data shown in Figure 250, remembering that this current uncertainty analysis is based on a limited set of data. These aircraft are typically measured only once and do not lend themselves to an extensive uncertainty analysis.

Table 21. Typical penetration fractional uncertainties resulting from the six influence factors. The signal-to-noise ratio was 65 dB.

| Influence factor | Typical fractional uncertainties (dB) | |
|---|---|---|
| | < 9 GHz | > 9 GHz |
| Signal-to-noise | 0.05 | 0.28 |
| Repeatability | 2.83 | 3.51 |
| Time gating | 1.68 | 1.00 |
| Range/distance correction | 0.56 | 0.56 |
| Extrapolation | 1.12 | 3.43 |
| Polarization mismatch | 0.51 | 0.51 |
| Drift | 0.09 | 0.08 |
| RSS (dB) | 4.01 | 5.27 |

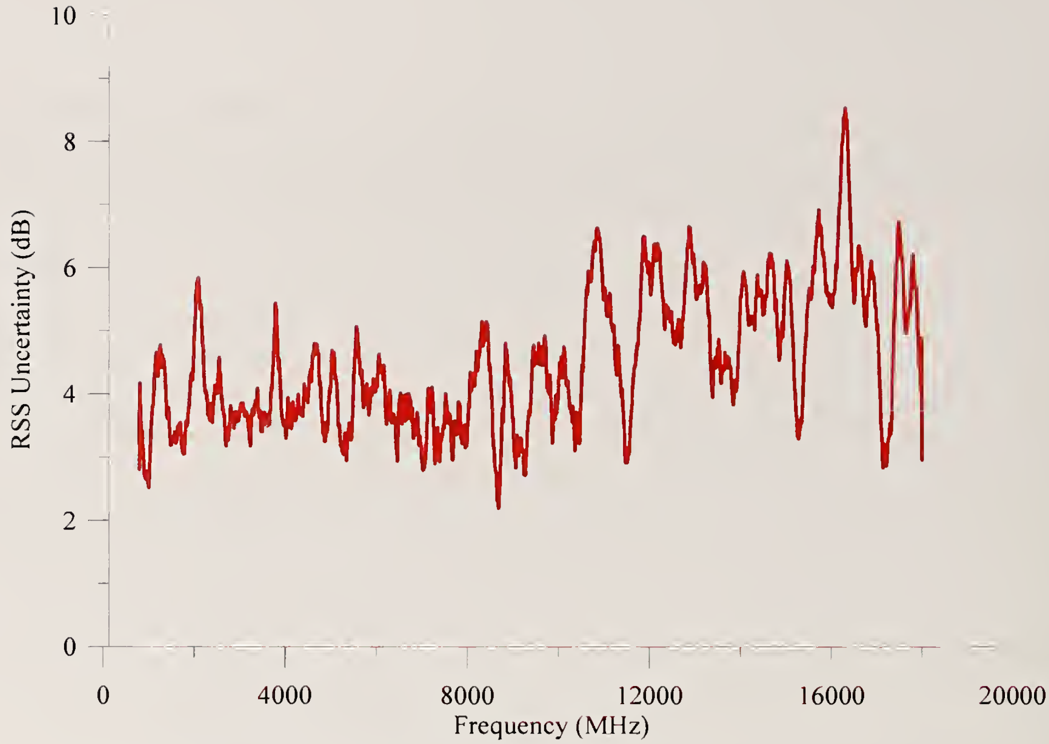


Figure 250. Combined standard uncertainty in penetration.

## 8. Summary and Conclusions

The data collected in this report will be used to provide guidelines for HIRF testing on various aircraft. We have reported on the penetration measurements taken on the FAA's 737-200 at the FAA facility in Atlantic City, New Jersey. The first part of the report discussed the initial theoretical analysis and numerical simulations prior to actual measurements. We have discussed extrapolation measurements taken to ensure that the measurements are in the far-field of the transmitting antenna. We have shown results for measurements taken at various azimuth angles around the outside of the aircraft with the receiving antenna in the main passenger cabin and the flight deck. We have looked at ground conditions and how they influence the measurements. This report also discussed the statistics for a series of internal measurements used to study the reverberant field characteristics within various cavities. We see that penetration typically decreases as frequency increases. This was an important measurement effort both to aid in understanding and to help define standard measurement procedures for HIRF testing.

The appendices are intended to provide understanding of DRG horn antenna and TEM horn antenna boresight gain characteristics, changes in the average power as a function of the number of positions measured, statistics for angular measurements for the Bombardier Global 5000 and the Beechcraft Premier IA, and numerical studies of the FAA 737-200 internal measurements.

We thank Robert Morrison and Anthony Wilson from the FAA in Atlantic City, New Jersey and David Walen from the FAA office in Renton, Washington for their excellent assistance and financial support for this work. We also thank John Ladbury of the Field Parameters and EMC Applications Project and Jolene Splett of the Statistical Engineering Division at NIST for their valuable input into the statistics of reverberation chambers and the general application of statistical analysis.

## 9. References

[1] Website http://www.faa.gov., accessed 5/15/09.

[2] L. Li, J. Xie, O. Ramahi, M. Pecht, B. Donham, Airborne operation of portable electronic devices," IEEE Antenna's and Prop. Mag, 44(4):30-39, (August 2002).

[3] B. Strauss, Avionics interference from portable electronic devices: review of the aviation safety reporting system database. 2002 Digital Avionics Systems Conference, 2:13E3-1 – 13E3-8, (2002).

[4] J.J. Ely, T.W. Shaver, G.L. Fuller, Ultrawideband electromagnetic interference to aircraft radios. NASA Report TM-2002-211949, (October 2002).

[5] K. J. Moeller, K. L. Dudley, C. C. Quach, S. Koppen, In-flight characterization of the electromagnetic environment inside an airliner. NASA Report TP-2001210831, (March 2001).

[6] M.O. Hatfield, W. P. Pluim, W. Price, Investigation of in-situ shielding effectiveness testing of transport aircraft. 2003 IEEE Symp. Electromag. Compat. 1:414-418 (August 2003).

[7] G. J. Freyer, M. O. Hatfield, T. A. Loughry, Cavity to cavity coupling measurements in commercial aircraft and the implications for on-board operation of personal electronic devices 1996 15th AIAA/IEEE Conf. Digital Avionics Systems, 333-338 (October 1996).

[8] G. J. Freyer, M. O. Hatfield, M. B. Slocum, Characterization of the electromagnetic environment in aircraft cavities excited by internal and external sources. 1996 15th AIAA/IEEE Conf. Digital Avionics Systems, 327-332, (October 1996).

[9] G. J. Freyer, M. O. Hatfield, T. A. Loughry, R. Johnk, D. M. Johnson, Shielding effectiveness measurements for a large commercial aircraft. 1995 IEEE Symp. Electromag. Compat., 383-386 (August 1995).

[10] P.R. Rimbey, D. B. Walen, Consistent approach to describing aircraft HIRF protection. NASA Contractor Report 195067, (March 1995).

[11] N. J. Carter, D. A. Bull, EMC testing of whole aircraft. IEE Colloq. EMC Large Systems, 4:1-5, (1994).

[12] N. J. Carter, Aircraft EMC, the past, the present and the future: an overview. IEE Colloq. EMC Aerospace, 3:1-7, (November 1996).

[13] N. J. Carter, P. E. Willis, EMC testing of high-integrity digital systems in aircraft. IEE Colloq. EMC in High Integrity Digital Systems, 4:1-9, (May 1991).

[14] F. Heather, High intensity radiatied field external environments for civil aircraft. Naval Air Warfare Center Aircraft Division. 1999 IEEE Symp. Electromag. Compat. 2: 963-968, (August 1999).

[15] SAE Aerospace Group, Guide to certification of aircraft in a high intensity radiated field (HIRF) environment. SAE ARP5583 (January 2003).

[16] C. A. Grosvenor, R. T. Johnk, D. R. Novotny, N. Canales, C. M. Weil, J. Veneman, A two-phase airframe shielding performance study using ultrawideband measurement systems. Natl. Inst. Stand. Technol. NISTIR 6622 (January 2003).

[17] R.T. Johnk; Ultrawideband shielding evaluation of a business jet. SAE Lightning Committee Meeting (May 2006).

[18] C.A. Grosvenor, D. R. Novotny, D. Camell, G. Koepke, R. T. Johnk, Shielding Penetration Measurements on a Bombardier Global 5000, Natl. Inst. of Stand. Technol. Technical Note 1547, May 2008.

[19] C.A. Grosvenor, D. R. Novotny, D. Camell, G. Koepke, R. T. Johnk, Shielding Penetration Measurements on a Hawker-Beechcraft Premier IA, Natl. Inst. of Stand. Technol. Technical Note 1548. August 2008.

[20] S. V. Georgakopoulos, C. R. Birtcher, C. A. Balanis, HIRF penetration through apertures: FDTD versus measurements. IEEE Trans. Electromag. Compat., 43(3):282-293 (August 2001).

[21] T. Panaretos, C. A. Balanis, C.R. Birtcher, HIRF penetration into simplified fuselage using a reverberation chamber approach. IEEE Trans. Electromag. Compat. 43(7):667-670 (August 2005).

[22] J. M. Ladbury, T. H. Lehman, G. H. Koepke, Coupling to devices in electrically large cavities or why classical emc evaluation techniques are becoming obsolete. 2002 Intl Symp. on Electromagnetic Compatibility, 2: 648-655 (August 2002).

[23] D. M. Johnson, M. O. Hatfield, G. J. Freyer, RF coupling measurements on passenger aircraft avionics exposed to cavity-mode excitation. 1996 14th AIAA/IEEE Conf. Digital Avionics Systems, 427-432 (November 1995).

[24] J. M. Stone, N. J. Carter, Statistical analysis of aircraft coupling measurements. IEE Colloq. Role of Statistics EMC Specif. Design and Clearance, 6:1-7, (May 1992).

[25] D. A. Hill, M. T. Ma, A. R. Ondrejka, B.F. Riddle, M. L. Crawford, R. T. Johnk, Aperture excitation of electrically large, lossy cavities. Natl. Inst. Stand. Technol. Tech. Note 1361, (September 1993).

[26] J. M. Ladbury, T. H. Lehman, G. H. Koepke, Coupling to devices in electrically large cavities or why classical EMC evaluation techniques are becoming obsolete. 2002 IEEE Symp. Electromag. Compat. (August 2002).

[27] C. A. Grosvenor, D. Novotny, R. T. Johnk, S. Canales, J. Veneman, Shielding effectiveness measurements using the direct illumination technique, 2002 IEEE Symp. Electromag. Compat. 389-394 (August, 2002).

[28] M.C. Dosch, The effect of ground reflections on electric field measurements using a HIRF LLCW test system. 1993 IEEE Intl. Symp. Electromag. Compat. 116-119 (August 1993).

[29] P. F. Wilson, D. A. Hill, C. L. Holloway, On determining the maximum emissions from electrically large sources. 2002 IEEE Trans. Electromagnetic Compatibility, 44(1): 79-86 (February 2002).

[30] G. Koepke, D. Hill, J. Ladbury, Directivity of the test device in EMC measurements. 2000 IEEE Symp. Electromag. Compat., 2:535-539, (August 2000).

[31] P. F. Wilson, Emission and Immunity Testing: Test Object Electrical Size and Its Implication. 2004 IEEE Trans. Electromagnetic Compatibility, 2: 349-352 (August 2004).

[32] D. Novotny, et.al. Details for Processingg Directional Shielding Measurements of Leaky Reverberant Cavities. 2009 Intl. Symp. On Electromagnetic Compatibility, (August 2009).

[33] Website http://www.we-intl.com/rfoil.html accessed 1/21/09.

[34] C. A. Grosvenor, R. T. Johnk, D.R. Novotny, S. Canales, B. Davis, J. Veneman, TEM horn antenna design principles. Natl. Inst. of Stand. Techn. Technical Note 1544. (January 2007).

[35] J. Graham, D. Hibbard, D.Martin, S. Yencer, D. Novotny, C. Grosvenor, N. Canales, R. Johnk, L. Nagy, T. Roach, Outdoor vehicular test range turntable impact on electric-field uniformity study. 2008 IEEE Symp. Electromag. Compat., 1-6, (August 2008).

[36] R. Johnk, D. Novotny, C. Grosvenor, N. Canales, J. Graham, D. Martin, S. Yencer, D. Hibbard, T. Roach, L. Nagy, An electric-field uniformity study of an outdoor vehicular test range. 2006 IEEE Symp. Electromag. Compat., 2:404-409, (August 2006).

[37] R. T. Johnk, B. Archambeault, D. Novotny, Using joint time-frequency analysis to enhance time-domain numerical emc simulations. 2003 Annual Report Interference Technology (2003).

[38] C. T. A. Johnk, Engineering electromagnetic fields and waves. John Wiley & Sons, p. 346 (1988).

[39] R. C. Wittmann, M. H. Francis, L. A. Muth, R. L. Lewis, Proposed uncertainty analysis for RCS Measurements. Natl. Inst. Stand. Technol. NISTIR 5019 (January 1994).

[40] J. R. Taylor, An introduction to error analysis. University Science Books, Sausolito, CA, (1997).

[41] B. N. Taylor, C. E. Kuyatt, Guidelines for evaluating and expressing the uncertainty of NIST measurement results. Natl. Inst. Stand. Technol. Tech. Note 1297 (September 1994).

[42] E. B. Larsen, R. L. Ehret, D. G. Camell, G. H. Koepke, Calibration of antenna factor at a ground screen field site using an automatic network analyzer. 1989 Intl. Symp on Electromagnetic Compatibility, 1: 19-24 (August 1989).

[43] R. Johnk, A. Ondrejka, "Time-domain calibrations of D-dot sensors," Natl. Inst. Stand. Technol. Tech. Note 1392, (February 1998).

## Appendix A: TEM and DRG Horn Boresight Gain Characteristics

The DRG and TEM horn antennas used in this effort were calibrated before we deployed our system in Atlantic City. This technique can be used to derive antenna gain with a specified resistive load (typically 50 Ω) at the antenna terminals. An accurate method for doing this is the three-antenna method. As the name implies, three transmission measurements are made with three combinations of the three antennas. This procedure is described in detail in reference [42]. This process yields three equations that can be readily solved for either gain or antenna factor. The gain characteristics of our DRG horn antennas are shown in Figure A1; those for our 36 cm TEM horns are shown in Figure A2; and those for our 1.2 m TEM horns are shown in Figure A3. The gains displayed in these figures include the antenna input mismatch, which accounts for the reduction of gain at the lower frequencies. The DRG horn antenna gain, plotted in Figure A1 shows that the low-frequency cutoff of these antennas occurs around 750 MHz. As the frequency is reduced, the input mismatch increases, which accounts for a rapid decrease in antenna gain. Mismatch and gain are not cause and effect, but a combination of both aperture beam forming and a better input match accounts for the increasing gain at the higher frequencies. A maximum gain of approximately 15 dB occurs at 16,000 MHz. The 36 cm antenna results, which are plotted in Figure A2, show a maximum gain of approximately 7 dB realized at 4,000 MHz. Results for a NIST 1.2 m horn antenna are plotted in Figure A3. This horn is longer, and it has a resistive taper, which improves the low-frequency performance. The maximum frequency of this antenna is 1500 MHz, due to balun performance limitations, and a maximum gain of 7 dB occurs at this frequency as well.

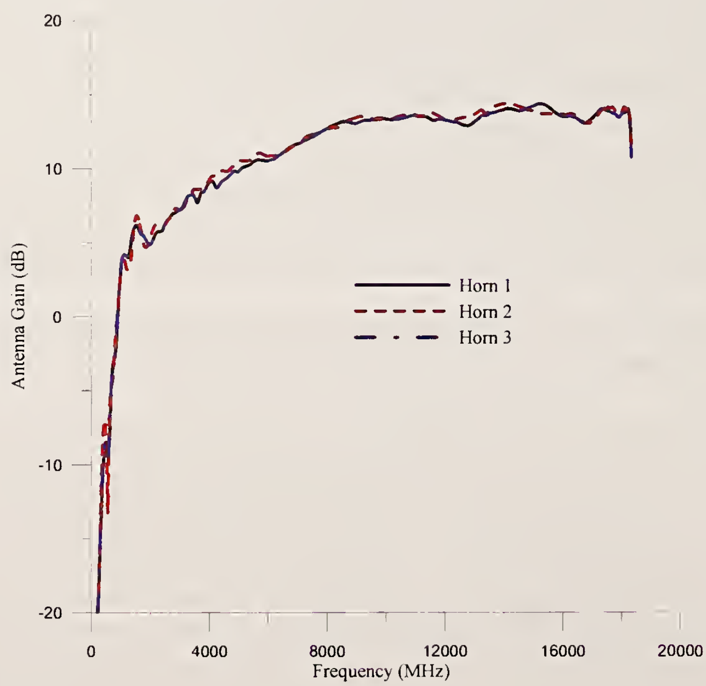


Figure A1. Measured boresight antenna gain for a DRG horn antenna. The gains plotted here include the input mismatch effects, which account for the rapid decrease below 750 MHz.

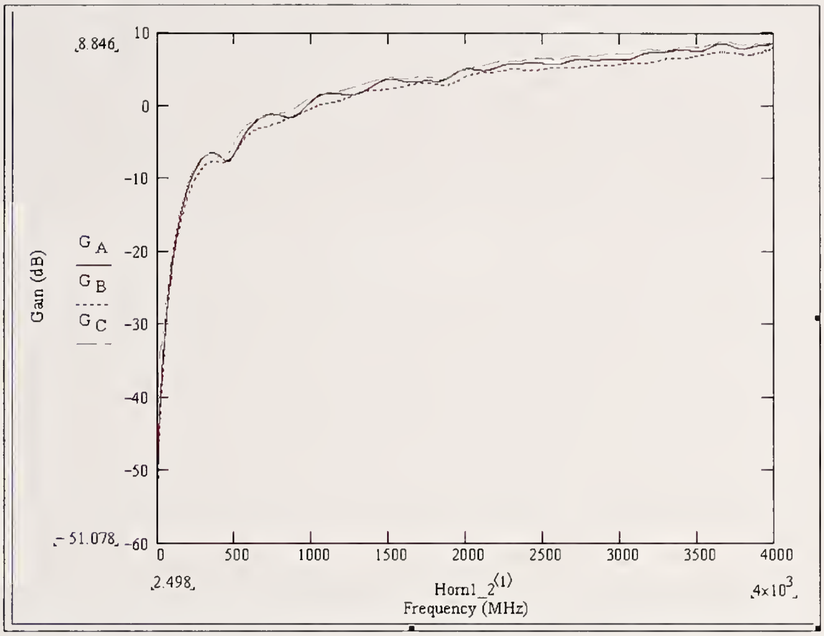


Figure A2. Measured boresight antenna gain for three identical NIST 36 cm TEM horn antennas. The gains plotted here include the input mismatch effects, which account for the rapid decrease below 100 MHz.

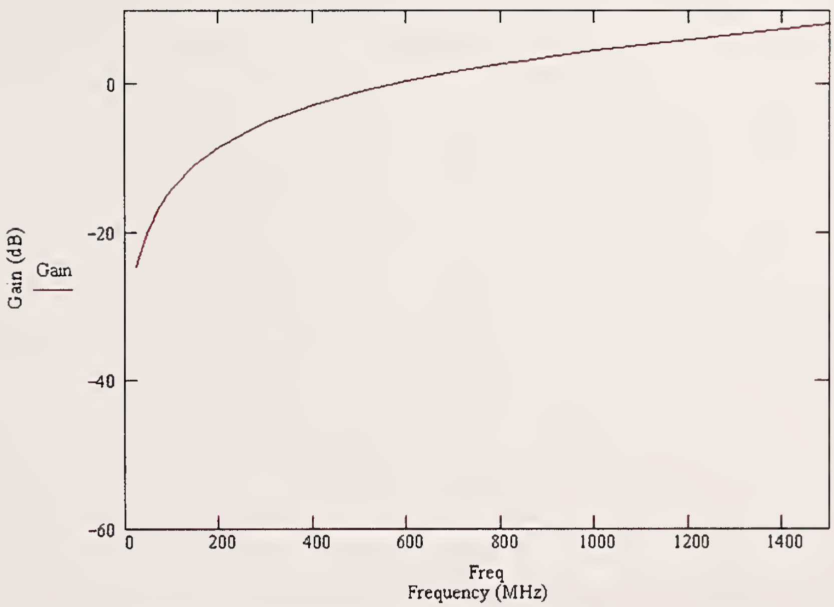


Figure A3. Measured boresight antenna gain for a NIST 1.2 m TEM horn antenna. The gains plotted here include the input mismatch effects, which account for the rapid decrease below 50 MHz.

## Appendix B. Number of Positions vs. Average Power

In Section 6.3.2 we showed that to fully characterize the Bombardier Global 5000 around one plane of the aircraft, the number of positions required is 1197 at 1 GHz, 5973 at 5 GHz, and 21505 at 18 GHz. Since this is in practice impossible to achieve, we decided to look at the statistics and average power as a function of position for the Bombardier Global 5000. The goal is to provide data as a function of the number of positions and frequencies and how the average power seen by the aircraft changes.

For this analysis we randomly chose measured positions around the aircraft, computed the average for these measurements and then added more positions, computed the average, etc. For the first computation, we chose 6 angular positions, which included the following angular positions, (1) 0°, (2) 40°, (3) 90°, (4) 135°, (5) 180°, and (6) 345°. We then added 2 more angular positions, (7) 120°, (8) 20° for a total of 8 positions. For a ten position average we added the angular positions (9) 150°, and (10) 60°. We added the following angular positions for a 13 position average: (11) 330°, (12) 70°, and (13) 110°. For a 17-position average, these additional angular positions were added: (14) 125°, (15) 160°, (16) 340°, and (17) 190°. Adding the following five angular positions results in a 22-position average: (18) 30°, (19) 100°, (20) 140°, (21) 170°, (22) 350°. And finally for all 29 positions, we computed the average by adding the final 7 angular positions: (23) 10°, (24) 50°, (25) 80°, (26) 130°, (27) 145° (28) 335°, (29) 355°. A plot showing how the penetration changes as a function of angular position is shown in Figure B1. Whisker Box plots are shown in Figure B2 for various included angular positions. This shows that as more positions are included in the average, the median, maximum, and minimum values do not vary by more than a few decibels at the frequencies shown. We then wanted to look at how the average power changes as more positions are added and this plot is shown in Figure B3 as a function of frequency and the number of included positions. We see that at approximately 17 included positions the average value tends to approach some constant value. Further research needs to be done on this analysis, because this was done on just one aircraft.

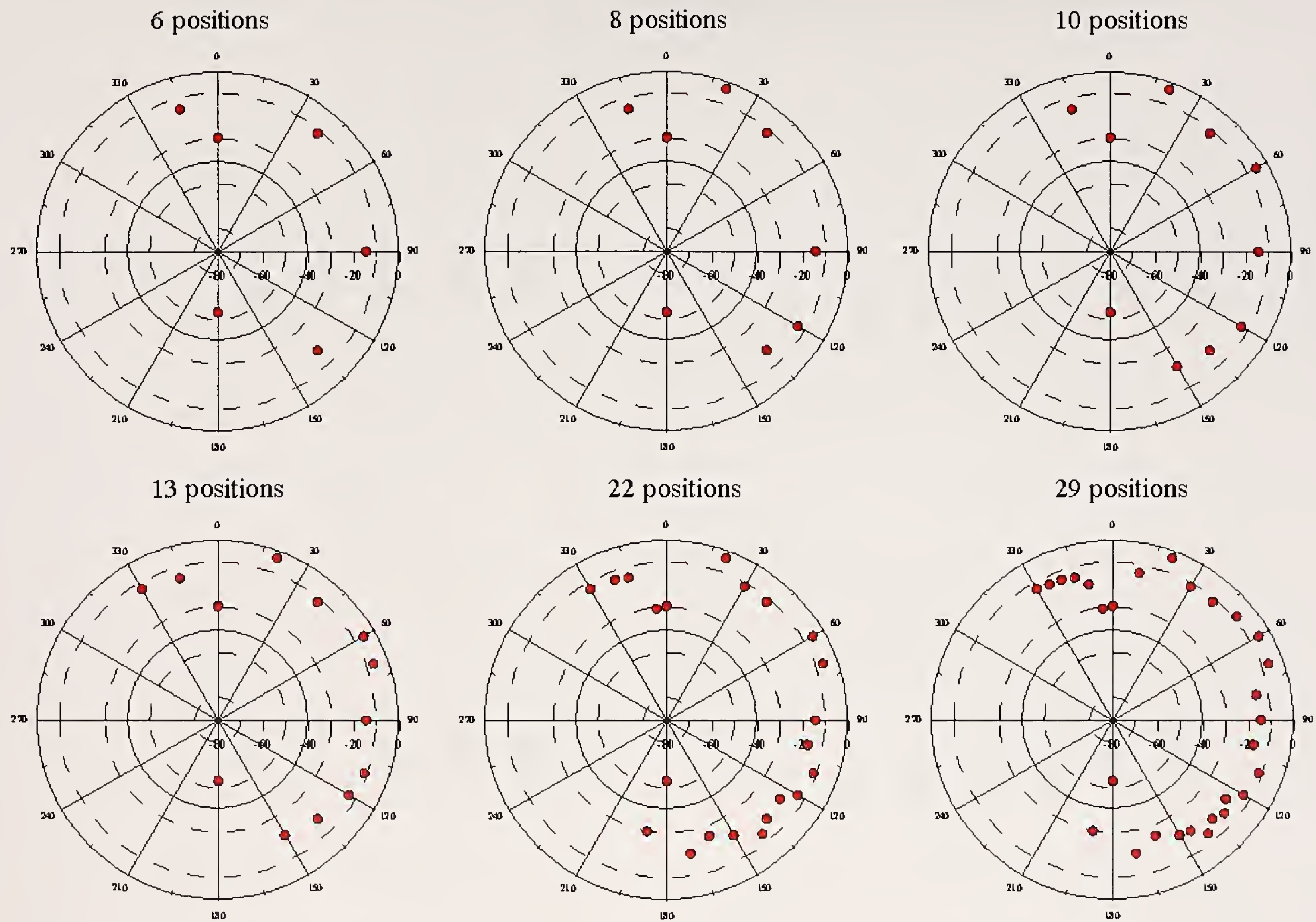


Figure B1. Pattern changes as a function of added angular positions at 5 GHz for the Bombardier Global 5000.

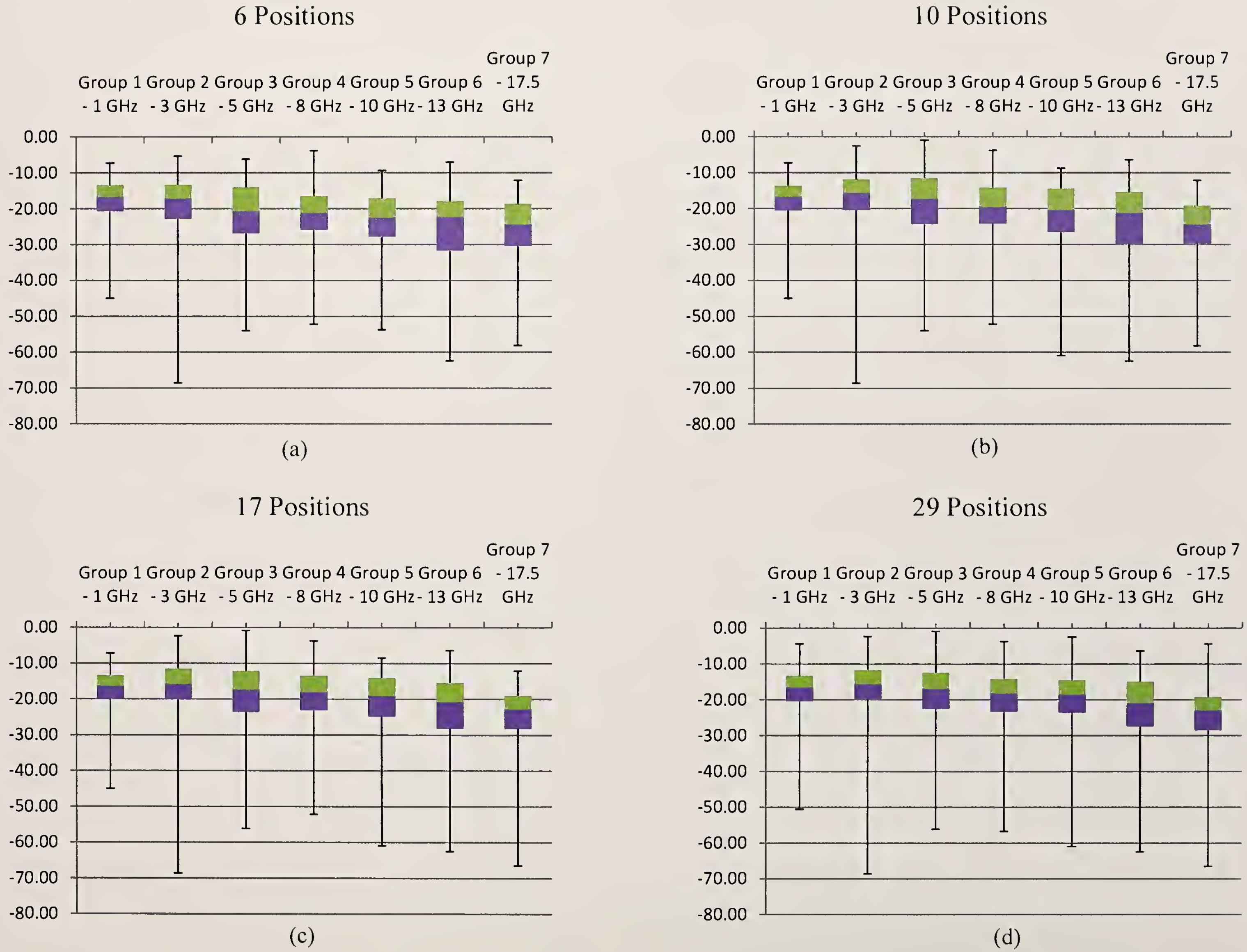


Figure B2. Whisker-Box plots showing how the median changes as a function of frequency and number of added positions.

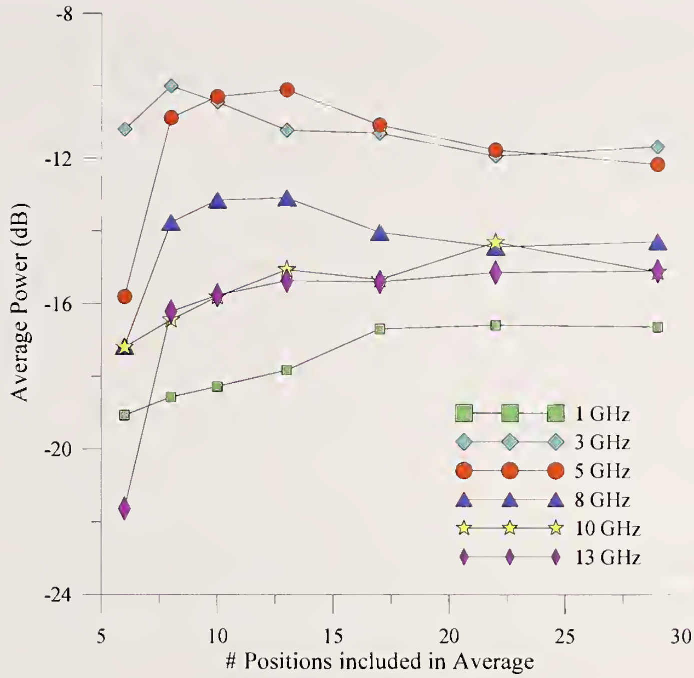


Figure B3. The average power as a function of frequency and number of added positions.

## Appendix C. Whisker-Box Plots for Bombardier Global 5000 and Hawker-Beechcraft Premier IA

Throughout the first part of this report, we have presented whisker-box plots of the insertion loss as a function of position for various compartments in the aircraft. In this appendix, we would like to present whisker-box plots for some of the angular scans of the measurements on the Bombardier Global 5000 and the Hawker-Beechcraft Premier IA. These plots provided insight into the spread of data and the maximum and minimum values at each position around the aircraft. Also, it shows how the data change as the averaging bandwidth changes.

Figures C1, C2, and C3 show whisker-box plots for the Bombardier Global 5000 with the receiving antenna in the main passenger cabin for results centered at 1000 MHz over a 50 MHz bandwidth, a 100 MHz bandwidth, and a 200 MHz bandwidth. If we track one angular position of 50° across all three bandwidths we derive the statistics shown in Table C1. We see that the data change the most from a 50 MHz bandwidth to a 100 MHz bandwidth. The median changes from −14.42 dB to −12.60 dB, the maximum changes from −8.42 dB to −6.57 dB, and the minimum changes from −20.14 dB to −36.16 dB, and the spread in the data from the 25$^{th}$ percentile to the 75$^{th}$ percentile changes from 4.10 dB to 5.23 dB. The statistics stay the same in looking at a 100 MHz bandwidth around 1000 MHz to a 200 MHz bandwidth. Let's look at another angular position of 180° in Table C2. We see the data change the most from a 50 MHz bandwidth to a 100 MHz bandwidth, although less at this angle. The median changes from −26.67 dB to −25.76 dB, the maximum changes from −21.30 dB to −15.92 dB, the minimum does not change, and the spread in the data from the 25$^{th}$ percentile to the 75$^{th}$ percentile changes from 5.42 dB to 6.14 dB. The statistics stay the same for the maximum and the minimum when changing from the 100 MHz bandwidth at 1000 MHz to the 200 MHz bandwidth. The other changes are small compared to the first comparison. We typically use a 200 MHz frequency averaging bandwidth to smooth the data for the DRG horn antennas and we typically use a 50 MHz frequency averaging for the TEM horn antennas.

Let's look at some data for the TEM horn antenna in Figures C4, C5, and C6. Figures C4, C5, and C6 show whisker-box plots for the Beechcraft Premier IA with the receiving antenna in the main passenger cabin for results centered at 1000 MHz over a 50 MHz bandwidth, a 100 MHz bandwidth, and a 200 MHz bandwidth. If we track one angular position of 50° across all three bandwidths we derive the statistics shown in Table 3. We see that the data change the most from a 50 MHz bandwidth to a 100 MHz bandwidth. The median changes from –5.35 dB to −5.08 dB, the maximum changes from −2.36 dB to −1.71 dB, and the minimum does not change, and the spread in the data from the 25$^{th}$ percentile to the 75$^{th}$ percentile changes from 4.09 dB to 3.07 dB. When the bandwidth changes from 100 MHz to 200 MHz, the median changes from –5.08 dB to −5.84 dB, the maximum does not change, and the minimum changes from −20.85 dB to −23.64 dB, and the spread in the data from the 25$^{th}$ percentile to the 75$^{th}$ percentile changes from 3.94 dB to 4.07 dB. Let's look at another angular position of 180° in Table 4. We see the data change the most from a 50 MHz bandwidth to a 100 MHz bandwidth, although less at this angle. The median changes from −9.45 dB to −11.38 dB, the maximum changes from −5.35 dB to −5.21 dB, the minimum does not change and the spread in the data from the 25$^{th}$ percentile to the 75$^{th}$ percentile changes from 0.40 dB to 6.14 dB. The statistics stay the same for the maximum and the minimum when changing from the 100 MHz bandwidth at 1000 MHz to the 200 MHz bandwidth. The other changes are small compared to the first comparison.

Table C1. Data statistics for the Bombardier Global 5000 at an angular position of 50° for three bandwidths of 50 MHz, 100 MHz, and 200 MHz.

| Bandwidth (MHz) | Median (dB) | 25$^{th}$ percentile (dB) | 75$^{th}$ percentile (dB) | Maximum (dB) | Minimum (dB) |
|---|---|---|---|---|---|
| 50 | −14.42 | −15.83 | −11.73 | −8.42 | −20.14 |
| 100 | −12.60 | −15.83 | −10.60 | −6.57 | −36.16 |
| 200 | −12.60 | −15.83 | −10.60 | −6.57 | −36.16 |

Table C2. Data statistics for the Bombardier Global 5000 at an angular position of 180° for three bandwidths of 50 MHz, 100 MHz, and 200 MHz.

| Bandwidth (MHz) | Median (dB) | 25th percentile (dB) | 75th percentile (dB) | Maximum (dB) | Minimum (dB) |
|---|---|---|---|---|---|
| 50 | −26.67 | −30.14 | −24.72 | −21.30 | −54.69 |
| 100 | −25.76 | −29.35 | −23.21 | −15.92 | −54.69 |
| 200 | −25.98 | −30.09 | −23.20 | −15.92 | −54.69 |

Table C3. Data statistics for the Beechcraft Premier IA at an angular position of 50° for three bandwidths of 50 MHz, 100 MHz, and 200 MHz.

| Bandwidth (MHz) | Median (dB) | 25th percentile (dB) | 75th percentile (dB) | Maximum (dB) | Minimum (dB) |
|---|---|---|---|---|---|
| 50 | −5.35 | −8.03 | −3.94 | −2.36 | −20.85 |
| 100 | −5.08 | −7.03 | −3.96 | −1.71 | −20.85 |
| 200 | −5.84 | −8.25 | −4.31 | −1.71 | −23.64 |

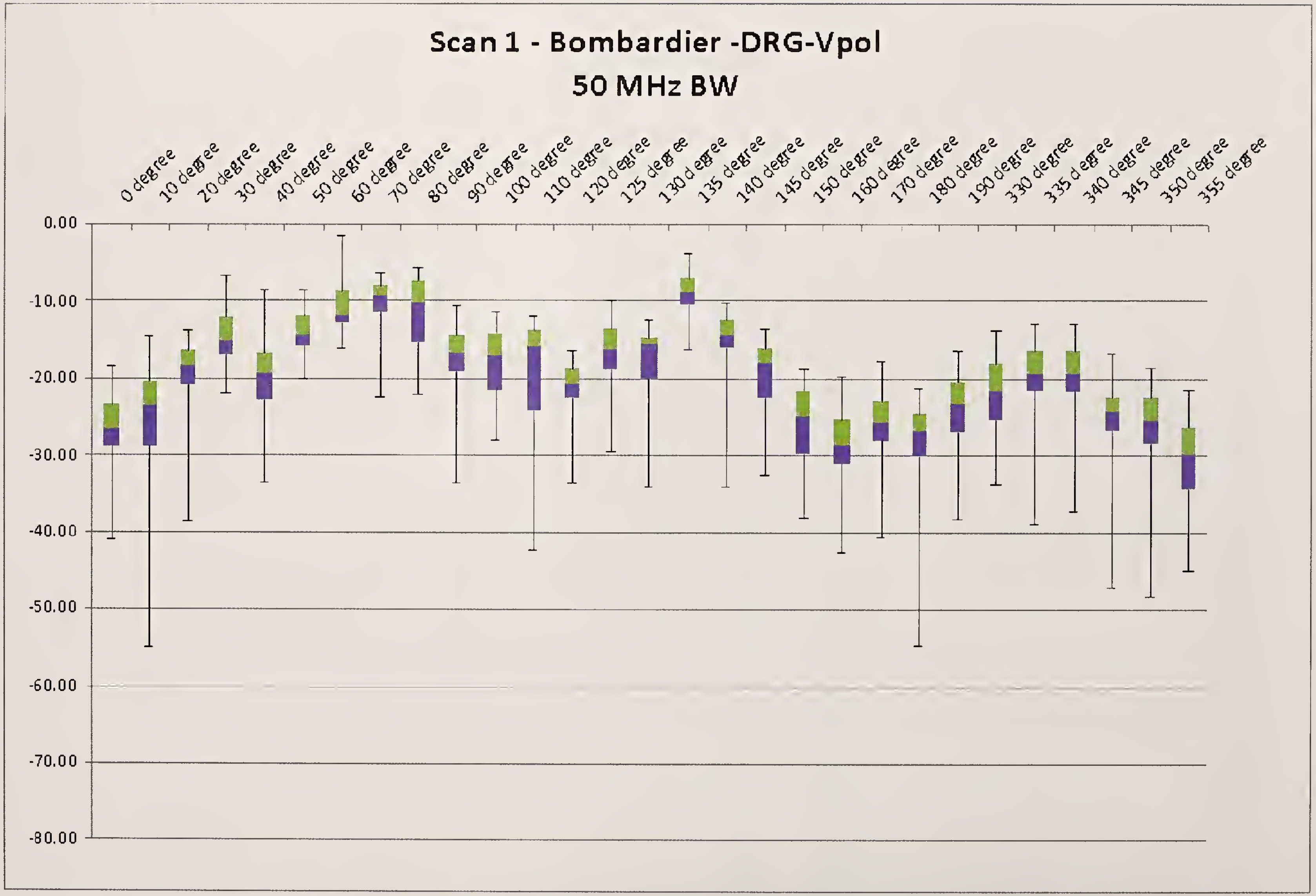


Figure C1. Whisker-box plots for the Bombardier Global 5000 with the receiving antenna in the main passenger cabin, showing results for the transmitting DRG horn antennas in the vertical polarization. These results cover a 50 MHz bandwidth centered around 1000 MHz.

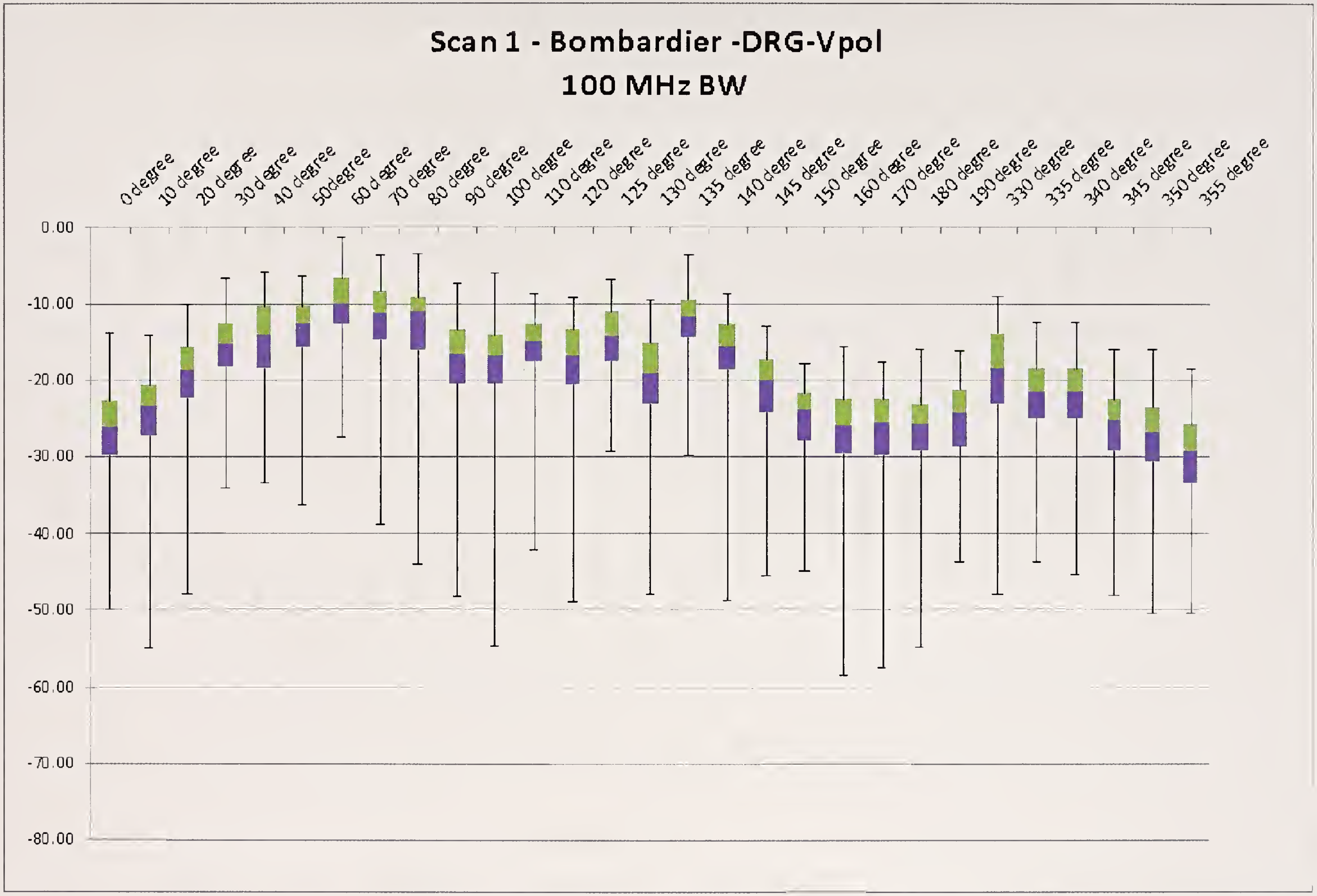


Figure C2. Whisker-box plots for the Bombardier Global 5000 with the receiving antenna in the main passenger cabin, showing results for the transmitting DRG horn antennas in the vertical polarization. These results cover a 100 MHz bandwidth centered around 1000 MHz.

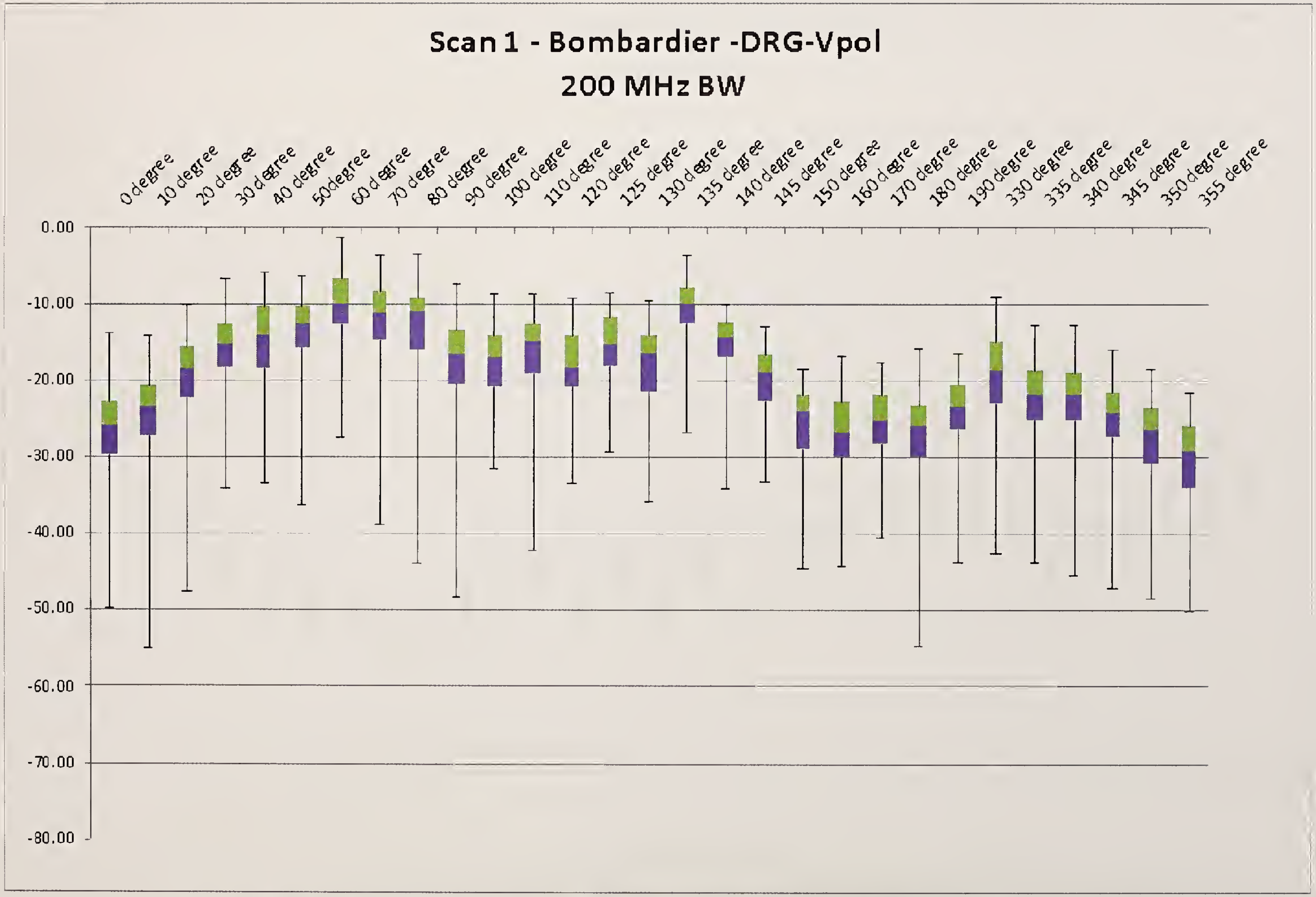


Figure C3. Whisker-box plots for the Bombardier Global 5000 with the receiving antenna in the main passenger cabin, showing results for the transmitting DRG horn antennas in the vertical polarization. These results cover a 200 MHz bandwidth centered around 1000 MHz.

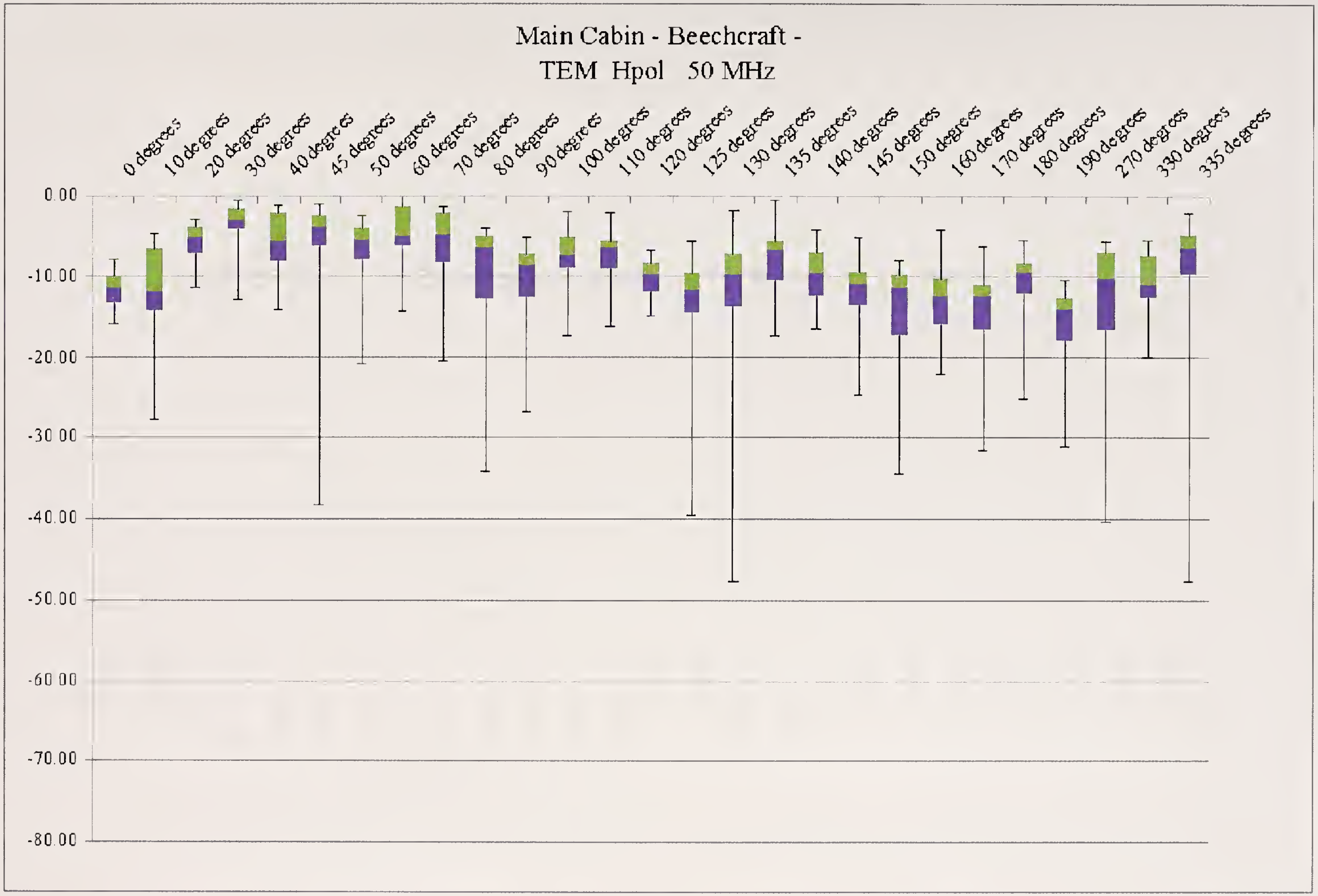


Figure C4. Whisker-box plots for the Beechcraft Premier IA with the receiving antenna in the main passenger cabin, showing results for the transmitting TEM horn antennas in the horizontal polarization. These results cover a 50 MHz bandwidth centered around 1000 MHz.

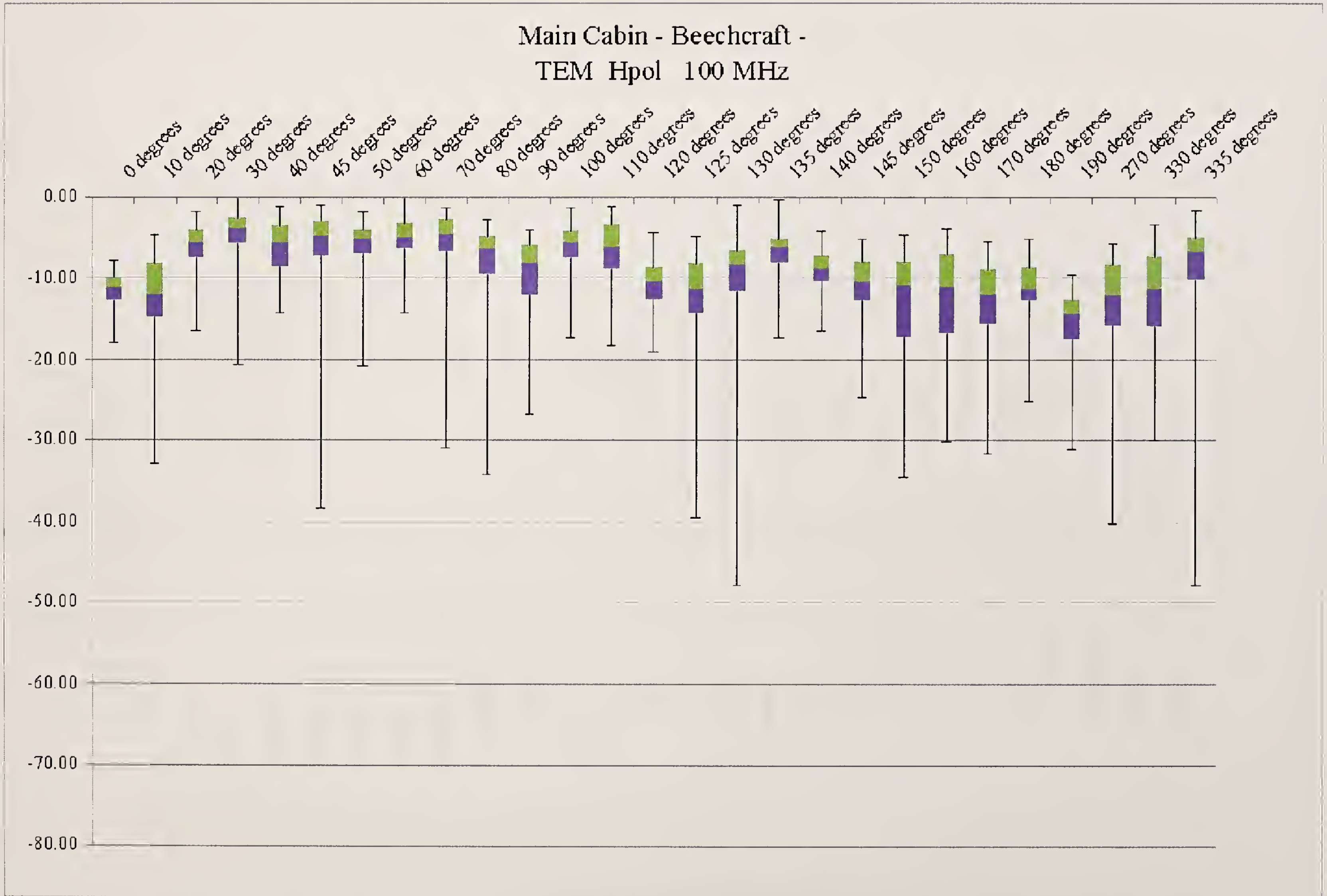


Figure C5. Whisker-box plots for the Beechcraft Premier IA with the receiving antenna in the main passenger cabin, showing results for the transmitting TEM horn antennas in the horizontal polarization. These results cover a 100 MHz bandwidth centered around 1000 MHz.

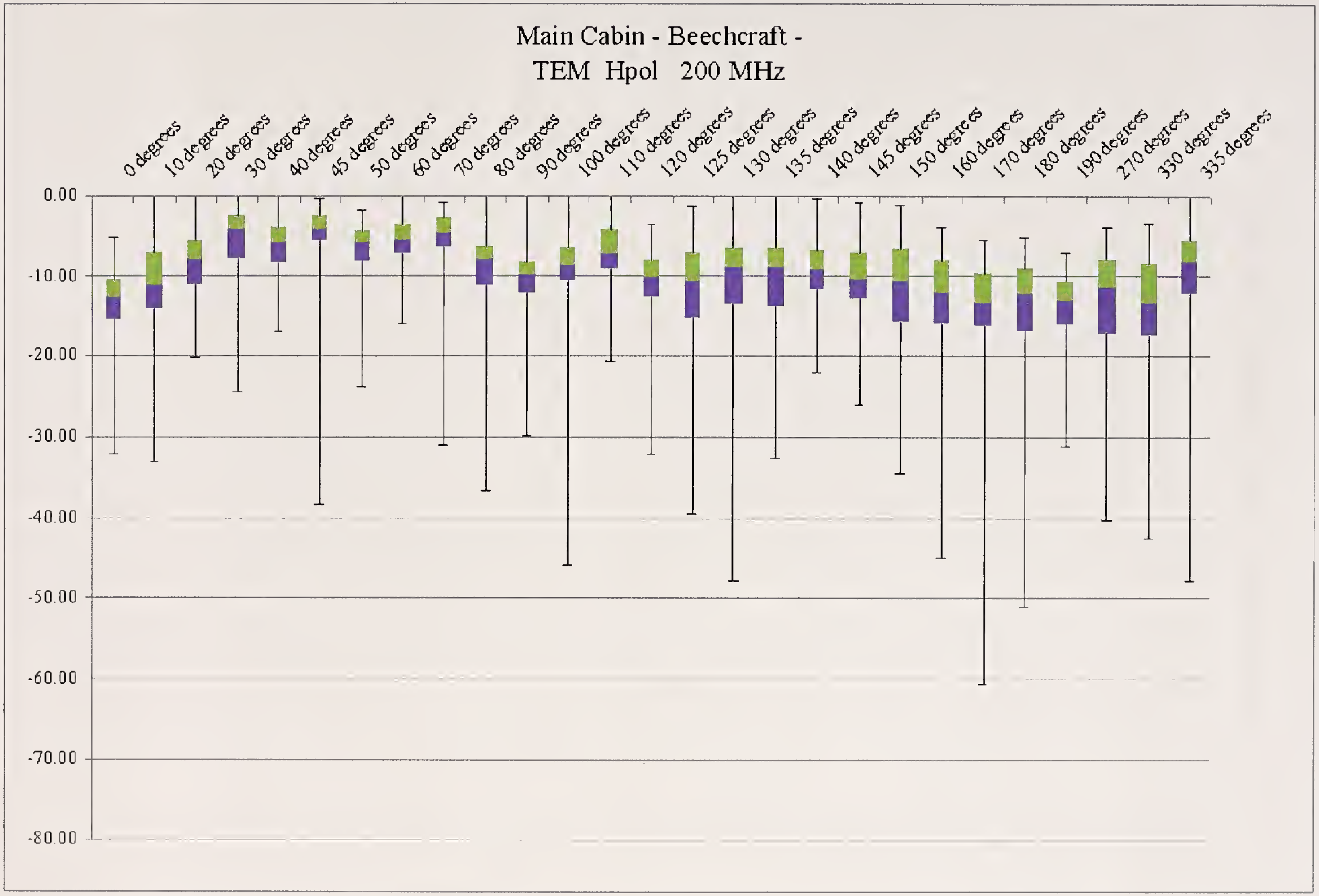


Figure C6. Whisker-box plots for the Beechcraft Premier IA with the receiving antenna in the main passenger cabin, showing results for the transmitting TEM horn antennas in the horizontal polarization. These results cover a 200 MHz bandwidth centered around 1000 MHz.

## Appendix D: Numerical Modeling of the 737-200

We have developed a numerical simulation study in order to help with our understanding of the propagation of electromagnetic fields both within and coupling to the outside of aircraft. This is intended to help us and the FAA understand more fully the impact of HIRF testing and HIRF field levels upon aircraft structures. We began with a well-characterized artifact that can be both measured and simulated in order to compare measurement with the model. We found that the model and the measurements agree to within some numerical error. We then adopted aircraft simulations by first developing a rectangular model and then later developing more complex structures that simulate a more realistic environment. Simulations in the present paper were completed at a frequency of 1 GHz but similar analyses could be extended to other frequencies. The only limitation at higher frequencies would be the increasing mesh size. We found that as the antenna is moved around inside the aircraft, the field behavior and propagation behavior change significantly. We also found that the seats inside the aircraft provide a certain amount of attenuation for the fields, and the apertures to the cargo bay help diffuse the fields inside the main cabin. For a dipole in the aft main cabin, the field levels from the dipole to the front of the main cabin drop from 100 V/m to 0.1 V/m. The propagation in the main cabin is also significantly impeded as the dipole is placed in the aft cargo bay. As we model the impact of windows, we find that leakage to the outside is not the same for every window; in other words, energy does not leak out of the windows equally; there is definite constructive and destructive interference that impacts the far-field radiation pattern of the aircraft. This changes as the transmitting antenna is moved around inside the aircraft.

Although a direct comparison to measured data are not available at this time, we do see the value of doing these types of measurements when confronting the validity of HIRF measurements and understanding the impact of testing procedures.

This work summarizes the initial numerical modeling studies undertaken to help us understand the interior aircraft propagation and to design test methodologies to address insight given here. The first task involved measuring and modeling a reference box artifact designed to provide a shielding value of approximately 20 dB (see Section 3). We compared the measurements and the model to give us confidence that the numerically modeled results are realistic. Using the model we can look at pattern effects, radiation effects and the complex field behavior set up inside the aircraft. The second section of this appendix shows the development of the aircraft model used to simulate the FAA's 737-200. The model builds up the aircraft from a basic structure and adds components such as compartments, seats, and windows until the final model is developed.

The software used to model the aircraft is a high-performance, full-wave electromagnetic field simulator using finite-element tetrahedra. In this package we can integrate the simulation, visualization, and solid modeling to obtain a complete picture of the simulated object. A three-dimensional model is drawn, material properties, input/output ports, boundaries are defined, and post-processing is used to look at either the S-parameters at certain ports or the fields on certain cut planes. Automatic meshing is used to further divide the region as the convergent criteria are approached.

## Appendix D1. The Reference Box Artifact

The measurements taken on the reference box, discussed in Section 3.1, were compared to a simulated reference box, and the results are briefly discussed here. We used the simulations to compare simulated and measured radiation patterns to ensure correctness of modeling software. A wire diagram of the simulated artifact with antennas is shown in Figure D1.

Because of the isotropic design of the box, we assume the measured radiation from the box is nearly uniform, with respect to angle. We do not assume this would hold true if holes were drilled on only one side of the box. We measured the box in four different environments: (1) the NIST reverberation chamber, with large modal density, (2) a large, enclosed industrial facility having some reverberant behavior, (3) the NIST anechoic chamber with virtually no environmental scattering [25–26], and (4) the NIST cone and ground plane facility located at NIST-Boulder, although in this case the cone was not used to generate a standard field for these measurements [43]. We built several models using varying paddle positions and then examined the complexity of the fields within the box and the radiation emanating from the 5 holes at the top of the box. This is shown in Figure D2. For the measurements we used a rotatable paddle and DRG horn antenna on the inside of the box and a DRG horn antenna on the outside of the box. We can see from Figure D2 the field complexity within the box and the complex radiation pattern outside the box. To simplify the model we replaced the dual-ridged horn within the box with a small dipole. This is a reasonable substitution, because in reverberation theory the gain of the antenna within the box is irrelevant and therefore simplifying the antenna reduces our solve time and allows us to use less memory in the model. Figure D3 shows the complex field behavior at the plane of the apertures, and Figure D4 shows the complex field behavior within and outside of the box with a dipole antenna as the source.

This particular model was created to simulate the measurements made in the lab. Figure D5 is a diagram showing the measurement setup in the lab. Measurements were taken at a distance of 1 m and 3 m away from the box with the 5 open radiation apertures of the box pointed upward (out through the page). The results of these measurements are shown in Figure D6, and the simulated radiated pattern is shown in Figure D7. We can see that the measured and simulated patterns are nearly identical in character. The radiation from the bottom of the box is less than that from the top of the box, where the radiating apertures are located. The patterns are not identical, possibly due to the apertures not being positioned exactly or other small variations in the model; however, they are similar enough that we feel the model is adequate to describe the complex field behavior in a realistic way.

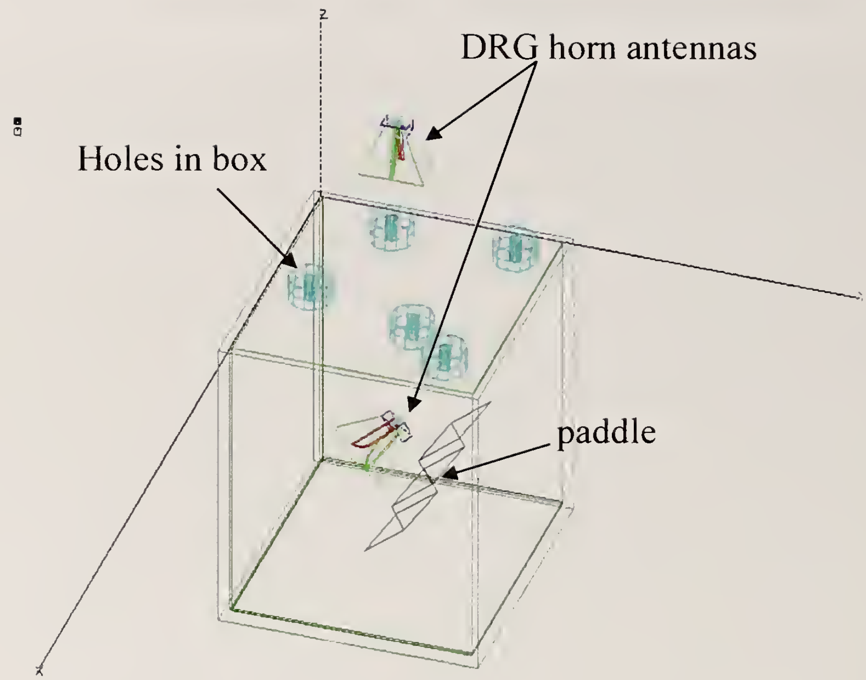


Figure D1. Wire diagram of simulated shielding artifact.

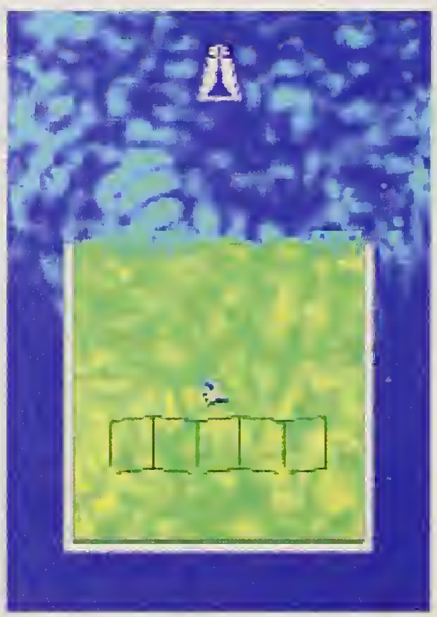

Figure D2. Complex field behavior inside simulated shielding artifact.

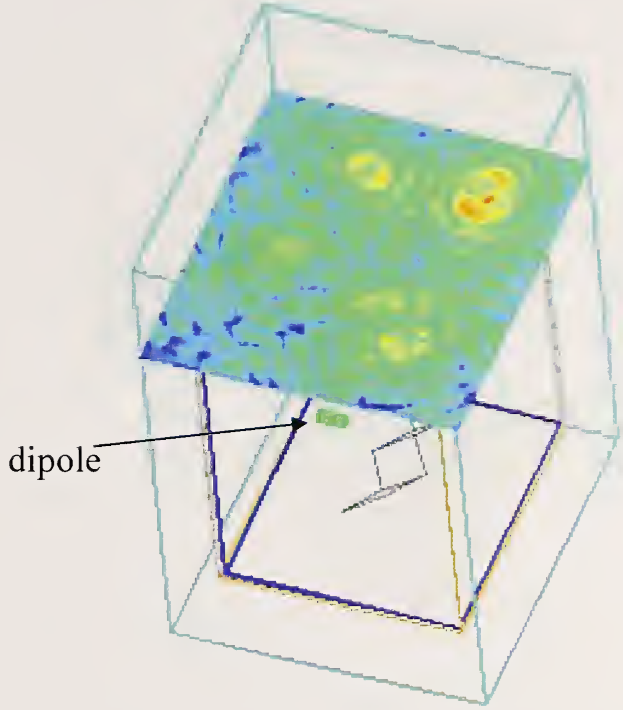


Figure D3. Dipole replacing dual-ridged guide antenna in shielding artifact.

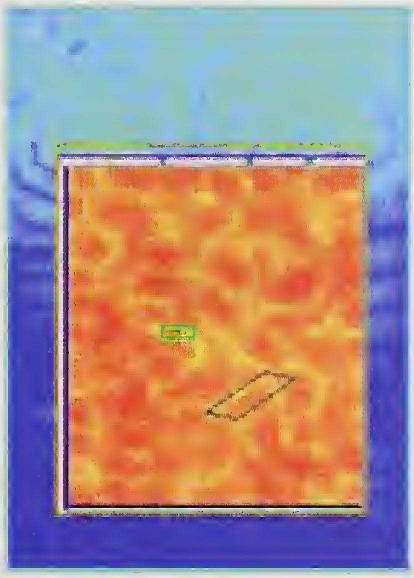

Figure D4. Complex field behavior in shielding artifact with DRG horn antenna replaced by dipole.

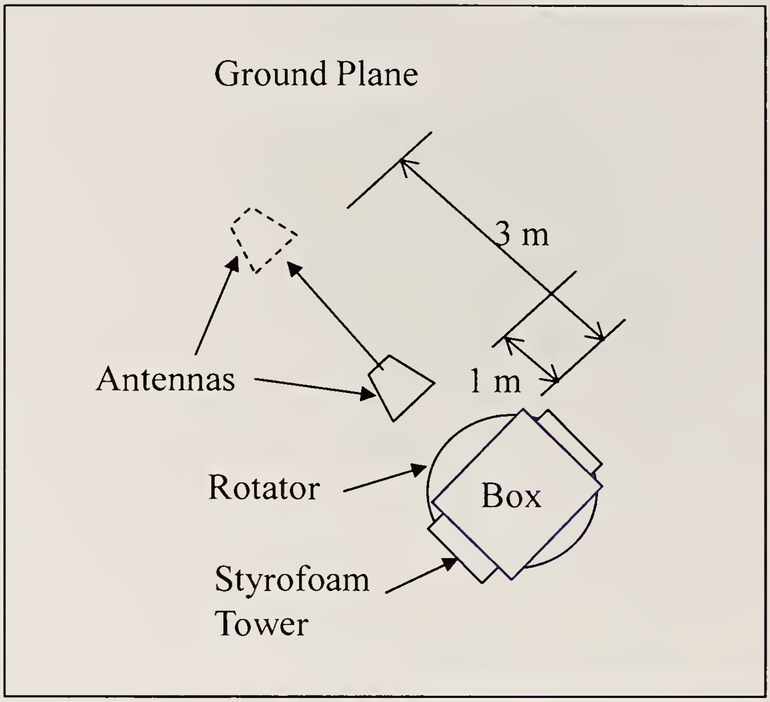


Figure D5. Measurement setup for shielding artifact.

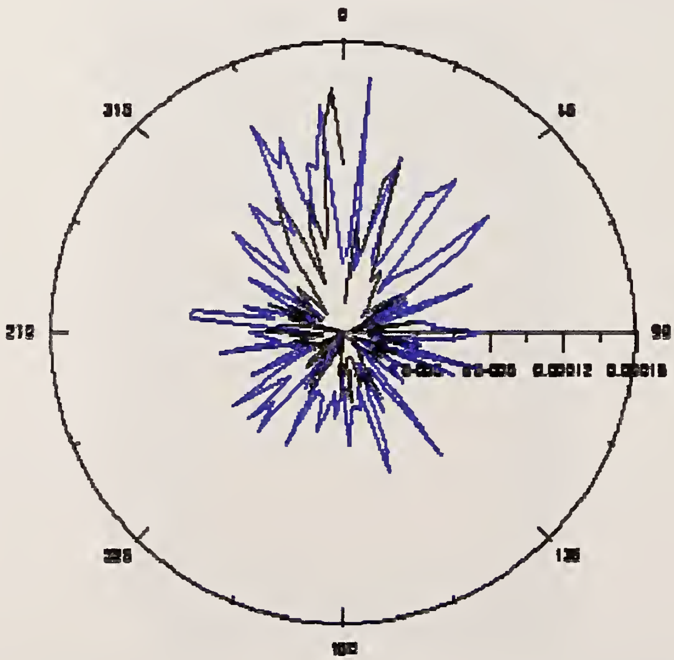


Figure D6. Measured radiation pattern from shielding artifact.

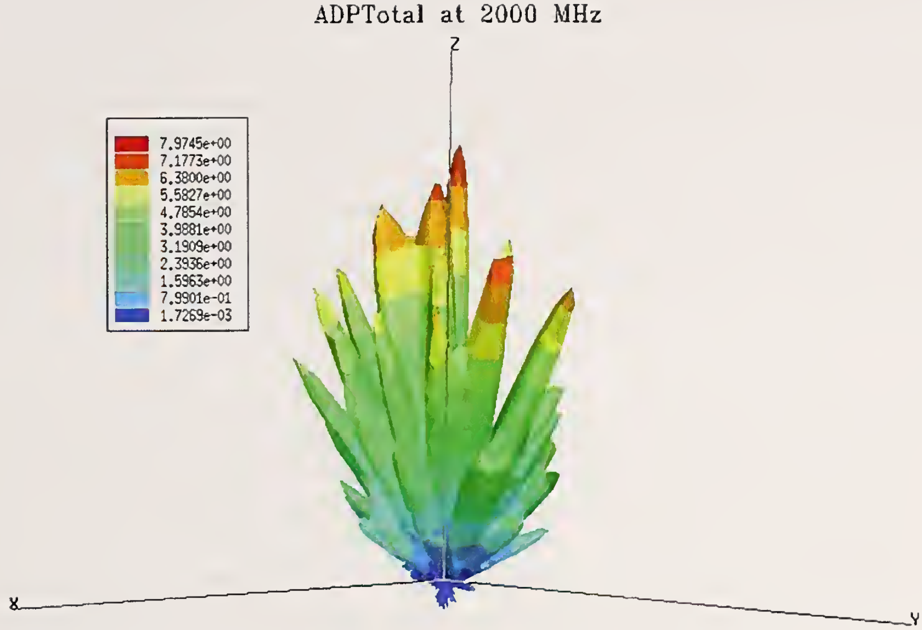


Figure D7. Simulated radiation pattern with 5 open apertures.

## Appendix D2. Simulation of the FAA's 737-200

We started the aircraft simulation model by placing a dipole into a simple rectangular box both with and without an aperture. The dipole is half-wavelength dipole resonant at 1 GHz, so the physical size is 15 cm. We saw that modal structure inside the box without the aperture could be affected by energy leaking in through a fairly large aperture in the side of the box when an aperture was included. For the next stage of development, the rectangular box was scaled to a rough approximation of the actual aircraft. Figure D8 shows the scaled rectangular box with the dipole source located toward the top of the model. Five apertures were added to simulate fields coupling to the outside of the model.

Although the scaled rectangular box is a good canonical model, we decided to develop an elliptical model that would be more realistic in terms of possible modal structure inside the cavity. A wireframe rendering of this elliptical model is shown in Figure D9. The dimensions of the model have been scaled down by a factor of 20, as shown in the figure. This model was based on the Boeing 737-200 aircraft located at the FAA Technical Center in Atlantic City, New Jersey. As shown in previous photos in Section 6, the aircraft seats were located in the first-class section of the aircraft and in the aft section of the aircraft. The seats in the middle section of the aircraft had been removed. This arrangement was the basis for our model. The seats were assigned a dielectric constant of about 2.6 in later models, and a bulk conductivity of $1\times10^{-16}$ Siemens/m, which are the values for polyethylene, a low-loss foam. We chose to eliminate metal backs for the seats, based on current airline standards.

Dimensional information from drawings of a 737-600 series aircraft were used because they are similar to those for the 737-200 series. The aircraft dimensions of a 737-600 are 31.25 m length, 3.54 m width and 4.14 m height. We scaled this down by a factor of 20 such that the model dimensions are 156.25 cm x 17.7 cm x 20.7 cm. We made the thickness of the aircraft hull 0.55 cm so that the radius of the inner ellipse is 8.85 cm x 10.35 cm. The hull was assigned properties for a perfect electrical conductor (pec) and the interior of the aircraft assigned vacuum properties. We do this to simplify the model and create a reference baseline upon which we can build. For the actual measurements we used our in-house developed TEM horn antennas and commercially available DRG horn antennas; whereas, for the model, we used a center-fed dipole antenna for the same reasons as discussed for the previous reference box model. The fuel tank sits between the forward and aft cargo bays, and in later models will be completely enclosed by a perfect electrical conductor.

We began with a simple model. Initially there are no coupling apertures to the outside of the aircraft. This eliminates the need for a radiation boundary and allows us to investigate the addition of various features inside the simulated aircraft before we complicate the model. Figure D10 shows one of the first developed models. The floor of the aircraft between the main cabin and cargo areas is modeled as a perfect electrical conducting sheet. In the first model, one aperture was cut in the center of this sheet. For this and subsequent models there is nothing to separate the fields from propagating through the main cabin into the flight deck or into the cargo bay areas at the front of the aircraft. In later models, we closed off the flight deck from the cargo bay areas but still maintain access from the main cabin, because the actual measurements showed that there was not a lot of shielding between the main cabin and flight deck. We set our solution frequency at 1 GHz. The modal structure inside in the main cabin is similar to those in the rectangular aircraft model, except that these modes have a longer resonant wavelength. Thus, the shape of the cavity appears to have an effect on the field structure. The electric fields leak through the flight deck and into the cargo bay area, but the fields couple more strongly through the single aperture in the floor. As we add more apertures, we will see that they become a dominant source of leakage into the cargo bays. For the next stage of model development we developed a floor structure that more closely approximates the structure found in an aircraft. The floor of an aircraft is composed of metal grid work over which a fiberglass panel is laid, creating a series of apertures in the floor. Although the exact dimensions of these openings are not known for our aircraft, our canonical model can provide a general understanding of the propagation and intensity of the fields coupling through these apertures. Figure D11 has the 15 apertures cut into the metal floor separating the main cabin and the cargo bay areas. This figure shows that the field intensity is more uniform in the cargo bay areas than for coupling from a single aperture. We also see a modal structure developing within the cargo bay. At this point there is still just a single cargo bay area into which fields can couple either from the main cabin through the flight deck or through the apertures in the floor. A 3-dimensional view of the fields is shown in Figure D12. The cuts are taken in the XZ and YZ planes of the dipole main cabin/cargo bay area. One of the first things we notice is that even though the dipole is located in the forward main cabin, we get a strong electric field at the back of the aircraft, due to moding. This tells us that a source in the front of the aircraft can create high field levels at the rear of the aircraft, and the fields can also appear at other vulnerable parts of the aircraft.

The next step in the creation of the model was to incorporate seats with the properties discussed above. We began by locating six seating areas in the "first class" section. We did not create individual seats but merely fused the three seats together to approximate the actual seating areas. We were also able to turn off certain apertures in the floor to simulate the forward and aft cargo bays without creating hard boundaries. Figure D13 is a wireframe model showing the six seats of polyethylene whose loss characteristics are given above. There are six apertures in the floor in the forward part of the aircraft to simulate openings to the forward cargo bay. There are nine apertures toward the rear of the aircraft to simulate openings to the aft cargo bay. The dipole antenna is located in the same position as previous models, and the fields are still allowed to couple through the flight deck around to the cargo bay areas. Adding a finite number of seats to the main cabin results in energy being lost from the fields, and so less fields propagate toward the back of the aircraft or down into the cargo bay areas. We see more localized areas of the field within the main cabin and cargo bay areas, so we no longer have a uniform field distribution inside the aircraft. The wireframe model geometry is shown in Figure D14 for the additional seating, and Figure D15 shows the field distribution. The model shows that the field distribution in the cargo bay areas now have a different modal structure due to the diminishing field strength, and we also see that the fields in the aft part of the main cabin are diminished by at least half in the presence of additional seating. We also note that the null in the electric field has moved toward the aft main cabin, which results in a longer wavelength and lower resonant frequency for the compartment.

The next stage in our model development was to separate the cargo bay areas into the forward cargo bay, the fuel tank, and the aft cargo bay, and look at the coupling into each of these individual compartments. During this first separation, we did not isolate the fuel tank completely from the main cabin but allowed the fields to penetrate the floor apertures. Figure D16 is a rotated view of the geometry along the YZ-plane to give us an idea of where the apertures intersect each of the cargo bay areas and how the fields behave when the fields are completely isolated from one compartment to the other. Figure D17 is a close-up view of the separation between the forward cargo bay and the fuel tank area, and Figure D18 shows the separation between the fuel tank area and the aft cargo bay. These views show us that the fields are not leaking through the walls of the individual compartments into adjacent compartments. The result of introducing more compartments is that the fields are further disrupted, the field levels are lower, and the behavior is more complex in the main cabin and cargo bay areas. Figure D19 shows the full model with the fuel tank isolated from the rest of the aircraft.

The next phase of the simulation involved creating an aperture to the outside of the aircraft. We began by adding just a single window that was approximately the size of the windows on a real aircraft, which are 35.6 cm (14 in.) x 35.6 cm (14 in.). We do not see much leakage through this small aperture and don't see much activity on the outside of the aircraft with a single aperture. We believe that this is because the window is acting like a waveguide with a cutoff frequency below 1 GHz, the solution frequency. We added an array of 10 windows on one side of the aircraft but didn't see much radiation, so we moved to 30 windows on a single side of the aircraft. This new model is shown in Figure D20. This is a close-in view of the windows closest to the radiating dipole. The field cut was taken in the center of the XZ-plane of the windows. We do see that the fields leak through some windows more strongly than others. Figure D21 shows the fields closer to the aft section of the aircraft away from the radiating dipole and we see that the fields do not appear to leak out of these windows, due to the fact that the field levels are lower. Figure D22 is the same model solved at 1.05 GHz. The field structure is quite a bit different even for such a small frequency difference.

The final step in the current step of modeling was to move the dipole around the interior of the aircraft as if a cell phone were emitting in different parts of the aircraft to understand field levels. The first location for cell phone radiation was in the forward cargo bay, as if someone had left it in a piece of luggage. Figure D23 shows the field levels in the XZ-plane cut along the XZ-axis of the dipole that is in the lower half of the aircraft. Figure D24 shows the field levels in the main passenger cabin for a dipole in the forward cargo bay. The fields in the aft cargo bay have made their way from the forward cargo bay, through the main cabin and have entered the aft cargo bay through the apertures in the floor. Figure D24 is a YZ-plane cut along the dipole axis showing how the fields propagate through the main cabin into the aft cargo bay. We see the field levels decrease as the fields propagate from the forward main cabin, possibly first class, through the seats and back into the aft of the main cabin. At this point, we have now also isolated the forward cargo bay from the flight deck by applying a metal separation, as was done previously to separate the cargo bay from the "fuel tank" area. The next thing we did was to move the cell phone into the aft cargo bay to look at the field propagation in the same three planes as in the previous position. Figure D26 shows the field levels along the XZ dipole plane which show fields in the cargo bay areas. The interesting thing is that this position is not reciprocal to the cell phone being in the forward cargo bay. There are virtually no fields propagating in the forward cargo bay when the cell phone is ringing in the aft cargo bay.

To obtain a somewhat three-dimensional view, we plotted the XZ/YZ planar cuts to look at the fields in the aircraft when the dipole was located in the aft cargo bay, as shown in Figure D26. The final location for the dipole (cell phone/source) was to move it toward the rear of the main cabin. Finally, we assembled "3D views" of the field distribution along these two planes as shown in Figures D27 and D28. Again, there are virtually no fields that make it into the forward cargo bay area or the flight deck. Most of the energy is dissipated in the rear of the aircraft and the aft cargo bay areas. What was interesting, and zoomed in on in Figure D27, was the localized field intensity where the seat locations are in the rear of the aircraft. These are specifically pointed out in Figure D28.

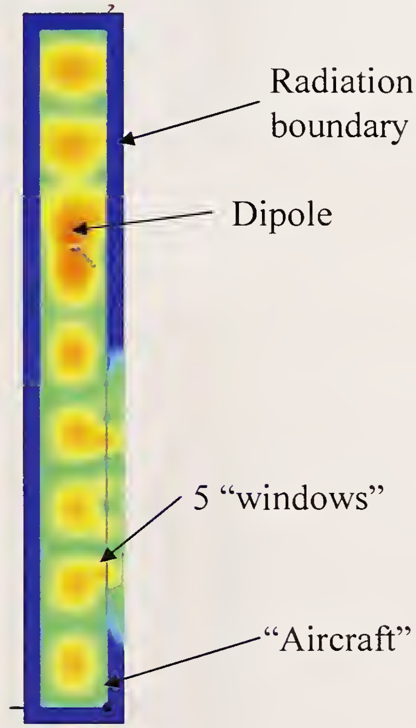


Figure D8. Rectangular model of scaled aircraft showing modal structure and leakage from five apertures.

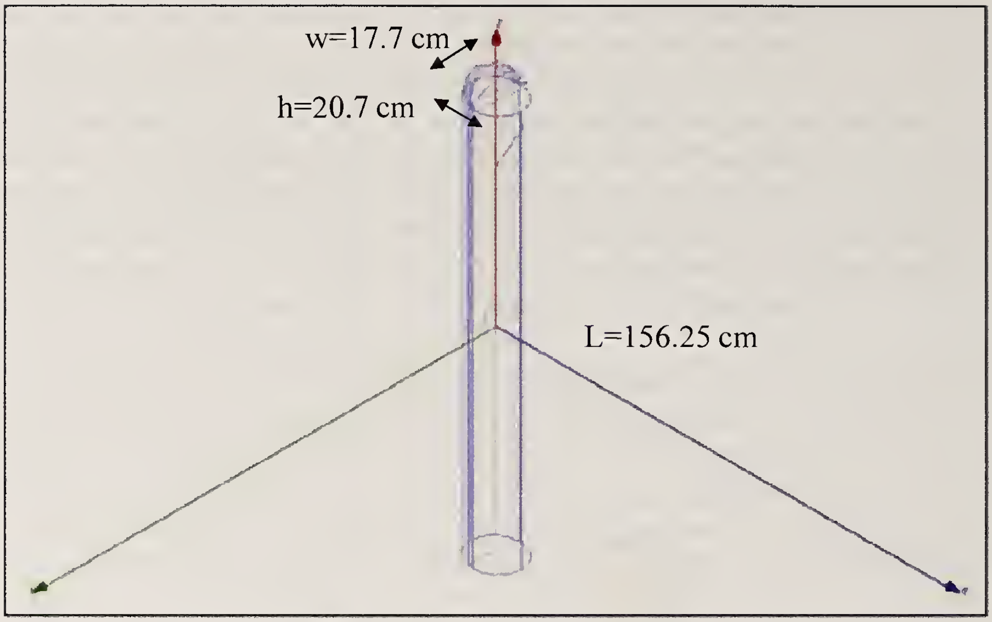


Figure D9. Wireframe diagram for elliptical aircraft model with dimensions.

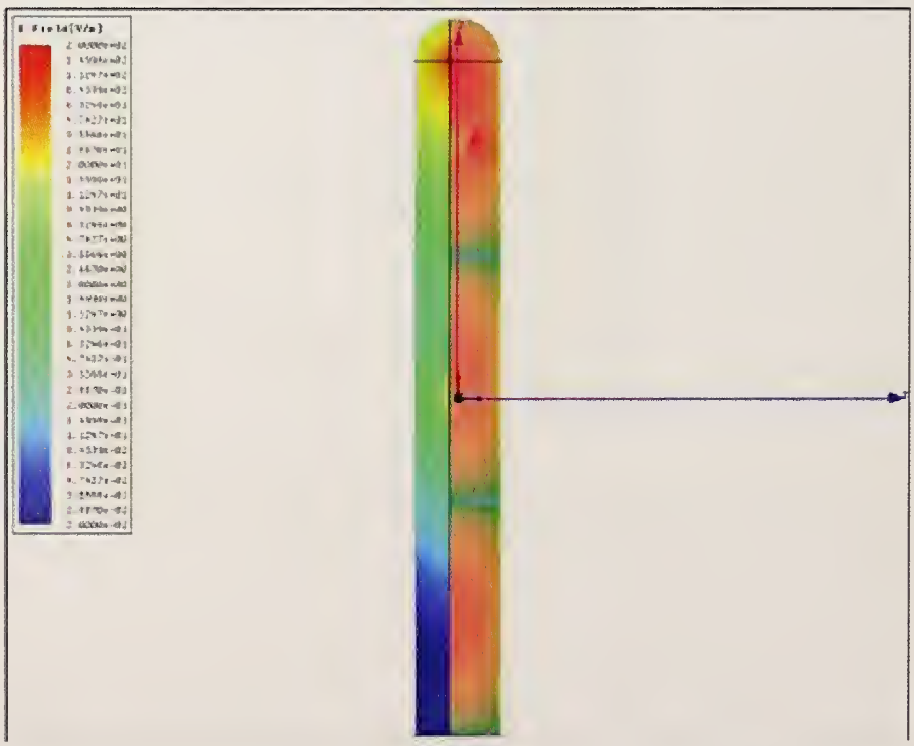

Figure D10. 737 elliptical model with no seats, no cargo bays, and 1 aperture cut into the floor.

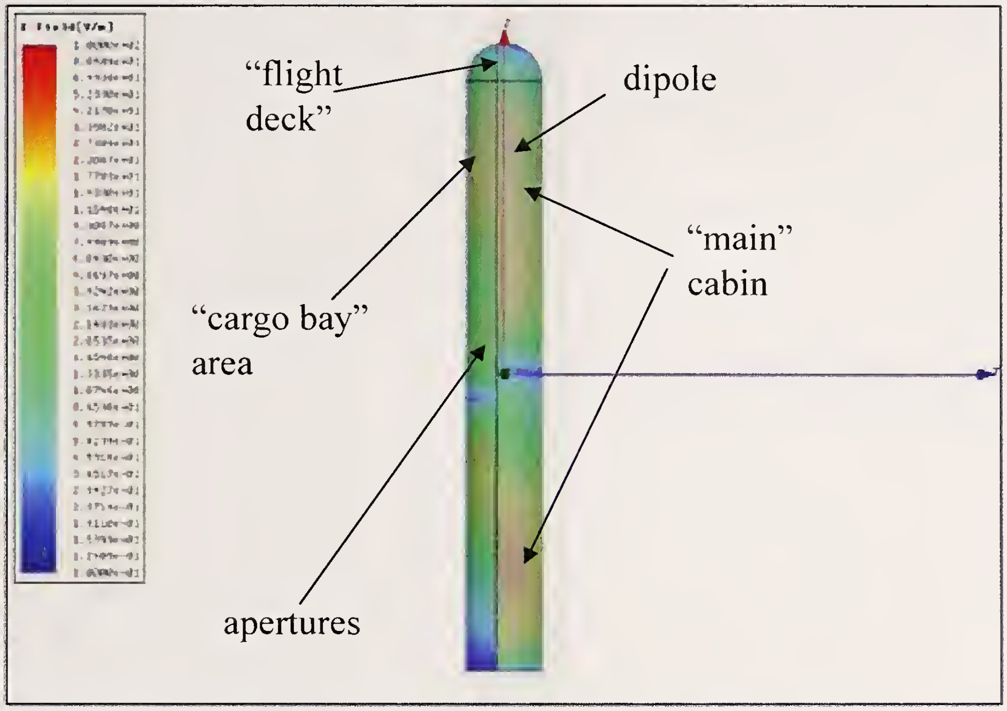


Figure D11. 737 elliptical model with no seats, no cargo bays, 15 apertures cut into metal floor between main cabin and cargo bay.

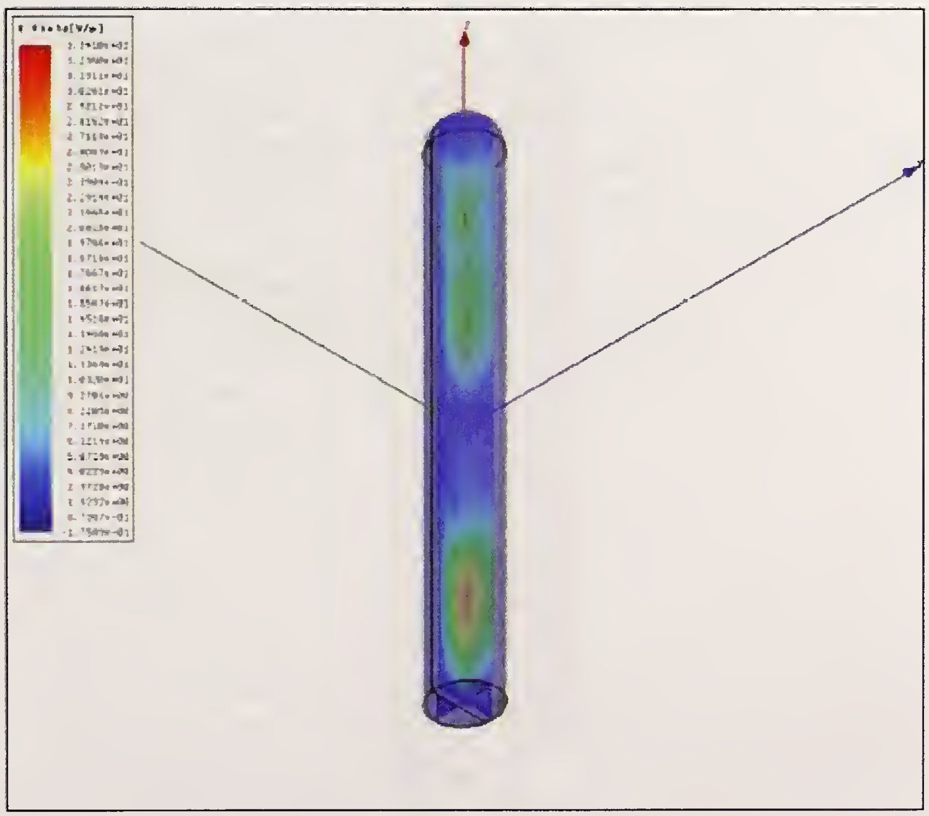

Figure D12. 737 elliptical model with E-field planar cuts along the XZ dipole plane and the main cabin/cargo bay YZ axis.

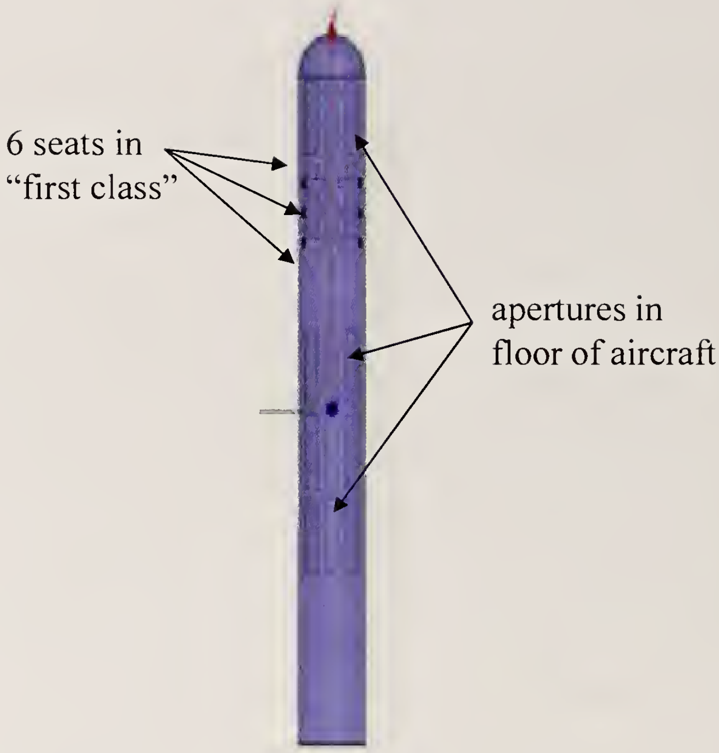


Figure D13. Wireframe model of the 737 elliptical model showing model geometry with 6 seats and 15 apertures.

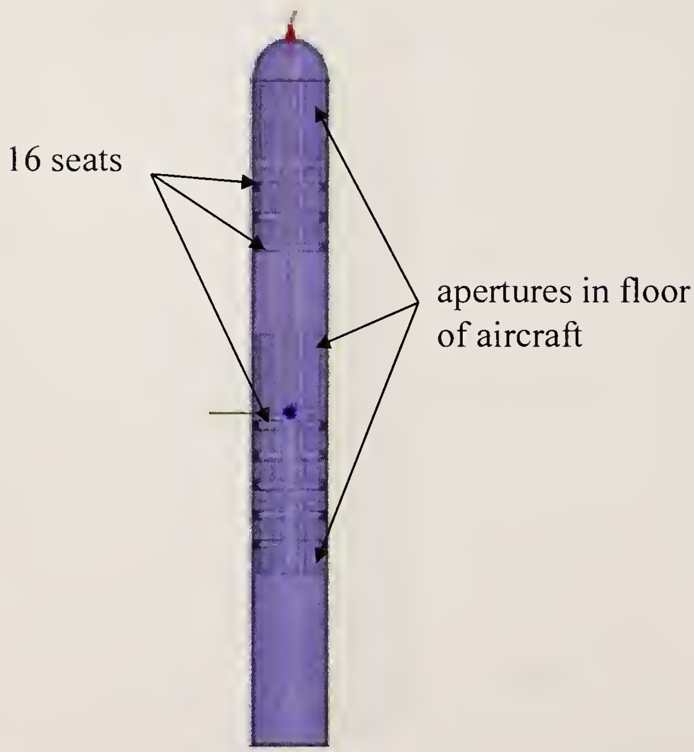


Figure D14. Wireframe model 737 elliptical model with 15 apertures to cargo bay area and 16 polyethylene seats.

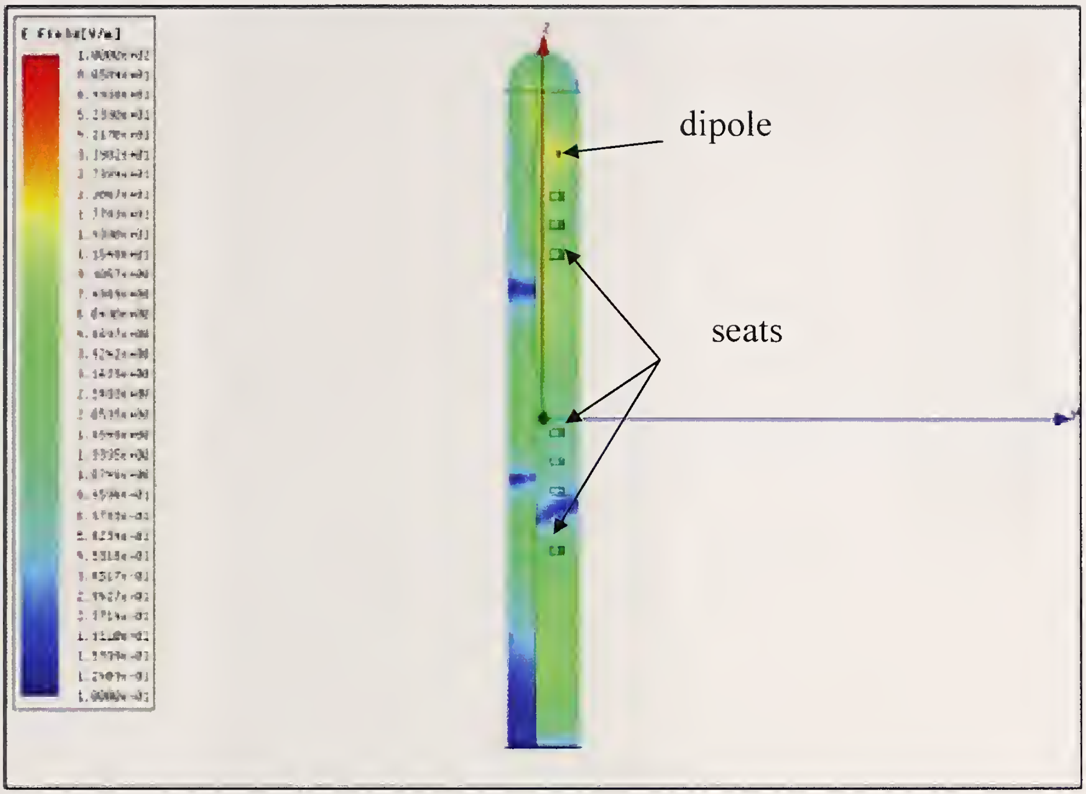


Figure D15. 737 elliptical model with 15 apertures in cargo bay area and 16 polyethylene seats.

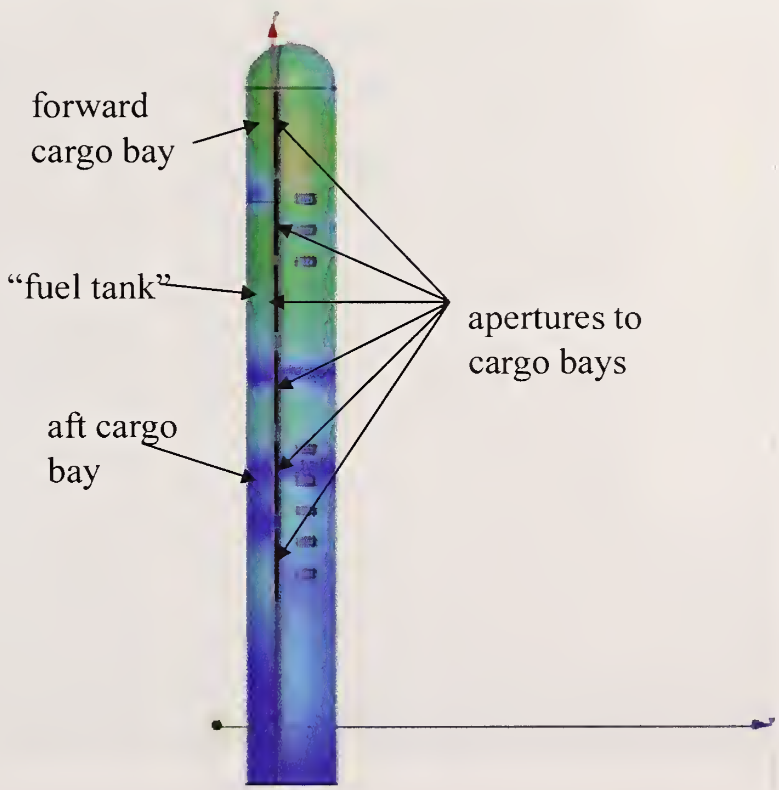


Figure D16. Full model with 16 seats, 15 apertures, no windows, and separate cargo compartments.

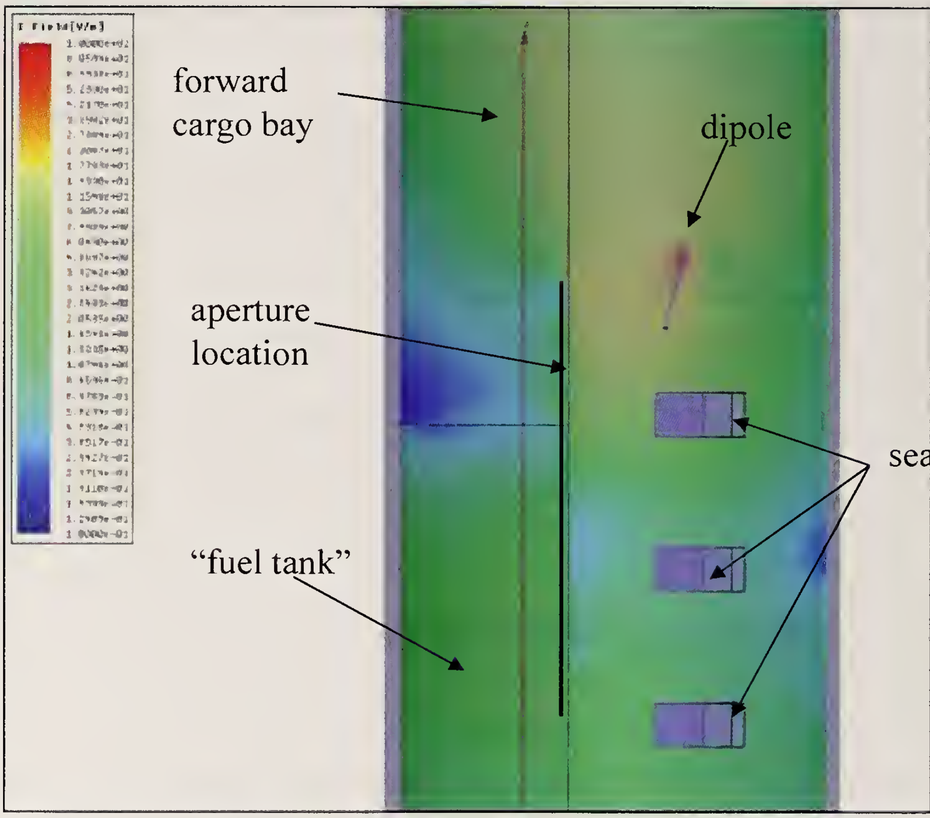


Figure D17. Close-up view showing separation between forward cargo bay and "fuel tank" area.


Figure D18. Close-up view of separation between "fuel tank" area , the aft cargo bay, and the aft main cabin.

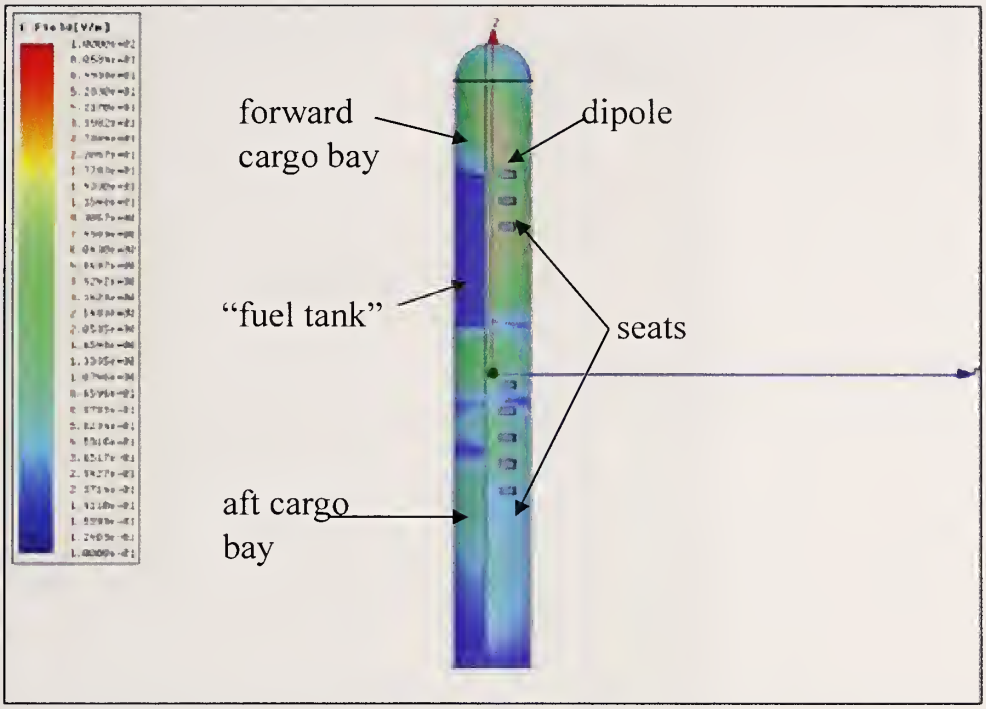


Figure D19. Model showing the isolation of the "fuel tank" area from the fields.

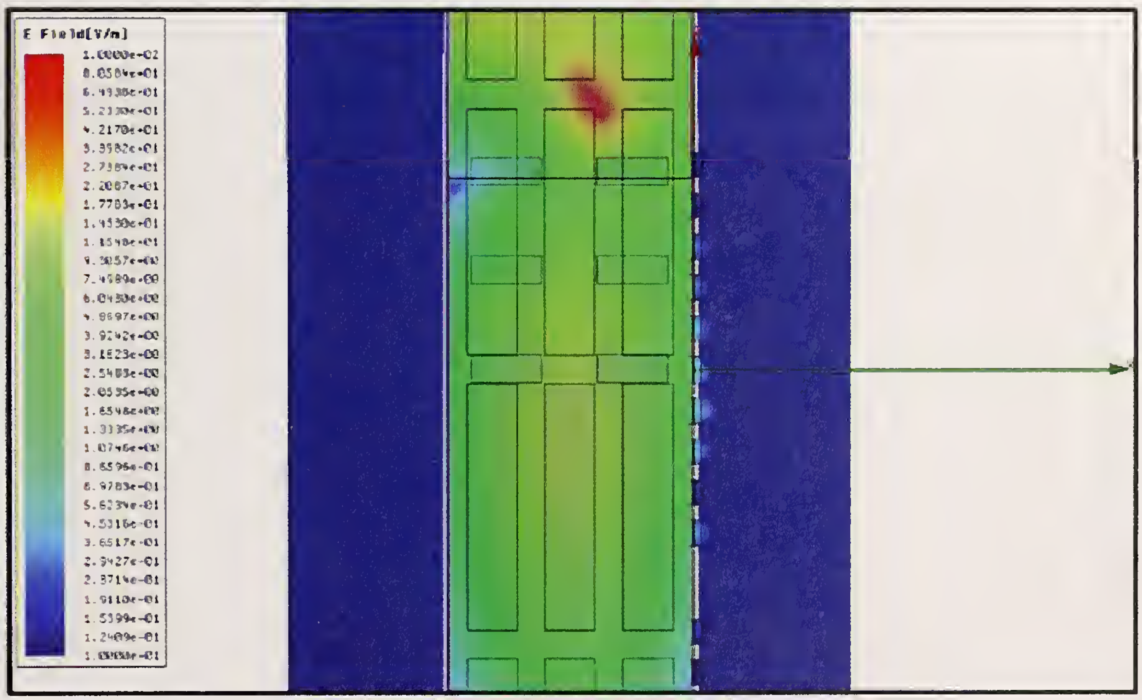


Figure D20. Radiation from windows located closest to dipole.

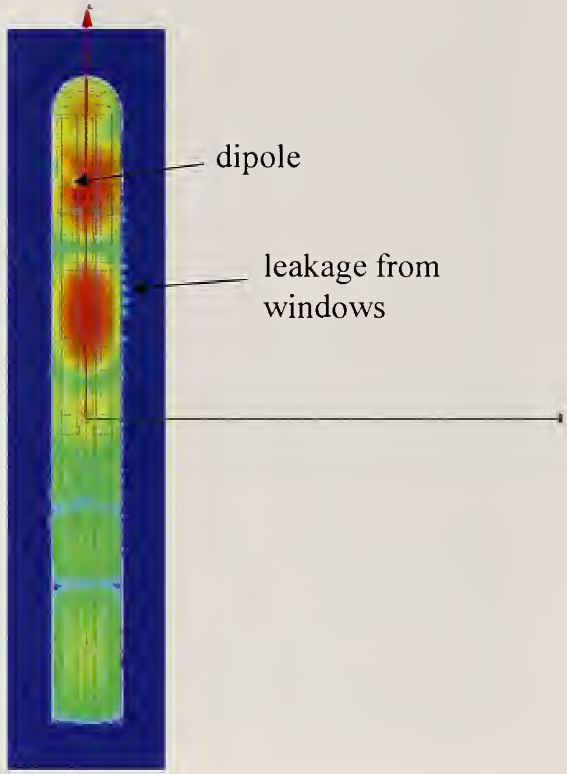


Figure D21 Fields inside and through windows at a solution frequency of 1.05 GHz.

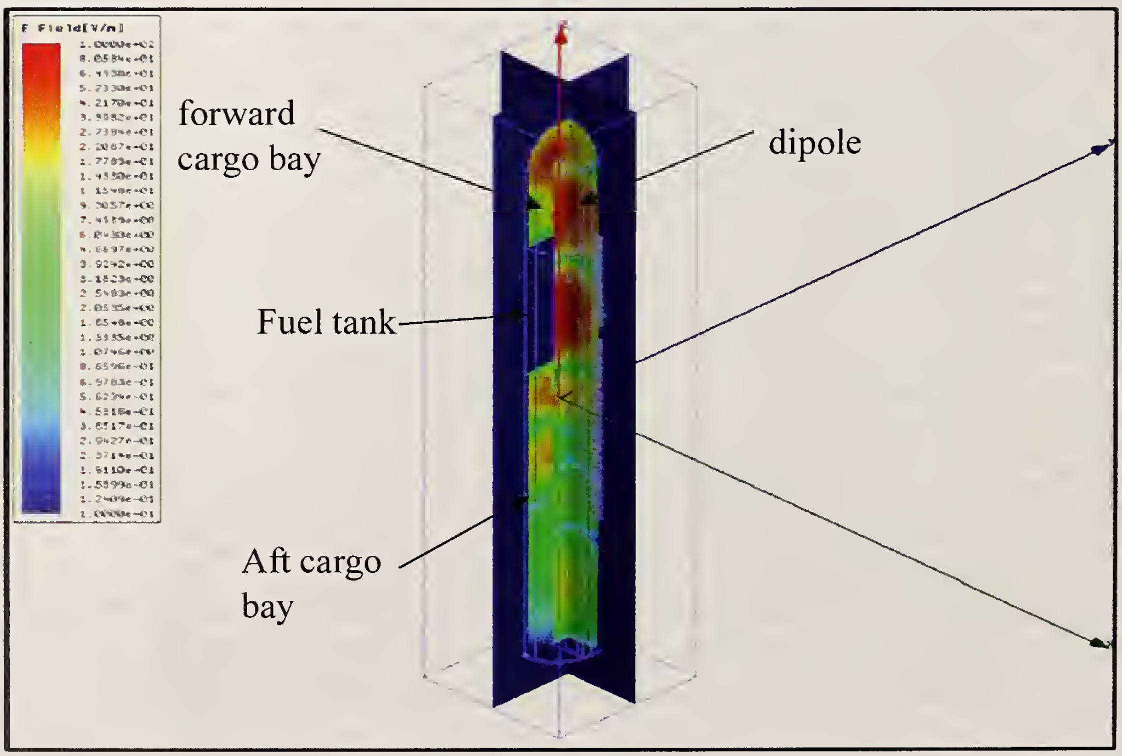


Figure D22. Planar cuts along cargo bay and windows at a solution frequency of 1.05 GHz.

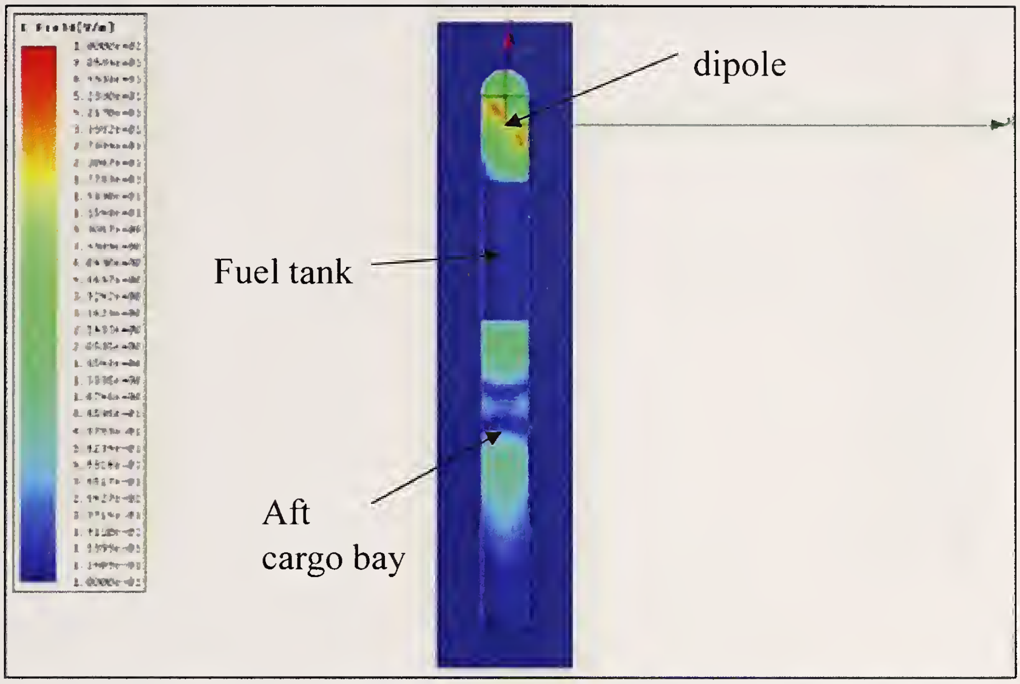


Figure D23. Fields in cargo bay areas, cut along the XZ dipole plane located in the forward cargo bay in the lower half of the aircraft.

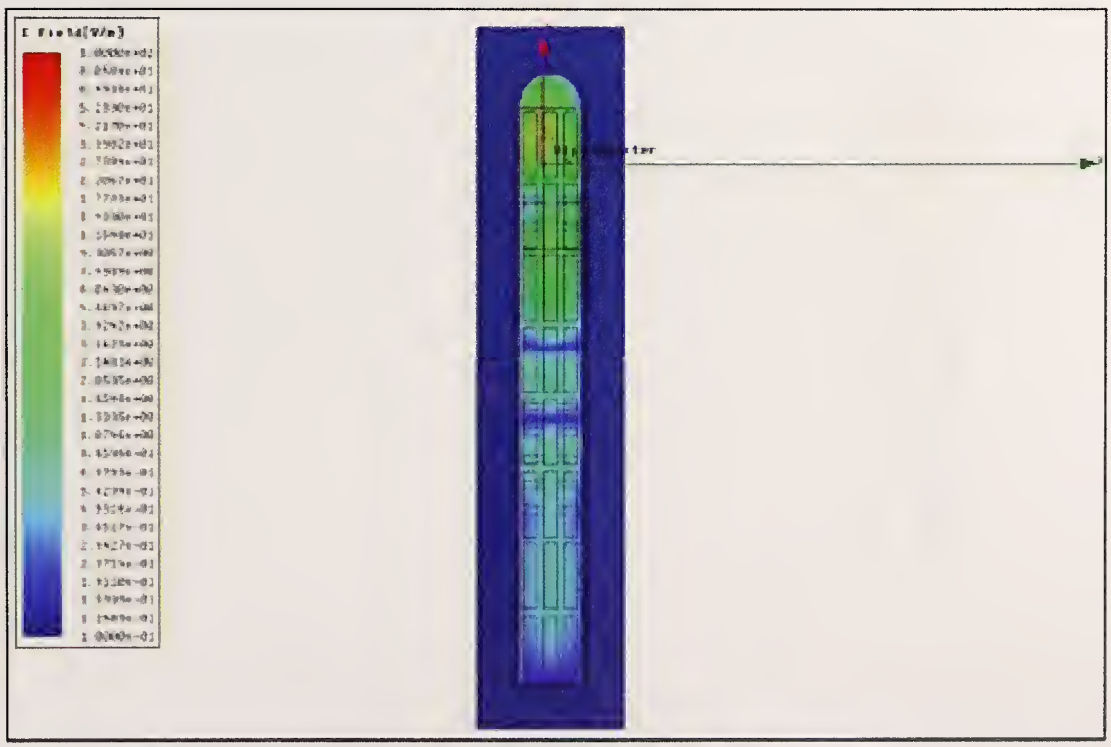

Figure D24. Field levels in main cabin with dipole in forward cargo bay. The cut is taken along the XZ dipole plane.

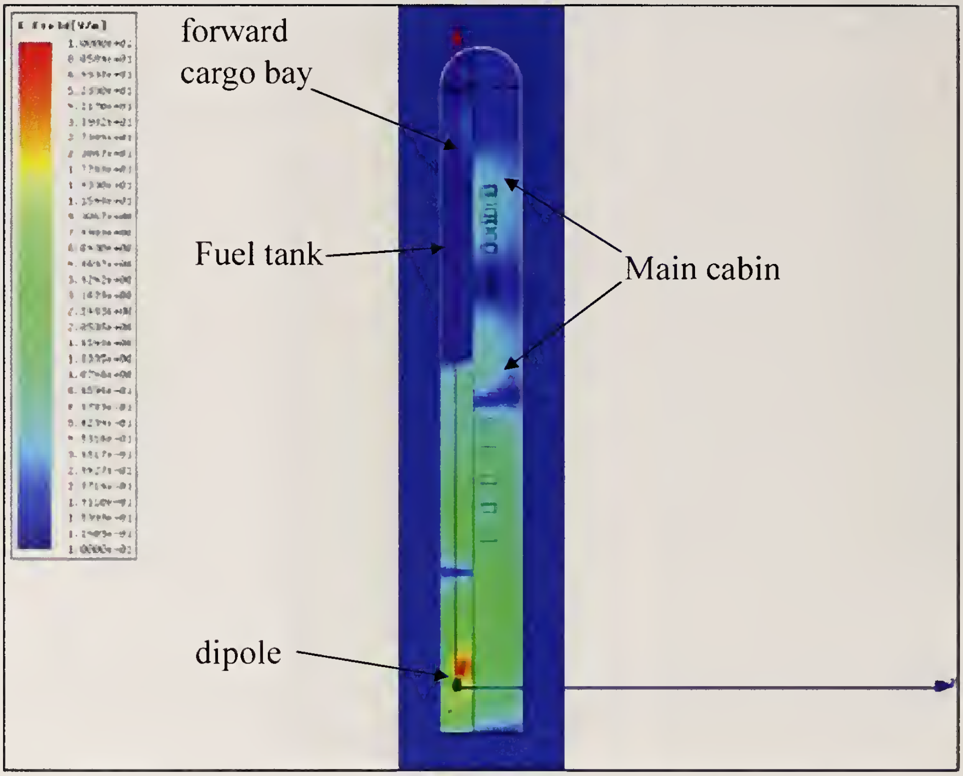


Figure D25. YZ plane cut along dipole axis showing fields propagating from aft cargo bay through main cabin and into forward cargo bay.

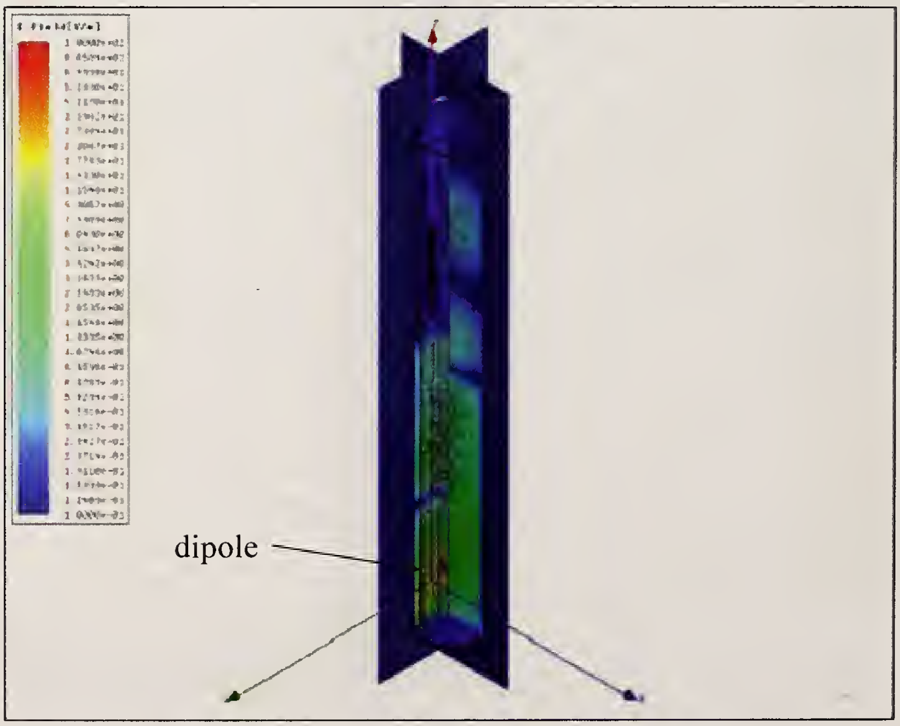


Figure D26. Fields in the XZ and YZ planes with the dipole in the aft cargo bay.

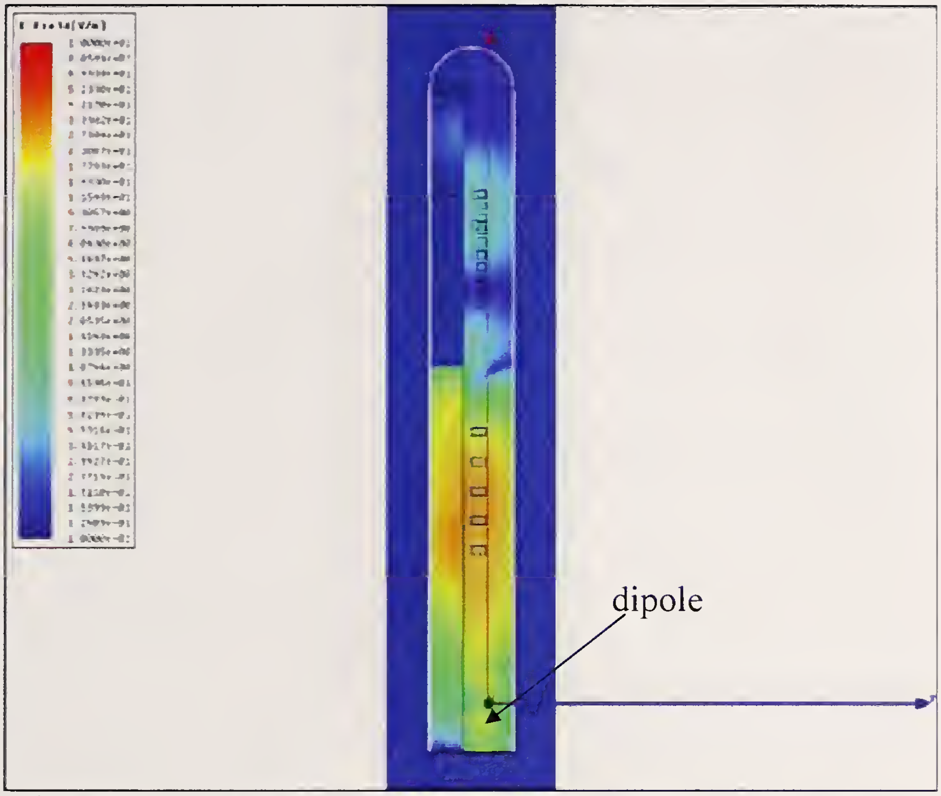


Figure D27. YZ dipole plane cut with the dipole located in the aft main cabin.

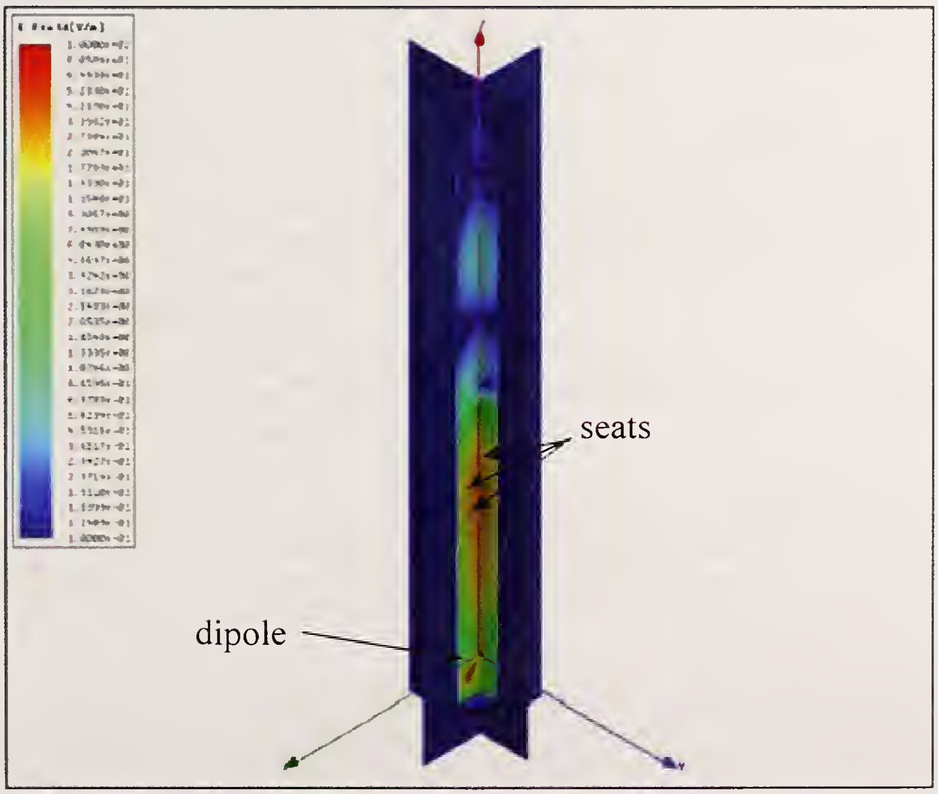


Figure D28. "3D" view of fields in aircraft with the dipole located in the aft main cabin.

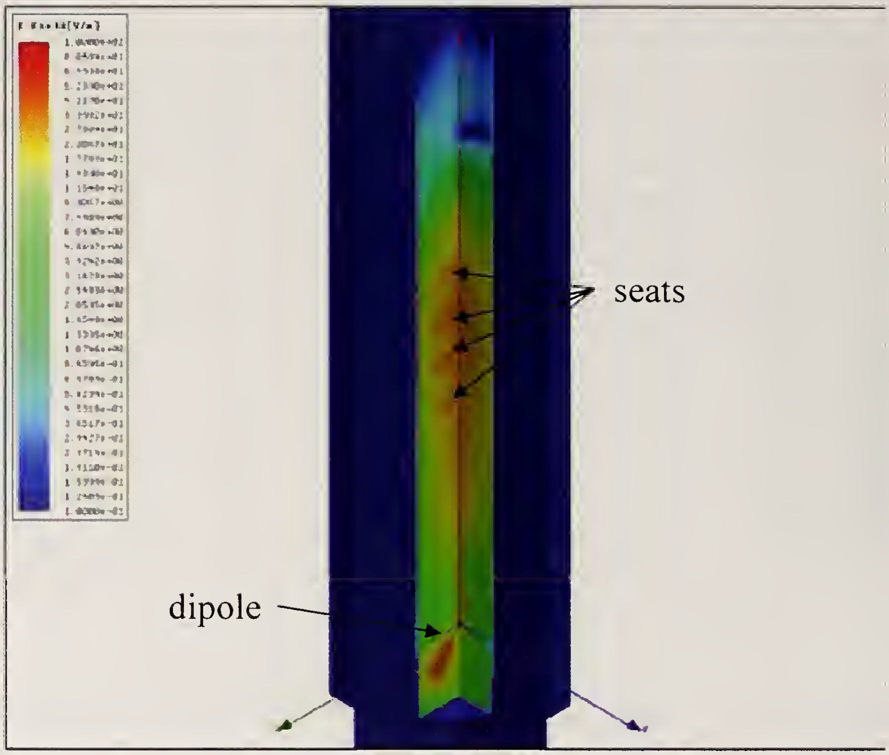


Figure D29. Zoom-in view of Figure D27 showing increased field intensity in the seats of the aircraft.

## Appendix E: 737-200 Measurement Equipment List*

The main equipment used in the evaluation of the Bombardier Global 5000 is listed below:

- Agilent N5230A PNA-L (300 kHz to 18 GHz) with a maximum of 16001 frequencies/trace.
- Hewlett Packard 8753ES VNA (30 kHz to 6 GHz) with a maximum of 1601 frequencies/trace.
- Insulated Wire (IW) Cables (4 m to 10 m)—we used phase-stabilized cables to avoid phase drift with temperature variations.
- Miteq Optical Fiber Link MDDR/MDDT (11 GHz version)—this unit has the ruggedness and temperature characteristics for field use.
- Miteq Optical Fiber Link SCMR/SCMT (18 GHz version)—this unit has the ruggedness and temperature characteristics for field use.
- HP 11713A Switch Controller and HP 3781 Switches
- HP 59306A Relay Actuator
- HP E3615A DC Power Supply for relay control
- AML 0120L2403 Amplifier for DRG antennas
- Harrison 6205 DC Power Supply
- Two 1.2 m TEM Horn Antennas designed and built at the NIST Boulder Laboratories
- One 36 cm TEM Horn Antenna designed and built at the NIST Boulder Laboratories
- Three 3115 DRG Horn Antennas
- NIST-developed "RADAR" Labview program used to perform time/frequency transformations, time gating, and signal processing
- NIST-developed "multical" Labview program used to perform multiband VNA calibrations and to circumvent the limitation of only 16001 frequency points. This program permits an arbitrarily large number of frequency points. In practice, we typically use as many as 48003 points.

---

* Certain commercial equipment, instruments, or materials are identified in this paper in order to adequately specify the experimental procedure. Such identification does not imply recommendation or endorsement by the National Institute of Standards and Technology, nor does it imply that the materials or equipment identified are necessarily the best available for the purpose.

# *NIST* *Technical Publications*

## *Periodical*

**Journal of Research of the National Institute of Standards and Technology**—Reports NIST research and development in metrology and related fields of physical science, engineering, applied mathematics, statistics, biotechnology, and information technology. Papers cover a broad range of subjects, with major emphasis on measurement methodology and the basic technology underlying standardization. Also included from time to time are survey articles on topics closely related to the Institute's technical and scientific programs. Issued six times a year.

## *Nonperiodicals*

**Monographs**—Major contributions to the technical literature on various subjects related to the Institute's scientific and technical activities.
**Handbooks**—Recommended codes of engineering and industrial practice (including safety codes) devel- oped in cooperation with interested industries, professional organizations, and regulatory bodies.
**Special Publications**—Include proceedings of conferences sponsored by NIST, NIST annual reports, and other special publications appropriate to this grouping such as wall charts, pocket cards, and bibliographies.
**National Standard Reference Data Series**—Provides quantitative data on the physical and chemical properties of materials, compiled from the world's literature and critically evaluated. Developed under a worldwide program coordinated by NIST under the authority of the National Standard Data Act (Public Law 90-396). NOTE: The Journal of Physical and Chemical Reference Data (JPCRD) is published bimonthly for NIST by the American Institute of Physics (AIP). Subscription orders and renewals are available from AIP, P.O. Box 503284, St. Louis, MO 63150-3284.
**Building Science Series**—Disseminates technical information developed at the Institute on building materials, components, systems, and whole structures. The series presents research results, test methods, and performance criteria related to the structural and environmental functions and the durability and safety characteristics of building elements and systems.
**Technical Notes**—Studies or reports which are complete in themselves but restrictive in their treatment of a subject. Analogous to monographs but not so comprehensive in scope or definitive in treatment of the subject area. Often serve as a vehicle for final reports of work performed at NIST under the sponsorship of other government agencies.
**Voluntary Product Standards**—Developed under procedures published by the Department of Commerce in Part 10, Title 15, of the Code of Federal Regulations. The standards establish nationally recognized requirements for products, and provide all concerned interests with a basis for common understanding of the characteristics of the products. NIST administers this program in support of the efforts of private-sector standardizing organizations.

*Order the* ***following*** *NIST publications—FIPS and NISTIRs—from the National Technical Information Service, Springfield, VA 22161.*

**Federal Information Processing Standards Publications (FIPS PUB)**—Publications in this series collectively constitute the Federal Information Processing Standards Register. The Register serves as the official source of information in the Federal Government regarding standards issued by NIST pursuant to the Federal Property and Administrative Services Act of 1949 as amended, Public Law 89-306 (79 Stat. 1127), and as implemented by Executive Order 11717 (38 FR 12315, dated May 11,1973) and Part 6 of Title 15 CFR (Code of Federal Regulations).
**NIST Interagency or Internal Reports (NISTIR)**—The series includes interim or final reports on work performed by NIST for outside sponsors (both government and nongovernment). In general, initial distribution is handled by the sponsor; public distribution is handled by sales through the National Technical Information Service, Springfield, VA 22161, in hard copy, electronic media, or microfiche form. NISTIR's may also report results of NIST projects of transitory or limited interest, including those that will be published subsequently in more comprehensive form.

**U.S. Department of Commerce**
National Bureau of Standards and Technology
325 Broadway
Boulder, CO 80305-3337